

**NMR analysis of dynamics and interactions of two
G protein-coupled receptors:
the HIV-1 coreceptor CCR5 and
the β_1 -adrenergic receptor**

Inauguraldissertation

zur

Erlangung der Würde eines Doktors der Philosophie

vorgelegt der

Philosophisch-Naturwissenschaftlichen Fakultät

der Universität Basel

von

Anne Grahl

aus Deutschland

Basel, 2020

Originaldokument gespeichert auf dem Dokumentenserver der Universität Basel

edoc.unibas.ch

Genehmigt von der Philosophisch-Naturwissenschaftlichen Fakultät
auf Antrag von

Prof. Dr. Stephan Grzesiek
Prof. Dr. Gebhard F. X. Schertler

Basel, den 11.12.2018

Prof. Dr. Martin Spiess
(Dekan)

Summary

This thesis aims to provide insight into structural and dynamic features of the pharmaceutical highly relevant membrane protein family of G protein-coupled receptors (GPCRs) by Nuclear Magnetic Resonance (NMR) spectroscopy. A quantitative description of the backbone dynamics of the turkey β_1 -adrenergic receptor (β_1 AR) was achieved by the analysis of NMR relaxation data. For the chemokine receptor and HIV-1 coreceptor CCR5 ligand interactions were studied by solution as well as solid-state NMR.

Chapter 1 provides an introduction to the potential and challenges of NMR for membrane protein analysis. The biological function of GPCRs and the current structural and dynamic knowledge are discussed with a particular focus on the turkey β_1 AR. Furthermore, the chapter describes the role of the chemokine receptor CCR5 as major coreceptor for HIV-1 infection and the potential of chemokine analogs as HIV-1 entry inhibitors and signaling modulators of CCR5.

Chapter 2 gives an overview of the relaxation phenomena observed in solution NMR to study protein dynamics. The theoretical basis for extracting dynamic information in the nano- to millisecond time range from experimental relaxation rates and conformational exchange is presented.

Chapter 3 presents a detailed picture of the global and local dynamics of the thermostabilized turkey β_1 AR obtained from experimental ^1H and ^{15}N NMR relaxation. Local backbone motions at 14 different sites of the β_1 AR in its apo form, six binary ligand complexes ranging from inverse agonists to agonists and a ternary agonist/G protein mimicking nanobody complex were investigated. Allosteric coupling across the β_1 -adrenergic receptor was revealed by the pivoting of transmembrane helix 6 on the extracellular side upon intracellular effector site binding. A manuscript with parts of these results is currently under revision (Grahl *et al.*, NMR backbone dynamics reveals mechanism of ligand to effector site allosteric coupling in the β_1 -adrenergic receptor). The final section of the chapter reports on the favorable effect of partial deuteration on the transverse relaxation and spectral appearance of β_1 AR.

Chapter 4 describes the successful expression of human, engineered CCR5 in insect cells and its characterization in different detergent micelles to yield a stable receptor sample for structural characterization. Insect cell expression schemes were implemented to obtain uniform or amino acid-specific isotope-labeled material for backbone NMR studies. CCR5 was globally characterized by ^{15}N relaxation rates indicating no significant nanosecond motions of the receptor independent from the detergent micelle, but exchange dynamics in the micro- to millisecond time range. Initial NMR data on CCR5 have been published (Franke, Opitz, Isogai, Grahl *et al.*, Production of isotope-labeled proteins in insect cells for NMR. *J. Biomol. NMR*, 2018). In addition, promising initial cryo-electron microscopy images of CCR5 have been obtained, which may allow a future full analysis.

Chapter 5 describes the characterization of the potent anti-HIV-1 entry inhibitor 5P12-RANTES-E66S at physiological pH. Interactions studies were conducted with detergent micelles and heparin disaccharide as a model for the binding to the glycosaminoglycan layer on the cell surface.

Chapter 6 provides insight into the complex of CCR5 with the chemokine analog 5P12-RANTES-E66S. A stable, monomeric complex was obtained, and initially characterized by solution NMR. An extended binding interface for CCR5 could be mapped on isotope-labeled 5P12-RANTES-E66S and micro- to millisecond dynamics of the complex-bound

chemokine analog could be detected. High-quality solid-state NMR spectra of the immobilized chemokine•receptor complex were obtained promising for future detailed characterization.

Chapter 7 describes the initial characterization of wild type-like human β_2 -adrenergic receptor by backbone NMR experiments.

Results from this thesis have been or shall be published as follows:

Published:

1. Franke, B., Opitz, C., Isogai, S., Grahl, A., Delgado, L., Gossert, A. D., & Grzesiek, S. (2018). Production of isotope-labeled proteins in insect cells for NMR. *Journal of Biomolecular NMR*, 22(3), 1–12.

Submitted:

2. Grahl, A., Isogai, S., Sharpe, T., & Grzesiek, S. NMR backbone dynamics reveals mechanism of ligand to effector site allosteric coupling in the β_1 -adrenergic receptor. *Nature Communications*, (2018, in revision)

Planned:

1. Grahl, A., Kosol S., Lewandowski, J. R., Grzesiek, S. Interaction of the anti-HIV chemokine analog 5P12-RANTES-E66S with CCR5 studied by NMR. (Chapter 6)
2. Grahl, A., Franke, B., Grzesiek, S. Improvement in isotope-labeling strategies in insect cells for the G protein-coupled receptors CCR5 and β_2 -AR. (Chapter 4 and 7)
3. Goldie, K., Grahl, A., Righetto, R., Eshriew, E. K., Grzesiek, S., Stahlberg, H. The cryo-EM structure of CCR5 in complex with RANTES. (Chapter 4)

Acknowledgments

I would like to thank everyone who by his or her willing support and help made this thesis possible. I had the great pleasure to work with very talented and remarkable individuals throughout the last five years. First and foremost, I would like to express my sincere gratitude to my supervisor Prof. Dr. Stephan Grzesiek for giving me the opportunity and liberty to conduct my thesis in his laboratory. His guidance, the knowledge and expertise that he kindly shared, his help in research and writing, as well as his mentorship, patience and persistence is highly appreciated. I would also like to express my gratitude for his trust to give me the opportunity to work on several methods and projects.

I must offer my profoundest gratitude to my thesis committee members Prof. Dr. Gebhard Schertler and Prof. Dr. Timm Maier for being advisors and guidance. This includes all insightful comments on my work and the evaluation of my progress. In particular, I am grateful to Prof. Dr. Gebhard Schertler for kindly accepting to co-referee my thesis.

This thesis is the result of a combined effort and I have greatly benefited from the helpful nature of several people. Dr. Irena Burmann welcomed me in the group and introduced me to insect cell cultures and the handling of membrane proteins. Dr. Shin Isogai taught me about research in general, experiment planning and execution and introduced me to the concepts and challenges of GPCRs by NMR. He was always available for discussions about the project, providing ideas and suggestions. The fruitful discussions about science and his continuous support are highly appreciated. I would like to express my gratitude to Marco Rogowski for his significant contribution regarding the expression and purification of RANTES. Marco's and Ines Hertel-Hering's efforts also guaranteed the smooth running of the laboratory.

Furthermore, I wish to thank Dr. Christian Opitz for the help on handling and labeling of insect cells. In addition, I am grateful for the discussions and lessons taught on problem solving.

Dr. Bastian Franke deserve my thanks for his help to improve insect cell labeling strategies for CCR5. I would like to thank Drs. Judith Habazettl and Hans-Jürgen Sass for many discussions about the practical and theoretical aspects of NMR and research life.

I am obliged to Dr. Layara Akemi Abiko for helpful discussions on the β_1 AR. I very much appreciated her good company and her enthusiasm. I am particularly grateful to Alexandra Meng and Drs. Judith Habazettl, Bastian Franke and Christian Opitz for proofreading parts of this thesis and their helpful comments on it.

And finally, I would like to acknowledge Drs. Lydia Nisius and Maciej Wiktor for laying a fruitful foundation for my thesis work before I even started. I also would like to thank all the past and present members of the Grzesiek group for their support and for enriching my ideas. My thanks also extend to the present and past members of the Hiller group, especially Dr. Morgane Callon for her guidance during my rotation in Prof. Dr. Sebastian Hiller's lab and for his support and discussions.

Prof. Dr. Józef R. Lewandowski and the Drs. Simone Kosol and Carl Öster are highly acknowledged for the collaboration for the solid-state projects. I have been very privileged to get to know Józef. He welcomed me in his group, taught me solid-state NMR and was always available for good scientific advices.

A special thanks goes to Prof. Dr. Henning Stahlberg and Dr. Kenneth Goldie for proposing the cryo-EM project on CCR5 and the beautiful data arising from it.

I thank Dr. Timothy Sharpe for his assistance and help using the Biophysics Facility instrumentation to get a better understanding of my biological systems. Furthermore, I would

like to acknowledge PD Dr. Daniel Häussinger, who has been a great source of expertise in organic chemistry and helped me with the purification of maraviroc.

I am grateful to the Fellowship for Excellence for the financial support during my thesis, interesting travels and the freedom to find an inspiring project at the Biozentrum. I would like to thank Marcel Scheiwiller for his support.

I would like to express my sincere gratitude to Diana Rueda, Chee-Seng Hee and Dominik Alexander Herbst for their friendship and unconditional support in every difficult situation. I would like to thank Layara Abiko, Elisabeth Lambert, Joka Pipercevic, Johanna Ude, and Guillaume Mas for the good times with them that helped me throughout my thesis.

Lastly, I am deeply grateful for all the support from my family and friends. Ever since, they have provided me a home and have believed in my pursuit, however stubborn. I am forever indebted to my parents, who gave me all opportunities in life.

Contents

Summary	iii
Acknowledgments	vii
Abbreviations and symbols	xiii
1 Introduction	1
1.1 <i>NMR spectroscopy of membrane proteins</i>	1
Membrane proteins	1
Solution NMR studies	2
1.2 <i>G protein-coupled receptors</i>	3
The G protein-coupled receptor superfamily	3
GPCR function.....	3
GPCR structures.....	5
GPCR dynamics and solution NMR studies	6
β_1 AR as model for GPCRs.....	7
Biology of CCR5 and its involvement in disease	8
The chemokine RANTES	10
RANTES analogs	11
The structure of CCR5 in complex with 5P7-RANTES	13
1.3 <i>Aims of the thesis</i>	14
2 Relaxation and dynamics	15
Relaxation in NMR	15
Mechanism of relaxation.....	15
Observable time scales of motions	16
Calculation of relaxation rates.....	17
Exchange processes	18
NMR linewidth.....	19
3 A high-resolution description of the backbone dynamics of the β_1-adrenergic G protein-coupled receptor from NMR relaxation data	21
Organization of the chapter	21
3.1 <i>NMR backbone dynamics reveals mechanism of ligand to effector site allosteric coupling in the β_1-adrenergic receptor</i>	22
3.2 <i>Additional dynamics data on the β_1-adrenergic receptor</i>	69
Results.....	69
Conclusions and perspectives.....	74
Materials and Methods	76

3.3	<i>Improved relaxation behavior of a deuterated β_1-adrenergic receptor</i>	77
	Introduction.....	77
	Results.....	77
	Conclusions and perspectives.....	80
	Materials and Methods	80
4	Insect cell expression and characterization of CCR5	83
	Organization of the chapter	83
	Introduction.....	84
4.1	<i>Characterization of CCR5 expressed in insect cells</i>	85
	Results.....	85
	Conclusions and perspectives.....	102
	Materials and Methods	104
4.2	<i>Production of isotope-labeled proteins in insect cells for NMR</i>	111
5	Detergent and heparin disaccharide interactions of 5P12-RANTES-E66S	137
	Introduction.....	137
	Results.....	137
	Conclusions and perspectives.....	141
	Materials and Methods	141
6	Interaction of 5P12-RANTES-E66S with CCR5	143
	Introduction.....	143
	Results.....	144
	Conclusions and perspectives.....	155
	Materials and Methods	157
7	Initial characterization of ^{15}N-valine-labeled human β_2-adrenergic receptor	
	by NMR	159
	Introduction.....	159
	Results.....	159
	Conclusions and perspective.....	161
	Materials and Methods	162
	References	165

Abbreviations and symbols

Å	0.1 nm
a.u.	arbitrary unit
β ₁ AR	beta-1 adrenergic receptor
CCL5	C-C motif chemokine ligand 5
CCR5	C-C chemokine receptor type 5
CHS	cholesteryl hemisuccinate
CP	cross polarization
CPM	N-[4-(7-diethylamino-4-methyl-3-coumarinyl)phenyl]maleimide
CRINEPT	cross relaxation-enhanced polarization transfer
CRS	chemokine recognition site
CSA	chemical shift anisotropy
CV	column volume
CXCR4	CXC chemokine receptor 4
Da	dalton, g mol ⁻¹
DDM	n-dodecyl-β-D-maltopyranoside
DEER	double electron-electron resonance
DM	n-decyl-β-D-maltopyranoside
DSS	dimethyl silapentane sulfonate
<i>E. coli</i>	Escherichia coli
ECL	extracellular loop
EDTA	ethylenediaminetetraacetic acid
EM	electron microscopy
FC-12	Fos-choline-12
FID	free induction decay
GDP	guanosine diphosphate
GPCR	G protein-coupled receptor
GRK	GPCR kinase
GTP	guanosine triphosphate
h	hours
HIV	human immunodeficiency virus
hpi	hours post infection
HSQC	heteronuclear single quantum coherence
HRP	horseradish peroxidase
ICL	intracellular loop
IMAC	immobilized ion affinity chromatography
INEPT	insensitive nuclei enhancement by polarization transfer
LMNG	Lauryl maltose neopentyl glycol
MALS	multi-angle light scattering
MAS	magic angle spinning
MD	molecular dynamics
MIP-1α	macrophage inflammatory protein-1α
MIP-1β	macrophage inflammatory protein-1β
MWCO	molecular weight cut-off

NMR	nuclear magnetic resonance
NOE	nuclear Overhauser effect
NOESY	nuclear Overhauser enhancement spectroscopy
OS	oriented samples
PAGE	polyacrylamide gel electrophoresis
PBS	phosphate buffered saline
PDB	RCSB Protein Data Bank, www.rcsb.org/pdb
PE	phycoerythrin
ppm	parts per million
RANTES	regulated on activation, normal T cell expressed and secreted
SEC	size-exclusion chromatography
SHIV	simian/human immunodeficiency virus
SDS	sodium dodecyl sulfate
SEC	size-exclusion chromatography
Sf9	Spodoptera frugiperda
S/N	signal-to-noise ratio
TBS	Tris buffered saline
TBST	Tris buffered saline with Tween
TM	transmembrane
TROSY	transverse relaxation optimized spectroscopy
wt	wild type
YE	yeast extract

1 Introduction

1.1 NMR spectroscopy of membrane proteins

Membrane proteins

Membranes are cell barriers to separate organelles from the cytosol and the intracellular content from the extracellular environment. Besides the lipid bilayer responsible for the barrier function, membranes contain proteins to provide exchange of matter and information. 30 to 40 % of all expressed human genes encode for membrane proteins serving as pores, transporters, adhesion molecules, enzymes and receptors (1, 2). Membrane proteins are essential for cellular homeostasis and human health. Hence, they are major targets for drug developments (3, 4).

Membrane proteins are classified as either peripheral or integral. The first are water-soluble proteins tethered by a fatty acid or other hydrophobic anchor to the membrane. The latter are water insoluble and span the membrane once or several times. The transmembrane segment of integral membrane proteins consists either of β -sheets or α -helical secondary structures. The β -sheets form barrels in the outer membrane of prokaryotic origin and are stabilized by interstrand hydrogen bonds. α -helical membrane proteins occur in eukaryotic membranes and prokaryotic inner membranes and span the membrane once or several times. Multi-transmembrane helical structures are stabilized by hydrophobic contacts between the helices and are less stable than β -barrels.

Despite their high pathophysiological impact, structures of membrane proteins currently (2018) represent less than 2 % of the protein data base (PDB) (5). Structural work on membrane proteins requires the removal from their natural membrane environment and the reconstitution in membrane mimetics such as micelles, bicelles, nanodiscs, phospholipid bilayers or amphipols (6, 7).

The first low-resolution membrane protein structure was obtained by electron microscopy (EM) in 1975 of bacteriorhodopsin using tilt series micrographs of its the natural two-dimensional crystal, the purple membrane (8). The first high-resolution structure of a membrane protein was obtained by X-ray crystallography of the photosynthetic reaction center (9). Since then most structures of membrane proteins have been solved by this technique. The introduction of the lipidic cubic phase (10) and other advances have further improved the success rate and resolution of this method (11, 12). The recent breakthrough in detector technology has made it possible to obtain high-resolution structures of large membrane proteins and membrane protein complexes by single-particle cryo-EM (13). Progress in this field is ongoing to reduce the required particle size to the range of 50-100 kDa (14).

Nuclear Magnetic Resonance (NMR) spectroscopy is an alternative for obtaining atomic resolution structures of membrane proteins (7, 15). Most importantly, this method also provides information on protein dynamics which allows to connect structural knowledge to the function of a protein.

Advanced, heteronuclear NMR studies require the labeling by the stable isotopes ^2H , ^{13}C , ^{15}N (16), which is well-established for heterologous expression in *E.coli*. Such labeling is considerably more difficult for eukaryotic expression systems. However, recent progress in this field allows now to also label challenging membrane proteins for their study by NMR (17-19).

Solution NMR studies

Membrane proteins can be studied by solution NMR in solubilized form as particles reconstituted into detergent micelles, bicelles or nanodiscs (20). Solution NMR studies are limited by the size of the particle, which is especially critical for membrane proteins. Besides the protein also the membrane mimetic contributes to the apparent molecular weight. This leads to large rotational correlation times, and in consequence to short transverse magnetization times and broad lines (Chapter 2). The quality of the spectra is hence diminished manifesting itself in low sensitivity and resonance signal overlap. Experimental methods to extend the size limit in solution have been developed such as transverse relaxation optimized spectroscopy (TROSY) (21) or cross relaxation-enhanced polarization transfer (CRINEPT) (22). Deuteration of proteins to reduce strong dipolar couplings of protons also improves the relaxation properties and reduces the resonance linewidth (23, 24). Furthermore, segmental or selective labeling can reduce the signal overlap especially occurring in α -helical regions (25-27).

Combining such approaches has led to the structure determination of β -barrel and α -helical membrane proteins (28, 29). Furthermore, solution NMR strongly contributes to the understanding of membrane proteins by giving insights into their intrinsic dynamics, ligand binding and lipid interactions (30-34).

Solid-state NMR studies

In contrast to solution NMR, the solid-state NMR analysis of membrane protein is not limited by the size of the particle. Instead resolution and sensitivity are determined by the orientation-dependence of spin interactions such as dipolar coupling or chemical shift anisotropy. These strong anisotropic interactions are manifested in broad lines and can be overcome by oriented samples (OS) (35, 36) or magic angle spinning (MAS) (37). Membrane protein structures have been solved by OS solid-state NMR using magnetically aligned bicelles or mechanically aligned lipid bilayers (38-40).

MAS solid-state analysis with ^{15}N - and ^{13}C -based experiments have been used for membrane proteins in proteolipid 2D crystals, precipitates or microcrystals (41-43). Combination of MAS at frequencies above 40 kHz, deuteration and high magnetic field strength makes it possible to record proton-based experiments by suppressing the strong homonuclear dipolar couplings and reducing the linewidth (44-48). Ultra-fast MAS frequencies at 100 kHz and higher now even provides high-quality spectra of protonated samples in the solid state (49). Solid-state NMR has been used to solve the structure of membrane proteins, but has also given insight into function, dynamics and ligand interactions (15, 50-55). Recently, even the study of membrane proteins in their native environment has become possible by advanced labeling and solid-state NMR techniques (56-58).

1.2 G protein-coupled receptors

The G protein-coupled receptor superfamily

G protein-coupled receptors (GPCRs) form the largest class of human membrane proteins, transducing signals from the extracellular environment to the cellular interior. So far over 800 genes encoding for GPCRs have been identified, which corresponds to 4 % of the human genome (59, 60). Based on phylogenetic analysis, they have been divided into 5 superfamilies or 4 classes: rhodopsin-like receptors (class A), secretin and adhesion receptors (class B), glutamate receptors (class C) and frizzled/taste2 receptors (class F) (60, 61). Class A has 719 members in humans (62). GPCRs share a common architecture consisting of an extracellular N-terminal sequence, seven transmembrane helices connected by three intra- and extracellular loops, and an intracellular C-terminal sequence. The structural diversity of GPCRs is generated by varying length and structure of the nonmembrane regions. Although they share a common fold, GPCRs accommodate a wide diversity of ligands in the orthosteric ligand-binding pocket on their extracellular side. These range from photons to ions, and from small molecules like neurotransmitters and hormones to proteins like chemokines (63, 64). GPCRs are involved in disorders of the central nervous system, metabolic dysregulation, and cancer, as well as inflammatory, infectious and cardiac diseases (65). Due to their high impact on pathophysiological processes and easy accessibility by drugs, GPCRs are key pharmaceutical targets. Nowadays, ~35 % of marketed drugs are directed towards GPCRs (66-68).

GPCR function

The classical paradigm of GPCR function involves a cycle wherein extracellular ligand binding induces activation and downstream signaling followed by inactivation and receptor recycling (Figure 1.1). In detail, ligand binding to the extracellular orthosteric ligand binding pocket induces conformational changes at the intracellular side of the receptor and enables binding of heterotrimeric G protein. Thereby, the GPCR acts as a guanine exchange factor (GEF), facilitating the turnover from GDP to GTP-bound G protein and triggering the dissociation of heterotrimeric G protein into G_α and $G_{\beta\gamma}$ subunits, which can both initiate downstream signaling cascades (69-71). Heterotrimeric G proteins are classified according to their G_α subunit as G_s (stimulatory), G_i (inhibitory) or G_q , each leading to different downstream signaling pathways such as activation of protein kinase A and cAMP production, inhibition of protein kinase A and hyperpolarization or activation of phospholipase C and calcium influx (72). Phosphorylation of the GPCR C-terminus by a G protein-coupled receptor kinase (GRK) and the subsequent binding of arrestin (73, 74) leads to the desensitization of G protein signaling due to the steric hindrance of the binding. Furthermore, bound arrestin acts as a scaffold for clathrin-mediated internalization of GPCRs via endosomes and thereby decreases the receptor density on the cell surface (75). Receptors are either degraded or recycled to the cell membrane via the trans-Golgi network (76, 77). Besides the classic role in GPCR desensitization, additional functions for arrestin have been revealed: (i) arrestin can bind to GPCRs without prior G protein binding and phosphorylation (78), (ii) arrestin can initiate downstream signaling by itself (79), and (iii) arrestin-bound GPCRs in internalized compartments can simultaneously bind and activate G proteins (80).

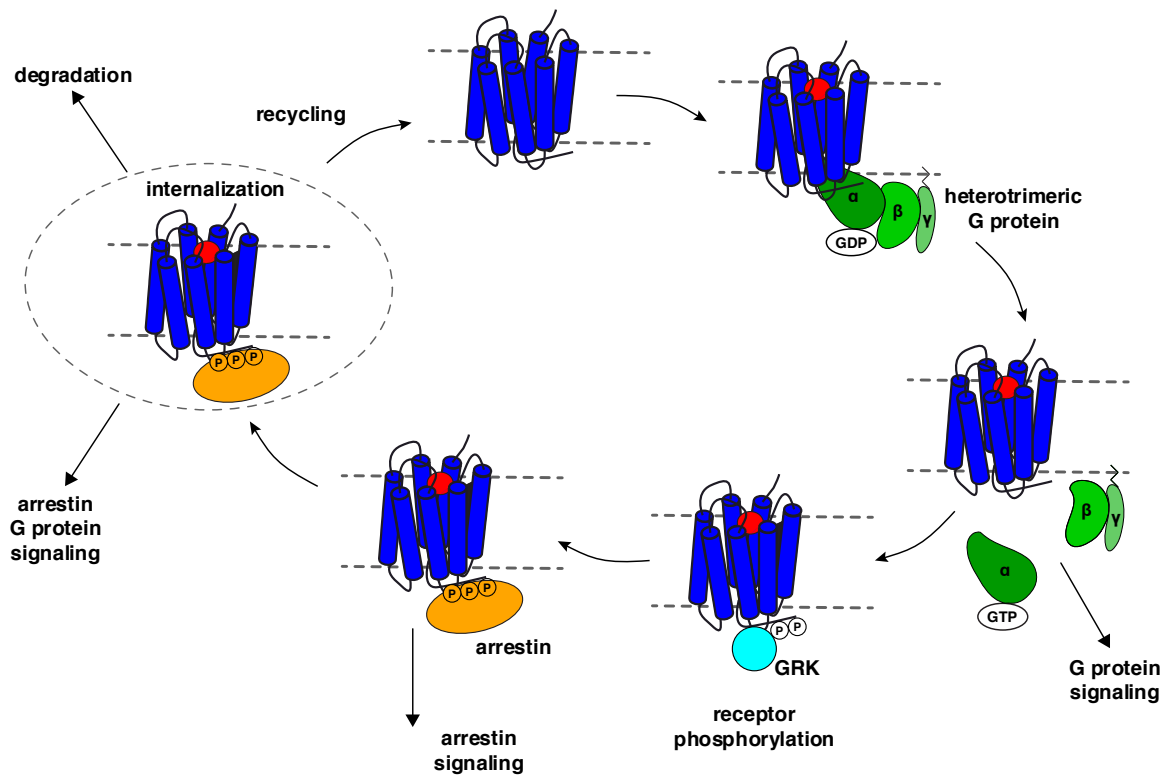


Figure 1.1 GPCR functional cycle, intracellular interaction partners and signaling pathways.

Based on their efficacy of G protein activation (Figure 1.2), orthosteric GPCR ligands are classified as agonists, antagonists, or inverse agonists. In the absence of any ligand, many GPCRs display a basal activity of G protein activation. Full agonists then induce the maximal G protein activation, whereas partial agonists induce lower activation. Antagonists bind to the receptor and compete with other ligands, but do not affect its basal level. Finally, inverse agonists inhibit the basal activity.

The concept of functional selectivity or biased signaling was introduced for GPCR ligands that preferentially activate one distinct downstream signaling pathway e.g. G protein vs. arrestin.

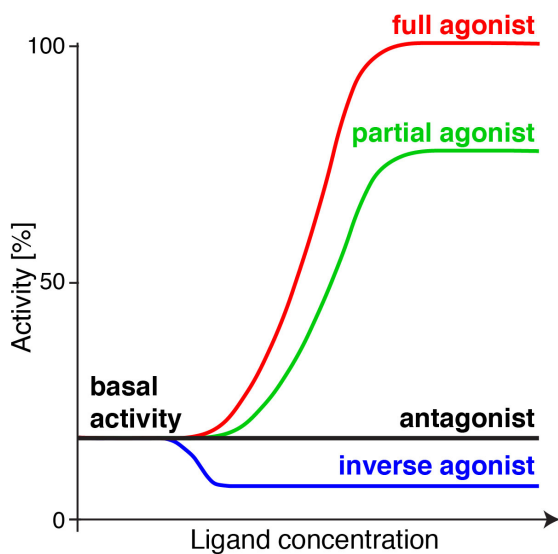


Figure 1.2 Pharmacological classification of different ligands based on GPCR activity.

GPCR structures

Rhodopsin, a light-sensitive receptor essential for photo transduction, was the first solved high-resolution structure of a GPCR and revealed the common transmembrane architecture of seven α -helices (81). It can be extracted from natural sources. Structural work on other GPCRs has remained challenging due to their low expression levels, low stability outside their natural membrane environment and conformational heterogeneity of the receptors (82). Protein engineering for receptor stabilization e.g. introduction of point mutations, truncation of flexible regions and insertion of fusion proteins, as well as functional expression in higher eukaryotic systems, was leading to sufficient receptor material for structural studies (83, 84). Furthermore, lipidic cubic phase and the usage of nanobodies facilitated the crystallization of GPCRs (11, 78, 79). These combined efforts have resulted in the structure elucidation of the human β_2 -adrenergic receptor (β_2 AR) as the first non-rhodopsin GPCR in 2007 (85, 86).

Nowadays, 386 structures of 52 unique GPCRs have been published, representing members of the classes A, B, C and F (87). Binary complexes of class A GPCRs with orthosteric ligands ranging from inverse agonists to agonists have been solved mostly in an inactive conformation (Figure 1.3a), and only few receptors like the A_{2A} adenosine receptor showed an intermediate-active state (88, 89). A breakthrough in the work on GPCRs was the elucidation of the active structure in complex with G protein as well as with G protein-mimicking nanobodies (90-92). The active structures revealed major conformational rearrangements on the intracellular side of the receptor, comprising as dominant features a 14 Å outward movement of transmembrane helix 6 (TM6) and a helical extension of TM5 to accommodate G protein binding (Figure 1.3b). GPCR structures have also been solved in complexes with arrestin (93, 94).

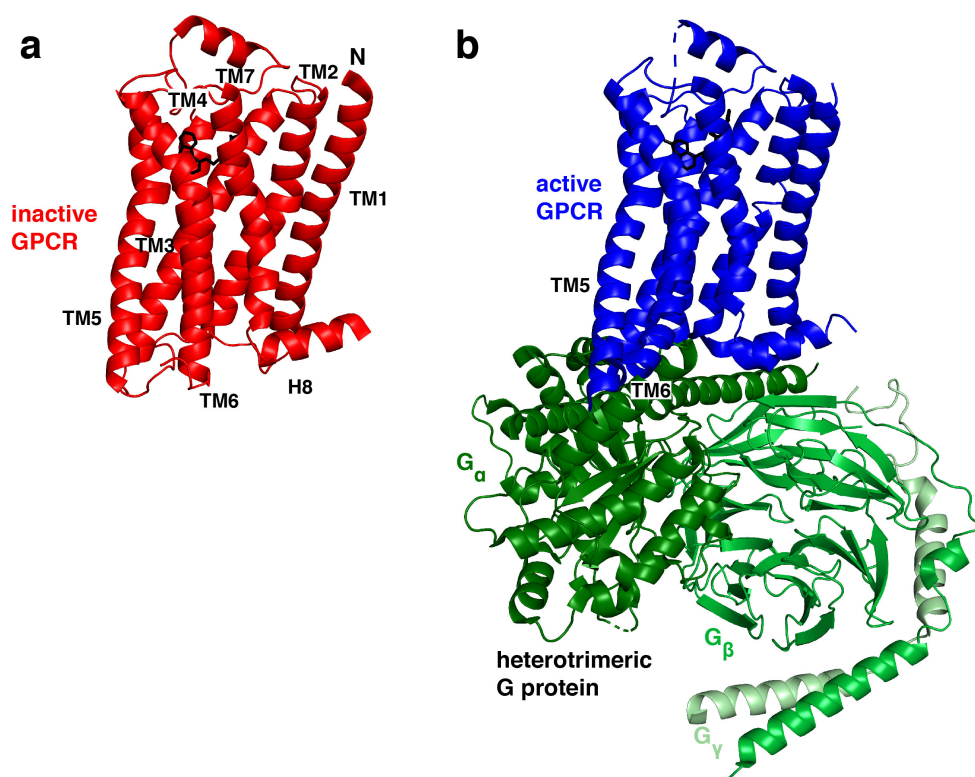


Figure 1.3 Inactive and active crystal structure of a GPCR. The orthosteric ligands are shown as black sticks. **(a)** Binary complex of β_2 AR with inverse agonist carazolol (2RH1) shown in red. **(b)** Ternary complex of agonist-bound β_2 AR with heterotrimeric G protein (3SN6) depicted in blue and green respectively.

The only GPCR apo structure, that of CXCR1, has been obtained from solid-state NMR (38). Solution NMR has provided the structures of two seven-helical GPCR-like receptors, the archaeobacterial sensory rhodopsin and bacterial proteorhodopsin (95, 96).

Current progress in cryo-electron microscopy has now yielded structures of several GPCR-G protein complexes with different G_α subunits (97-100).

GPCR dynamics and solution NMR studies

High-resolution structural and dynamical information on GPCRs is needed to understand their ligand selectivity, signal transduction from ligand binding pocket to the intracellular side, the formation of signaling complexes from apo receptors as well as the bias for G protein or arrestin signaling. Whereas detailed structural insights are obtained by the rapidly increasing number of solved GPCR structures, each of them represents only a snapshot of a single conformation. However, GPCRs are highly dynamic and, interchanging among a multitude of distinct conformations to fulfill their intrinsic function (101, 102). Therefore, knowledge on the dynamics is required to fully understand GPCR function.

Several biophysical methods have been applied to determine amplitudes and timescales of GPCR dynamics. Electron paramagnetic resonance (EPR) and fluorescence spectroscopy have provided distance distributions between conformations, their lifetimes as well as the time scale of receptor activation for a few reporter sites (103-107). Molecular dynamic (MD) simulations have given insights into ligand binding and transition from the active to the inactive receptor states (108-111).

High-resolution dynamic descriptions of GPCRs can be obtained by solution NMR at the atomic level and on the time scale from picoseconds to seconds, with no or only minimal invasiveness on the protein. Still, GPCRs are a challenging target for NMR. First, their high apparent molecular weight in membrane mimetics leads to fast decay of transverse magnetization and broad linewidths. Additionally, internal dynamics contributes to the line broadening. Second, due to their mostly α -helical content, the spectral dispersion is limited. Third, most GPCRs require higher eukaryotic cells for functional expression, and only recent progress has provided more economical ways of uniform or amino acid-specific isotope labeling in such systems (112-114).

So far, most NMR studies on GPCRs have been carried out on side chains due to their favorable spectroscopic properties using ^{13}C -methyl-tagged lysines (115), ^{19}F -labeled cysteines (107, 116) and ^{13}C -methyl groups of methionine or alanine (117-120). The reporter sites revealed information on local conformational equilibria, the dynamics upon receptor activation, effects of the membrane mimetic and the basal activity of GPCRs.

In contrast, backbone NMR can report on backbone geometry and hydrogen bonding and gives more insights into long-range motions. Earlier work on GPCRs had only revealed residues from the flexible C-terminus as other resonances were broadened beyond detection (121, 122). In 2016, the first detailed backbone NMR analysis of a detergent-solubilized GPCR, the thermostabilized turkey β_1 -adrenergic receptor in its apo state and various ligand forms, was published using selectively labeled ^{15}N -valines as reporter sites (114). A high-resolution ^1H - ^{15}N spectrum has also been obtained of uniformly labeled, engineered rat neurotensin receptor 1 in nanodiscs, but no further analysis was reported (123). More recently well-resolved ^1H - ^{15}N spectra have also been obtained from the wild-type-like A_{2A} adenosine receptor and, combined with tryptophan side-chain analysis, have revealed an allosteric switch between the ligand-binding pocket and the intracellular side (124).

β_1 AR as model for GPCRs

Adrenergic receptors are class A GPCRs and are widely expressed in peripheral tissues and the neuronal system. They are activated by their endogenous ligands noradrenaline and adrenaline, which are hormones and neurotransmitters affecting heart and lung function, blood pressure, metabolism and the nervous system.

The β_1 -adrenergic receptor (β_1 AR) is important for the cardiovascular system and is highly expressed in the heart. Antagonists and inverse agonists of β_1 AR such as atenolol are used as drugs to treat hypertension and heart disease (125). The turkey β_1 AR has been used for structural studies due to its higher expression level and stability compared to its human homolog (126). For successful structure elucidation, point mutations as well as truncations of the N-terminus, third intracellular loop and C-terminus have been introduced, leading to increased receptor stability (127). This stabilizes β_1 AR towards an inactive state with decreased affinity for agonists (128). Several crystal structures of β_1 AR in complex with orthosteric ligands ranging from antagonists to agonists have been solved (129). The structures are almost completely superimposable independent of the ligand nature (Figure 1.4a). In contrast, backbone NMR studies of ^{15}N -valine-labeled β_1 AR indeed have revealed distinct differences of structure and dynamics between apo form, antagonist as well as agonist complexes showing a modulated equilibrium between active and inactive states (Figure 1.4b, c, d) (114).

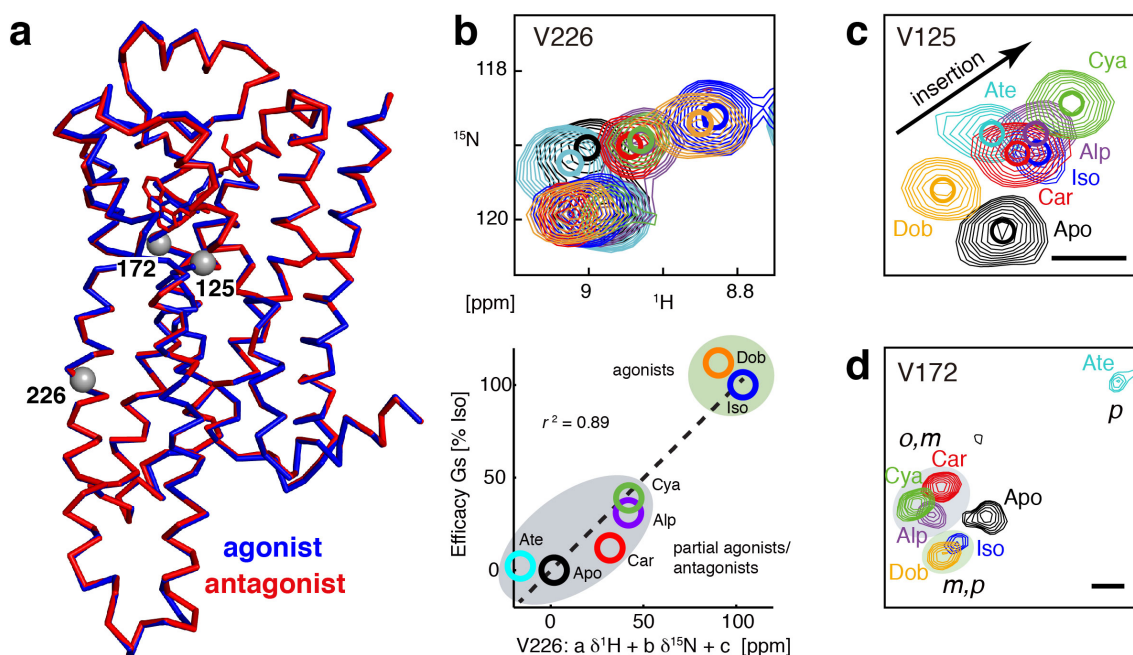


Figure 1.4 Heterogeneous response of turkey β_1 AR to various ligands as revealed by backbone NMR. **(a)** Alignment of β_1 AR crystal structures in complex with antagonist (carvedilol, 4AMJ, chain B) and agonist (isoprenaline, 2Y03, chain B) shown as ribbons in red and blue, respectively. Valines 125, 172 and 226 are depicted as grey spheres. **(b)** Correlation of ligand-induced chemical shift changes for V226 at the intracellular side and G_s efficacy. **(c-d)** Ligand-induced chemical shift changes in the orthosteric binding pocket responding to **(c)** ligand-insertion depth for V125 and **(d)** ligand head-group substitution for V172. Panels **b-d** are adapted from Isogai *et al.* (114).

Resonances in the vicinity of the ligand pocket showed a heterogeneous response to ligands according to their chemical structure and affinity (Figure 1.4c, d). The chemical shift response at the intracellular side of TM5 correlated linearly to ligand efficacy for G protein pathway

activation (Figure 1.4b). In the ternary, active state with the G protein-mimicking nanobody, large spectral changes were observed for resonances in TM3 to TM6 and the extracellular side of the receptor (114). Recent side-chain NMR studies with ^{13}C -methyl reporter sites have furthermore revealed differences at the intracellular side between a basal active $\beta_1\text{AR}\cdot\text{G}$ protein-mimicking nanobody complex and the active ternary complex with an agonist (119).

Biology of CCR5 and its involvement in disease

CCR5 is a class A GPCR expressed on the surface of immune effector cells (leukocytes) including macrophages, antigen-presenting cells, T cells, and natural killer cells, but also non-immune cells located mostly in the central nervous system (130, 131).

Binding of its endogenous chemokine ligands MIP-1 α (macrophage inflammatory protein-1 α , CCL3), MIP-1 β (CCL4) and RANTES (regulated on activation, normal T cell expressed and secreted, CCL5) activates intracellular pathways, which are triggering inflammation and immune response (132, 133). CCR5 is involved in several pathophysiological processes such as infections (e.g. Hepatitis C, HIV-1 and dengue virus), inflammatory diseases (e.g. rheumatoid arthritis, inflammatory bowel disease, atherosclerosis and multiple sclerosis) and cancer (130, 134, 135).

CCR5 has received much attention since it was identified as the coreceptor for HIV-1 (human immunodeficiency virus-1), the infection causing AIDS (acquired immunodeficiency syndrome) (136-139). Cell entry of HIV-1 requires the sequential interaction of the viral spike complex with the membrane proteins CD4 and CCR5 on the host cell surface (Figure 1.5) (140, 141). The HIV-1 envelope spike is a trimer of the viral surface glycoprotein gp120 in complex with the transmembrane glycoprotein gp41. Initial gp120 binding to CD4 on the cell surface triggers a conformational change, which exposes the V3 loop of gp120 as recognition site for CCR5. The subsequent binding to CCR5 in turn triggers a conformational change of gp41, which then inserts into the host membrane, leading to the fusion of viral and host cell membranes and the release of the virion into the cell (142).

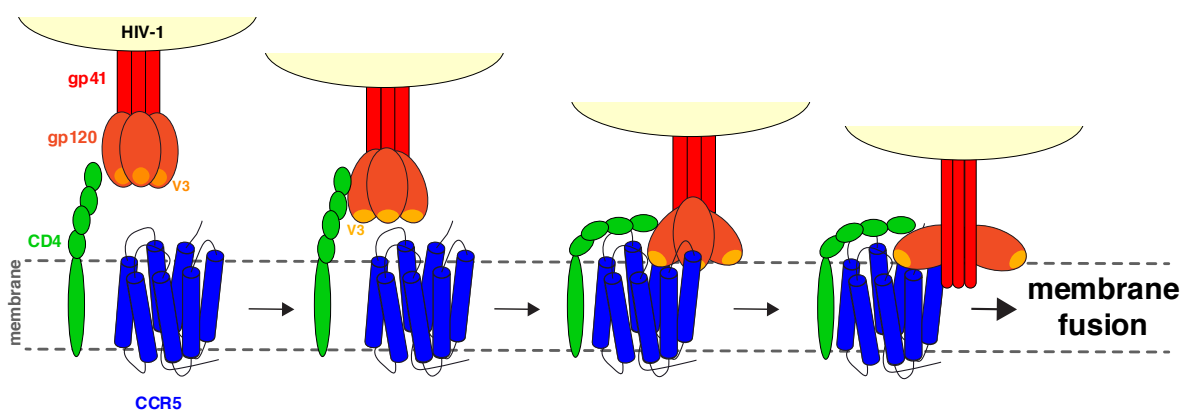


Figure 1.5 Model for HIV-1 cell entry as essential step for infection. HIV-1 envelope glycoproteins gp120 and gp41 interact with host cell-membrane components. Upon gp120 binding to CD4, a conformational change is triggered and the V3 binding epitope for CCR5 is exposed. Following binding to the coreceptor, a major conformational change enables gp41 to fuse with the host cell membrane leading to the release of viral material into the cellular interior.

Besides CCR5, the chemokine receptor CXCR4 also acts as coreceptor for HIV-1, forming the basis for HIV-1 tropism (143, 144). R5-tropic strains bind CCR5 and are associated with initial infections and person-to-person transmission, whereas X4-tropic strains recognize

CXCR4 in later stages of the disease (145). Humans homozygous for the CCR5 Δ 32 allele are resistant to virus infection (146, 147). The CCR5 Δ 32 allele contains a premature stop signal in the extracellular loop 2 (ECL2) of CCR5, leading to protection from infection due to a non-functional HIV-1 coreceptor.

Due to these mechanisms, CCR5 has become an important target for HIV-1 prevention and therapy. Small-molecule ligands of CCR5 have been developed as HIV-1 therapeutics, and maraviroc is the first marketed drug of this class (148-150). Drug development on CCR5 is especially focusing on CCR5 for HIV-1 prevention. Orally administered drugs are promising for prophylaxis strategies (151) whereas topically applied microbicides block the sexual transmission of HIV-1 (152).

The crystal structure of engineered CCR5 bound to the inverse agonist maraviroc was solved in 2013 (153) and shows the typical fold of a GPCR with seven transmembrane helices followed by a short, solvent-exposed α -helix at the C-terminus (Figure 1.6a). The extracellular space is stabilized by two disulfide bonds connecting the N-terminus and ECL3 as well as ECL1 and ECL2 (154). The ligand-binding pocket is less buried and more solvent accessible than in other class A GPCR structures, providing space for the chemokine protein ligands. The inverse agonist maraviroc is deeply inserted into the ligand-binding pocket and stabilizes the receptor in an inactive conformation. Maraviroc is classified as an allosteric HIV-1 entry inhibitor and stabilizes CCR5 in a conformation that prevents binding of gp120 (155-157).

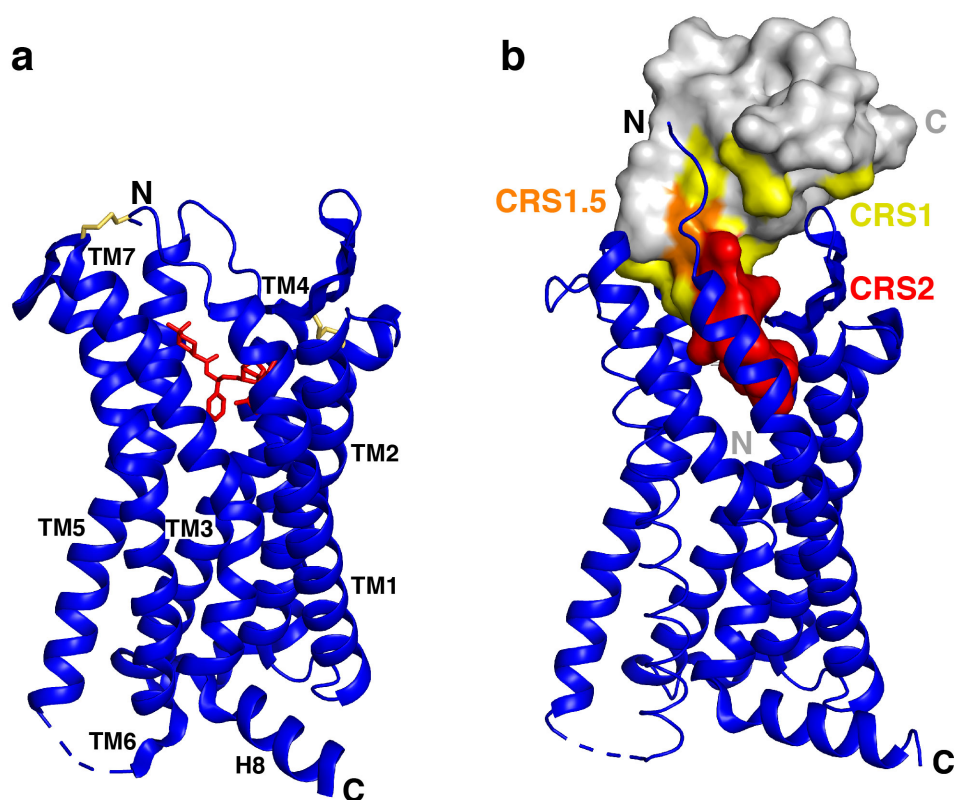


Figure 1.6 Crystal structures of CCR5. **(a)** CCR5 in complex with maraviroc (4MBS, chain A). The protein backbone and maraviroc are shown in blue and red, respectively. The extracellular disulfide bonds are depicted as yellow sticks. **(b)** Structure of the CCR5•5P7-RANTES complex (5UIW). CCR5 and 5P7-RANTES are shown in ribbon and surface representation, respectively. The CCR5 interaction surfaces are mapped on 5P7-RANTES and color coded as follows: CRS1 (yellow), CRS1.5 (orange) and CRS2 (red).

Although small-molecule drugs like maraviroc show promising effects as HIV-1 entry inhibitors, viral resistance develops due to mutations in gp120, which then binds to CCR5 already occupied by maraviroc (158, 159).

Posttranslational modifications are essential for the functionality of CCR5. The first disulfide bond connecting the N-terminus and ECL3 is required for high-affinity chemokine binding (160). The N-terminus, not resolved in the crystal structure, is modified by O-glycosylation and tyrosine sulfation, required for high-affinity ligand binding (161, 162). Tyrosine sulfation is also important for the binding of gp120 (161, 163). Whereas the palmitoylation of three C-terminal cysteines anchors CCR5 to the membrane and facilitates receptor trafficking (164), the phosphorylation of C-terminal serines by GRKs is important for arrestin interaction (165).

The chemokine RANTES

CCR5 belongs to the class A subfamily of chemokine receptors, which consists of 18 GPCRs and 4 atypical decoy receptors in humans. Binding of chemokines to CCR5 induces directed cell migration, which is called chemotaxis (166). The ~50 human chemokines are small secreted proteins that are divided into the subclasses C, CC, CXC, and CX₃C based on the arrangement of their N-terminal cysteines. The chemokine receptors are named according to the main chemokine subclass to whom they are binding. Many chemokines bind to multiple receptors, and also receptors can recognize several chemokines, thereby creating a dense network of interactions. Chemokines have two distinct physiological interaction partners, i.e. glycosaminoglycan and chemokine receptors, which cooperatively control their function of attracting immune cells to the site of inflammation (167). Chemokines are secreted in response to inflammatory signals. Glycosaminoglycan concentrates them on the cell surface or extracellular matrix and generates an immobilized gradient. This directs migrating leukocytes towards the inflammation site. The interaction of chemokines with chemokine receptors and glycosaminoglycan is almost mutually exclusive (168). Chemokine receptors bind mostly monomeric chemokines whereas glycosaminoglycan stabilizes chemokine oligomerization

The chemokine RANTES (CC-chemokine ligand 5, CCL5) is secreted by endothelial cells and activated leukocytes. Its binding to CCR1, CCR3 and CCR5 (C-C chemokine receptor type 5) triggers the immune response. RANTES shows the typical fold of a chemokine (Figure 1.7a). The N-terminus is followed by two conserved cysteines, a long N-loop and a 3₁₀ helix turn. The core is formed by three antiparallel β -sheets separated by short loops which are named 30s-, 40s- and 50s-loop, respectively. The C-terminus forms an α -helix. The disulfide bonds from the N-terminus to the core stabilize the structure. RANTES dimerizes through an intermolecular β -sheet formed between the N-termini of two monomers. Dimers can further form higher oligomers by interactions between the second β -sheet of one part of the dimer with the C-terminal α -helix of a second dimer (Figure 1.7b). The oligomerization of RANTES is reinforced by the interaction with glycosaminoglycan (169).

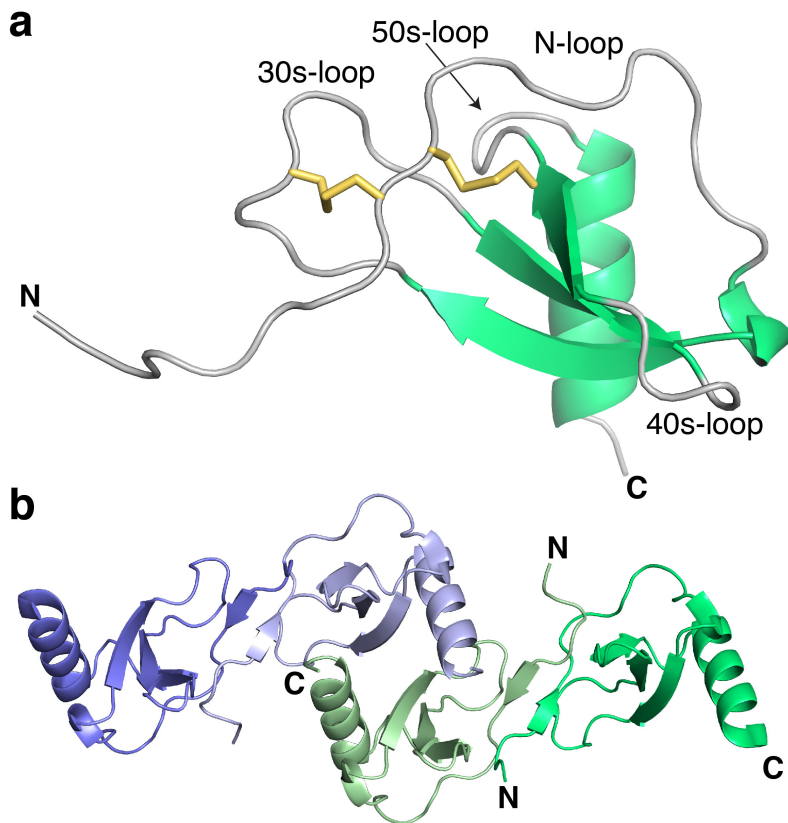


Figure 1.7 Structures of RANTES. **(a)** RANTES monomer (1B3A, chain A) with β -strands and helical regions shown in green. The two disulfide bonds are depicted as yellow sticks. **(b)** Model of RANTES oligomerization (2L9H). Dimerization occurs through an intramolecular β -sheet between two monomers (chain A and B in blue and light blue as well as chain C and D in green and pale green). Tetramers are formed from two dimers in green and blue, respectively. The tetrameric form can be extended into large elongated polymers by repetition of the subunits.

Binding of the agonist RANTES to CCR5 triggers two distinct intracellular pathways (170, 171). At low RANTES concentrations, the high-affinity signaling pathway leads to the dissociation of heterotrimeric G_i protein thereby triggering calcium influx and chemotaxis. At high RANTES concentrations, the low-affinity pathway activates the T cell via a protein tyrosine kinase (172, 173). CCR5 is desensitized by arrestin resulting in the internalization of the receptor and its recycling via the trans-Golgi network back to the plasma membrane.

RANTES analogs

MIP-1 α , MIP-1 β and RANTES, the endogenous ligands of CCR5, have been shown to counteract HIV-1 infection even before CCR5 had been identified as coreceptor (174). RANTES showed the highest potency among the endogenous ligands and made RANTES a lead structure in the development of novel HIV-1 entry inhibitors (175). Proteolytic truncation of wild type (wt) RANTES by two residues on the N-terminus provides stronger HIV-1 inhibition, but reduces G protein activation as well as chemotaxis (176, 177). Further truncation and mutation analysis revealed that antiviral activity and pro-inflammatory function can be uncoupled by modifications of the RANTES N-terminus (178, 179). The analog PSC-RANTES, chemically modified at the N-terminus, was capable of protecting macaques from simian/human immunodeficiency virus (SHIV) in vaginal-transmission experiments (180). Screening of mutations within the first 9 residues has led to several

RANTES analogs showing strong anti-HIV potency with differing pharmacological effects on CCR5 (Table 1.1) (181). All mutations are localized before the first cysteine, keeping the RANTES core unaffected. These fully recombinant RANTES analogs are interesting as topically applied microbicides, due to their lower production costs in comparison to the chemically synthesized PSC-RANTES (182). The superior HIV-1 entry inhibition by RANTES analogs arises either from the steric hindrance of the gp120 binding to the CCR5•RANTES complex on the cell surface or by internalization of this complex (Figure 1.8) (183, 184). The large interaction surface of chemokine analogs with CCR5 compared to small ligands such as maraviroc reduces viral escape mechanisms and even causes coreceptor switching (185).

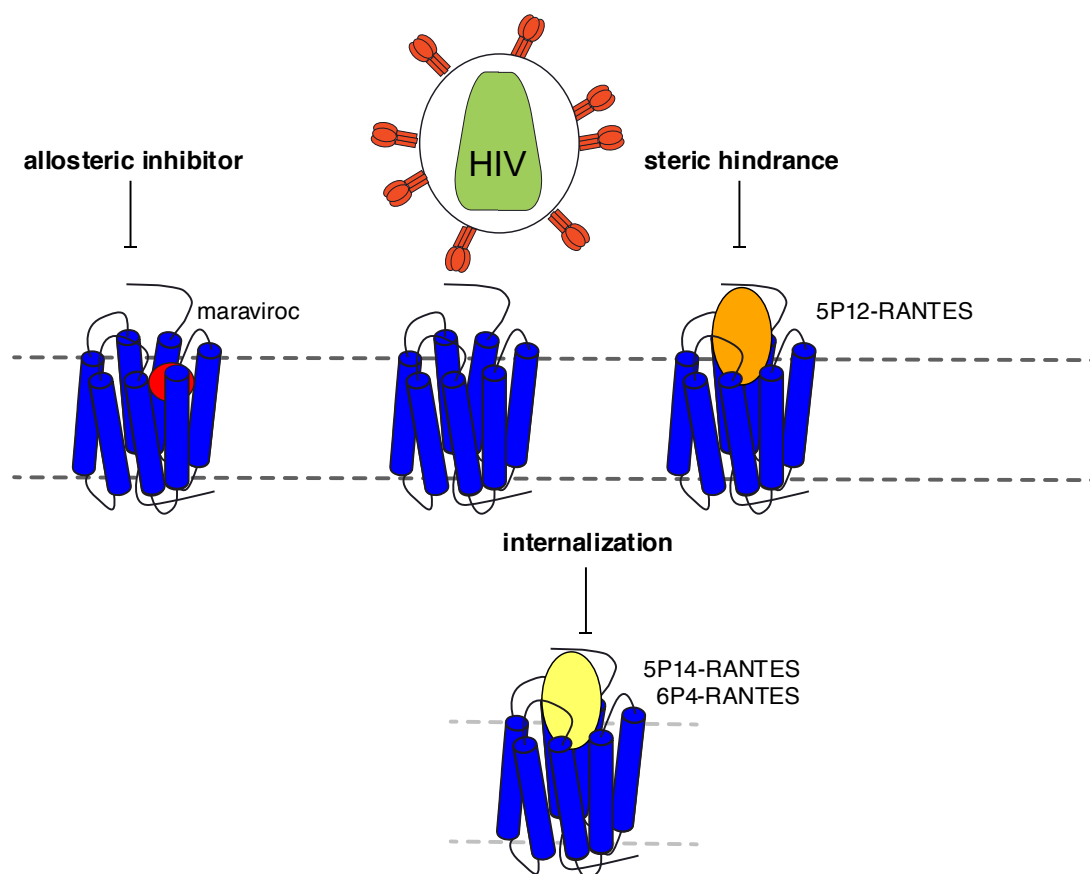


Figure 1.8 Different approaches of blocking HIV-1 entry via CCR5 using allosteric inhibition by small molecules such as maraviroc or RANTES analogs for steric hindrance or receptor internalization.

5P12-RANTES binds CCR5 with low nanomolar affinity and inhibits HIV-1 entry via steric hindrance. Its antagonistic properties reduce the risk of inflammation as a side effect (182). 5P12-RANTES is currently being tested in clinical trials as topically applied HIV-1 entry inhibitor (135, 186). PSC-, 6P4- or 5P14-RANTES trigger the sequestration of CCR5 from the cell surface and thereby inhibit HIV-1 infection. 6P4- or PSC-RANTES exhibit stronger agonistic effects than wt-RANTES and activate G protein signaling, while 5P14-RANTES acts as a biased agonist causing arrestin recruitment in a G protein-independent manner (187, 188).

Binding of PSC-, 5P14- or wt-RANTES to CCR5 leads all to receptor internalization. The superior efficacy of 5P14- and PSC-RANTES vs. wt-RANTES as HIV-1 entry inhibitors arises

from the longer intracellular retention time. The latter is determined by the duration of arrestin interaction, which controls the subsequent pathway for receptor internalization (189).

CCR5 bound by wt-RANTES is recycled from the endosome and trafficked back to the cell membrane via the trans-Golgi network. The CCR5•PSC-RANTES complex is recycled via the same pathway, but stays longer in the Golgi network. In contrast, CCR5•5P14-RANTES is not recycled to the cell surface, but remains in the endosome.

Table 1.1 N-terminal modifications of RANTES analogs and their pharmacological properties. Data have been compiled from references (177, 181, 182, 190).

Name	N-terminal sequence	G protein signaling	Receptor internalization	Pharmacology	Anti-HIV potency [pM]	Affinity [nM]
wt ¹⁾	SPYSSDTPCC	Yes	Yes	Agonist	<130 nM	1-10
PSC	***SSDTPCC ²⁾	Yes	Yes	Strong agonist	25	1-10
5P12	QGPPLMATQSCC	No	No	Antagonist	28	1.6
5P7	QGPPLMALQSCC	No	No	Antagonist	17	-
6P4	QGPFGDIVLACC	Yes	Yes	Strong agonist	21	-
5P14	QGPPLMSLQVCC	No	Yes	Antagonist/ biased agonist	26	-

¹⁾ wild type

²⁾ *** = (*n*-nonanoyl)-*des*-Ser¹-[L-thiopropyl]², L-cyclohexylglycyl³

The structure of CCR5 in complex with 5P7-RANTES

In addition to the maraviroc complex structure (Figure 1.6a), the structure of CCR5 in complex with the antagonist RANTES analog 5P7-RANTES has been solved recently (Figure 1.6b) (191). In both structures CCR5 is in an inactive form. The extracellular parts of CCR5 position the core of 5P7-RANTES above the ligand-binding site, and the chemokine N-terminus inserts into the transmembrane helix bundle coordinating similar residues as the small-molecule ligand maraviroc.

Previously solved receptor•chemokine complexes (192, 193) and the CCR5•5P7-RANTES structure have revealed three epitopes for the interaction: CRS1 (chemokine recognition site 1) is formed by the receptor N-terminus, which contacts the core of the chemokine between N-loop and 40s-loop. CRS1.5 is formed by CCR5 residues P19 and C20, which pack against the conserved disulfide bonds of the chemokine. CRS2 is the transmembrane binding pocket of the receptor, which accommodates the chemokine N-terminus.

1.3 Aims of the thesis

Although the surge of crystal structures solved in recent years has increased tremendously the structural knowledge of GPCRs, the dynamics underlying the function of these intrinsically flexible proteins is not well understood. The goal of this thesis was to determine dynamics and ligand interactions of GPCRs by NMR. Specific aims were to

- (i) to determine the functional backbone dynamics of GPCRs by relaxation experiments using the turkey β_1 AR and CCR5 as examples
- (ii) obtain stable, detergent reconstituted CCR5 from insect cell expression for ligand interaction, structural and dynamical studies
- (iii) improve amino acid-specific isotope-labeling strategies in insect cells
- (iv) characterize the RANTES analog 5P12-RANTES-E66S under physiological conditions and study its interaction with heparin disaccharide as a proxy for the physiological glycosaminoglycan interaction
- (v) develop conditions for stable complex formation of CCR5 with 5P12-RANTES-E66S and to study this complex by solution and solid-state NMR

2 Relaxation and dynamics

Relaxation in NMR

NMR can provide dynamical information for any atom with a magnetically active nucleus by the analysis of relaxation parameters. In equilibrium, spin $\frac{1}{2}$ nuclei are aligned either parallel or antiparallel to an external magnetic field B_0 (z-axis) according to the Boltzmann distribution. After perturbation of this equilibrium, e. g. by a radio-frequency pulse, the magnetization returns back to the Boltzmann equilibrium. This phenomenon is called relaxation and the observables of this process in NMR experiments are the relaxation rates. The relaxation rates depend on the motions of the atoms and hence dynamic information can be derived.

Longitudinal R_1 relaxation describes the process of restoring the initial, unperturbed z-magnetization. The return to the Boltzmann equilibrium is due to changes in the populations of the two spin states via spin transitions. Transverse R_2 relaxation describes the decay of transverse magnetization that is caused by the loss of phase coherence of individual spins as well as by their return to the z-axis. R_2 relaxation is observable as the signal decrease of the free induction decay (FID), the time domain NMR signal, and corresponds to an increase of linewidth in the frequency domain.

Mechanism of relaxation

Brownian motion causes time-dependent, local magnetic field fluctuations in a molecular system of spins leading to relaxation. For spin $\frac{1}{2}$ nuclei like ^{15}N and ^1H , relaxation is caused by local field fluctuations arising from anisotropic interactions such as chemical shift anisotropy (CSA) or dipolar interaction (194). Relaxation can also be caused by quadrupolar interactions for nuclei with spins larger than $\frac{1}{2}$ and by the spin-rotation interaction for small molecules.

The dipolar interaction occurs when one nuclear spin experiences the local magnetic field of another spin nearby. Due to the rotational tumbling of the molecule the direction and magnitude of this local magnetic field fluctuates. The strength of the dipolar interaction (D) is proportional to the magnetic moments of the two interacting spins and depends on the distance between them and the angle of their internuclear vector relative to the external magnetic field B_0

$$D = \frac{\mu_0}{4\pi} \frac{\hbar\gamma_1\gamma_2}{r_{12}^3} (3\cos^2\theta - 1)$$

with μ_0 being the vacuum permeability, \hbar the reduced Planck constant, γ_i the gyromagnetic ratio of the spin i , r_{12} the distance between the two interacting nuclei and θ the angle of the internuclear vector relative to B_0 .

Chemical shift anisotropy is caused by an asymmetric electron distribution and induces a local orientation-dependent magnetic field at the spin position. Rotational motion changes the magnitude and direction of this field. The strength of the CSA (C) is given by

$$C = \frac{\gamma B_0 \Delta\sigma}{\sqrt{3}} (3\cos^2\theta - 1)$$

with B_0 being the strength of the external magnetic field, γ the gyromagnetic ratio of the spin, $\Delta\sigma$ the size of the CSA and θ the angle of the CSA principal axis relative to B_0 .

For protons, dipolar interactions with other protons or directly bound heteronuclei (e.g. ^{15}N) are the dominant relaxation mechanisms. Relaxation of ^{15}N spins is dominated by dipolar interaction with directly bound protons and the ^{15}N CSA.

More than one relaxation mechanism can act on the spin, sometimes causing interference (cross-correlation) between them and affecting the relaxation rates. One prominent example is the cross-correlation between ^{15}N - ^1H dipolar coupling and ^{15}N CSA leading to changes in the local magnetic field experienced by ^{15}N spins. The favorable relaxation properties arising from this cross-correlation are used in TROSY NMR experiments (21).

The time dependence of the local fields enters into the relaxation rates via the Fourier transform of the autocorrelation function of the interaction leading to relaxation. This autocorrelation function depends on the motion of the particle. The Fourier transform of the autocorrelation function is called spectral density $J(\omega)$. Its value at a given frequency ω describes the amount of motion present at this frequency.

For an isotropically diffusing, spherical particle the spectral density function is given by

$$J(\omega) = \frac{\tau_c}{1 + \omega^2\tau_c^2}$$

with τ_c being the rotational correlation time and ω the frequency.

Small molecules experience fast rotational motions described by a small rotational correlation time τ_c and a broad spectral density function. Large molecules undergo slower motions, i.e. have larger τ_c , leading to a larger spectral density at frequencies around $\omega = 0$. For molecules in the slow-motion limit ($\omega\tau_c \gg 1$) with ω being the Larmor frequency of the nuclei, $J(\omega)$ is much smaller than $J(0)$. The latter then dominates the transverse relaxation for large molecules.

Observable time scales of motions

The observable relaxation rates depend on the amplitude and velocity of local motions at the site of the nucleus and the overall rotational correlation time τ_c of the entire molecule, which is determined by its overall shape (195). Hence, insight into local and global dynamics as well as the size of the molecule can be gained from measurements of these relaxation rates.

Motions comparable or faster than the overall rotational correlation time τ_c of typical proteins (tens of nanoseconds) in solution lead to relaxation by the modulation of anisotropic interactions such as dipolar coupling and CSA. The respective relaxation rates are most sensitive to motions at the Larmor frequencies of the observed nuclei, corresponding to nanosecond time scale. Their analysis yields the overall rotational correlation time τ_c of the particle as well as amplitude and correlation times τ_m of faster local motions. Fast motions are identified by smaller R_2 and larger R_1 rates. For very fast local motions in the picosecond time range, the determination of the local correlation τ_m is rather imprecise and only a local order parameter S^2 is used as an estimate for the angular space averaged by the interaction (196).

A further time window of motions can be observed in the micro- to millisecond regime stemming from the modulations of isotropic interactions such as the chemical shift. These motions manifest themselves in an increase of the R_2 rates and thereby linewidth, and are usually called exchange broadening. For completeness, it should also be mentioned that

motions slower than about one second can be monitored directly via individual NMR experiments (real-time NMR).

Calculation of relaxation rates

The density matrix is the statistical description of the state of an ensemble of nuclear spins. The Redfield equation describes the relaxation of this density matrix back to thermal equilibrium as a function of random perturbations (197)

$$\frac{d\tilde{\sigma}(t)}{dt} = - \sum_{\alpha,\beta} [\hat{V}_\alpha, [\hat{V}_\beta^\dagger, \tilde{\sigma}(t) - \tilde{\sigma}_{eq}]] J_{\alpha,\beta}(\omega_\beta) = -\hat{R}(\tilde{\sigma}(t) - \tilde{\sigma}_{eq})$$

with $\tilde{\sigma}(t)$ being the density matrix in the rotating frame at time t , $\tilde{\sigma}_{eq}$ its equilibrium value, V the interaction spin operator responsible for relaxation, $J(\omega)$ the spectral density function, and α,β are indices corresponding to the decomposition of the interaction according to the Larmor frequencies of the system and \hat{R} the relaxation superoperator, i.e. the Redfield matrix. The elements of the Redfield relaxation matrix are the relaxation rates.

The relaxation rates of the ^{15}N spin in a ^{15}N - ^1H two spin system with dipolar coupling and CSA as relaxation mechanisms contains spectral densities sampled at frequencies $\omega = 0$ and the Larmor frequencies ω_N , ω_H and $\omega_N \pm \omega_H$.

In particular, the transverse in-phase ($N^+ = N_x + iN_y$) and anti-phase (N^+H_z) R_2 , and the longitudinal (N_z) R_1 relaxation rates of the ^{15}N spin are

$$R_2(N^+) = \frac{B_0^2 \Delta \sigma_N^2 \gamma_N^2}{20} [4J(0) + 3J(\omega_N)] + \frac{\mu_0^2 \hbar^2 \gamma_H^2 \gamma_N^2}{320\pi^2 r_{NH}^6} [4J(0) + 6J(\omega_H) + 3J(\omega_N) + J(-\omega_H + \omega_N) + 6J(\omega_H + \omega_N)]$$

$$R_2(N^+H_z) = \frac{B_0^2 \Delta \sigma_N^2 \gamma_N^2}{20} [4J(0) + 3J(\omega_N)] + \frac{\mu_0^2 \hbar^2 \gamma_H^2 \gamma_N^2}{320\pi^2 r_{NH}^6} [4J(0) + 3J(\omega_N) + J(-\omega_H + \omega_N) + 6J(\omega_H + \omega_N)]$$

$$R_1(N_z) = \frac{B_0^2 \Delta \sigma_N^2 \gamma_N^2}{10} [3J(\omega_N)] + \frac{\mu_0^2 \hbar^2 \gamma_H^2 \gamma_N^2}{320\pi^2 r_{NH}^6} [6J(\omega_H + \omega_N) + J(-\omega_H + \omega_N) + 3J(\omega_N)]$$

The cross-correlation rate between ^{15}N - ^1H dipolar-coupling and ^{15}N CSA is given as:

$$\eta = \frac{B_0 \Delta \sigma_N \mu_0 \hbar \gamma_H \gamma_N^2}{40\pi r_{NH}^3} [4J(0) + 3J(\omega_N)]$$

Experimental R_1 and η relaxation rates can be used to extract the rotational correlation time τ_c of the protein. Transverse relaxation rates can have additional contributions from exchange processes (see below). The ^{15}N antiphase magnetization (N^+H_z) is further relaxed by the dipolar interaction of the H_z spin state with additional nearby protons H^a . This increases the relaxation rate by

$$R_1(H_z) = \frac{\mu_0^2 \hbar^2 \gamma_H^4}{320\pi^2 r_{HH^a}^6} [J(0) + 3(\omega_H) + 6J(2\omega_H)]$$

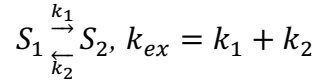
The total transverse magnetization rates in the absence of chemical exchange during the nitrogen evolution of a ^1H - ^{15}N heteronuclear single quantum coherence (HSQC) or ^1H - ^{15}N TROSY experiment are given by the following terms

$$R_2(\text{HSQC}) = \frac{[R_2(N^+) + R_2(N^+H_z) + R_1(H_z)]}{2}$$

$$R_2(\text{TROSY}) = \frac{[R_2(N^+) + R_2(N^+H_z) + R_1(H_z)]}{2} - \eta$$

Exchange processes

Under certain conditions the exchange between different conformations of a molecule can be monitored by NMR. In the simplest case, the position of an NMR-observable nucleus exchanges at a rate k_{ex} between two magnetically distinct sites S_1 and S_2 with Larmor frequencies differing by $\Delta\omega$ (198, 199).



The following cases can be distinguished: (i) if the rate of exchange k_{ex} is slow compared to $\Delta\omega$ ($k_{\text{ex}} \ll \Delta\omega$), two distinct resonances are observed with relative intensities according to their populations, (ii) if the exchange is in the intermediate time range ($k_{\text{ex}} \approx \Delta\omega$), coalescence of the two signals with severe line broadening occurs, (iii) if the exchange is fast ($k_{\text{ex}} \gg \Delta\omega$), a single resonance is observed at the population-averaged frequency.

Chemical exchange contributes to transverse relaxation due to the loss of phase coherence, corresponding to line broadening, via the fluctuations of the resonance frequency. The contributions of exchange to the relaxation are small for slow or fast exchange and large for intermediate exchange.

The Bloch-McConnell equation describes the evolution of magnetization under conformational exchange (198). The time dependence of the transverse magnetization $M_{1,2}^+(t)$ for states $S_{1,2}$ with frequencies $\omega_{1,2}$ is given by

$$\frac{d}{dt} \begin{bmatrix} M_1^+ \\ M_2^+ \end{bmatrix} = \begin{bmatrix} -k_1 + i\omega_1 - R_2 & k_2 \\ k_1 & -k_2 + i\omega_2 - R_2 \end{bmatrix} \begin{bmatrix} M_1^+ \\ M_2^+ \end{bmatrix}$$

where the same exchange-free relaxation rate R_2 is assumed for both states.

Solving the differential equation gives the time dependence of the magnetization $M^+(t)$ which decays with a rate constant

$$R_{\text{ex}} + i\omega = \bar{k} + i\bar{\omega} - \sqrt{\bar{k}^2 - \Delta\omega^2 - 2i\Delta\omega\Delta k}$$

$$\text{with } \bar{\omega} = \frac{\omega_1 + \omega_2}{2}, \Delta\omega = \frac{\omega_1 - \omega_2}{2}, \bar{k} = \frac{k_1 + k_2}{2}, \Delta k = \frac{k_1 - k_2}{2}$$

The latter equation connects the experimentally observable exchange broadening R_{ex} and frequency position ω to the rates $k_{1,2}$ as well as the frequencies $\omega_{1,2}$ at the two sites. Hence the rate constants may be derived from R_{ex} and ω , if $\omega_{1,2}$ are known.

NMR linewidth

The linewidth of a resonance in the frequency domain originates from the decay of the FID in the time domain. It is modulated by the loss of transverse phase coherence during the experiment. The observed linewidth is defined as the full width at half height (FWHH) of the resonance peak:

$$\Delta\nu_{FWHH} = \frac{R_2}{\pi} \text{ [Hz]} \text{ or } \omega_{FWHH} = 2R_2 \left[\frac{\text{rad}}{\text{s}} \right]$$

The observed R_2 rate is composed of the exchange-free transverse relaxation rate $R_{2,0}$, the exchange contribution R_{ex} and the inhomogeneity of the magnetic field R_{inhom} (order of ~ 1 Hz) (199).

$$R_2 = R_{2,0} + R_{ex} + R_{inhom}$$

Hence the exchange contribution R_{ex} can be determined from the knowledge of R_2 , $R_{2,0}$, and R_{inhom} .

3 A high-resolution description of the backbone dynamics of the β_1 -adrenergic G protein-coupled receptor from NMR relaxation data

Organization of the chapter

This chapter describes the dynamics of the thermostabilized turkey β_1 -adrenergic receptor studied by backbone NMR. The first section (3.1) is a reprint of a submitted manuscript by Grahl *et al.* (2018), which describes the backbone dynamics of TS- β_1 AR and TS- β_1 AR(A227Y/L343Y) investigated by ^{15}N relaxation data. The following section (3.2) presents additional data supporting the intrinsic dynamics of β_1 AR, which were not included in the manuscript. The last section (3.3) reports on the improved relaxation properties of partially deuterated TS- β_1 AR, which was obtained by growing insect cells on deuterated yeastolate.

3.1 NMR backbone dynamics reveals mechanism of ligand to effector site allosteric coupling in the β_1 -adrenergic receptor

Original Manuscript

Grahl, A., Isogai, S. Sharpe, T., Grzesiek, S.

NMR backbone dynamics reveals mechanism of ligand to effector site allosteric coupling in the β_1 -adrenergic receptor

Nature Communications (2018, in revision)

NMR backbone dynamics reveals mechanism of ligand to effector site allosteric coupling in the β_1 -adrenergic receptor

Anne Grahl¹, Shin Isogai¹, Timothy Sharpe², Stephan Grzesiek^{1,*}

¹ Focal Area Structural Biology and Biophysics, Biozentrum, University of Basel, CH-4056 Basel, Switzerland

² Biophysics Core Facility, Biozentrum, University of Basel, CH-4056 Basel, Switzerland

*Address correspondence to:

Stephan Grzesiek

Focal Area Structural Biology and Biophysics, Biozentrum

University of Basel, CH-4056 Basel, Switzerland

Phone: ++41 61 267 2100

FAX: ++41 61 267 2109

Email: Stephan.Grzesiek@unibas.ch

Keywords: membrane protein, GPCR, solution NMR, NMR relaxation, chemical exchange, isotope labeling

Abstract

G protein-coupled receptors (GPCRs) are transmembrane signal transducers that trigger intracellular responses upon binding of extracellular ligands. The >800 GPCRs in the human proteome are key regulators of physiological processes and highly attractive drug targets. Despite breakthroughs in GPCR crystallography, their transmembrane signaling mechanism is presently not well understood due to the lack of dynamical information. Here we provide highly detailed, quantitative information on the dynamics of the detergent-solubilized β_1 -adrenergic receptor in its apo form, in response to 6 ligands ranging from antagonists to agonists, as well as in an agonist/G protein mimetic nanobody (Nb80) complex from precise measurements of four types of ^{15}N NMR relaxation rates at 14 backbone amide sites. These data capture the functional motions elicited by the ligands and lead to stringent conclusions about the underlying signal transmission mechanism.

Whereas significant motions in the micro- to millisecond time range occur throughout the receptor, particularly pronounced ligand-dependent motions corresponding to a two-state equilibrium are observed for TM6 (transmembrane helix 6) residue V314 at the extracellular ligand entry tunnel. This equilibrium is strongly shifted by the binding of Nb80 at the intracellular side giving direct insight into the allosteric signal transmission. All observations can be explained by a pivoting motion of TM6, which is modulated by the different functional states of the receptor. This mechanism describes quantitatively the allosteric coupling between ligand and effector site and correlates antagonistic function as well as ligand affinity with the presence of an *orthosteric*, hydrophobic substitution of its head group. Since TM6 movement upon G protein binding is conserved in GPCRs, this mechanism of allosteric transmission is expected to be of general significance.

Introduction

G protein-coupled receptors (GPCRs) are transmembrane signal transducers, which convert the extracellular binding of a wide array of ligands to specific intracellular responses via G protein, arrestin, and other pathways. As regulators of crucial physiological processes, the more than 800 GPCRs within the human proteome have long been prime drug targets.¹ Advances in their structural stabilization by protein engineering and conformation-specific antibodies, as well as in crystallization methods for membrane proteins have led to a surge of available crystal structures in the last decade²⁻⁸. These have provided frozen snapshots of various functional states comprising inactive forms in complexes with antagonists and various active forms in complexes with agonists, G protein, G protein mimicking antibodies, and arrestin.

However, evidence from EPR, NMR, fluorescence spectroscopic data and molecular dynamics simulations indicates that GPCRs are highly dynamic and sample several conformations in any particular functional state. Consequently, signal transmission from the ligand to the effector site is thought to occur by continuous shifts of dynamic equilibria rather than by discrete jumps between distinct conformational substates^{4,9-17}. Thus, the key to understanding GPCR function is the accurate and precise description of its functional motions at atomic resolution – simultaneously at many sites throughout the receptor. No such comprehensive description of GPCR dynamics exists at present.

In principle, NMR spectroscopy can provide precise dynamical information for any atom site with a magnetically active nucleus by the analysis of relaxation parameters. In practice, NMR observation of GPCRs is strongly limited in sensitivity and resolution by intrinsically broad line widths and by difficulties in isotope labeling, as most GPCRs at present can only be produced in functional form in higher eukaryotic cells, which cannot synthesize amino acids from simple isotope-labeled precursors. For these reasons, NMR observations of GPCR dynamics have been confined mostly to chemical shift changes induced by different ligands and to the qualitative description of line broadening effects in selectively ¹³C-labeled side chain methyl groups^{10,11,13,18-20} or ¹⁹F-labeled side chains^{9,15,21,22}.

The NMR detection of main chain atomic nuclei is less sensitive, but in particular ¹H-¹⁵N resonances have the advantage of directly reporting on backbone and H-bond conformational changes with functional relevance. Despite early efforts²³, such ¹H-¹⁵N

backbone resonances have only recently been detected at high resolution, allowing their shifts to be correlated to functional receptor states^{14,17,24}.

Here we have obtained a comprehensive, quantitative description of the backbone dynamics based on ¹⁵N relaxation rates of a thermostabilized mutant of the turkey β_1 -adrenergic receptor (TS- β_1 AR), which had been prepared in isotope-labeled form in insect cells^{14,25} and solubilized in detergent. The data provide a precise description of the overall rotational motion in the detergent micelle and give evidence of extensive local motions in the micro- to millisecond regime throughout the receptor. Residue V314(6.59) [the number in parenthesis corresponds to the Ballesteros-Weinstein numbering²⁶] situated at the extracellular end of transmembrane helix 6 (TM6) in immediate vicinity of the ligand binding pocket shows particularly pronounced dynamic behavior, which correlates with the ligand affinity and the binding of the G protein mimetic nanobody Nb80 at the intracellular side of TM6. All observations can be explained quantitatively by a simple mechanical model, in which the pivoting motion of TM6 dynamically couples the ligand pocket and the effector site.

Results and Discussion

3.1.1.1 Global backbone dynamics

To determine the global backbone dynamics of TS- β_1 AR, we measured several ¹⁵N relaxation rates at 14 and 21 T (600 and 900 MHz ¹H frequency) magnetic field as averages over all residues by 1D ¹H-detected experiments carried out on ¹⁵N/²H (~60 %)-labeled TS- β_1 AR²⁵ bound to the antagonist alprenolol and reconstituted in decyl maltoside (DM) micelles (Figure S1, Table S1). At the limited resolution of the 1D spectra, the longitudinal ¹⁵N R_1 rates appear uniform with values of 0.34 s⁻¹ at 14 T and 0.20 s⁻¹ at 21 T in agreement with the expected field dependence of the slow tumbling limit. Correspondingly, dipolar coupling/CSA cross correlation rates η are also uniform and increase from 38 s⁻¹ at 14 T to 49 s⁻¹ at 21 T. Individual isotropic rotational correlation times τ_c derived from these rates are very similar with an average of 38 ± 3 ns (Table S1). This correlation time is in very good agreement with the value of 35 ± 1 ns calculated by the Stokes-Einstein relation from the 101 kDa mass determined in a separate multi-angle light scattering (SEC-MALS) experiment. This indicates that β_1 AR rotates at the same speed as the entire micelle and therefore a significant additional nanosecond motion of the GPCR relative to the detergent can be excluded. In contrast, the average transverse ¹⁵N R_2 rates of 56 s⁻¹ (89 s⁻¹) at 14 T (21 T) are larger than the 47 s⁻¹ (63 s⁻¹)

expected for a spherical molecule tumbling at a τ_c of 38 ns. This reveals a contribution from exchange broadening on the micro- to millisecond range, which increases at higher field.

3.1.1.2 Residue-specific dynamics

To derive residue-specific insights on this phenomenon, ^{15}N relaxation rates were also measured on TS- β_1 AR labeled selectively by ^{15}N -valine¹⁴. Using only well-resolved ^1H - ^{15}N resonances together with the available assignments (Figure S2a), $^{15}\text{N}_z R_1$ and $^{15}\text{N}_x R_2$ relaxation rates could be determined reliably for 14 of the total 26 valines of TS- β_1 AR in complex with the antagonist alprenolol at 14 T and 21 T (Figure 1). Besides one residue [tentatively assigned to V320(ECL3)], the $^{15}\text{N} R_1$ rates are uniform and agree well with the values of 0.32 s^{-1} (0.19 s^{-1}) at 14 T (21 T) expected for a rotational correlation time of 38 ns derived from the 1D analysis. Since V320 is located in extracellular loop 3, the observed higher R_1 may indicate increased nanosecond mobility in this region.

$^{15}\text{N}_x R_2$ rates were determined by a spin-echo experiment²⁷ with a CPMG ^{15}N 180° -pulse spacing of 0.5 ms ($\nu_{\text{CP}} = 2 \text{ kHz}$). Lower effective field strengths ν_{CP} were impractical due to the required ^1H decoupling and the short $^{15}\text{N}_x T_2$ of 10-20 ms. Figure 1b shows that the $^{15}\text{N}_x R_2$ rates are uniform for the detected residues, but are slightly (~ 10 - 20 s^{-1}) higher than the rates of 47 s^{-1} (14 T) and 63 s^{-1} (21 T) expected for the rotational correlation time of 38 ns. Again this must be attributed to exchange broadening. A full quantitative analysis by CPMG dispersion would be desirable, but is not possible due to (i) the practicable lower limit of the CPMG field strength and (ii) the low sensitivity of the experiment, which required ~ 4 days of measurement for a single rate determination using a concentrated ($400 \mu\text{M}$) sample.

We therefore developed a robust protocol for line shape analysis of both ^1H - ^{15}N TROSY and HSQC experiments using time domain fitting to extract ^{15}N transverse relaxation rates. These experiments required only 24 hours of measurement time to reach sufficient signal to noise ratios ($> \sim 10$) even for the weakest peaks in a typical $100 \mu\text{M}$ sample. The line shape analysis revealed TROSY $^{15}\text{N}_x^1\text{H}_\beta$ (Figure 1c) and HSQC $^{15}\text{N}_x^1\text{H}_z/^{15}\text{N}_x$ (Figure S3) R_2 rates, which are considerably larger than the exchange-free rates $R_{2,0}$ expected for a τ_c of 38 ns. Reassuringly, the calculated exchange contributions ($R_{\text{ex}} = R_2 - R_{2,0}$) are very similar for the TROSY and HSQC detection (Figure S3) and range from ~ 20 to $\sim 140 \text{ s}^{-1}$. They are thus significantly larger than the ones observed in the spin-echo experiments, which are clearly quenched by the 2 kHz CPMG field and therefore indicate exchange rates on the order of

10^3 - 10^4 s⁻¹. The R_{ex} values determined by the line shape analysis also contain contributions from inhomogeneous line broadening. However, based on the quality of the spectrometer shimming, these are estimated to be smaller than 1 s⁻¹ for ¹⁵N resonances. For most residues, R_{ex} is rather uniform with an average of ~ 30 s⁻¹ and has no significant field dependence between 14 and 21 T. This indicates highly asymmetric exchange broadening between a dominant and a minor state with an exchange rate slower than their frequency difference $\Delta\omega$, i.e. typically ~ 1 ppm or ~ 500 s⁻¹. In contrast, residues V172(4.56) located close to the ligand head group as well as V202(ECL2) and V314(6.59) at the extracellular ligand entry site show particularly large R_{ex} values in the ~ 100 s⁻¹ range (Figure 1c). For V172(4.56) and V314(6.59), R_{ex} also increases significantly with the magnetic field, corresponding to the intermediate to fast exchange regime with rates $\geq \Delta\omega$.

3.1.1.3 ¹⁵N chemical shifts and R_2 rates reveal two-site exchange at the ligand entry site

We had previously observed that the ¹H-¹⁵N resonance position and line width of residue V314(6.59) located close to the extracellular entry tunnel of the orthosteric ligand binding site (Figure 1d) correlated with the ligand affinity in complexes of TS- β_1 AR.¹⁴ This finding is particularly interesting, since the affinity of agonist ligands increases by two pK units when G protein or the G protein mimic Nb80 bind to the effector site at the intracellular ends of TM5-7^{14,28} – an effect which clearly shows the allosteric coupling between extracellular ligand binding and intracellular effector sites. Agonist-bound complexes of the highly thermostabilized TS- β_1 AR were not competent to bind and activate G protein. However, the more native-like TS- β_1 AR(A227Y/L343Y) mutant showed efficient G protein activation and also binding to the G protein mimicking nanobody Nb80. Intriguingly the resonance of V314(6.59) exhibited a very strong shift to a hitherto unidentified position upon binding of Nb80 to TS- β_1 AR(A227Y/L343Y) in complex with the agonist isoprenaline, giving direct evidence of transmembrane signal transmission.

To obtain more insight into this phenomenon we have assigned this resonance in the ternary complex TS- β_1 AR(A227Y/L343Y)•isoprenaline•Nb80 by a V314A point mutation (Figure S2b) and analyzed all assigned ¹H-¹⁵N resonances of TS- β_1 AR(A227Y/L343Y) and TS- β_1 AR in apo form and in binary complexes with six orthosteric ligands ranging from antagonists to agonists (Figures 2, S4, S5, S6, Table S2). Although TS- β_1 AR is unable to bind Nb80, its resonance positions and line shapes are very similar to TS- β_1 AR(A227Y/L343Y) in all binary complexes and the apo forms. In particular, similarly extensive exchange broadening

is observed for V172(4.56), V202 (ECL2), and V314(6.59) indicating that the thermostabilizing Y227A and Y343L mutations do not severely affect the internal receptor dynamics in the absence of an effector-site ligand.

Figure 2b shows the particular behavior of the V314(6.59) ^1H - ^{15}N TROSY resonance positions of TS- $\beta_1\text{AR}$ (A227Y/L343Y) in its apo form, in the binary orthosteric, as well as in the ternary isoprenaline•Nb80 complexes. Correlations between ^{15}N chemical shift, line width and ligand affinity are clearly apparent. The resonances of the high-affinity antagonist ligand (carvedilol, cyanopindolol and alprenolol) complexes cluster in the downfield region with narrow line widths, whereas those of the low-affinity ligands, i.e. the agonists isoprenaline and dobutamine as well as the inverse agonist atenolol, are upfield shifted and broadened. Of note, the used ligand concentrations (1 mM) were large enough to exclude significant line broadening effects from exchange between free and ligand-bound receptor forms. A quantitative analysis (Table S3) reveals a strong, linear correlation of the ligand pK_D values ranging over six orders of magnitude to the ^{15}N chemical shifts (Figure 2c) as well as an inverse correlation to the ^{15}N exchange broadening R_{ex} (Figure 2d). Strikingly, the addition of Nb80 to the TS- $\beta_1\text{AR}$ (A227Y/L343Y)•isoprenaline complex shifts the V314(6.59) ^{15}N resonance by ~ 7 ppm and the ^1H resonance by ~ 0.3 ppm in the upfield direction. As a result the V314(6.59) resonances of all TS- $\beta_1\text{AR}$ (A227Y/L343Y) complexes and its apo form fall approximately on a single line in the ^1H - ^{15}N TROSY. This indicates that all these functional states of V314(6.59) can be described approximately by a dynamic equilibrium between two extreme conformational states S_1 and S_2 , which exchange with respective rate constants $k_{1/2}$:



State S_1 is predominantly populated by the high-affinity antagonist ligand complexes, which have the most downfield shifted resonances (>116 ppm ^{15}N , >7.35 ppm ^1H), whereas state S_2 is predominantly populated by the active ternary complex, which has the most upfield shifted resonances (~ 105 ppm ^{15}N , ~ 6.95 ppm ^1H). Resonances of the low-affinity ligand complexes in the center between these extreme positions correspond to conformational mixtures with similar populations of both states. Due to intermediate exchange in the micro- to milliseconds regime, these resonances show severe line broadening effects. As the positions of the resonances correlate to the pK_D values, this explains the strong dependence of the line width on the ligand affinity, but it does not explain the affinity dependence of the resonance

position itself (see below). The broad V314(6.59) ^{15}N resonance of the TS- $\beta_1\text{AR}$ (A227Y/L343Y) apo form is located at about one fifth from the high-affinity antagonist ligand complexes in the direction of the active ternary complex, consistent with a basal activity of the apo receptor and a V314(6.59) active-state population of about 20 %.

The two-site exchange at V314(6.59) is corroborated by the behavior of the $^1\text{H}/^{15}\text{N}$ resonances of V202(ECL2) in the immediate vicinity in ECL2. These also fall approximately on one line for the apo form as well as the various ligand complexes and display similar broadening (Figures 1, S6). In contrast, the ligand-dependent shift variation and broadening of the $^1\text{H}/^{15}\text{N}$ resonances of V172(4.56) located close to the ligand head group is more heterogeneous and depends strongly on the chemical nature of the ligand head group (Figure S6)¹⁴.

3.1.1.4 Quantitative fit of V314(6.59) two-site exchange

The frequency ω and exchange broadening contribution R_{ex} of the dominant resonance in a system undergoing two-site exchange depends on the rate constants $k_{1/2}$ according to the Bloch-McConnell equation^{29,30}

$$R_{\text{ex}} + i\omega = \bar{k} + i\bar{\omega} - \sqrt{\bar{k}^2 - \Delta\omega^2 - 2i\Delta\omega\Delta k} \quad (2)$$

where $\omega_{1/2}$ are the frequencies in conformational states $S_{1/2}$ and $\bar{\omega} = \frac{\omega_1 + \omega_2}{2}$, $\Delta\omega = \frac{\omega_1 - \omega_2}{2}$, $\bar{k} = \frac{k_1 + k_2}{2}$, $\Delta k = \frac{k_1 - k_2}{2}$. Using a fit to the position and exchange broadening of the V314(6.59) ^{15}N resonances, we obtained the $k_{1/2}$ exchange rates for TS- $\beta_1\text{AR}$ (A227Y/L343Y) in its apo and all complex forms. Identical $\omega_{1/2}$ frequencies derived from a global optimization and corresponding to 116.2/105.6 ppm were used for all cases. All fitted ω and R_{ex} values agree within experimental error to the experimental data for TS- $\beta_1\text{AR}$ (A227Y/L343Y) (Figure 3). The same satisfying agreement was obtained for the analogous analysis of the V314(6.59) ^{15}N resonances in all observed forms of TS- $\beta_1\text{AR}$ (Figure S5, S7). The latter are very similar to TS- $\beta_1\text{AR}$ (A227Y/L343Y), but have minor shifts towards the inactive antagonist-bound conformation, corroborating the less active character of TS- $\beta_1\text{AR}$ (Figure S7). Fitted rate constants $k_{1/2}$ as well as the derived free energies of states S_1 and S_2 , and activation barriers for both constructs are summarized in Table S3. Remarkably the activation barriers for the $S_1 \rightarrow S_2$ transition fall in a narrow range of $\sim 21 \pm 2$ kT units for all ligand-bound and apo forms of

both β_1 AR constructs, giving further confidence into the robustness of the two-site exchange description.

3.1.1.5 *A mechanical model of the allosteric coupling between ligand and G protein binding site*

Based on the chemical shift and line broadening of the V314(6.59) ^{15}N resonance we can distinguish four different cases of conformational behavior for this residue, corresponding to the high-affinity antagonist complexes, the apo form, the low-affinity ligand complexes, and the active state-mimicking isoprenaline•Nb80 complex (Figure 4a). The complex with the high-affinity antagonist carvedilol mainly populates conformational state S_1 having a $2.8 kT$ lower free energy than state S_2 , which has only $\sim 6\%$ population. The transition to state S_2 occurs at a rate k_1 of $2.1 \cdot 10^3 \text{ s}^{-1}$, corresponding to an activation barrier of $21.9 kT$ at 304 K. The reverse transition is about 17 times faster. An inspection of the crystal structure of β_1 AR in complex with carvedilol (PDB code: 4AMJ) shows that the bulky ligand head group is deeply inserted into the orthosteric ligand binding pocket and directed towards the upper part of TM6, which may prevent a closing of the pocket by an inward movement of TM6 (Figure S8c). No crystal structure exists for the apo receptor. The equilibrium of the apo form (Figure 4a) is shifted more towards state S_2 having 17% population and concomitantly increased forward and decreased reverse rates. Presumably the empty ligand pocket is filled with water allowing an easier movement of V314(6.59) towards the active state S_2 .

The complexes with the low-affinity ligands populate S_2 even more than the apo state, e.g. 34% for isoprenaline. These ligands lack the bulky substitutions in the *ortho* position of the benzene head group pointing towards TM6 and V314, which are present in the high-affinity antagonists. In the complex with isoprenaline (PDB code: 2Y03, Figure S8c), this benzene head group is not as deeply inserted into the ligand binding pocket as in the carvedilol complex. However, since the *ortho* substitutions are absent, the steric restriction of TM6 is reduced as compared to carvedilol and apparently allows an increase of the S_2 population. This effect is not visible in the β_1 AR crystal structures where the positions of TM6 and in particular of V314(6.59) superimpose almost exactly for both complexes (Figure S8a,c). However, as previously remarked³¹ the isoprenaline catechol ring forms polar interactions with the TM6 residue N310(6.55). We speculate that compared to the apo state this attractive interaction shifts the equilibrium towards the active state S_2 .

Finally, the $\beta_1\text{AR}\cdot\text{isoprenaline}\cdot\text{Nb80}$ complex is almost completely trapped in the active state S_2 with a free energy that is 4.1 kT lower than in state S_1 and a reverse rate k_2 , which is strongly reduced to $\sim 10^2\text{ s}^{-1}$ (Figure 4a). Thus, the addition of Nb80 to $\beta_1\text{AR}\cdot\text{isoprenaline}$ shifts the $S_1 \rightleftharpoons S_2$ equilibrium of the extracellular V314(6.59) by 4.7 kT towards S_2 via an allosteric coupling from the G protein binding site. Unfortunately, no $\beta_1\text{AR}\cdot\text{isoprenaline}\cdot\text{Nb80}$ complex structure is available. However, structural insights into this phenomenon may be obtained from the homologous $\beta_2\text{AR}$. Since all structures of binary $\beta_1\text{AR}$ and $\beta_2\text{AR}$ complexes with orthosteric ligands are almost completely superimposable and also show very similar ligand positions and coordination, it is expected that ternary complexes with intracellular effectors will also be similar (Figure S8). The ternary agonist-bound $\beta_2\text{AR}$ complexes with G protein³² or G protein mimicking nanobodies^{28,33} strongly differ from all binary antagonist and agonist $\beta_1\text{AR}$ and $\beta_2\text{AR}$ complexes and show large movements at the intracellular sides of TM5, TM6 and their intervening loop ICL3, which form the binding site for the G protein (Figure S8b). In particular, the intracellular end of TM6 swings out from the G protein binding site by about 14 \AA ³². An alignment of the antagonist carazolol-bound $\beta_2\text{AR}$ structure (PDB code: 2RH1) with the ternary complex of the HBI agonist and a G-protein mimicking nanobody (PDB code 4LDL)³³, on the central region of the unaffected helices TM1-4,7 (Figure S8b,d,e, Figure 4) reveals that the TM6 motion extends to the extracellular end of TM6. This part moves in the opposite direction of the intracellular part towards the orthosteric ligand binding pocket, corresponding to a pivoting of TM6 around the center of the helix close to the conserved P288(6.50). As a consequence, residue V297(6.59), the $\beta_2\text{AR}$ equivalent of V314(6.59) in $\beta_1\text{AR}$, moves by 2.4 \AA towards the ligand. The ligand itself inserts more deeply into the binding pocket such that its benzene ring is in a similar position as for high-affinity antagonist ligands (Figure 4, Figure S8c,d,e). This conformation is stabilized by an extended polar network between N293(6.55) and H296(6.58) on TM6 and the ligand catechol group³³. The structure of the ternary $\beta_2\text{AR}\cdot\text{BI167107}\cdot\text{G}$ protein complex (PDB code 3SN6) is very similar to the $\beta_2\text{AR}\cdot\text{HBI}\cdot\text{Nb6B9}$ complex with respect to the orientation of the extra and intracellular parts of TM5 and TM6 (Figure S8b); however, low electron density at the extracellular side prevents a precise definition of individual atoms³².

3.1.1.6 The extreme V314(6.59) ¹⁵N chemical shift gives direct evidence of strong mechanical strain induced across TM6 by the effector site ligand

The extreme V314(6.59) ¹⁵N upfield shift by about 10 ppm in the β_1 AR•isoprenaline•Nb80 complex (Figure 2b) is the sign of a considerable weakening of the H-bond from the N atom and a distortion of the backbone geometry of V314(6.59).³⁴ Indeed, a detailed analysis of β_1 AR and β_2 AR structures corroborates this observation. In binary antagonist and agonist complexes of β_1 AR and β_2 AR, TM6 residues V295(6.57) and H296(6.58) form alpha-helical N_i•••O_{i-4} H-bonds, whereas residue V297(6.59) forms a 3₁₀-helical N_i•••O_{i-3} H-bond (all β_2 AR numbering, Figure 5a). In contrast in the ternary β_2 AR•HBI•Nb6B9 complex, the V297(6.59)N•••I294(6.56)O H-bond is broken ($d_{\text{NO}} = 4.1 \text{ \AA}$) and V295(6.57)O gets into H-bonding distance to V297(6.59)N ($d_{\text{NO}} = 3.0 \text{ \AA}$) albeit with very unfavorable H-bond angles (Figure 5c). At the same time, the phi-psi angles of the entire C-terminal segment of TM6 comprising residues I294(6.56) to I298(6.60) move outside of the most favored helical region of the Ramachandran plane (Figure 5b). This distortion coincides with the pivoting motion of the extracellular end of TM6 towards TM5 and a concomitant sideways motion of TM5 (Figure 5c). Apparently, a steric contact between residues V297(6.59) and Q197(5.36) transmits force between the extracellular ends of both helices, which in turn strains the backbone at V297(6.59) and causes its extreme ¹⁵N chemical shift. As these changes are induced by the G-protein mimicking nanobodies and presumably also the G protein, they provide direct evidence of the mechanical strain exerted by effector site ligands onto the orthosteric binding pocket and corroborate the TM6 pivoting model.

3.1.1.7 Correlation between conformational state free energy differences and pK_D

As the ¹⁵N chemical shift position of V314(6.59) in TS- β_1 AR(A227Y/L343Y) correlates to both pK_D of the ligand and the relative populations of states S_1 and S_2 , the derived free energy difference $E_{21} = E_2 - E_1$ between these states must also correlate to the pK_D value (Figure S9). The linear correlation (Pearson coefficient $r^2 = 0.67$) can be cast in the form $\Delta G_{\text{D}}/kT = \ln(10)pK_{\text{D}} = (1.1 \pm 0.2) E_{21}/kT + 1.1 \pm 0.5$. This indicates that the variation in free energy between states S_1 and S_2 can account for the total variation of ligand affinity and expresses quantitatively that the high-affinity ligands are antagonists and make the state S_2 unlikely. All of the investigated high-affinity ligands (cyanopindolol, carvedilol, alprenolol) possess a bulky hydrophobic substitution in the *ortho* position of their benzene head group pointing towards TM6 and V314(6.59) (Figure 2a). Apparently, this substitution increases the

ligand affinity by hydrophobic contacts and restricts the motion of the extracellular end of TM6, thereby making the active state S_2 much less favorable. Of note, ligands that lack this substitution have low affinity (dobutamine, isoprenaline, atenolol), but not all are agonists. Thus, atenolol is an inverse agonist, and we have shown previously that its *para*-acetamide group substantially disrupts the TM3–TM4–TM5 interface, which apparently prevents receptor activation via a separate mechanism.¹⁴

Conclusion

We have obtained a quantitative description of the backbone dynamics of a thermostabilized, yet active form of the turkey β_1 AR using NMR spectroscopy. The detergent-solubilized β_1 AR shows no significant nanosecond motions relative to the detergent micelle. However, increased ^{15}N R_2 relaxation rates indicate backbone motions in the micro- to millisecond range throughout the receptor. Particularly strong motions occur at residues V172(4.56), V202(ECL2), and V314(6.59) located in the vicinity of the ligand head group and at the entrance of the ligand binding pocket. The approximately linear behavior of the V202(ECL2) and V314(6.59) 2D ^1H - ^{15}N chemical shifts in all complex and apo forms of the receptor indicates that the entrance of the ligand-binding pocket exchanges between two main states, which are approximately realized in antagonist-inhibited complexes and the agonist-activated Nb80-bound complex, respectively. An excellent quantitative agreement with a two-state exchange model confirms this notion and provides exchange rates and free energy differences between these states for all forms of the receptor. These findings corroborate the concept that ligands induce the various functional states of GPCRs by shifting dynamic equilibria within an underlying conformational landscape rather than by discrete jumps.

The binding of Nb80 to the intracellular side of the agonist-bound receptor strongly shifts the conformational equilibrium at the extracellular ligand entry site, giving direct evidence of the allosteric transmembrane coupling. The concomitant chemical changes of V314(6.59) show the breaking of the H-bond from the V314(6.59)N atom and a distortion of the backbone at the ligand entry site. Apparently the nanobody induces a pivoting motion of TM6 around its center, which pushes the extracellular end of TM6 towards TM5 and causes significant mechanical strain. This motion can also be detected by careful inspection of crystal structures of the homologous agonist-bound β_2 AR nanobody or G protein complexes. A pivoting motion of TM6 in β_2 AR has been postulated before the availability of detailed crystal structures based on modeling of engineered activating metal ion sites³⁵. However, the motion

of the extracellular part of TM6 was predicted towards TM7 and not TM5. More recently, the formation of a lid-like structure by F193(ECL2) and Y308(7.35) over the orthosteric ligand-binding site in G protein or nanobody complexes of $\beta_2\text{AR}$ ³⁶ has been used to explain the observed hundredfold increase in agonist affinity^{14,28} upon binding of the effector. Here we provide direct evidence for a simple mechanical cause of this allosteric effect: intracellular G protein (mimic) binding pivots TM6 around its center thereby moving its extracellular part towards TM5 and compressing the ligand binding pocket. This increases ligand to receptor interactions and agonist affinity. Antagonist ligands do not allow this motion and thereby block effector binding.

These conclusions are based on a careful comparison of NMR chemical shift and relaxation behavior with existing crystal structures. The chemical shifts of backbone ¹⁵N nuclei are reasonably well understood and can be directly linked to defined backbone conformations. Such correlations are much less stringent for side chain nuclei. The variations in ¹⁵N shifts show that minute motions in the crystal structures, which may otherwise be considered as ‘structural noise’, are indeed highly significant for function. Thus, the combination of NMR and crystallographic information gives precise insights into the driving forces of biological function.

Experimental Section

Protein expression and purification

Expression in in baculovirus-infected Sf9 cells and purification of the ¹⁵N-valine-labeled turkey TS- $\beta_1\text{AR}$ and TS- $\beta_1\text{AR}$ (A227Y/L343Y) constructs were carried out as described previously.¹⁴ For assignment of the V314(6.59) resonance in complex with the Nb80-bound receptor a further V314A mutation was introduced into TS- $\beta_1\text{AR}$ (A227Y/L343Y) using the QuickChange site-directed mutagenesis method (Agilent) and expressed in ¹⁵N-valine-labeled form. Uniformly ¹⁵N(~90 %), ²H(~60 %)-labeled $\beta_1\text{AR}$ was obtained by supplementation of ¹⁵N, ²H-labeled yeastolate and ¹⁵N₂-glutamine to custom-made serum-free medium (SF4, BioConcept) devoid of amino acids and yeast extract medium as described.²⁵ For all constructs, binding of ligands and exchange between ligands was carried out as described¹⁴. The plasmid for Nb80 was a generous gift by Jan Steyaert and the Nb80 protein was purified according to the described procedure²⁸.

NMR experiments and data analysis

NMR samples were prepared with typical receptor concentrations of 100-150 μM in 20 mM TRIS HCl, 100 mM NaCl, $\sim 1\%$ DM, 0.02 % NaN_3 , 5 % D_2O , pH 7.5 and 1 mM ligand (except apo form) solution in a 250 μl Shigemi tube, following concentration of $\sim 15\ \mu\text{M}$ receptor solubilized in 0.1 % DM with a 50 kDa molecular weight cut-off centrifugal filter (Amicon). 2 mM sodium ascorbate was added to isoprenaline and dobutamine complex samples to prevent oxidation of the ligand.

All NMR experiments were performed on Bruker AVANCE 14.1 T (600 MHz ^1H frequency), 18.8 T (800 MHz), or 21.2 T (900 MHz) spectrometers equipped with a TCI cryoprobe at a temperature of 304 K with the exception of the apo TS- $\beta_1\text{AR}$ (A227Y/L343Y) ^1H - ^{15}N TROSY, which was recorded at 294 K due to limited stability. ^1H - ^{15}N TROSY or HSQC experiments were recorded as 120 or 80 (^{15}N) x 1024 (^1H) complex points and acquisition times of 24 ms or 16 ms (^{15}N) and 42 ms (^1H). For optimal sensitivity, the ^1H - ^{15}N transfer time was reduced to 3.0 ms. The experimental times using a 1 s interscan delay were adjusted to reach a signal to noise ratios of ~ 10 for the analyzed peaks, corresponding to ~ 24 h for a typical 100 μM receptor sample.

^{15}N R_1 and R_2 relaxation rates were determined using standard HSQC-based ^{15}N relaxation experiments^{27,37} with relaxation delays of 20, 2004 ms (20, 3004 ms) for R_1 and 2, 6, 12 ms (2, 6, 10 ms) for R_2 at 14.1 T (21.2 T). ^{15}N - ^1H dipolar-coupling/ ^{15}N CSA cross-correlation rates η were determined from a quantitative comparison of in-phase and anti-phase ^{15}N magnetization³⁸ using a cross relaxation delay of 12 ms.

All NMR spectra were processed with NMRPipe³⁹ and evaluated with SPARKY⁴⁰ or PIPP⁴¹. Resonance amplitudes of NMR relaxation spectra were extracted using the program nlinLS contained in NMRPipe³⁹. ^{15}N R_1 and R_2 rates and their error estimates were obtained determined by Monte Carlo fitting of the experimental amplitudes using Matlab (MathWorks, Inc.).

^{15}N R_2 rates were also determined by time-domain line shape fitting of H- ^{15}N TROSY or HSQC spectra using the nlinLS program contained in NMRPipe³⁹. For this, two-dimensional ^1H - ^{15}N resonances were created as exponentially damped sinusoids, apodized, one-time zero-filled and Fourier transformed with the same parameters as the experimental data. Amplitudes, frequencies, and decay constants were then varied to obtain the best least squares fit to the experimental spectra. A Monte Carlo error analysis of the fit parameters was carried out on

synthetic spectra created with random noise of the same root mean square as the experimental data. Reported errors on the fitted R_2 rates are standard deviations of fitted R_2 values of 20 such Monte Carlo simulations.

Multi-angle light scattering and viscosity measurements

SEC-MALS measurements on TS- β_1 AR in DM micelles were carried out at 299 K using a GE Healthcare Superdex 200 Increase 10/300 size-exclusion column on an Agilent 1260 HPLC with a column buffer of 20 mM TRIS HCl, 100 mM NaCl, pH 7.5 containing 0.76 % DM to match the NMR sample conditions. Elution was monitored by an absorbance detector (280 nm), a Wyatt Heleos II 8+ multiangle light scattering detector and a Wyatt Optilab rEX differential refractive index detector. Inter-detector delay volumes, band broadening corrections, and light-scattering detector normalization were calibrated using 2 mg/ml BSA solution (ThermoPierce) and standard protocols in ASTRA 6. The refractive index increment (dn/dc) of DM in column buffer was calculated as 0.141 ml/g from measurements of a series of samples with concentrations between 0.5 and 10 mg/ml, directly injected into the differential refractive index detector. Weight-averaged molar masses (Mw) for the protein-detergent complex (101 ± 2 kDa), and for the protein (36 ± 2 kDa) and detergent components (65 ± 3 kDa) of the complex were calculated using the protein conjugate method in the ASTRA 6 software (Wyatt Technology).

The viscosity of the receptor micelle suspension was estimated from a viscosity measurement of a 20 mM TRIS HCl, 100 mM NaCl, pH 7.5, 0.95 % DM suspension using an Anton Paar AMVn rolling-ball viscometer yielding a value of 0.840 cP at 304 K.

Theoretical relaxation rates and determination of rotational correlation times

Theoretical ^{15}N $R_1(N_z)$, $R_2(N_x)$ ²⁷, ^{15}N - ^1H dipolar-coupling/ ^{15}N CSA cross-correlation η ³⁸, and TROSY $R_2(N_x H_\beta)$ ⁴² rates were calculated using an isotropic Lipari-Szabo spectral density and the following parameters: $r_{\text{HN}} = 1.02$ Å, $S^2 = 0.85$, $\Delta\sigma_{\text{N}} = 170$ ppm, $\Delta\sigma_{\text{HN}} = 15$ ppm, $\theta = 20^\circ$, where θ is the angle between the unique axes of the CSA and dipolar tensors. Isotropic rotational correlation times τ_c were determined independently from measured ^{15}N $R_1(N_z)$ rates and ^{15}N - ^1H dipolar-coupling/ ^{15}N CSA cross-correlation rates η by inversion of the respective theoretical expressions. Effects of dipolar interactions from nearby protons onto the ^{15}N transverse relaxation rates in ^1H - ^{15}N TROSY and HSQC experiments were taken into account by the addition of half the ^1H - ^1H NOE transfer rate ($\frac{1}{320} \frac{\mu_0^2 \hbar^2 \gamma_{\text{H}}^4}{\pi^2 r_{\text{HH}}^6} \tau_c$) to $R_2(N_x H_\beta)$ and $R_2(N_x)$,

respectively, where $r_{HH} = 2.05 \text{ \AA}$ is an effective distance corresponding to the dipolar interaction with all protons adjacent to the amide proton in α -helical structures.⁴²

An independent estimate of the rotational correlation time τ_c was obtained from the 101-kDa molecular weight of the TS- β_1 AR DM micelle complex determined by SEC-MALS. Using literature values⁴³ for the partial specific volumes of protein (average value 0.735 ml/g, 0.36 mass fraction) and DM (0.815 ml/g, 0.64 mass fraction), the specific volume for the complex can be calculated as 0.786 ml/g. The non-hydrated radius r_{NH} of an assumed spherical detergent micelle is then 31.6 \AA . Assuming a hydration layer thickness r_W of 3.2 \AA , the isotropic rotational correlation time τ_c of the hydrated receptor detergent complex amounts to 35.2 ns using the Stokes-Einstein relation $\tau_c = \frac{4\pi\eta_S r_H^3}{3kT}$ with $r_H = r_{NH} + r_W$ and η_S being the viscosity of the receptor micelle suspension.

Fit of two-site exchange model

Theoretical ^{15}N frequencies ω and exchange broadening contributions R_{ex} predicted from the Bloch-McConnell equation (Eq. 1)^{29,30} were fitted to the observed frequencies and exchange contributions $R_{ex} = R_2 - R_{2,0}$ using Matlab (MathWorks, Inc.) to obtain the rate constants $k_{1/2}$ and their Monte Carlo (50 iterations) error estimates. The frequency positions $\omega_{1/2}$ of the states $S_{1/2}$ were derived from a global optimization over all receptor constructs and complex forms. Free energy differences between states S_1 and S_2 and between the transition state TS and S_1 according to the Eyring equation were obtained as $(E_2 - E_1)/kT = \log \frac{k_2}{k_1}$ and $(E_{TS} - E_1)/kT = \log \frac{kT}{h k_1}$ respectively.

Supporting Information

Supplementary Figures 1-9 showing further NMR evidence of β_1 AR dynamics and structural analyses of β_1 AR and β_2 AR (PDF)

Supplementary Table 1-3 listing determined ^{15}N relaxation rates and fitted parameters to two-site exchange dynamics for TS- β_1 AR and TS- β_1 AR(A227Y/L343Y) (XSLX)

Acknowledgments

This work was supported by the Swiss National Science Foundation (grants 31-149927 and 31-173089 to S.G.) and by a Fellowship for Excellence by the Biozentrum Basel International PhD Program (to A.G.). We gratefully acknowledge Dr. Frank Delaglio for help with line shape fitting using the NMRPipe software package as well as Drs. Hans-Jürgen Sass, Dmitry Veprintsev, Xavier Deupi, and Gebhard Schertler for helpful discussions.

Figure Legends

Figure 1. Residue-specific ^{15}N relaxation rates of alprenolol-bound ^{15}N -valine TS- $\beta_1\text{AR}$ at 304 K at 14 T (blue) and 21 T (red). (a) ^{15}N longitudinal (R_1) rates. Dashed lines represent theoretical R_1 rates of 0.32 s^{-1} (14 T) and 0.19 s^{-1} (21 T) for a rotational correlation time τ_c of 38 ns. Assignments marked by asterisks (V60, V320) are tentative. (b) ^{15}N transverse (R_2) rates determined by CPMG-based spin-echo experiments. Theoretical R_2 rates are 47.1 s^{-1} (14 T) and 62.7 s^{-1} (21 T). (c) ^{15}N R_2 rates from line shape analysis of ^1H - ^{15}N TROSY spectra. Theoretical R_2 rates are 18.1 s^{-1} (14 T) and 12.9 s^{-1} (21 T). (d) Crystal structure of $\beta_1\text{AR}$ in complex with carvedilol (4AMJ). The protein backbone and carvedilol are shown in ribbon and magenta stick respectively. The individual valines are depicted as spheres (blue: relaxation rates determined unambiguously; grey: resonances could not be analyzed due to overlap).

Figure 2. Evidence for two-site exchange of V314(6.59) at the ligand entry tunnel of TS- $\beta_1\text{AR}$ (A227Y/L343Y). (a) Chemical structures of the ligands used in the experiments. Ligand affinities⁴⁴ are indicated as pK_D values. (b) Selected region from ^1H - ^{15}N TROSYs showing the variation of the V314(6.59) ^1H - ^{15}N resonance in the apo form, orthosteric binary and ternary isoprenaline•Nb80 complexes at 21 T. Spectra are color-coded and marked according to the ligand. Cross peaks from other residues are marked with asterisks. A dashed line visualizes the approximate linear correlation between ^1H and ^{15}N chemical shifts of V314(6.59) in various receptor states indicative of two-site exchange. (c) V314(6.59) ^{15}N chemical shift (21 T) versus ligand affinity pK_D . The pK_D of the isoprenaline•Nb80 complex was assumed as $pK_D(\text{isoprenaline}) + 2$.¹⁴ The dashed line indicates the approximate linear correlation between V314(6.59) ^{15}N chemical shift and ligand affinity pK_D . The arrow highlights the shift of ^{15}N chemical shift and pK_D upon binding of Nb80 to the TS- $\beta_1\text{AR}$ (A227Y/L343Y)•isoprenaline complex. (d) V314(6.59) ^{15}N exchange broadening versus pK_D at 21 T (filled circles) and 14 T (filled triangles).

Figure 3. Comparison of TS- $\beta_1\text{AR}$ (A227Y/L343Y) V314(6.59) experimental and predicted ^{15}N frequencies ω and exchange broadening R_{ex} from fits to the two-site exchange model. (a) ^{15}N exchange rates R_{ex} at 21 T (filled circles) and 14 T (filled triangles). (b) ^{15}N frequencies ω . Symbols as in (a).

Figure 4. Schematic of allosteric coupling mechanism between effector site and orthosteric ligand site by two-site exchange involving TM6 pivoting. (a) Cartoon of V314(6.59) located at the ligand entry tunnel exchanging between the conformational states S_1 and S_2 . Four distinct situations are depicted for the (i) high affinity antagonist (carvedilol) complex, (ii) apo form, (iii) low-affinity agonist (isoprenaline) complex, and (iv) high-affinity agonist (isoprenaline) + Nb80 complex. Determined exchange rates $k_{1/2}$ and free energy differences are indicated for all cases. (b) Evidence for two conformations of V297 (6.59) (homolog to $\beta_1\text{AR}$ V314) and TM6 pivoting in response to nanobody binding in the crystal structures of $\beta_2\text{AR}$. Structures of the binary complex with the antagonist carazolol (2RH1) and of the ternary complex with agonist HBI and Nb6B9 (4LDL) were aligned on the central region

of the unaffected helices TM1-4,7 (shown in grey for 2RH1). TM6 is depicted in green for the antagonist complex and in magenta for the active ternary complex. The positions of the V297N atoms are indicated as spheres. For clarity TM5 is not shown. Chemical structures of the ligands are shown as sticks. The nanobody Nb6B9 is shown as an orange ribbon.

Figure 5. Evidence of the change in backbone geometry of the extracellular end of TM6 in β_1 AR and β_2 AR in response to orthosteric and effector site ligands. (a) Hydrogen bonding distance $N_i \cdots O_{i-4}$ and $N_i \cdots O_{i-3}$ for residues 6.54 to 6.60 for binary orthosteric ligand complexes [agonist(isoprenaline) $\cdot\beta_1$ AR (2Y03): blue, antagonist(carvedilol) $\cdot\beta_1$ AR (4AMJ): red, antagonist(carazolol) $\cdot\beta_2$ AR (2RH1): green] and the ternary agonist(HBI) \cdot Nb6B9 $\cdot\beta_2$ AR complex (4LDL, orange). The residue numbering is given in Ballesteros-Weinstein form and individually for β_1 AR and β_2 AR. (b) Phi and psi angles of the residues shown in (a) of the antagonist(carazolol) $\cdot\beta_2$ AR complex (green) and the ternary agonist(HBI) \cdot Nb6B9 $\cdot\beta_2$ AR complex (orange). The most favored (dark grey) and additionally allowed (light grey) helical regions⁴⁵ of the Ramachandran plot are indicated. Upon binding of the nanobody at the effector site, residues 6.56 to 6.60 move significantly towards the less favored regions of the Ramachandran plane (blue arrows). (c) Structures of the extracellular ends of TM5 and TM6 of the antagonist(carazolol) $\cdot\beta_2$ AR complex (green) and the ternary agonist(HBI) \cdot Nb6B9 $\cdot\beta_2$ AR complex (orange). The backbone from I294 to V297 is shown as sticks and coded by CPK colors. The hydrogen bonds from the V297(6.59)N atom in the two structures are indicated as dotted lines. The entire residues Q197(5.36) and V297(6.59) are shown as sticks.

References

1. Alexander, S. P. *et al.* THE CONCISE GUIDE TO PHARMACOLOGY 2017/18: G protein-coupled receptors. *British Journal of Pharmacology* **174**, S17–S129 (2017).
2. Caffrey, M. A comprehensive review of the lipid cubic phase or in meso method for crystallizing membrane and soluble proteins and complexes. **71**, 3–18 (2015).
3. Grisshammer, R. New approaches towards the understanding of integral membrane proteins: A structural perspective on G protein-coupled receptors. *Protein Sci* **26**, 1493–1504 (2017).
4. Manglik, A., Kobilka, B. K. & Steyaert, J. Nanobodies to Study G Protein-Coupled Receptor Structure and Function. *Annu. Rev. Pharmacol. Toxicol.* **57**, 19–37 (2017).
5. Carpenter, B. & Tate, C. G. Active state structures of G protein-coupled receptors highlight the similarities and differences in the G protein and arrestin coupling interfaces. *Curr. Opin. Struct. Biol.* **45**, 124–132 (2017).
6. de Graaf, C. *et al.* Extending the Structural View of Class B GPCRs. *Trends Biochem Sci* **42**, 946–960 (2017).
7. Smith, J. S., Lefkowitz, R. J. & Rajagopal, S. Biased signalling: from simple switches to allosteric microprocessors. *Nat Rev Drug Discov* **268**, 4625 (2018).
8. Hilger, D., Masureel, M. & Kobilka, B. K. Structure and dynamics of GPCR signaling complexes. *Nat. Struct. Mol. Biol.* **25**, 4–12 (2018).
9. Liu, J. J., Horst, R., Katritch, V., Stevens, R. C. & Wuthrich, K. Biased Signaling Pathways in β 2-Adrenergic Receptor Characterized by 19F-NMR. *Science* **335**, 1106–1110 (2012).
10. Kofuku, Y. *et al.* Efficacy of the β 2-adrenergic receptor is determined by conformational equilibrium in the transmembrane region. *Nat. Commun.* **3**, 1045–9 (2012).
11. Nygaard, R. *et al.* The dynamic process of beta(2)-adrenergic receptor activation. *Cell* **152**, 532–542 (2013).
12. Manglik, A. & Kobilka, B. The role of protein dynamics in GPCR function: insights from the β 2AR and rhodopsin. *Curr. Opin. Cell Biol.* **27**, 136–143 (2014).
13. Okude, J. *et al.* Identification of a Conformational Equilibrium That Determines the Efficacy and Functional Selectivity of the mu-Opioid Receptor. *Angew Chem Int Ed Engl* **54**, 15771–15776 (2015).

14. Isogai, S. *et al.* Backbone NMR reveals allosteric signal transduction networks in the beta1-adrenergic receptor. *Nature* **530**, 237–241 (2016).
15. Ye, L., Van Eps, N., Zimmer, M., Ernst, O. P. & Scott Prosser, R. Activation of the A2A adenosine G-protein-coupled receptor by conformational selection. *Nature* **533**, 265–268 (2016).
16. Latorraca, N. R., Venkatakrishnan, A. J. & Dror, R. O. GPCR Dynamics: Structures in Motion. *Chem Rev* **117**, 139–155 (2016).
17. Eddy, M. T. *et al.* Allosteric Coupling of Drug Binding and Intracellular Signaling in the A 2A Adenosine Receptor. *Cell* (2017).
18. Kofuku, Y. *et al.* Functional dynamics of deuterated β_2 -adrenergic receptor in lipid bilayers revealed by NMR spectroscopy. *Angew Chem Int Ed Engl* **53**, 13376–13379 (2014).
19. Chapman, K. *et al.* Ligand modulation of sidechain dynamics in a wild-type human GPCR. *eLife Sciences* **6**, e28505 (2017).
20. Solt, A. S. *et al.* Insight into partial agonism by observing multiple equilibria for ligand-bound and G s -mimetic nanobody-bound β_1 -adrenergic receptor. *Nat. Commun.* **8**, 1795 (2017).
21. Manglik, A. *et al.* Structural Insights into the Dynamic Process of β_2 -Adrenergic Receptor Signaling. *Cell* **161**, 1101–1111 (2015).
22. Staus, D. P. *et al.* Allosteric nanobodies reveal the dynamic range and diverse mechanisms of G-protein-coupled receptor activation. *Nature* **535**, 448–452 (2016).
23. Klein-Seetharaman, J. *et al.* Solution NMR spectroscopy of [α - ^{15}N]lysine-labeled rhodopsin: The single peak observed in both conventional and TROSY-type HSQC spectra is ascribed to Lys-339 in the carboxyl-terminal peptide sequence. *Proc. Natl. Acad. Sci. USA* **99**, 3452–3457 (2002).
24. Nasr, M. L. *et al.* Covalently circularized nanodiscs for studying membrane proteins and viral entry. *Nat. Methods* **14**, 49–52 (2016).
25. Opitz, C., Isogai, S. & Grzesiek, S. An economic approach to efficient isotope labeling in insect cells using homemade ^{15}N -, ^{13}C - and ^2H -labeled yeast extracts. *J. Biomol. NMR* **62**, 373–385 (2015).
26. Ballesteros, J. A. & Weinstein, H. Integrated methods for the construction of three-

- dimensional models and computational probing of structure-function relations in G protein-coupled receptors. *Methods in Neurosciences* **25**, 366–428 (1995).
27. Kay, L. E., Torchia, D. A. & Bax, A. Backbone dynamics of proteins as studied by ¹⁵N inverse detected heteronuclear NMR spectroscopy: application to staphylococcal nuclease. **28**, 8972–8979 (1989).
 28. Rasmussen, S. G. F. *et al.* Structure of a nanobody-stabilized active state of the $\beta(2)$ adrenoceptor. *Nature* **469**, 175–180 (2011).
 29. McConnell, H. REACTION RATES BY NUCLEAR MAGNETIC RESONANCE. *J. Chem. Phys.* **28**, 430–431 (1958).
 30. Palmer, A. G. NMR characterization of the dynamics of biomacromolecules. *Chem Rev* **104**, 3623–3640 (2004).
 31. Warne, T. *et al.* The structural basis for agonist and partial agonist action on a $\beta(1)$ -adrenergic receptor. *Nature* **469**, 241–244 (2011).
 32. Rasmussen, S. G. F. *et al.* Crystal structure of the $\beta(2)$ adrenergic receptor–Gs protein complex. *Nature* **477**, 549–555 (2011).
 33. Ring, A. M. *et al.* Adrenaline-activated structure of $\beta(2)$ -adrenoceptor stabilized by an engineered nanobody. *Nature* **502**, 575 EP —579 (2013).
 34. Xu, X.-P. & Case, D. A. Probing multiple effects on ¹⁵N, ¹³C α , ¹³C β , and ¹³C' chemical shifts in peptides using density functional theory. *Biopolymers* **65**, 408–423 (2002).
 35. Elling, C. E. *et al.* Metal ion site engineering indicates a global toggle switch model for seven-transmembrane receptor activation. *J. Biol. Chem.* **281**, 17337–17346 (2006).
 36. Devree, B. T. *et al.* Allosteric coupling from G protein to the agonist-binding pocket in GPCRs. *Nature* **535**, 182–186 (2016).
 37. Grzesiek, S. *et al.* Refined solution structure and backbone dynamics of HIV-1 Nef. *Protein Sci* **6**, 1248–1263 (1997).
 38. Tjandra, N., Szabo, A. & Bax, A. Protein Backbone Dynamics and ¹⁵N Chemical Shift Anisotropy from Quantitative Measurement of Relaxation Interference Effects. *J. Am. Chem. Soc.* **118**, 6986–6991 (1996).
 39. Delaglio, F. *et al.* NMRPipe: a multidimensional spectral processing system based on UNIX pipes. *J. Biomol. NMR* **6**, 277–293 (1995).

40. Goddard, T. D. & Kneller, D. G. *SPARKY, version 3*. (University of California, 2008).
41. Garrett, D., Powers, R., Gronenborn, A. & Clore, G. A common sense approach to peak picking in two-, three-, and four dimensional spectra using automatic computer analysis of contour diagrams. *J. Magn. Reson.* **95**, 214–220 (1991).
42. Pervushin, K. Impact of Transverse Relaxation Optimized Spectroscopy (TROSY) on NMR as a technique in structural biology. *Quarterly Reviews of Biophysics* **33**, 161–197 (2000).
43. Schuck, P., Zhao, H., Brautigam, C. A. & Ghirlando, R. *Basic Principles of Analytical Ultracentrifugation*. (CRC Press, 2016).
44. Baker, J. G., Proudman, R. G. W. & Tate, C. G. The pharmacological effects of the thermostabilising (m23) mutations and intra and extracellular (β 36) deletions essential for crystallisation of the turkey β -adrenoceptor. *Naunyn Schmiedebergs Arch. Pharmacol.* **384**, 71–91 (2011).
45. Ho, B. K., Thomas, A. & Brasseur, R. Revisiting the Ramachandran plot: Hard-sphere repulsion, electrostatics, and H-bonding in the α -helix. *Protein Sci* **12**, 2508–2522 (2003).

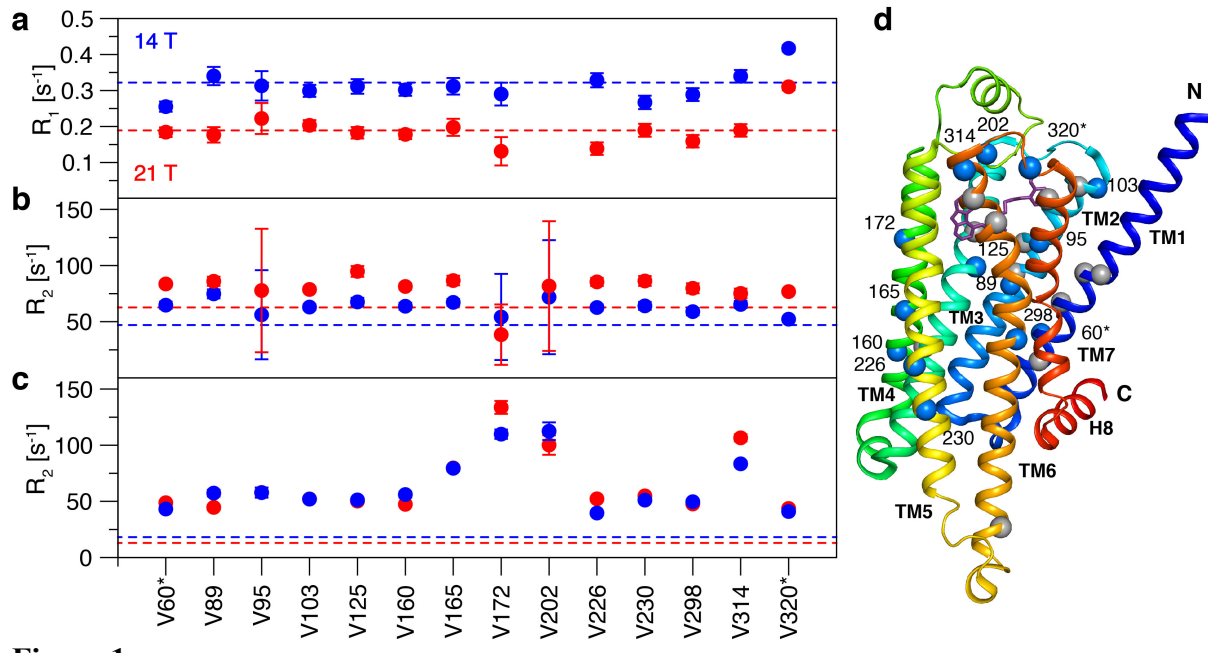


Figure 1

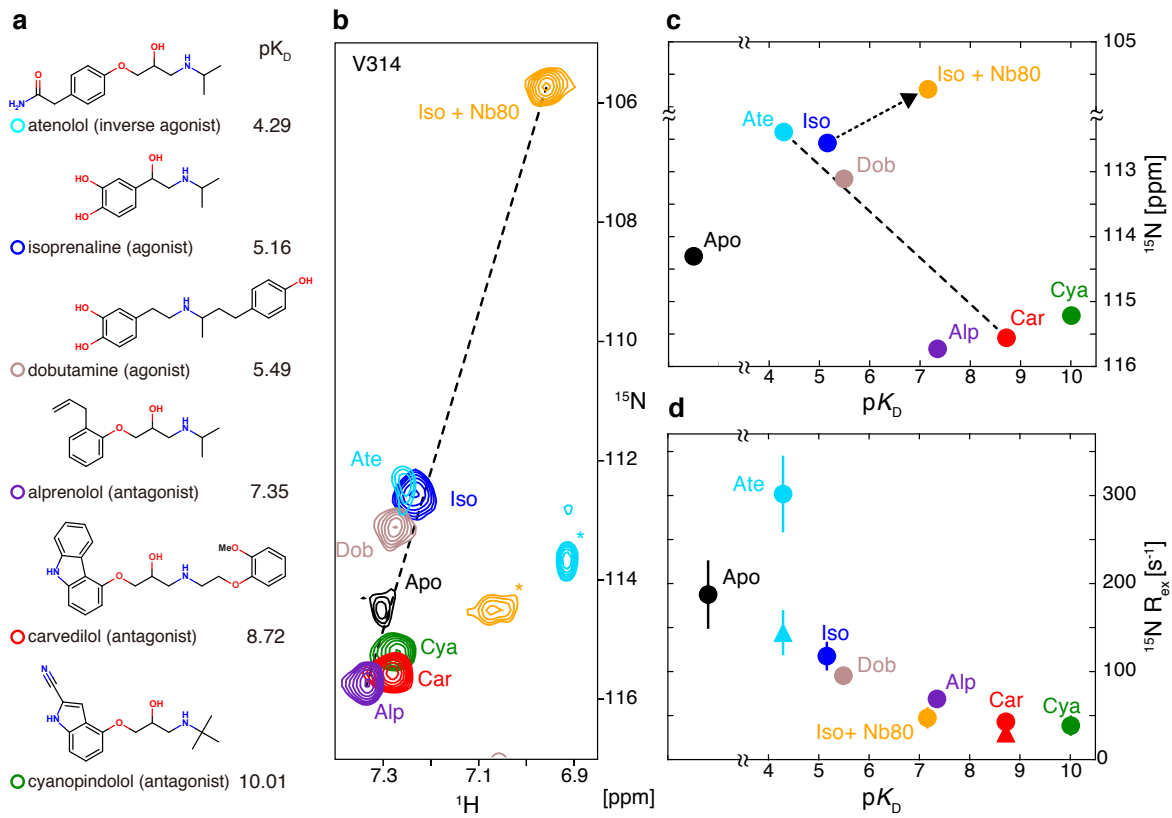


Figure 2

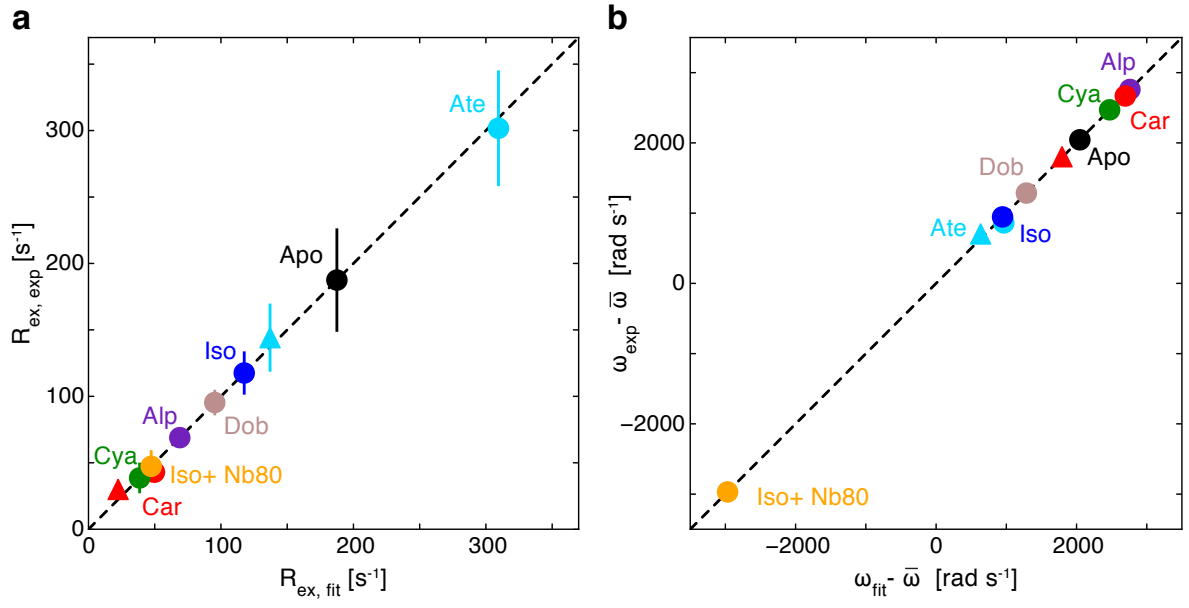


Figure 3

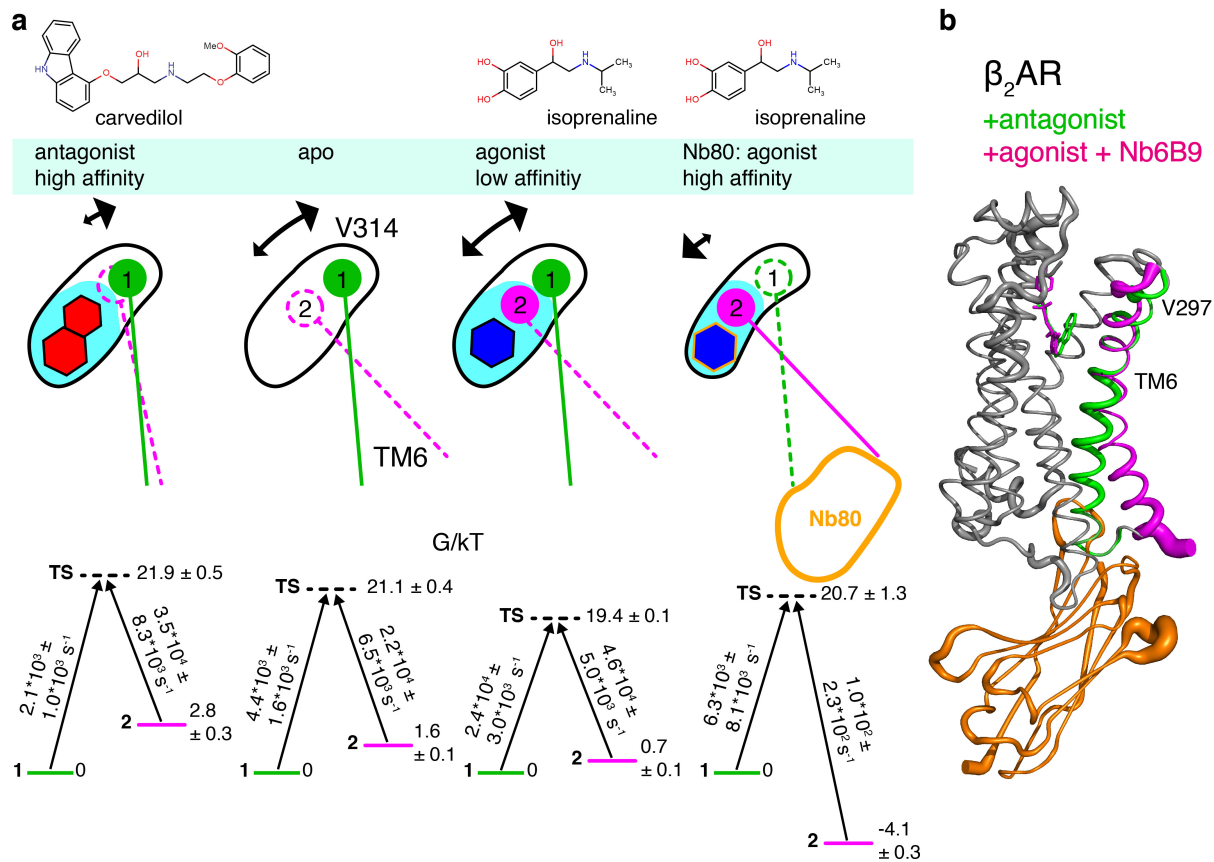


Figure 4

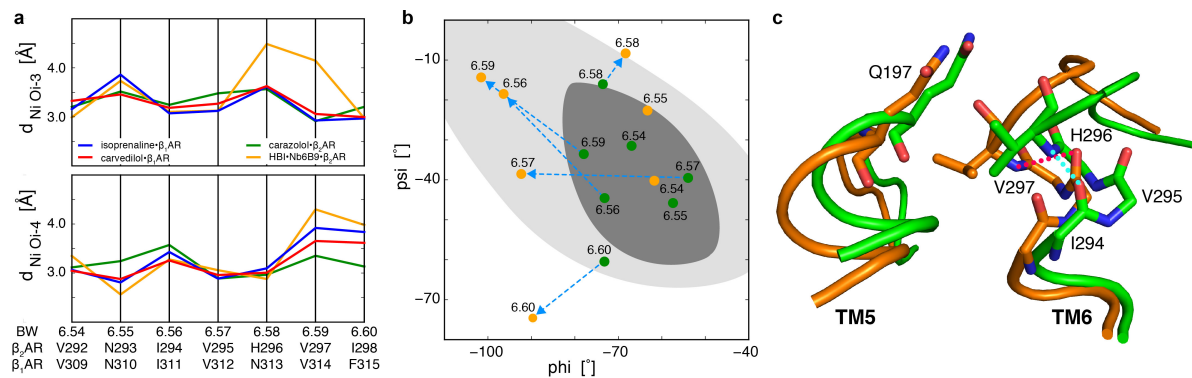


Figure 5

NMR backbone dynamics reveals mechanism of ligand to effector site allosteric coupling in the β_1 -adrenergic receptor

Anne Grahl¹, Shin Isogai¹, Timothy Sharpe², Stephan Grzesiek^{1,*}

¹ Focal Area Structural Biology and Biophysics, Biozentrum, University of Basel, CH-4056 Basel, Switzerland

² Biophysics Core Facility, Biozentrum, University of Basel, CH-4056 Basel, Switzerland

Supporting information

*Address correspondence to:

Stephan Grzesiek

Focal Area Structural Biology and Biophysics, Biozentrum

University of Basel, CH-4056 Basel, Switzerland

Phone: ++41 61 267 2100

FAX: ++41 61 267 2109

Email: Stephan.Grzesiek@unibas.ch

Figure Legends

Figure S1. Global backbone dynamics of β_1 AR determined from 1D ^1H -detected ^{15}N relaxation experiments. Experiments were carried out on ^2H (~60 %)/ ^{15}N -labeled, alprenolol-bound TS- β_1 AR in DM micelles at 21 T (**a,c,e**) and 14 T (**b,d,f**). Relaxation rates were determined from intensity ratios of attenuated (blue) vs. reference spectra (black). Determined relaxation rates as well as relaxation delays for R_1 and R_2 experiments are indicated. (**a,b**) ^{15}N longitudinal (R_1) relaxation experiments. (**c,d**) ^{15}N - ^1H dipolar coupling/ ^{15}N CSA cross-correlation experiments. The transfer time was 12 ms. (**e,f**) ^{15}N transverse (R_2) relaxation experiments.

Figure S2. ^1H - ^{15}N TROSY spectra of ^{15}N -valine-labeled β_1 AR (a) TS- β_1 AR•alprenolol at 14 T. Valine resonances, for which relaxation rates could be determined unambiguously, are labeled by residue-specific assignments. Tentative assignments are marked by asterisks. (b) Assignment of the V314 ^1H - ^{15}N resonance in the ternary TS- β_1 AR(A227Y/L343Y)•isoprenaline•Nb80 complex by point mutation. ^1H - ^{15}N TROSY spectra (21 T) of TS- β_1 AR(A227Y/L343Y) (orange) and TS- β_1 AR(A227Y/L343Y/V314A) (blue) in the presence of an equimolar amount of Nb80 and 1 mM isoprenaline. The resonance at 105.7 ppm (^{15}N) and 7.0 ppm (^1H) disappears due to the V314A point mutation and is assigned to V314. The others resonances show only minor changes. Further assignments transferred from the binary TS- β_1 AR(A227Y/L343Y)•isoprenaline complex are indicated.

Figure S3. Agreement of residue-specific ^{15}N R_{ex} rates derived by line shape fitting from ^1H - ^{15}N HSQC and TROSY spectra of ^{15}N -valine labeled TS- β_1 AR•alprenolol. R_{ex} rates are determined as $R_{\text{ex}} = R_2 - R_{2,0}$. (**a**) HSQC- and TROSY-derived R_{ex} at 21 T. Correlation coefficient $r^2 = 0.91$, RMSD = 11.4 s $^{-1}$ (**b**) as (a) at 14 T. $r^2 = 0.86$, RMSD = 17.3 s $^{-1}$.

Figure S4. Residue-specific ^{15}N R_2 rates of ^{15}N -valine TS- β_1 AR(A227Y/L343Y) and TS- β_1 AR in various states. ^{15}N R_2 rates are derived from line shape fitting of ^1H - ^{15}N TROSY spectra (Table S2) of (**a**) TS- β_1 AR(A227Y/L343Y) in apo form, orthosteric binary and ternary isoprenaline•Nb80 complexes at 21 T and (**b**) TS- β_1 AR in apo form and orthosteric binary complexes at 19 T. Data for the various forms are color-coded.

Figure S5. Evidence for two-site exchange of V314 at the ligand entry tunnel of TS- β_1 AR (**a**) ^1H - ^{15}N -chemical shift response of V314 in apo form and binary orthosteric complexes at 19 T. Spectra are color-coded and marked according to the ligand. Cross peaks from other residues are marked with asterisks. A dashed line visualizes the approximate linear correlation between ^1H and ^{15}N chemical shifts of V314(6.59) in various receptor states indicative of two-site exchange. (**c**) V314(6.59) ^{15}N chemical shift (19 T) versus ligand affinity $\text{p}K_{\text{D}}$. The dashed line indicates the approximate linear correlation between V314(6.59) ^{15}N chemical shift and ligand affinity $\text{p}K_{\text{D}}$. (**d**) V314(6.59) ^{15}N exchange broadening versus $\text{p}K_{\text{D}}$ at 21 T (filled circles), 19 T (filled diamonds), and 14 T (filled triangles).

The V314(6.59) ^1H - ^{15}N chemical shifts and line widths for all forms of TS- $\beta_1\text{AR}$ are very similar to the fully active TS- $\beta_1\text{AR}$ (A227Y/L343Y) (Figure 2), albeit the ^{15}N positions are moderately (<0.8 ppm) moved downfield towards the inactive antagonist-bound conformation, corroborating the less active character of TS- $\beta_1\text{AR}$. Compared to $\beta_1\text{AR}$ (A227Y/L343Y), fitted exchange rate constants $k_{1/2}$ are slightly reduced and the activation barriers slightly increased, respectively (Table S3). Of note, the V314(6.59) resonance of apo TS- $\beta_1\text{AR}$ is severely broadened and shifted completely to the cluster of resonances of the inactive antagonist-bound complexes. Accordingly, its activation barrier increases by about 2.4 kT relative to $\beta_1\text{AR}$ (A227Y/L343Y) and also its inactive state S_1 is more stabilized by about 0.6 kT (Figure S7). Thus, V314(6.59) is almost completely in the inactive conformation in apo TS- $\beta_1\text{AR}$, albeit it still exchanges with the active conformation to some extent. These results clearly show that the presence of tyrosines 227 and 343 in $\beta_1\text{AR}$ (A227Y/L343Y) shifts the equilibrium of the receptor towards the active state and at the same time decreases the activation barrier of the transition.

Figure S6. Evidence for dynamics at the orthosteric binding pocket and extracellular loop 2 of TS- $\beta_1\text{AR}$ (A227Y/L343Y) and TS- $\beta_1\text{AR}$ in various states. (a) V172(4.59) and (b) V202(ELC2) ^1H - ^{15}N TROSY resonances of TS- $\beta_1\text{AR}$ (A227Y/L343Y) in apo form, orthosteric binary and ternary isoprenaline•Nb80 complexes at 21 T. (c) V172(4.59) and (d) V202(ELC2) ^1H - ^{15}N TROSY resonances of TS- $\beta_1\text{AR}$ (A227Y/L343Y) in apo form and orthosteric binary complexes at 19 T.

Figure S7. Fit to ^{15}N resonance behavior and schematics of two-site exchange model for V314 in TS- $\beta_1\text{AR}$. (a) Comparison of experimental and fitted ^{15}N exchange rates R_{ex} at 21 T (filled circles), 19 T (filled diamonds), and 14 T (filled triangles). (b) Comparison of experimental and fitted ^{15}N frequencies ω . Symbols as in (a). (c) Cartoon of V314(6.59) located at the ligand entry tunnel exchanging between the conformational states S_1 and S_2 . Three distinct situations are depicted for the (i) high affinity antagonist (carvedilol) complex, (ii) apo form, and (iii) low-affinity agonist (isoprenaline) complex. Determined exchange rates $k_{1/2}$ and free energy differences are indicated for all cases.

Figure S8. Crystal structures of turkey $\beta_1\text{AR}$ and human $\beta_2\text{AR}$ in various ligand-bound forms. All structures were aligned on the central regions of TM1-4 and TM7. (a) Superposition of $\beta_1\text{AR}$ and $\beta_2\text{AR}$ backbone structures in complexes with antagonists ($\beta_1\text{AR}$ • carvedilol: green, 4AMJ_B; $\beta_2\text{AR}$ •carazolol: blue, 2RH1) and agonists ($\beta_1\text{AR}$ •isoprenaline: magenta, 2Y03_B; $\beta_2\text{AR}$ •FAUC50: cyan, 3PDS). (b) Superposition of $\beta_2\text{AR}$ backbone structures in binary complex with antagonist ($\beta_2\text{AR}$ •carazolol: blue, 2RH1) and ternary complexes ($\beta_2\text{AR}$ •HBI•Nb6B9: orange, 4LDL; $\beta_2\text{AR}$ •BI167107•G protein: yellow, 3SN6). (c-e) Superpositions of the backbone structures shown in (a,b) around the orthosteric ligand binding pocket towards TM6. The ligands are indicated as sticks with CPK colors. (c) Antagonist complex $\beta_1\text{AR}$ •carvedilol (green) and agonist complex $\beta_1\text{AR}$ •isoprenaline (magenta). (d) Agonist complex $\beta_2\text{AR}$ •FAUC50 (cyan) and ternary complex $\beta_2\text{AR}$ •HBI•Nb6B9 (orange). (e)

Agonist complex $\beta_1\text{AR}\cdot\text{isoprenaline}$ (magenta) and ternary complex $\beta_2\text{AR}\cdot\text{HBI}\cdot\text{Nb6B9}$ (orange).

Figure S9. Correlation between the free energy differences of the two main conformational states for V314(6.59) and ligand affinity in TS- $\beta_1\text{AR}$ (A227Y/L343Y). The free energy differences $E_{21} = E_2 - E_1$ between the states S_1 and S_2 are determined from the two-site exchange model (Table S3) and plotted against the ligand affinity $\text{p}K_{\text{D}}$. An approximate linear correlation is evident (Pearson coefficient $r^2 = 0.67$), which can be fitted as $\Delta G_{\text{D}}/kT = \ln(10)\text{p}K_{\text{D}} = (1.1 \pm 0.2) E_{21}/kT + 1.1 \pm 0.5$ (dashed line).

21 T

14 T

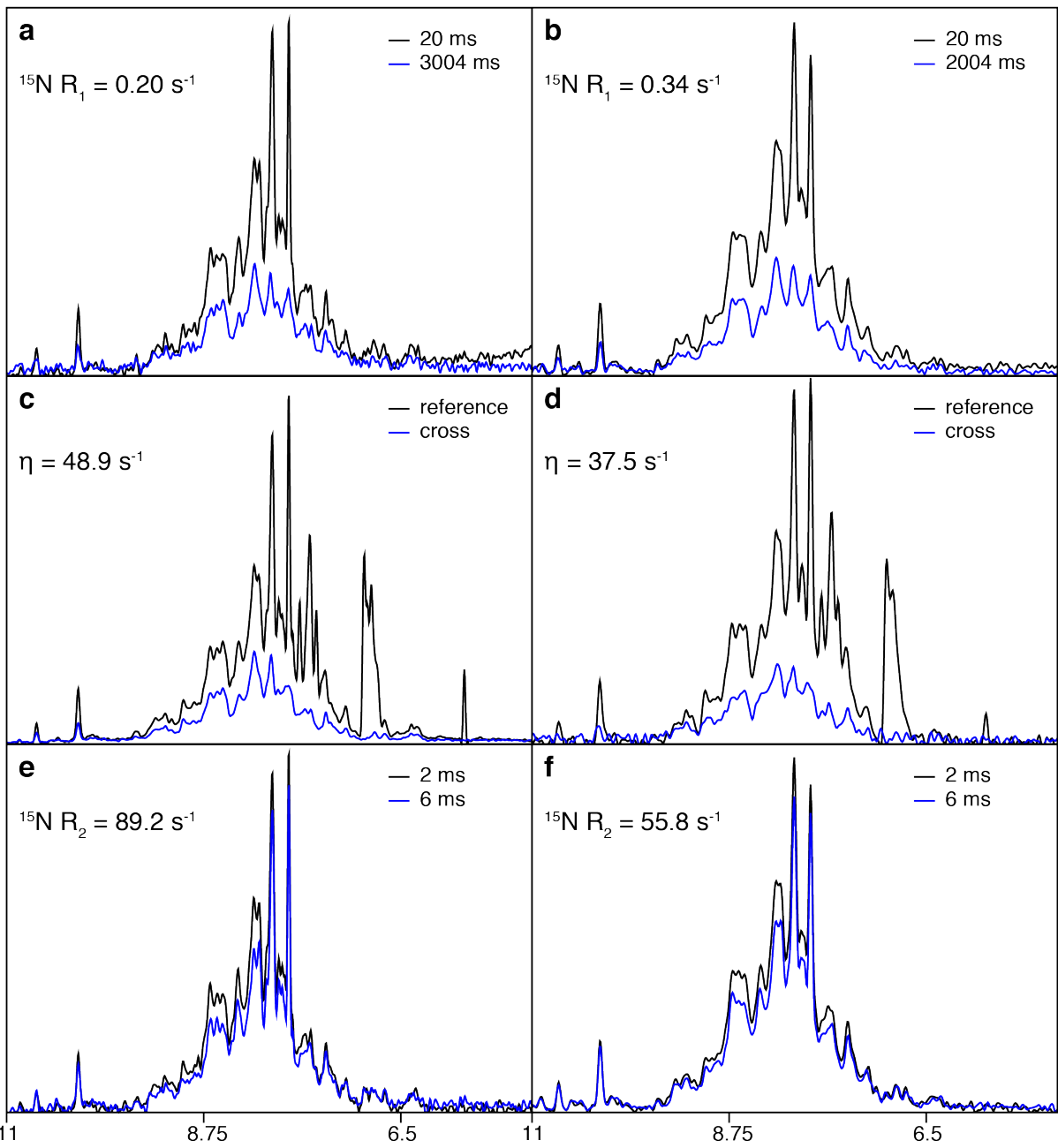


Figure SI 1

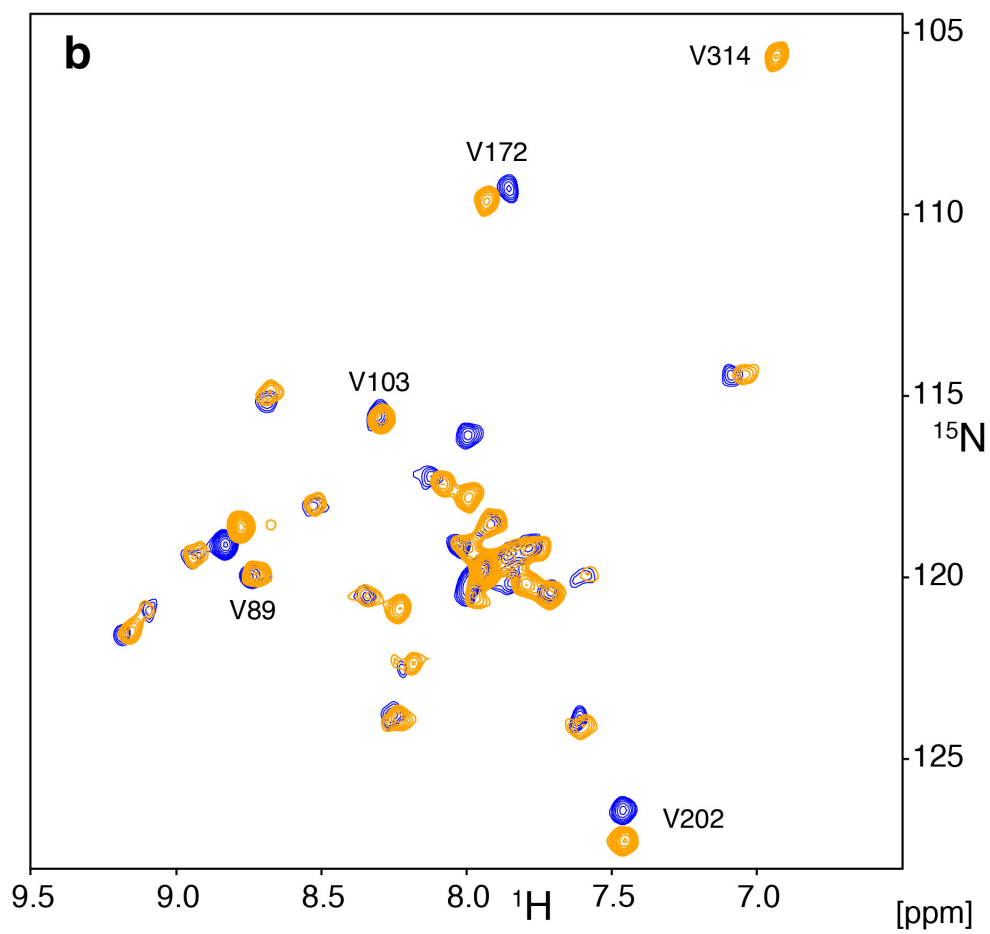
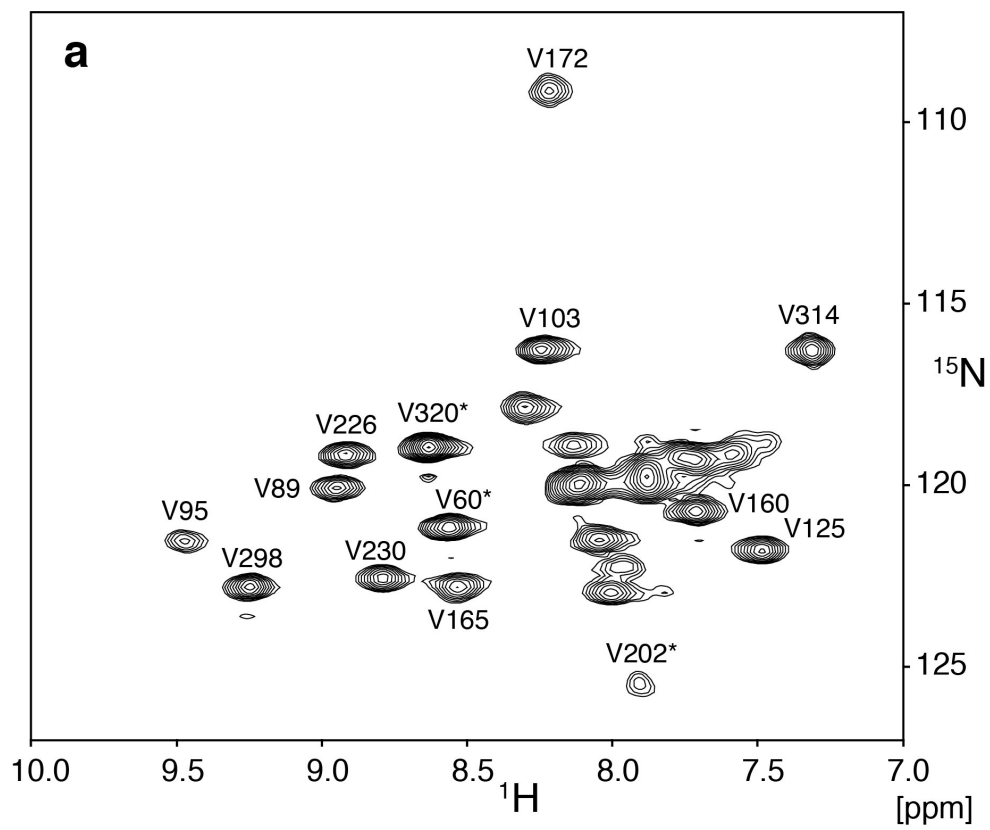


Figure SI 2

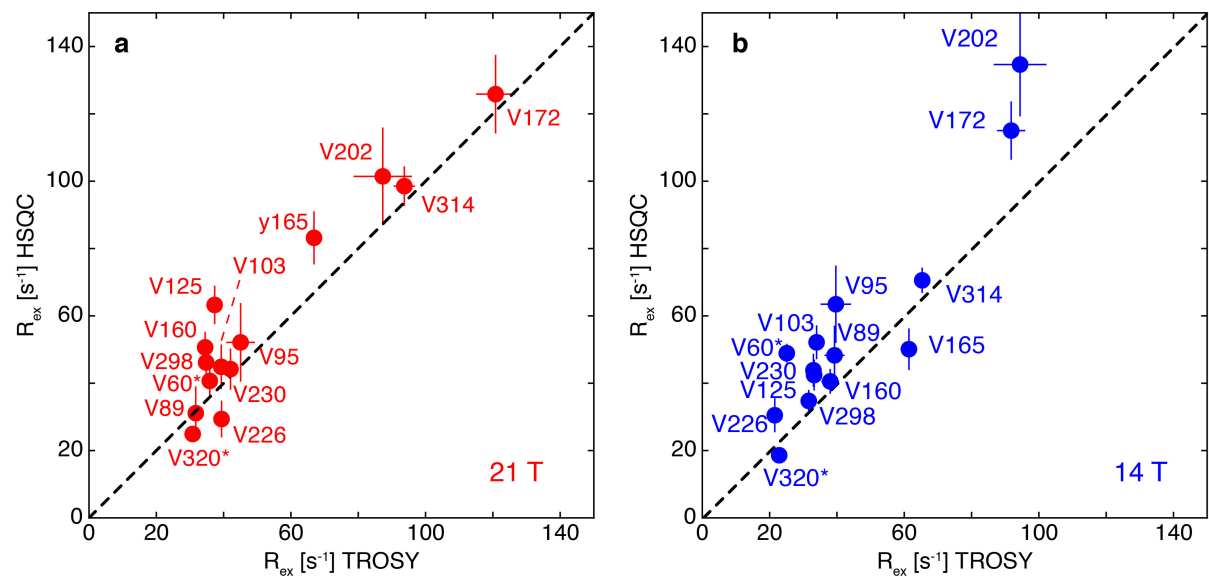


Figure SI 3

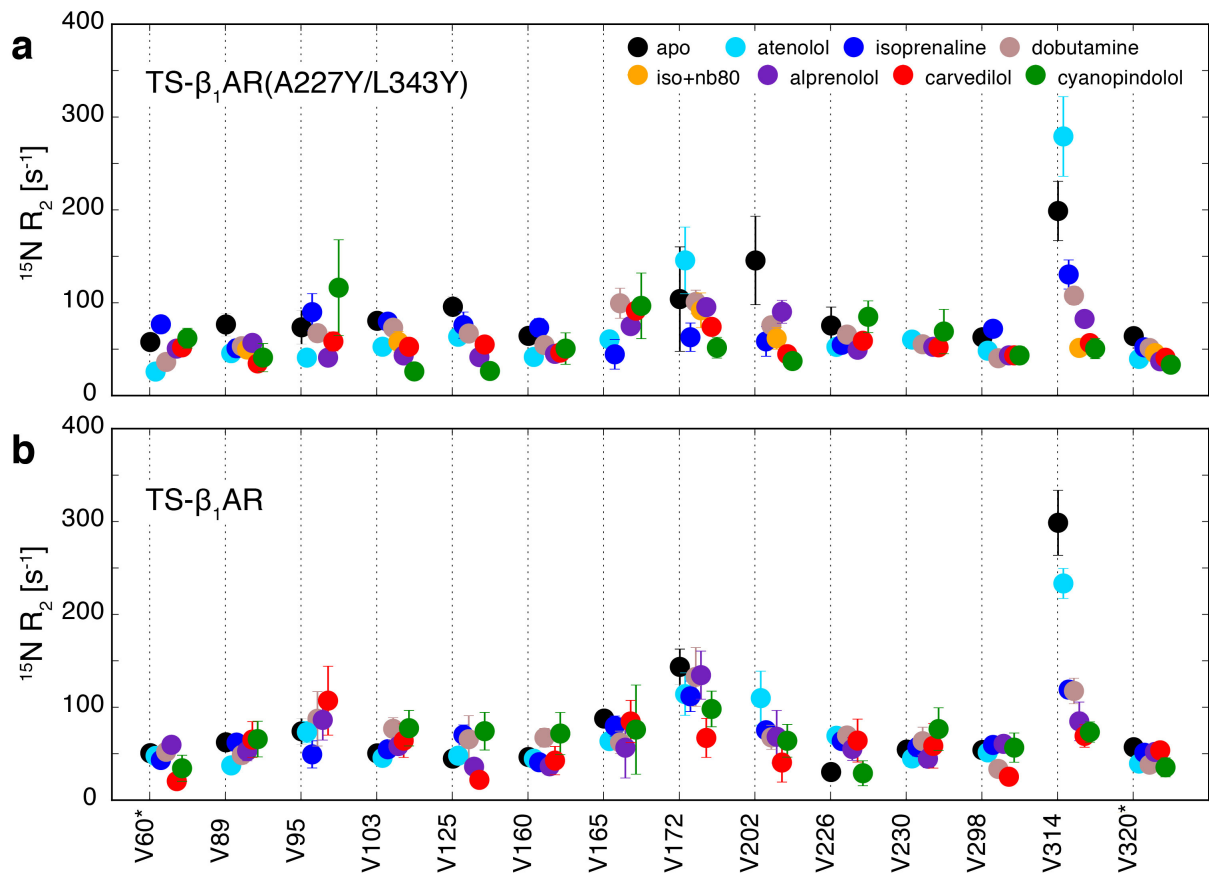


Figure SI 4

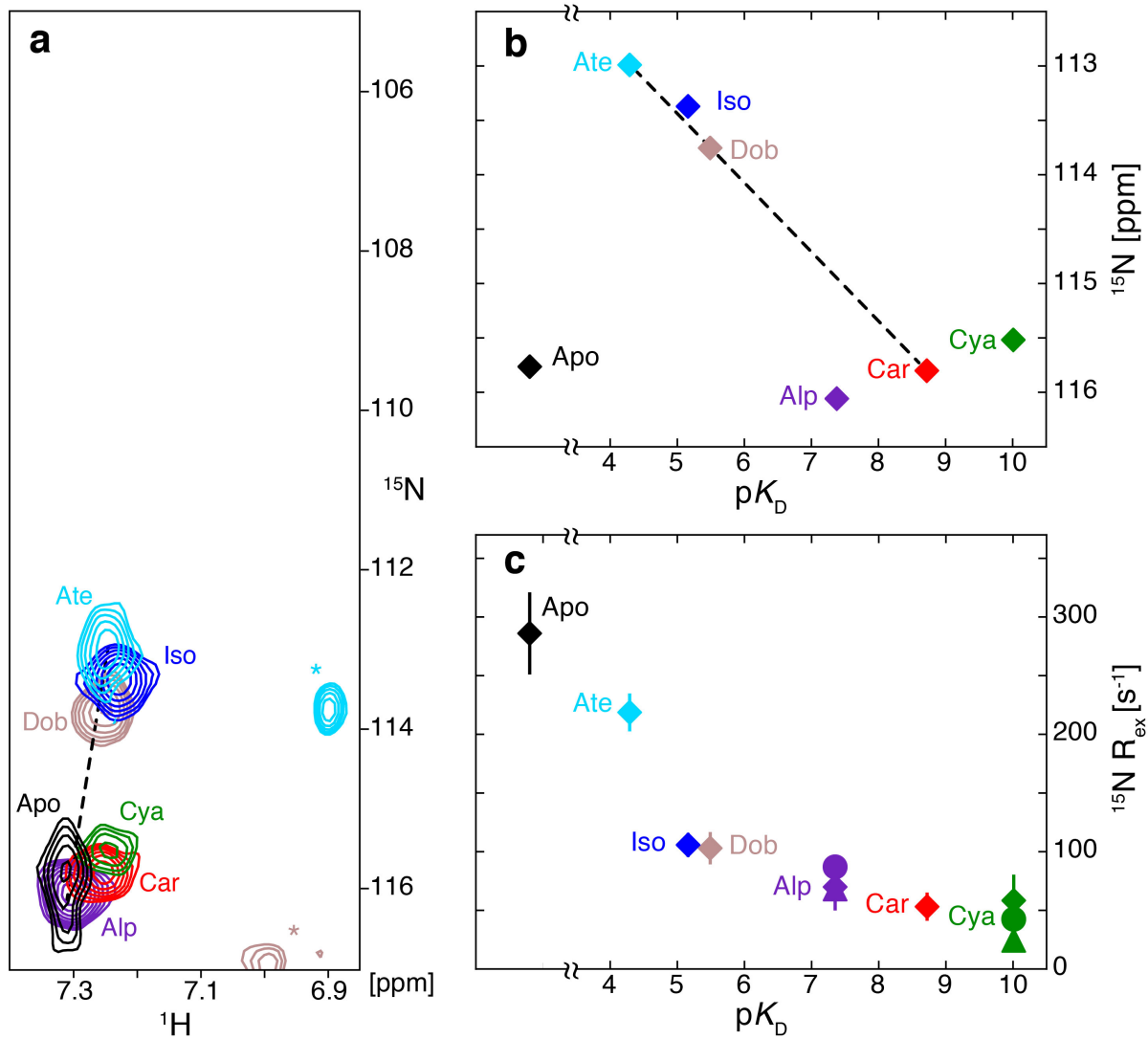


Figure SI 5

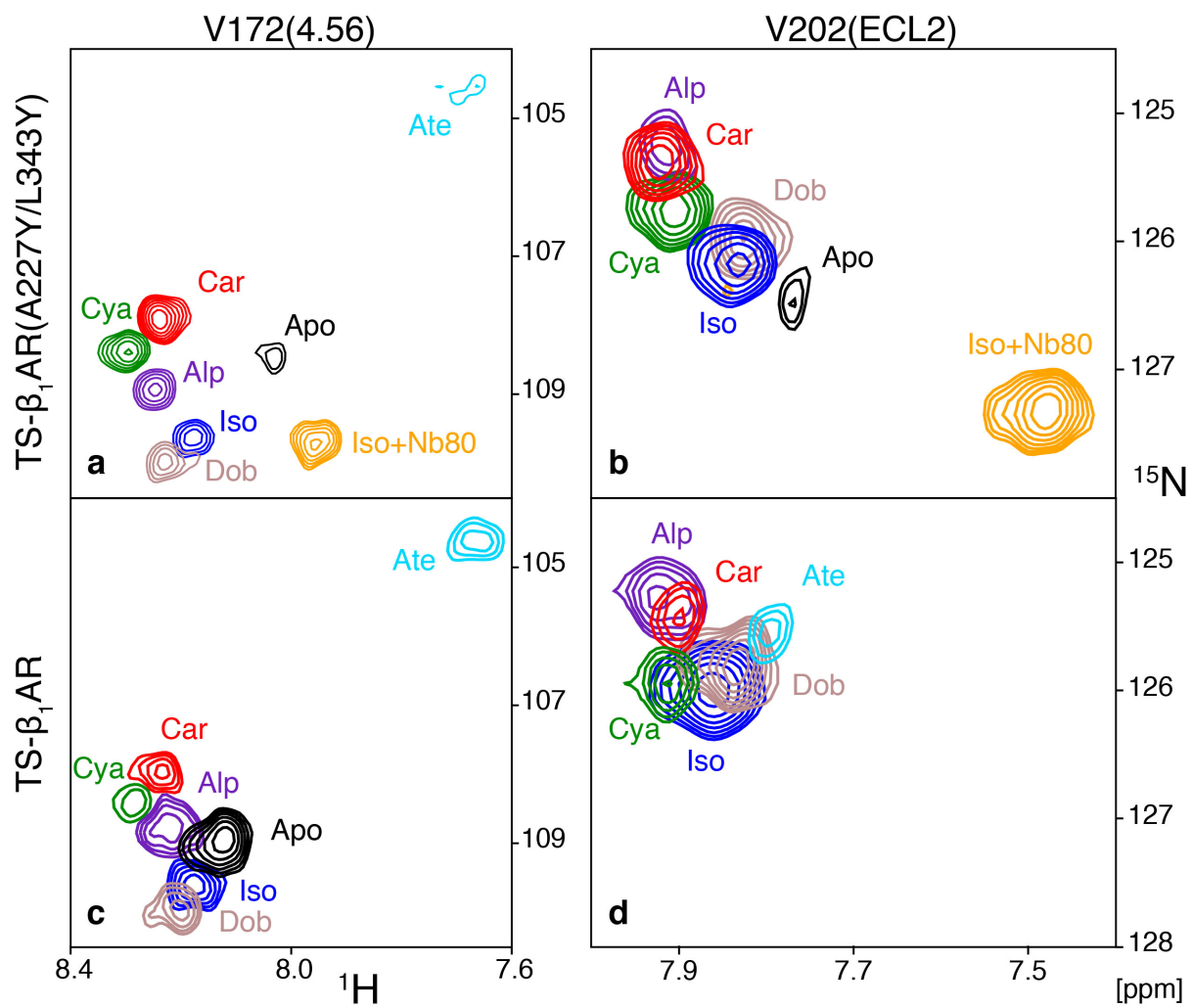


Figure SI 6

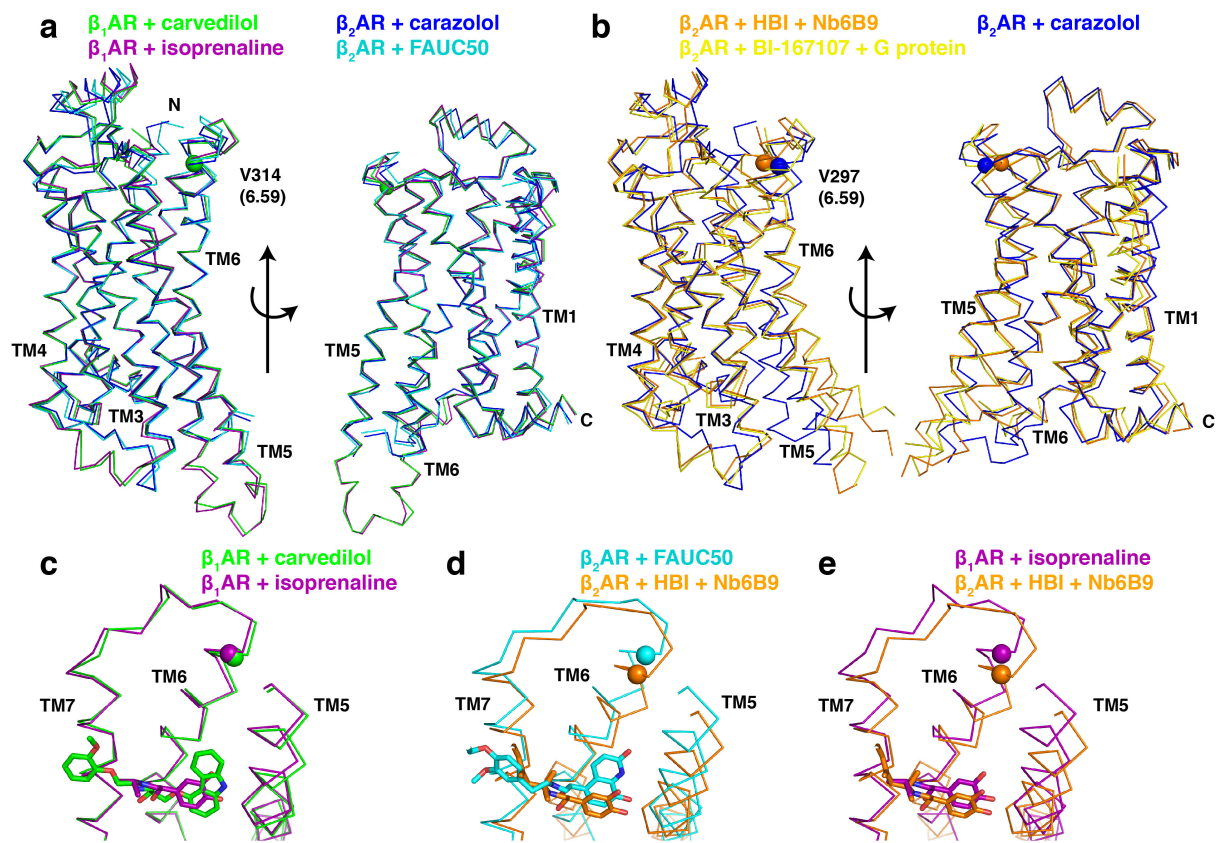


Figure SI 8

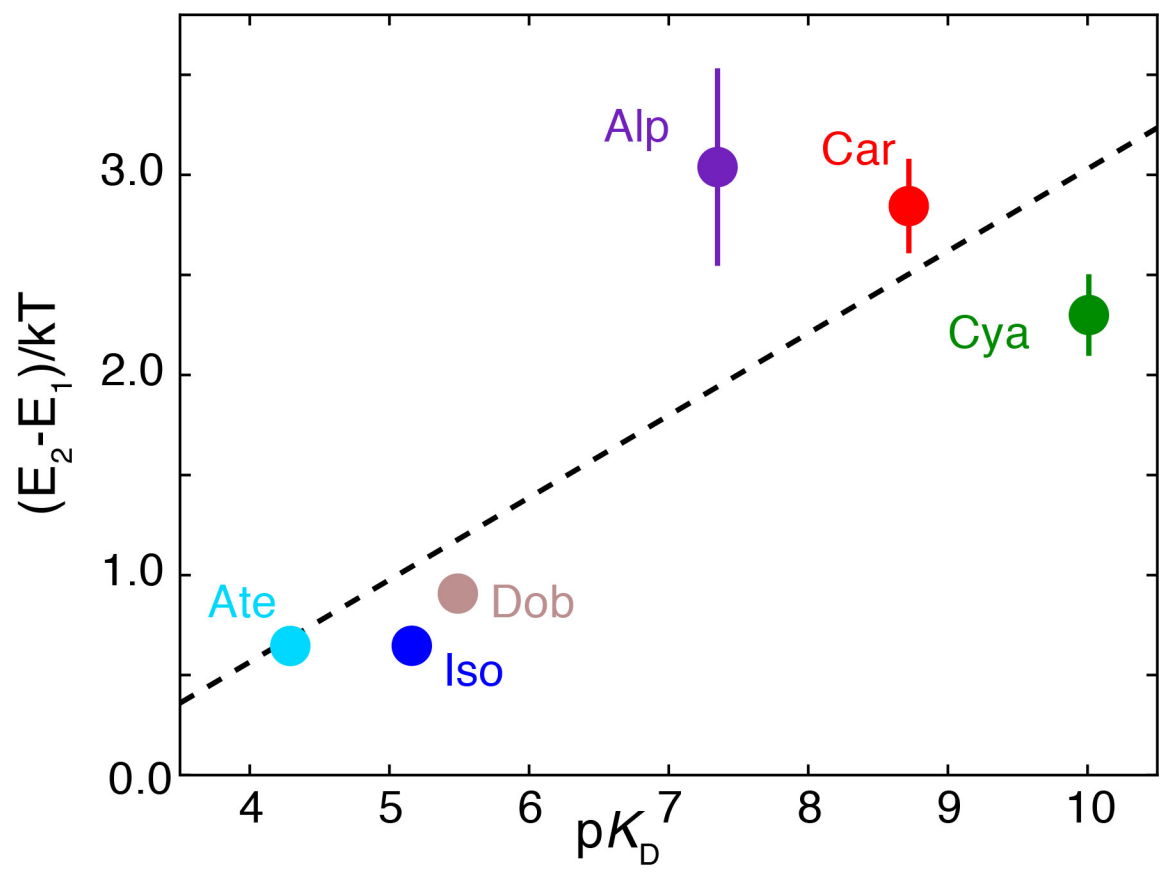


Figure SI 9

Supplementary Tables for

NMR backbone dynamics reveals mechanism of ligand to effector site allosteric coupling in the β_1 -adrenergic receptor

Anne Grah¹, Shin Isogai¹, Timothy Sharpe², Stephan Grzesiek¹

¹ Focal Area Structural Biology and Biophysics, Biozentrum, University of Basel, CH-4056 Basel, Switzerland

² Biophysics Core Facility, Biozentrum, University of Basel, CH-4056 Basel, Switzerland

Corresponding author: Stephan Grzesiek (stephan.grzesiek@unibas.ch)

This Excel file includes:

Table S1: Average relaxation data and molecular weight of ²H (~60%)/¹⁵N-labeled, alprenolol-bound TS- β_1 AR in DM micelles

Table S2: ¹⁵N R₂ rates of all evaluated valine ¹⁵N resonances from line shape analysis of TS- β_1 AR(A227Y/L343Y) and TS- β_1 AR in various forms

Table S3: Spectral data of V314 resonance in TS- β_1 AR(A227Y/L343Y) and TS- β_1 AR in various forms and parameters derived from fit to two-site exchange model

Table S1: Average relaxation data and molecular weight of ^2H (~60%)/ ^{15}N -labeled, alprenolol-bound TS- β_1 AR in DM micelles

Field	R1	$\Delta R1$	R2	$\Delta R2$	η	$\Delta\eta$	τ_c (R1)	$\Delta\tau_c$ (R1)	τ_c (n)	$\Delta\tau_c$ (n)
21.2	0.20	0.03	89.2	13.4	48.9	9.7	37.0	5.6	37.1	7.4
14.1	0.34	0.05	55.8	8.4	37.5	7.5	37.5	5.6	42.7	8.5

MW(MALS)	ΔMW (MALS)	τ_c (MALS)	$\Delta\tau_c$ (MALS)	$\langle\tau_c\rangle$	$\Delta\langle\tau_c\rangle$
101.4	2.2	35.2	0.8	38.0	3.2

Column legend

Field	magnetic field strength [T]
R1	15N R1 [1/s] extracted from 1D traces of 2D experiments
$\Delta R1$	error in 15N R1 [1/s]
R2	15N R2 [1/s] extracted from 1D traces of 2D experiments
$\Delta R2$	error in 15N R2 [1/s]
η	15N-1H dipolar-coupling/15N CSA cross-correlation rate [1/s]
$\Delta\eta$	error in 15N-1H dipolar-coupling/15N CSA cross-correlation rate [1/s]
τ_c (R1)	rotational correlation time τ_c determined from 15N R1 [ns]
$\Delta\tau_c$ (R1)	error of τ_c (R1) [ns]
τ_c (n)	rotational correlation time τ_c determined from η [ns]
$\Delta\tau_c$ (n)	error of τ_c (n) [ns]
MW(MALS)	mean molecular weight [kDa] of the protein detergent complex obtained from three independent SEC-MALS experiments
ΔMW (MALS)	error in MW (MALS) [kDa]
τ_c (MALS)	rotational correlation time τ_c determined from molecular weight by Stokes-Einstein relation
$\Delta\tau_c$ (MALS)	error of τ_c (MALS) [ns]
$\langle\tau_c\rangle$	average τ_c from R1 and η at 21.2 T and 14.1 T [ns]
$\Delta\langle\tau_c\rangle$	error in $\langle\tau_c\rangle$ [ns]

Table S3: Spectral data of V314 resonance in TS- β_1 AR(A227Y/L343Y) and TS- β_1 AR in various forms and parameters derived from fit to two-site exchange model

construct	ligand	Field	1H	15N	$\Delta\omega$	$\omega_{exp}-\bar{\omega}$	$\Delta\omega_{exp}-\bar{\omega}$	R2,0	Rex,exp	$\Delta R_{ex,exp}$	$\omega_{fit}-\bar{\omega}$	Rex,fit
TS- β_1 AR	alprenolol	14.1	7.33	116.11	2012.5	1988.9	76.5	18.1	68.3	3.1	1959.4	68.2
TS- β_1 AR	alprenolol	18.8	7.31	116.06	2683.3	2625.4	102.0	14.0	69.9	20.8	2636.0	81.7
TS- β_1 AR	alprenolol	21.2	7.33	116.05	3018.7	2946.7	114.7	14.0	87.0	3.3	2974.5	86.2
TS- β_1 AR	apo	18.8	7.32	115.76	2683.3	2475.5	102.0	14.0	286.0	35.0	2475.5	286.0
TS- β_1 AR	atenolol	18.8	7.26	112.99	2683.3	1062.0	102.0	14.0	218.7	16.1	1062.0	218.7
TS- β_1 AR	carvedilol	18.8	7.26	115.80	2683.3	2494.4	102.0	14.0	53.1	12.0	2494.4	53.1
TS- β_1 AR	cyanopindolol	14.1	7.27	115.49	2012.5	1753.0	76.5	18.1	24.5	3.1	1761.0	20.2
TS- β_1 AR	cyanopindolol	18.8	7.26	115.52	2683.3	2350.1	102.0	14.0	58.4	22.0	2349.6	35.7
TS- β_1 AR	cyanopindolol	21.2	7.27	115.53	3018.7	2650.8	114.7	12.9	42.5	3.3	2644.3	45.1
TS- β_1 AR	dobutamine	18.8	7.26	113.75	2683.3	1450.9	102.0	14.0	102.9	13.8	1450.9	102.9
TS- β_1 AR	isoprenaline	18.8	7.24	113.37	2683.3	1256.2	102.0	14.0	105.8	10.1	1256.2	105.8
TS- β_1 AR(A227Y/L343Y)	alprenolol	21.2	7.33	115.72	3018.7	2760.3	114.7	12.9	68.9	5.7	2760.3	68.9
TS- β_1 AR(A227Y/L343Y)	apo	21.2	7.20	114.38	3018.7	1990.7	114.7	12.9	187.5	38.9	1990.8	187.5
TS- β_1 AR(A227Y/L343Y)	atenolol	14.1	7.29	112.75	2012.5	704.0	76.5	18.1	144.1	25.6	634.5	137.0
TS- β_1 AR(A227Y/L343Y)	atenolol	21.2	7.25	112.41	3018.7	861.5	114.7	12.9	301.7	43.6	964.3	309.5
TS- β_1 AR(A227Y/L343Y)	carvedilol	14.1	7.31	115.62	2012.5	1803.1	76.5	18.1	30.0	3.8	1793.3	22.4
TS- β_1 AR(A227Y/L343Y)	carvedilol	21.2	7.28	115.56	3018.7	2668.0	114.7	12.9	42.9	5.3	2693.9	49.8
TS- β_1 AR(A227Y/L343Y)	cyanopindolol	21.2	7.26	115.22	3018.7	2470.7	114.7	12.9	38.6	11.5	2470.7	38.6
TS- β_1 AR(A227Y/L343Y)	dobutamine	21.2	7.28	113.15	3018.7	1285.9	114.7	12.9	95.3	9.6	1286.0	95.3
TS- β_1 AR(A227Y/L343Y)	isoprenaline	21.2	7.24	112.56	3018.7	946.4	114.7	12.9	117.6	16.3	946.4	117.6
TS- β_1 AR(A227Y/L343Y)	isoprenaline+Nb80	21.2	6.96	105.73	3018.7	-2968.7	114.7	15.6	47.3	12.2	-2968.3	47.3

construct	ligand	χ^2	k1	$\Delta k1$	k2	$\Delta k2$	E1-E2	$\Delta E2-E1$	ETS-E1	$\Delta ETS-E1$
TS- β_1 AR	alprenolol	5.8E-01	1.08E+02	1.62E+01	3.05E+03	6.80E+02	3.34	0.10	24.79	0.15
TS- β_1 AR	apo	7.9E-07	4.20E+02	1.85E+02	3.61E+03	1.97E+03	2.15	0.61	23.44	0.44
TS- β_1 AR	atenolol	6.5E-07	8.54E+03	1.17E+03	1.94E+04	1.77E+03	0.82	0.10	20.42	0.14
TS- β_1 AR	carvedilol	1.1E-08	6.99E+02	8.48E+02	1.78E+04	1.17E+04	3.24	0.66	22.93	1.21
TS- β_1 AR	cyanopindolol	3.6E+00	2.96E+03	8.75E+02	4.41E+04	6.64E+03	2.70	0.18	21.49	0.30
TS- β_1 AR	dobutamine	1.3E-07	1.14E+04	2.25E+03	3.81E+04	5.05E+03	1.20	0.10	20.13	0.20
TS- β_1 AR	isoprenaline	1.7E-07	1.42E+04	1.97E+03	3.91E+04	4.38E+03	1.01	0.09	19.92	0.14
TS- β_1 AR(A227Y/L343Y)	alprenolol	2.0E-07	9.93E+02	8.96E+02	2.07E+04	8.45E+03	3.04	0.39	22.58	0.90
TS- β_1 AR(A227Y/L343Y)	apo	3.9E-07	4.83E+03	1.18E+03	2.28E+04	4.39E+03	1.55	0.15	20.99	0.24
TS- β_1 AR(A227Y/L343Y)	atenolol	1.7E+00	9.20E+03	1.14E+03	1.75E+04	1.96E+03	0.65	0.05	20.35	0.12
TS- β_1 AR(A227Y/L343Y)	carvedilol	5.8E+00	2.05E+03	1.01E+03	3.53E+04	8.26E+03	2.84	0.28	21.85	0.49
TS- β_1 AR(A227Y/L343Y)	cyanopindolol	3.8E-08	7.11E+03	5.04E+03	7.08E+04	3.15E+04	2.30	0.26	20.61	0.71
TS- β_1 AR(A227Y/L343Y)	dobutamine	4.7E-07	2.25E+04	3.64E+03	5.58E+04	6.17E+03	0.91	0.11	19.45	0.16
TS- β_1 AR(A227Y/L343Y)	isoprenaline	4.9E-08	2.41E+04	2.96E+03	4.59E+04	4.97E+03	0.65	0.07	19.39	0.12
TS- β_1 AR(A227Y/L343Y)	isoprenaline+Nb80	1.0E-05	6.31E+03	8.10E+03	1.00E+02	2.28E+02	-4.14	0.33	20.73	1.28

Column legend

construct	β_1 AR construct
ligand	ligand(s) used for experiment
Field	magnetic field strength [T]
1H	V314 1H chemical shift [ppm]
15N	V314 15N chemical shift [ppm]
$\Delta\omega$	$(\omega_1 - \omega_2)/2$ [rad/s]
$\omega_{exp}-\bar{\omega}$	deviation of experimental 15N frequency ω_{exp} from center frequency $\bar{\omega}$ [rad/s]
$\Delta\omega_{exp}-\bar{\omega}$	estimated error in $\omega_{exp}-\bar{\omega}$ [rad/s]
R2,0	theoretical exchange-free transverse relaxation rate based on τ_c [1/s]
Rex,exp	experimental exchange contribution to R2 (Table S2, Rex = R2-R2,0) [1/s]
$\Delta R_{ex,exp}$	estimated error in Rex from Monte Carlo analysis [1/s]
$\omega_{fit}-\bar{\omega}$	deviation of fitted 15N frequency ω_{fit} from center frequency $\bar{\omega}$ [rad/s]
Rex,fit	fitted exchange contribution to R2 [1/s]
χ^2	chi-square (normalized to estimated errors) of fit to two-state exchange model to Rex and $\Delta\omega_{exp}-\bar{\omega}$
k1	fitted k1 [1/s]
$\Delta k1$	estimated error in k1 from Monte Carlo analysis [1/s]
k2	fitted k2 [1/s]
$\Delta k2$	estimated error in k2 from Monte Carlo analysis [1/s]
E1-E2	difference of free energy of states S1 and S2 [kJ]
$\Delta E2-E1$	estimated error in E1-E2 from Monte Carlo analysis [kJ]
ETS-E1	Eyring activation barrier for S1->S2 transition calculated from k1 [kJ]
$\Delta ETS-E1$	estimated error in ETS-E1 from Monte Carlo analysis [kJ]

3.2 Additional dynamics data on the β_1 -adrenergic receptor

The following data on β_1 AR dynamics have so far not been included in a publication.

Results

V172 reveals active conformation in the binary agonist complex

Valine 172(4.56) is located below the orthosteric ligand binding pocket of β_1 AR, close to the ligand head group. The residue was described in the initial work on TS- β_1 AR (114), showing that its resonance position clusters according to the substitution pattern of the ligand head group. As compared to complexes with antagonists containing *ortho*-, *meta*-substitutions, distinct chemical shifts were observed for the agonist isoprenaline and partial agonist dobutamine with *meta*-, *para*-substitutions.

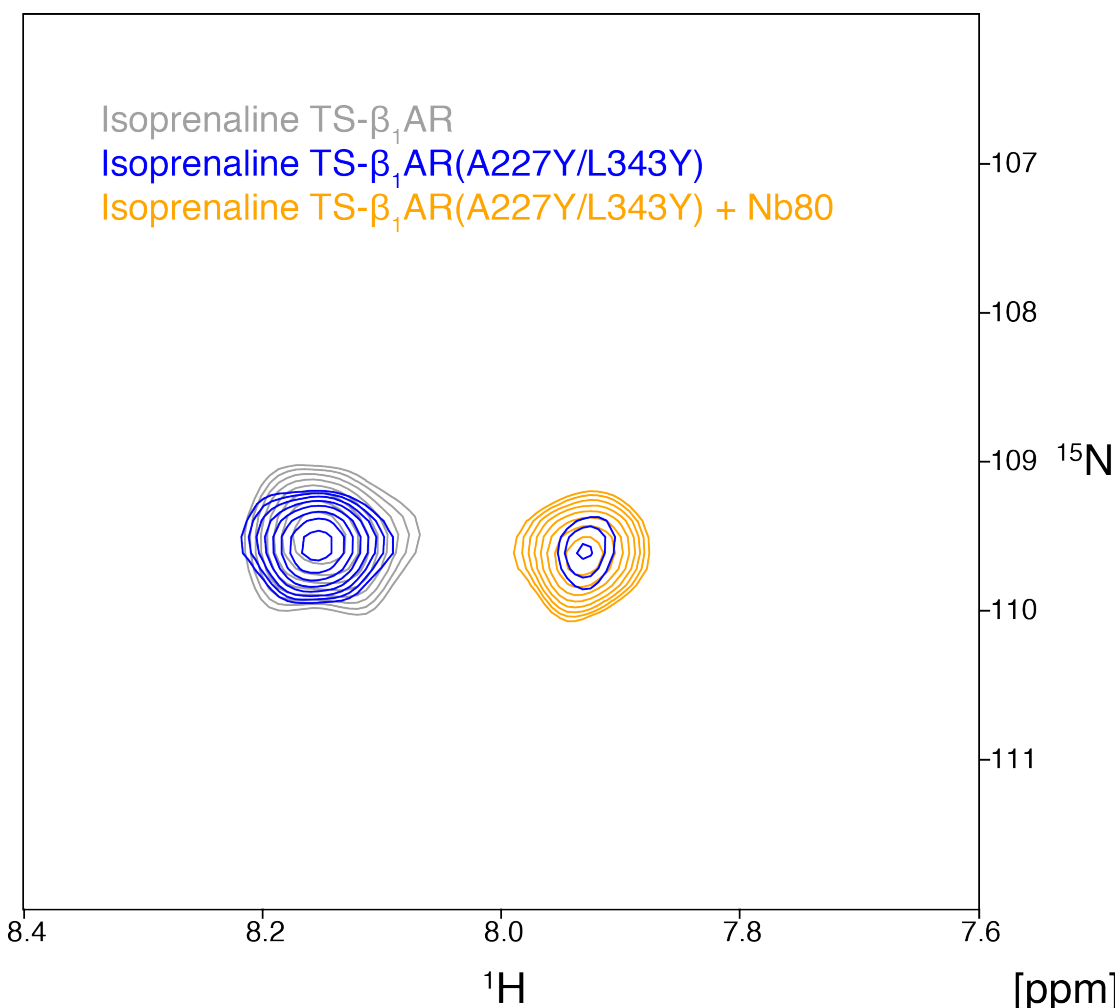


Figure 3.1 Evidence for two-site exchange of V172 in agonist-bound form. Resonance in binary complexes of TS- β_1 AR (grey) or TS- β_1 AR(A227Y/L343Y) (blue) with isoprenaline as well as in ternary TS- β_1 AR(A227Y/L343Y)•Nb80•isoprenaline complex (orange).

In isoprenaline-bound TS- β_1 AR and TS- β_1 AR(A227Y/L343Y) the ^1H - ^{15}N resonances of V172 had the same position (Figure 3.1). Interestingly, an additional weaker ^1H - ^{15}N resonance appeared 0.23 ppm upfield shifted in the ^1H dimension for the TS- β_1 AR(A227Y/L343Y) construct. Its position was identical with V172 in the ternary TS- β_1 AR(A227Y/L343Y)•isoprenaline•Nb80 complex. Hence, two conformations were observed for V172 in TS- β_1 AR(A227Y/L343Y)•isoprenaline, with the downfield shifted resonance representing the inactive state S_1 and the upfield shifted resonance representing the active state S_2 . This observation is striking, because for all local dynamics analyzed so far in Chapter 3.1 only a single peak was detected. In these cases, the conformational exchange was too fast to resolve separate peaks for active and inactive state.

The peak intensities of V172 in the TS- β_1 AR(A227Y/L343Y)•isoprenaline complex ($7.1 \cdot 10^6$ a.u. for S_1 and $2.7 \cdot 10^6$ a.u. for S_2) correspond to relative populations of 73 % inactive and 27 % active state. The two observed peaks for V172 are characteristic for exchange in the slow time regime. Therefore, the exchange rate for V172 in TS- β_1 AR(A227Y/L343Y)•isoprenaline is slower than $1.3 \cdot 10^3 \text{ s}^{-1}$ based on the chemical shift separation of 0.23 ppm at 900 MHz (^1H field strength). This is considerably slower than the exchange rates of $7 \cdot 10^4 \text{ s}^{-1}$ determined from the line shape analysis of V314 in the TS- β_1 AR(A227Y/L343Y)•isoprenaline complex (Chapter 3.1).

In contrast for the TS- β_1 AR•isoprenaline complex, only one V172 resonance corresponding to the inactive state S_1 with an intensity of $9.9 \cdot 10^6$ a.u. was observed. Since the noise level is $1.4 \cdot 10^6$ a.u., the population of the active state S_2 must be smaller than 12.3 %. Thus, the mutations Y227A(5.58) and Y343L(7.53) at the intracellular side of TM5 and TM7 shift the conformational equilibrium of V172 located close to the ligand binding pocket towards the inactive state S_1 .

Interestingly, for TS- β_1 AR(A227Y/L343Y) in complex with the partial agonist dobutamine, also only one V172 resonance was detected corresponding to the inactive state S_1 (intensity $5.3 \cdot 10^6$ a.u., noise $7.8 \cdot 10^5$ a.u., data not shown). Thus, the active S_2 state population must be below 12.8 % and is therefore smaller than for the complex with the full agonist isoprenaline.

Investigation of Nb60 binding to TS- β_1 AR(A227Y/L343Y)

GPCRs are in a dynamic equilibrium and sample several conformations in any particular functional state (107, 113, 116). Ligand binding shifts these functional equilibria as exemplarily shown for residue V226(5.57) in TS- β_1 AR (Figure 1.4b) (114). Stabilization of the fully active state requires simultaneous agonist and intracellular effector site binding from G protein or G protein mimicking nanobody Nb80 (91, 114). Recently, the nanobody 60 (Nb60) has been developed, which stabilizes an inactive conformation of the β_2 AR (200). ^{19}F NMR experiments of β_2 AR bound to the antagonist carazolol showed that the conformational equilibrium shifted from an inactive receptor with mostly closed ionic lock between R131(3.50) and E268(6.30) towards a disengaged ionic lock. Crystal structures revealed a similar binding site for Nb60 in complex with β_2 AR•carazolol as for Nb80 in the β_2 AR agonist complex, which is located between the intracellular ends of TM3, TM4 and TM6 (91, 200).

We tested whether binding of Nb60 to TS- β_1 AR(A227Y/L343Y) in complex with the antagonist carvedilol or the inverse agonist atenolol would change the conformational equilibrium.

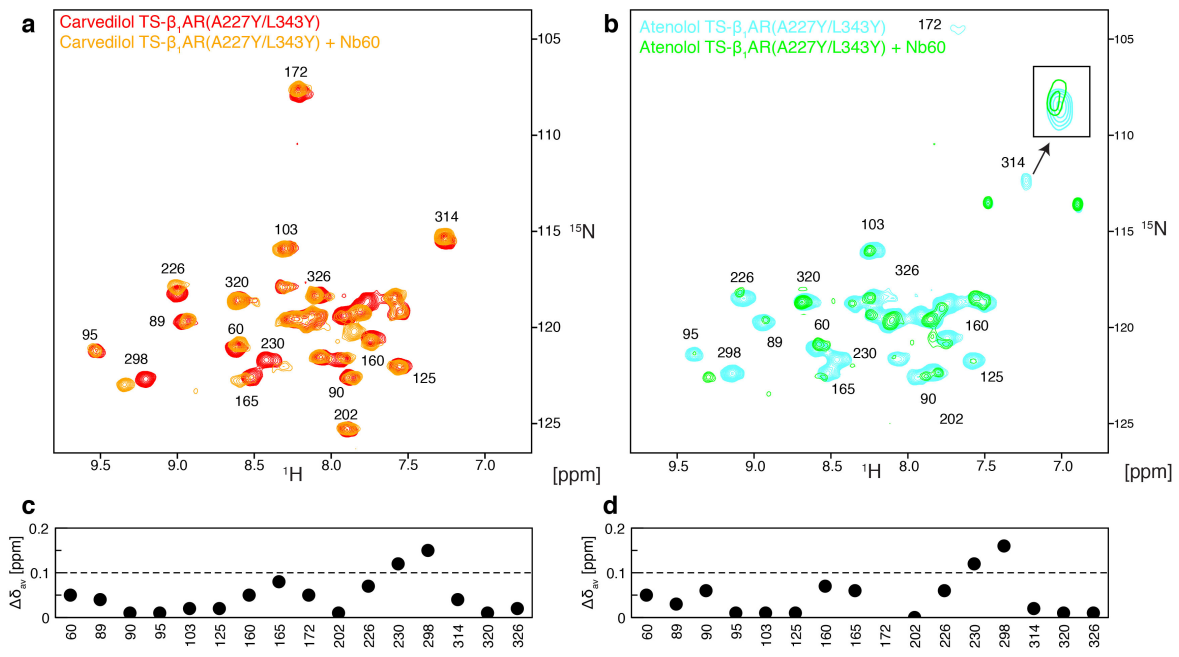


Figure 3.2 Effect of nanobody Nb60 on ^1H - ^{15}N TROSY spectra of ^{15}N -valine-labeled TS- β_1 AR(A227Y/L343Y). (a) Binary TS- β_1 AR(A227Y/L343Y)•carvedilol complex before (red) and after (orange) addition of Nb60. (b) Binary TS- β_1 AR(A227Y/L343Y)•atenolol complex before (cyan) and after (green) addition of Nb60. (c) Weighted chemical shift differences $\Delta\delta_{av} = [\Delta\delta_H^2 + (\Delta\delta_N/5)^2]^{1/2}$ between TS- β_1 AR(A227Y/L343Y)•carvedilol and TS- β_1 AR(A227Y/L343Y)•carvedilol•Nb60. (d) Average chemical shift difference between TS- β_1 AR(A227Y/L343Y)•atenolol and TS- β_1 AR(A227Y/L343Y)•atenolol•Nb60.

Only minor spectral changes were observed upon addition of Nb60 to the binary complexes of TS- β_1 AR(A227Y/L343Y) with the antagonist carvedilol (Figure 3.2a) or the inverse agonist atenolol (Figure 3.2b), respectively. The chemical shift changes upon Nb60 addition are very similar for the carvedilol and atenolol complexes (Figure 3.2c, d). For residue V226(5.57), whose chemical shift correlates linearly with G protein efficacy (114), no significant change in state is observed. In contrast V230(5.61) and V298(6.43) at the intracellular side of the receptor shows significant chemical shift changes. However, it cannot be distinguished whether Nb60 induces a significantly different conformation of the receptor or whether the chemical shift changes originate from very limited local structure changes due to the nearby Nb60. No significant changes for V172, V202 or V314 at the extracellular side were observed upon binding of Nb60. Interestingly, thermostabilizing mutations in TS- β_1 AR shifted V314 slightly towards the inactive conformation compared to TS- β_1 AR(A227Y/L343Y) (Chapter 3.1). Thus, binding of Nb60 to TS- β_1 AR(A227Y/L343Y) does not seem to stabilize the inactive state of V314 in the same way as the thermostabilizing point mutations. Furthermore, the two-site exchange of V314 is modulated by ligand affinity. It has been shown for β_2 AR that Nb60 has a negative allosteric effect on the affinity of agonists and a negligible effect on antagonists (200). Therefore, it would be interesting to study V314 in the agonist TS- β_1 AR(A227Y/L343Y)•isoprenaline complex upon addition of Nb60. Due to time restrictions and the presumed low-affinity of isoprenaline for the unstable TS- β_1 AR(A227Y/L343Y) sample, these experiments have not been carried out yet.

Variation in $^1\text{H}^{\text{N}}$ T_2 for different ligand states

Routinely, 1D proton spectra were recorded to assess quality and stability of the samples during the NMR analysis of TS- β_1 AR and TS- β_1 AR(A227Y/L343Y) in various ligand-bound states. A field dependence and variation between ligands was observed for the amide proton T_2 times as determined by the jump-return spin-echo sequence (Figure 3.3) (201). The differences are close to the error estimates of the measurements and need to be carefully interpreted.

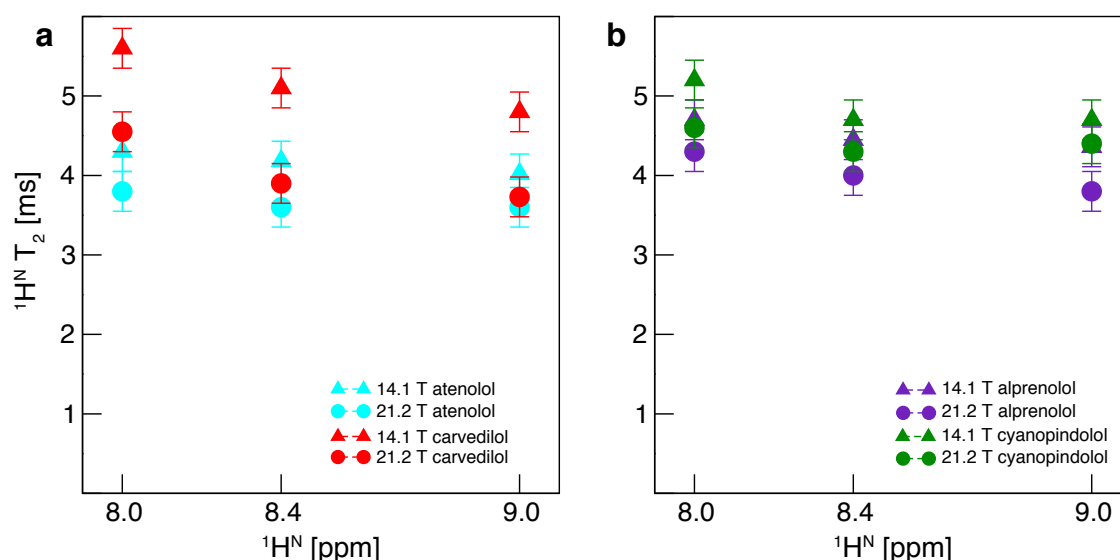


Figure 3.3 $^1\text{H}^{\text{N}}$ T_2 times of (a) TS- β_1 AR(A227Y/L343Y) and (b) TS- β_1 AR in various ligand-bound forms at 14.1 and 21.2 T determined from jump-return spin-echo experiment recorded with relaxation delays of 0.2 ms and 4.2 ms. The signal decay was analyzed at 8.0, 8.4 and 9.0 ppm and errors of 0.25 ms were estimated.

Interestingly, $^1\text{H}^{\text{N}}$ T_2 times for the complex of TS- β_1 AR(A227Y/L343Y) with the low-affinity ligand atenolol (pK_{D} 4.3) were decreased by almost 1 ms relative to the high-affinity ligand carvedilol (pK_{D} 8.7) (Figure 3.3a) at 14.1 T. This trend was also observed at 21.2 T, but less pronounced. The amide T_2 times decreased overall at the higher field. A similar effect was observed for TS- β_1 AR (Figure 3.3b) where the $^1\text{H}^{\text{N}}$ T_2 time was reduced by about 0.5 ms in the alprenolol (pK_{D} 7.3) relative to the cyanopindolol (pK_{D} 10.0) complex. We can only speculate on the reasons for these trends. Possibly high-affinity ligands stabilize a slightly more compact structure than low-affinity ligands, thereby reducing dynamics and solvent exchange.

Residue-specific dynamics

To further investigate these effects, $^1\text{H}^{\text{N}}$ R_2 rates were determined from line shape fitting of ^1H - ^{15}N TROSY spectra as described for the ^{15}N dimension in Chapter 3.1 (Figure 3.4). The proton rates especially for the TS- β_1 AR(A227Y/L343Y) construct were associated with considerable errors due to the low signal-to-noise ratio caused by the low stability of the samples.

Nevertheless, V172 (atenolol), V103 (apo), V226 (apo) and V320 (apo) in TS- β_1 AR(A227Y/L343Y) showed significantly increased $^1\text{H}^{\text{N}}$ R_2 rates compared to others. The variation was not observed in the TS- β_1 AR construct indicating that this construct is more rigid.

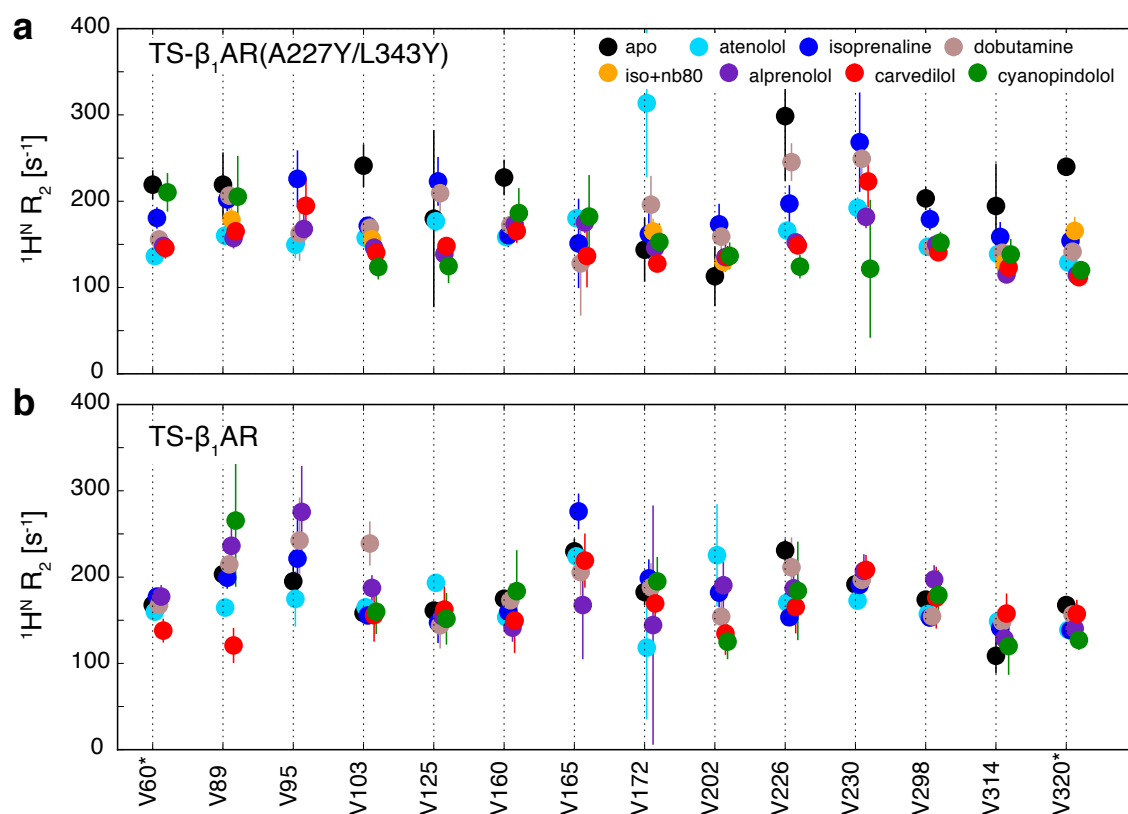


Figure 3.4 Residue-specific ^1H R_2 rates of ^{15}N -valine TS- β_1 AR(A227Y/L343Y) and TS- β_1 AR in various states. ^1H R_2 rates are derived from line shape fitting of ^1H - ^{15}N TROSY spectra of (a) TS- β_1 AR(A227Y/L343Y) in apo form, orthosteric binary and ternary isoprenaline•Nb80 complexes at 21.2 T and (b) TS- β_1 AR in apo form and orthosteric binary complexes at 18.8 T. Data for the various forms are color coded. Assignments marked by asterisks (V60, V320) are tentative.

In addition, also peak intensities were determined for various TS- β_1 AR and TS- β_1 AR(A227Y/L343Y) states (Figure 3.5). The peak intensities were normalized relative to the tentatively assigned resonance of V320, located in extracellular loop 3. The latter resonance is the most intense resonance in the spectrum due to high nanosecond mobility as evidenced by increased ^{15}N R_1 rates (Chapter 3.1).

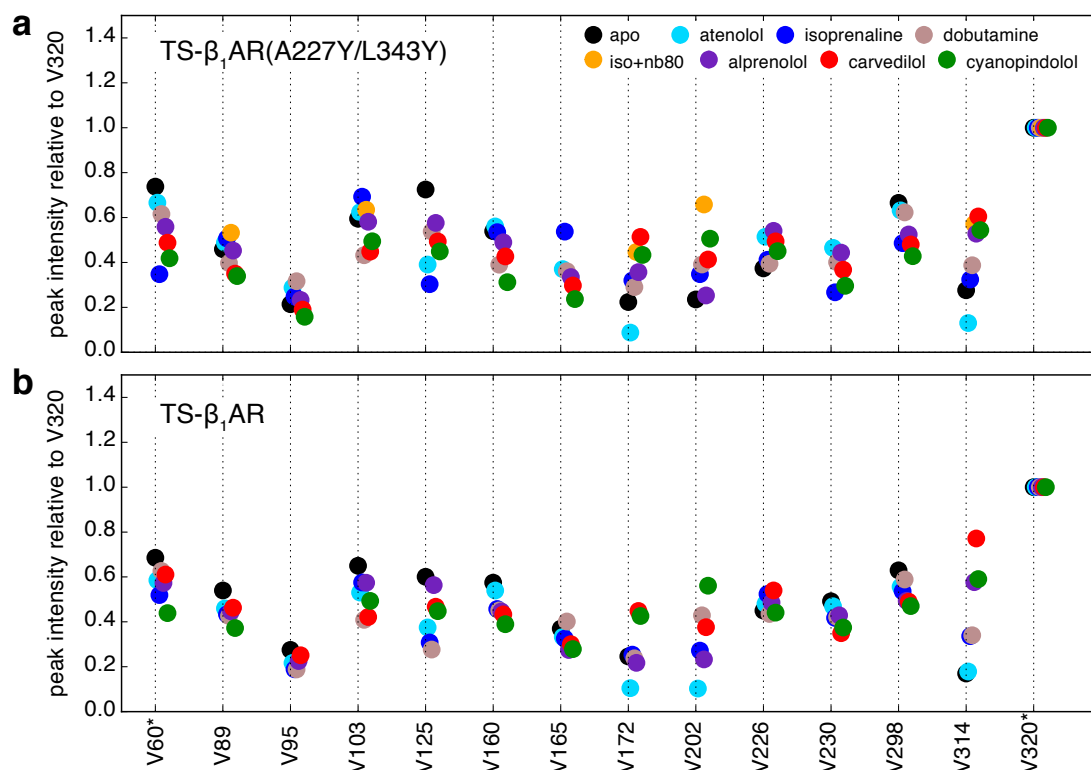


Figure 3.5 Relative peak intensities of individual ^{15}N -valine resonances of TS- β_1 AR(A227Y/L343Y) and TS- β_1 AR in various states relative to V320. **(a)** TS- β_1 AR(A227Y/L343Y) in apo form, orthosteric binary and ternary isoprenaline•Nb80 complexes at 21.2 T and **(b)** TS- β_1 AR in apo form and orthosteric binary complexes at 18.8 T. Data for the various forms are color coded. Assignments marked by asterisks (V60, V320) are tentative.

The largest variations in peak intensity between different receptor forms were observed for V172, V202 and V314, which corresponds to their variations in ^{15}N R_2 rates (Chapter 3.1). Relative peak intensities are strongly reduced for V172, V202 and V314 in the atenolol-bound receptor, indicating the flexibility of the extracellular side in the low-affinity ligand state. The relative peak intensities increased for V202 and V314 in the ternary TS- β_1 AR(A227Y/L343Y)•isoprenaline•Nb80 complex compared to the binary TS- β_1 AR(A227Y/L343Y)•isoprenaline complex, revealing the stabilization of the extracellular region by allosteric coupling from Nb80.

The peak intensity was very low for V95(2.58). This resonance also showed increased ^{15}N and ^1H R_2 rates. V95 is located in the middle of TM2, facing towards the exterior, and might experience increased solvent exchange. Overall, the variation in peak intensities for valine resonances seems to be reduced in TS- β_1 AR compared to the TS- β_1 AR(A227Y/L343Y) construct corroborating the higher flexibility of the TS- β_1 AR(A227Y/L343Y) construct.

Conclusions and perspectives

The turkey β_1 AR solubilized in DM micelles was established as a model to study backbone dynamics of GPCRs by solution NMR. It is hoped that the methods for analysis can be used for more challenging receptor systems (see Chapter 4 and 7). Besides the global and site-

specific ^{15}N relaxation rates describing the dynamics in Chapter 3.1, further details on the intrinsic flexibility of $\beta_1\text{AR}$ derived from additional experiments were presented here.

V172 below the ligand binding pocket revealed a two-site exchange in the binary agonist-bound TS- $\beta_1\text{AR}$ (A227Y/L343Y)•isoprenaline complex, in which conformation S_1 corresponds to the inactive receptor state and S_2 to the active form as observed in the ternary complex with Nb80. The exchange rate is slower than $1.3 \cdot 10^3 \text{ s}^{-1}$ and the states S_1 and S_2 are populated by 77 % and 23 %, respectively. In contrast, the exchange for V314 occurs with a rate of $7.0 \cdot 10^4 \text{ s}^{-1}$, and the populations are 66 % and 34 %, respectively. Apparently, the relative populations of inactive and active states are similar for the resonances V172 and V314, but the exchange rates differ by a factor of 60. Thus, the receptor motions at the extracellular end of TM6 and in TM4 below the ligand head group clearly occur on different time scales. A similar behavior has been postulated based on MD simulations describing the inactivation process of $\beta_2\text{AR}$ (108). In the latter, transitions in the microsecond range occurred asynchronously in different parts of the receptor. This led the author to propose that different regions of the receptor are connected only as a loosely coupled network.

The binding of Nb60 to TS- $\beta_1\text{AR}$ (A227Y/L343Y) in complex with carvedilol or atenolol did not lead to major spectral changes. From the data available so far, it is not clear whether Nb60 shifts the conformational equilibrium towards a different inactive state of $\beta_1\text{AR}$ as shown for $\beta_2\text{AR}$ (200). Future experiments with a ternary complex of Nb60 with the agonist isoprenaline would be of high interest, because Nb60 is described as a negative allosteric regulator in contrast to the positive allosteric regulator Nb80 (200).

Differences in the amide proton T_2 times of TS- $\beta_1\text{AR}$ and TS- $\beta_1\text{AR}$ (A227Y/L343Y) for various ligand states indicate that exchange dynamics are also observable in the ^1H dimension, but the relaxation properties of protons are more difficult to interpret due to the solvent influence.

All relaxation experiments on $\beta_1\text{AR}$ have been conducted in decyl maltoside (DM) micelles. It could be that the spectral appearance changes in a different detergent such as lauryl maltose neopentyl glycol (LMNG), especially for residues facing the exterior. Studies of $\beta_2\text{AR}$ have shown that the choice of detergent influences the observable exchange regime for side-chain reporter sites on the intracellular end of TM6 (202). Additionally, dynamics may be different in a lipid environment as compared to detergents. The exchange rates between active and inactive states are slower in lipid-filled nanodiscs than in dodecyl maltoside (DDM) micelles, and the relative active state population is increased as shown for a ^{13}C -methyl group of methionine below the orthosteric ligand binding pocket in $\beta_2\text{AR}$ (117). Quantifying ^{15}N backbone dynamics in a lipid environment will be the next experimental challenge for the understanding of GPCRs. Another layer in the complex regulation of GPCRs could be added by varying the lipid composition. In particular charged lipid headgroups have been shown to be allosteric regulators of the human $\beta_2\text{AR}$ (203).

Materials and Methods

Expression and Purification of Nb60

The plasmid for Nb60 was a generous gift from Prof. Jan Steyaert, Vrije Universiteit Brussel, Belgium, and the Nb60 protein was purified according to the described procedures (200).

TS- β_1 AR and TS- β_1 AR(A227Y/L343Y) expression and purification

Detailed protocols are presented in Chapter 3.1.

NMR experiments and data analysis

NMR samples were prepared and ^1H - ^{15}N TROSY spectra were recorded as described in Chapter 3.1. Nb60 was added in equimolar (relative to the receptor) amounts to binary TS- β_1 AR(A227Y/L343Y)•atenolol or TS- β_1 AR(A227Y/L343Y)•carvedilol complex samples.

Amide proton T_2 times were determined from a jump-return spin-echo experiment (201). All NMR spectra were processed with NMRPipe (204) and evaluated with SPARKY (205) or NMRPipe (204).

^1H R_2 rates were determined by time-domain line shape fitting of ^1H - ^{15}N TROSY using the nlinLS program contained in NMRPipe (204). The procedure is explained in more detail in Chapter 3.1.

3.3 Improved relaxation behavior of a deuterated β_1 -adrenergic receptor

Introduction

In the previous chapters amino acid-specific labeled β_1 AR was used to analyze the receptor by backbone NMR due to the reduced spectral complexity for such a large protein. So far, 14 valines were used, which may give only partial insight into the complex behavior of a protein with over 300 residues. The amino acid-specific labeling also required initial resonance assignment by tedious point mutations (114), because the backbone connectivity necessary for conventional triple-resonance assignment is lost. Additionally, the transverse relaxation of the protonated receptor with an apparent molecular weight of 100 kDa is very fast. As a consequence, even TROSY versions of triple-resonance assignment experiments like HNCO, HNCA, HNCOCA are of limited use for assignment due to the low transfer efficiency and sensitivity. Deuteration diminishes the relaxation losses during such experiments by reducing the effect of dipolar relaxation from nearby protons. Progress in isotope labeling and especially deuteration of proteins expressed in insect cells has made it possible to obtain uniformly ^2H , ^{15}N -labeled β_1 AR (112) (Chapter 3.1). Here, the improved relaxation properties of this deuterated β_1 AR sample are presented.

Results

^1H - ^{15}N TROSY spectra of TS- β_1 AR at two magnetic field strengths

TS- β_1 AR was uniformly isotope labeled by growing insect cells on ^2H , ^{15}N yeastolate and protonated $^{15}\text{N}_2$ -glutamine. ^1H - ^{15}N TROSY spectra of a 160 μM alprenolol-bound, partially deuterated ^2H (55 %)/ ^{15}N (78 %) TS- β_1 AR sample were recorded at 14.1 T and 21.2 T (Figure 3.6). Well-resolved spectra were observed at both field strengths, although the spectral dispersions is obviously lower at 14 T. Between 230 and 260 out of the expected 304 backbone resonances for TS- β_1 AR were observed. The receptor was expressed using protonated $^{15}\text{N}_2$ -glutamine. Therefore, glutamine and the amino acids alanine, asparagine, aspartate, glutamate and glycine, which metabolically interconvert with it, were partially protonated and not detected due to lower sensitivity. In the future, the spectral quality can be further improved by using deuterated glutamine.

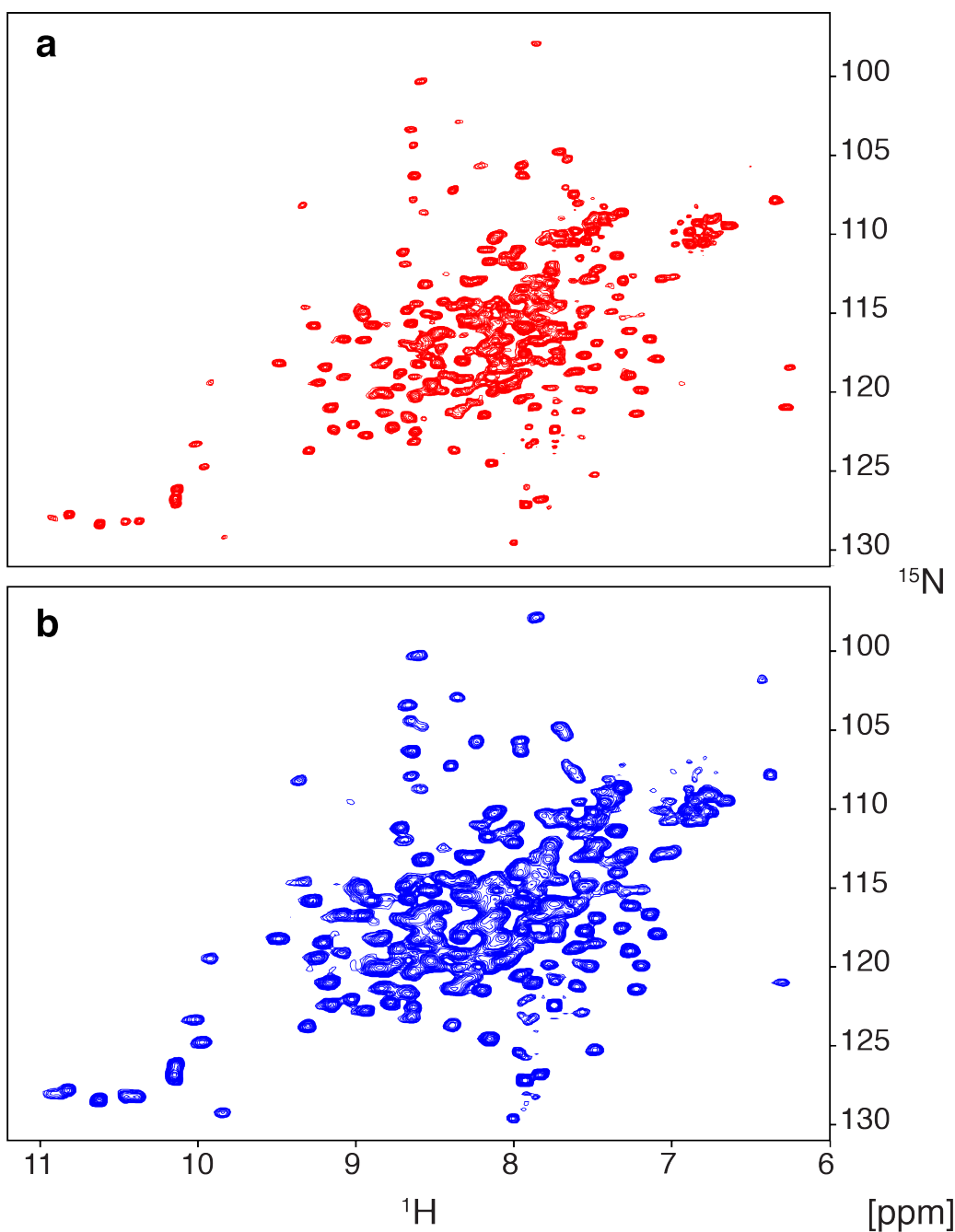


Figure 3.6 ^1H - ^{15}N TROSY spectrum of $160\ \mu\text{M}$ ^2H (55 %)/ ^{15}N (78 %), alprenolol-bound TS- $\beta_1\text{AR}$ in DM micelles recorded at 304 K for 3 hours at (a) 21.2 T and (b) 14.1 T.

The ^1H - ^{15}N TROSY spectra of alprenolol-bound ^2H (55 %)/ ^{15}N (78 %) TS- $\beta_1\text{AR}$ recorded at 14.1 T and 21.2 T are very similar in appearance. Yet the signal intensity was somewhat lower (average 0.88) at 21.2 T than at 14.1 T (Figure 3.7), indicating that for some resonances, fast to intermediate exchange occurs. The average ^{15}N R_2 rates, used to describe the global backbone dynamics of $\beta_1\text{AR}$ measured on ^2H (55 %)/ ^{15}N (78 %) TS- $\beta_1\text{AR}$ (Chapter 3.1), also indicated a slightly higher exchange contribution at 21.2 T than at 14.1 T.

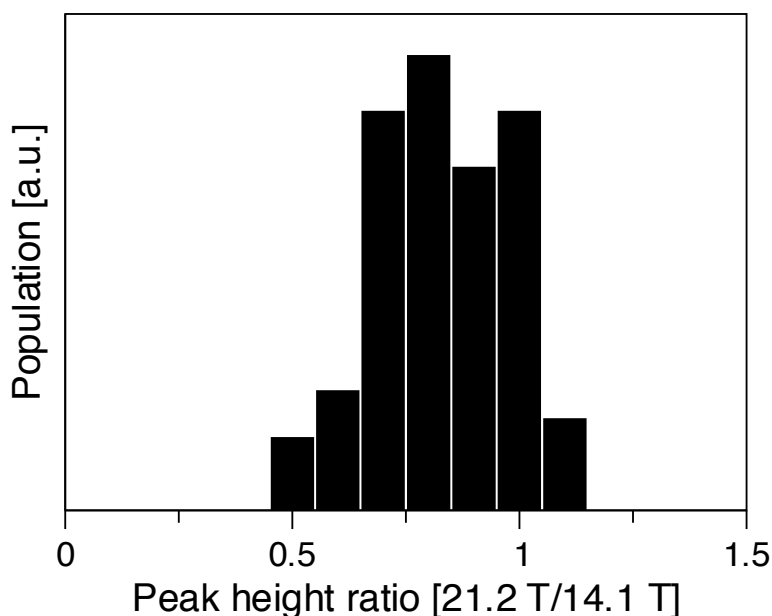


Figure 0.1 Comparison of signal amplitudes in ^1H - ^{15}N TROSY spectra of ^2H (55 %)/ ^{15}N (78 %), alprenolol-bound TS- $\beta_1\text{AR}$ in DM micelles recorded at 14.1 T and 21.2 T. Histogram of relative peak heights from ^1H - ^{15}N TROSY spectra at 14.1 T and 21.2 T. Only well-resolved peaks were used for the analysis. The average peak height ratio is 0.88.

T₂ times for protonated and deuterated TS- $\beta_1\text{AR}$

Even partial deuteration improved already the transverse relaxation properties of the receptor-detergent complex (Table 3.1) Measurement of amide proton T_2 times showed an increase from 4.3 (3.7) ms at 14.1 (21.2) T for a protonated receptor to 6.8 (5.7) ms at 14.1 (21.2) T for the (55 %)/ ^{15}N (78 %) TS- $\beta_1\text{AR}$ sample. Likewise, ^{15}N TROSY ($^{15}\text{N}_x^1\text{H}_\beta$) T_2 times increased by one third from 23.1 (21.0) ms at 14.1 (21.2) T for the protonated receptor to 30.3 (28.5) ms at 14.1 (21.2) T for the partially deuterated TS- $\beta_1\text{AR}$. The ^1H - ^{15}N TROSY spectra for the partially deuterated TS- $\beta_1\text{AR}$ were recorded within 3 hours, which reduced the measurement time by a factor of ~ 3.5 as compared to protonated NMR samples, due to the resulting higher sensitivity.

Table 3.1 Effect of partial deuteration on the transverse relaxation times of alprenolol-bound TS- $\beta_1\text{AR}$ at 14.1 T and 21 T. $^1\text{H}^{\text{N}}$ and $^{15}\text{N}_x^1\text{H}_\beta$ T_2 times were determined for ^{13}C , ^{15}N -glycine, ^{13}C , ^{15}N -valine, ^{15}N -leucine-labeled or ^2H (55 %)/ ^{15}N (78 %)-labeled receptor. $^1\text{H}^{\text{N}}$ T_2 were determined from the signal decay above 8.4 ppm. $^{15}\text{N}_x^1\text{H}_\beta$ T_2 times were determined from the average signal decay of 1D ^1H -detected ^{15}N experiments.

Isotope labeling	Field [T]	$^1\text{H}^{\text{N}}$ T_2 [ms]	$^{15}\text{N}_x^1\text{H}_\beta$ T_2 [ms]
^{13}C , ^{15}N -Gly, ^{13}C , ^{15}N -Val, ^{15}N -Leu	14.1	4.3	23.1
^{13}C , ^{15}N -Gly, ^{13}C , ^{15}N -Val, ^{15}N -Leu	21.2	3.7	21.0
^2H (55 %)/ ^{15}N (78 %)	14.1	6.8	30.3
^2H (55 %)/ ^{15}N (78 %)	21.2	5.7	28.5

Conclusions and perspectives

The partially deuterated ^2H (55 %)/ ^{15}N (78 %)-labeled TS- $\beta_1\text{AR}$ yielded high-quality NMR spectra at two field strengths. The spectral quality may be further improved by increasing isotope incorporation. The incorporation levels of ^2H (55 %)/ ^{15}N (78 %) are lower than the previously reported ≥ 60 % for ^2H and 90 % for ^{15}N (112). This lower labeling was the result of a variation in the isotope labeling of the used yeastolate. It can obviously be increased by an improved yeastolate preparation as well as by the use of deuterated glutamine.

Nevertheless, already the partial deuteration has very favorable effects on amide proton and ^{15}N TROSY T_2 relaxation times as compared to the protonated receptor. It indicates that conventional triple-resonance experiments may become feasible for resonance assignment instead of the point-mutation strategy used so far. Deuteration has a high impact on sensitivity, resolution and magnetization transfer efficiency for those heteronuclear experiments.

At the moment, TS- $\beta_1\text{AR}$ was studied in DM micelles with an apparent molecular weight of 100 kDa, which is at the upper limit for backbone NMR studies of a fully protonated system. A next step towards the understanding of $\beta_1\text{AR}$ dynamics would be the reconstitution in a membrane mimetic such as nanodiscs, which are more similar to the natural lipid environment, but have molecular weights in the 150 to 200 kDa range (206). Very likely for such experiments, deuteration will be required to reduce the fast transverse relaxation caused by the slow tumbling of the high-molecular-weight complex.

Materials and Methods

Isotope labeling and purification of TS- $\beta_1\text{AR}$

Preparation of ^2H , ^{15}N yeastolate and expression of uniformly labeled TS- $\beta_1\text{AR}$ in insect cells by supplementation of ^2H , ^{15}N -yeastolate and $^{15}\text{N}_2$ -glutamine was carried out by Christian Opitz as previously described (112). ^{13}C , ^{15}N -glycine-, ^{13}C , ^{15}N -valine- and ^{15}N -leucine-labeled TS- $\beta_1\text{AR}$ was expressed by Shin Isogai (114).

TS- $\beta_1\text{AR}$ solubilized in DM was purified by Shin Isogai as described previously (114). The NMR samples were prepared in a Shigemi tube with concentrations of 160 μM (^2H , ^{15}N -labeled) or 400 μM (^{13}C , ^{15}N -Gly, ^{13}C , ^{15}N -Val, ^{15}N -Leu-labeled) in a volume of 250 μl in 20 mM TRIS (pH 7.5), 1 mM of alprenolol, 100 mM NaCl, 0.1 % DM, 0.02 % NaN_3 and 5 % D_2O .

NMR experiments and data analysis

All NMR experiments were performed on Bruker AVANCE 14.1 T (600 MHz ^1H frequency) or 21.2 T (900 MHz) spectrometers equipped with a TCI cryoprobe at a temperature of 304 K. Amide proton T_2 times were determined from a jump-return spin-echo experiment (201). ^{15}N TROSY spin-echo T_2 times were determined from 1D ^1H -detected experiments with relaxation delays of 0.2 ms, 30.2 ms (^2H , ^{15}N) or 0.2 ms, 18.2 ms (^{15}N) with ^1H - ^{15}N transfer times of 3.6 ms (^2H , ^{15}N) or 3 ms (^{15}N). ^1H - ^{15}N TROSY experiments were recorded as 140 (^{15}N) x 1024 (^1H) complex points and acquisition times of 28 ms (^{15}N) and 42 ms (^1H). For optimal sensitivity, the ^1H - ^{15}N transfer time was reduced to 3.6 ms and the interscan delay set to 1 s.

All NMR spectra were processed with NMRPipe (204) and evaluated with SPARKY (205) or NMRPipe (204).

4 Insect cell expression and characterization of CCR5

Organization of the chapter

After a short introduction to the chemokine receptor CCR5, the first section (4.1) describes its expression in insect cells, its detergent optimization for solution NMR studies, protocols for amino acid-specific and uniform ^2H , ^{15}N isotope labeling, the initial characterization by ^1H - ^{15}N TROSY and relaxation experiments, as well as initial cryo-EM studies. The second section (4.2) is a reprint of the original publication by Franke, Opitz, Isogai, Grahl *et al.* (19) containing some of the NMR data on CCR5 of the first section.

Introduction

CCR5 is a member of the class A GPCRs, which all share the seven α -helical transmembrane architecture. As a chemokine receptor, it is involved in inflammation and immune response, and it is the major coreceptor for HIV-1 entry. CCR5 requires posttranslational modifications such as tyrosine sulfation and O-glycosylation of the N-terminus for high-affinity ligand binding (161, 162). In addition, two extracellular disulfide bonds stabilize the receptor and increase its ligand affinity (160). Such posttranslational modifications are obtainable in higher eukaryotes such as insect cells, a well-established expression system for functional GPCRs (84). However, heteronuclear NMR requires isotope-labeled proteins. As insect cells have only a limited capacity to synthesize amino acids, the labeling must be achieved by supplementing isotope-labeled amino acids to the medium. Therefore, insect cells are not as commonly used for NMR applications as *E. coli*, where labeling can be achieved in inexpensive minimal medium (19, 207). In the last years, affordable isotope-labeling strategies have been developed for insect cells based on depleting amino acids and other proteinaceous material from the medium and supplementing isotope-labeled amino acids (19). For amino acid-specific labeling, an isotope-labeled amino acid can be added to a minimal medium depleted of that specific one, resulting in labeling incorporation above 90 % (208). For uniform labeling of proteins, inexpensive isotope-labeled algae extract or yeast extract can be supplemented to the medium (112, 209).

Prior studies have shown that isotope-labeled wild-type CCR5 can be expressed in insect cells, but the NMR spectra of the detergent-reconstituted receptor had very broad lines (210). The low stability of the wild-type receptor outside of its natural environment precluded extensive structural studies (211). Engineering of CCR5 has led to increased sample homogeneity and stability in detergent micelles (153). This approach culminated in the crystal structures of CCR5 in complex with the small molecule maraviroc (inverse agonist) and the chemokine analog 5P7-RANTES (antagonist) (153, 191).

Albeit tremendous structural insight has been obtained for CCR5, its underlying dynamics, which allow binding of ligands ranging from small molecules to proteins and triggering distinct intracellular responses, are not understood. These features can be studied by NMR and make CCR5 an interesting and challenging target. In the following section, protein engineering and improved isotope-labeling strategies in insects were combined to make CCR5 accessible to backbone NMR studies.

4.1 Characterization of CCR5 expressed in insect cells

Results

Construct design

The design of a CCR5 construct for NMR studies was based on the engineered CCR5 used in crystallographic studies (153). The stabilized CCR5 construct carries four point mutations C58Y(1.60), G163N(4.60), A233D(6.33) and K303E(8.49) as well as N- and C-terminal modifications (Figure 4.1). The A233D mutation was reported to keep CCR5 in an inactive state, abolish G protein signaling and decrease the affinity for its endogenous ligand MIP1- α (153). C58Y, G163N and K303E mutations increased the stability in detergent micelles and receptor homogeneity. The four mutations together increase the melting temperature from 59 to 66 °C. The C-terminus is truncated after the soluble helix 8, removing 32 amino acids (Δ 320-352). FLAG and His_{10x} tags are incorporated at the C-terminus, allowing the detection of CCR5 by Western blot and the purification by immobilized ion affinity chromatography (IMAC). The affinity tags can be removed using PreScission protease. A hemagglutinin signal sequence for targeting membrane insertion during insect-cell expression is inserted N-terminally prior to CCR5's natural sequence (212). For crystallization, a rubredoxin fusion protein was placed in the intracellular loop 3 (ICL3) to reduce flexibility and increase crystal contacts. This construct will be called CCR5-rub in the following chapters. For NMR studies, the ICL3 was left intact, and the construct will be referred to as CCR5-4m.

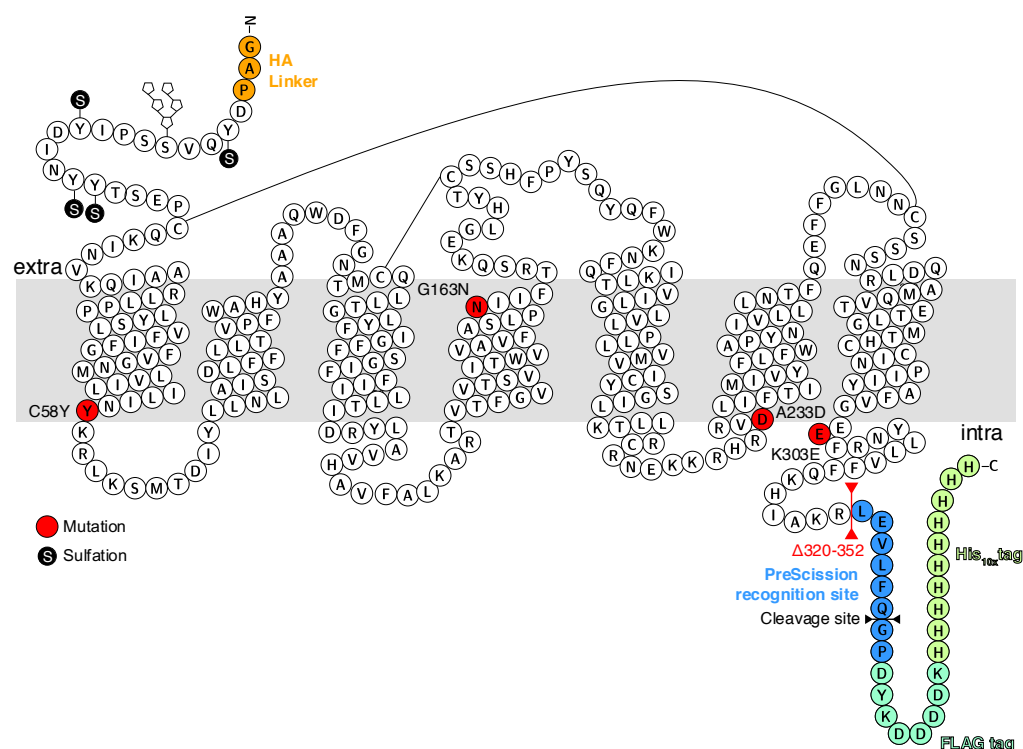


Figure 4.1 Sequence and topology of engineered CCR5-4m. Residues are colored as follows: mutations in red, linker from HA hemagglutinin signal sequence in orange, PreScission recognition site in blue, FLAG tag in green and His_{10x} tag in bright green. Two distinct disulfide bonds in the extracellular space are shown as solid lines. Posttranslational modifications by tyrosine sulfation or O-glycosylation of serine are indicated. The red line indicates truncation of the C-terminus after residue 319.

Small-scale expression of CCR5 in insect cells

CCR5-4m was expressed in Sf9 insect cells in small cultures to determine the optimal virus titer to cell ratio. Western blot analysis using a poly-His antibody was performed of samples taken at 24, 48 and 72 hours post infection (hpi) (Figure 4.2a). A strong band above 25 kDa corresponding to CCR5-4m was increasing over time, with the highest yield at 48 to 72 hpi using a virus titer of 10 mL/L. Due to ‘gel shifting’, which is often observed for membrane proteins interacting with sodium dodecyl sulfate during SDS PAGE (213), CCR5-4m appeared around 25 kDa and not at its expected molecular weight of 40 kDa. The weaker band above 50 kDa corresponds to a CCR5-4m dimer.

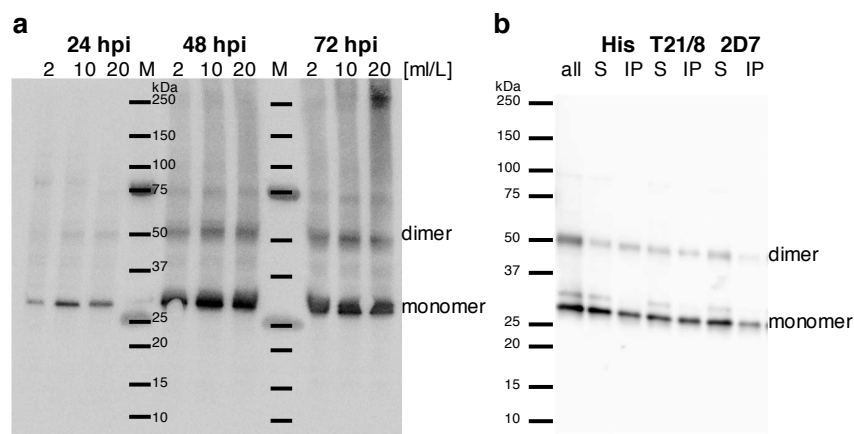


Figure 4.2 (a) Western blot analysis of Sf9 small-scale cultures to determine functional virus titer. CCR5-4m was detected using a poly-His antibody. Cells were infected with virus stocks corresponding to 2, 10 and 20 mL per 1 L of cell culture. Samples were taken at 24, 48, 72 hpi. **(b)** Immunoprecipitation with antibodies recognizing CCR5-4m. Lane 2 (all) contains solubilized CCR5-4m in DDM/CHS micelles. Supernatant (S) and immunoprecipitate (IP) fractions are shown for the C-terminal-specific poly-His antibody (His), the N-terminal-sequence-specific CCR5 antibody T21/8 (T21/8) and the conformation-specific CCR5 antibody 2D7 (2D7).

The structural integrity of CCR5-4m expressed in insect cells was tested after solubilization by immunoprecipitation with antibodies recognizing different regions of the receptor (Figure 4.2b). Both T21/8, an antibody recognizing an N-terminal sequence of CCR5, and a poly-His antibody, recognizing the C-terminal His tag, pulled CCR5-4m in the experiment, proving that neither N-terminal nor C-terminal truncation occurred. CCR5-4m was also immunoprecipitated by the 2D7 antibody, which recognizes a conformation-dependent epitope in the extracellular loop 2 and proves the conformational integrity of the receptor (214, 215).

Large-scale expression and purification

CCR5-4m was expressed in large-scale insect-cell cultures, and the membrane preparation and purification were adapted from Tan *et al.* (153). Membranes containing CCR5-4m were isolated from the cell material by several rounds of homogenization and ultracentrifugation. Membrane solubilization in presence or absence of maraviroc was achieved in two detergent conditions. Mixed dodecyl maltoside (DDM)/cholesteryl hemisuccinate (CHS) micelles were used as in the crystallographic studies (153), benefitting from the micelles' high stability due to the incorporation of the cholesterol homolog and the induced bicelle-like shapes (216). Pure DDM micelles were also tested due to their lower molecular weight being more favorable for

NMR studies. Purification of detergent-solubilized CCR5-4m was achieved by IMAC, yielding a 95 % pure protein as judged from samples on Coomassie-stained SDS-PAGE (Figure 4.3a). Additional to the monomeric state, a weaker dimer band was detected (Figure 4.3a, lanes 9 and 22). A size-exclusion chromatography (SEC) step was introduced to further increase the sample homogeneity (Figure 4.3b). CCR5-4m in DDM/CHS micelles showed a high level of aggregates and a monomeric peak corresponding to ~194 kDa, which was not fully resolved. CCR5-4m in DDM micelles contained less aggregates, and the monomeric peak eluted at a volume corresponding to ~104 kDa. The procedure yielded ~0.3 mg maraviroc-bound CCR5 in DDM micelles per liter of insect-cell culture. The structural integrity after purification was validated by immunoprecipitation with the 2D7 antibody (Figure 4.3c).

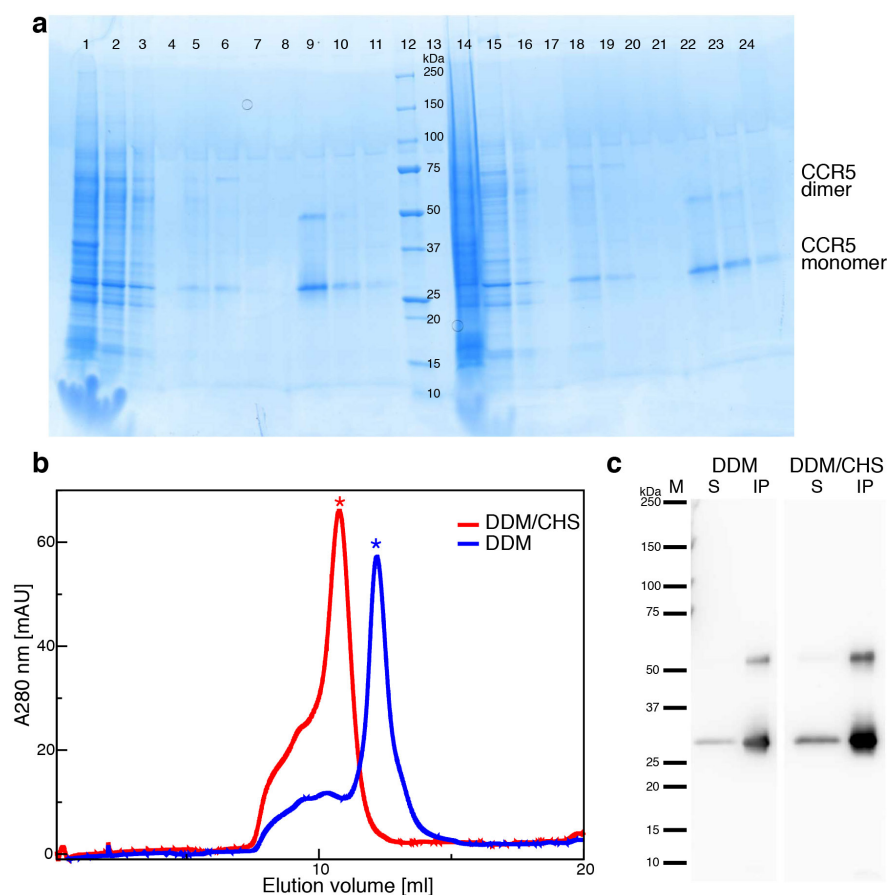


Figure 4.3 Purification and quality control of CCR5-4m in DDM and DDM/CHS micelles. **(a)** Coomassie-stained SDS-PAGE of CCR5-4m solubilized in DDM/CHS (1-11) and DDM (14-24) at various steps of the purification. Initial solubilized material (1 and 14), supernatant of solubilization (2 and 15), flow-through (3 and 16), wash fractions 1-3 (5-7 and 18-20) and elution fractions 1-3 (9-11 and 22-24). Molecular-weight marker in lane 14 and empty lanes 4, 8, 13, 17 and 21. **(b)** Size-exclusion analysis of CCR5-4m in DDM/CHS (red) and DDM (blue) micelles. Both samples contain oligomeric species and a monomeric fraction indicated by an asterisk. **(c)** Immunoprecipitation with conformation-specific CCR5 antibody 2D7. Supernatant (S) and immunoprecipitate (IP) fractions for CCR5-4m purified in DDM and DDM/CHS.

Thermostability of CCR5-4m

The stability of CCR5-4m in various detergents was characterized by the CPM microscale fluorescence stability assay (Figure 4.4). The assay probes temperature-induced unfolding of

GPCRs in detergent micelles by detecting the exposure of free cysteines (217). The thiol-specific fluorochrome N-[4-(7-diethylamino-4-methyl-3-coumarinyl)phenyl]maleimide (CPM) reacts with cysteines forming a fluorescent thiol adduct whereas the free dye has almost no fluorescence signal (218).

Melting temperatures of 66.4 °C in the apo form and 78.4 °C in complex with maraviroc were obtained for CCR5-4m in DDM/CHS micelles, which are higher than the previously reported 59.9 °C and 67.3 °C, respectively (153). These differences may be related to differences in the microscale fluorescence stability assay and the heating rate used to determine the thermal unfolding. The melting temperature of 48.5 °C (apo form) and 69.1 °C (maraviroc-bound) is lower in pure DDM micelles, but still sufficient for NMR experiments. DM, a short-chain detergent used for NMR studies of β_1 AR (114), would be advantageous due to a lower molecular weight of the solubilized receptor complex. However, the melting temperature of maraviroc-bound CCR5-4m in DM was only 49 °C. Hence the receptor was significantly destabilized in this detergent. As a consequence, DM was not considered further.

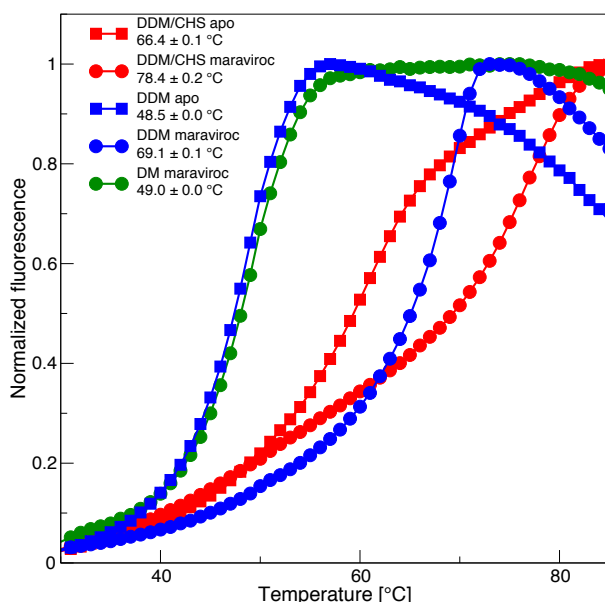


Figure 4.4 CPM assay reveals temperature-induced unfolding of CCR5-4m in different detergent conditions. Melting curves are shown for apo form (filled square) or maraviroc-bound (filled circle) CCR5-4m in DDM/CHS (red), DDM (blue) and DM (green). The melting temperature was determined as the maximum of the computed derivative of the melting curve.

Analysis of secondary structure by NMR

The integrity of the protein structure for CCR5-4m in DDM or DDM/CHS was further assessed by NMR using a jump-return spin-echo sequence (201). The one-dimensional ^1H NMR spectra were analyzed for signal dispersion in the amide region (6-10 ppm) (Figure 4.5a, b). Broad lines were observed, which are caused by the large size of the protein-micelle complex and exchange broadening (see below). Narrow lines might arise from flexible regions. Compared to the preparation in DDM/CHS, CCR5-4m in DDM showed more fine structure and more intensity above 8.4 ppm. Amide transverse relaxation $^1\text{H}^{\text{N}}$ T_2 times at 298 K were estimated by recording the spin-echo 1D experiment with two relaxation delays (0.2 and 2.2 ms) in a buffer containing 10 % (v/v) glycerol. The estimated relative intensity ratios above

8.6 ppm revealed a $^1\text{H}^{\text{N}}$ T_2 time of ~ 1.7 ms in DDM micelles and < 1.3 ms in DDM/CHS micelles. The difference might be caused by the increased molecular weight by incorporation of CHS in the micelle. Compared to $\beta_1\text{AR}$ ($^1\text{H}^{\text{N}}$ $T_2 \sim 4$ ms), the transverse relaxation time is largely reduced, but this could be improved later by a change of glycerol content, temperature, and magnetic field strength (see below).

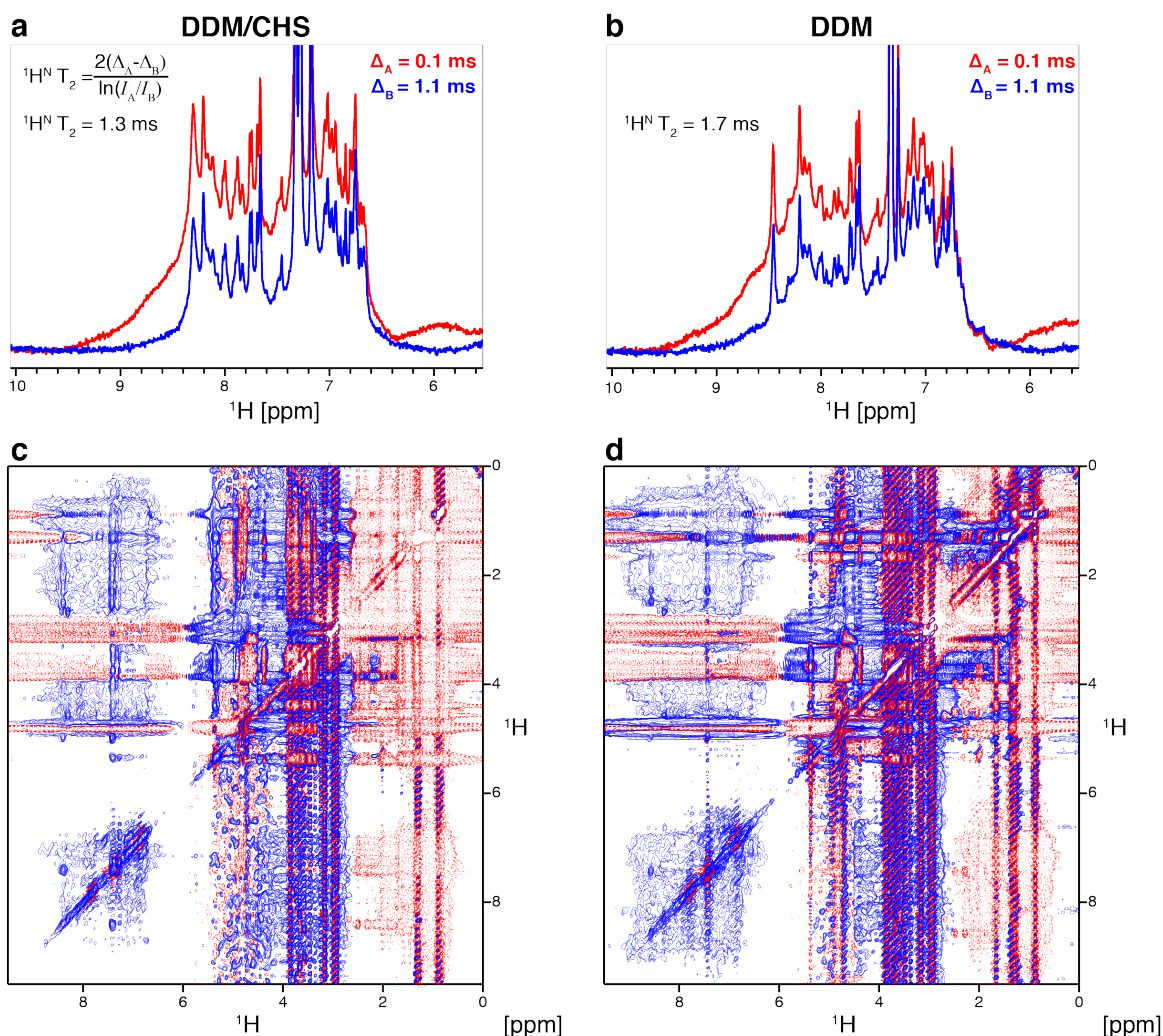


Figure 4.5 NMR analysis of unlabeled CCR5-4m using proton NMR at 298 K on a 900 MHz spectrometer. The jump-return spin-echo ^1H spectra of maraviroc-bound (a) 110 μM CCR5-4m in DDM/CHS and (b) 90 μM CCR5-4m in DDM. The experiments were recorded using effective relaxation delays 2Δ of 0.2 and 2.2 ms to estimate the $^1\text{H}^{\text{N}}$ T_2 time. 2D-NOESY spectra with jump-return detection of (c) 110 μM CCR5-4m with maraviroc in DDM/CHS and (d) 90 μM CCR5-4m with maraviroc in DDM.

To obtain more insight into the spectral quality of unlabeled CCR5-4m in DDM and DDM/CHS micelles, 2D ^1H - ^1H NOESY experiments were recorded, where cross peaks arise from dipolar coupling between protons close in space (< 5 Å) (Figure 4.5c, d). Despite the low resolution and strong detergent signals, the amide region was well dispersed, and clear amide/aliphatic and amide/amide (H^{N} - H^{N}) cross peaks were observed. The latter indicate α -helical regions, which is the dominant secondary structure in CCR5.

The spectral quality was better for CCR5-4m reconstituted in DDM than in DDM/CHS micelles as judged by the increased spectral dispersion in the amide region and higher number

of $^1\text{H}^{\text{N}}\text{-}^1\text{H}^{\text{N}}$ cross peaks. Thus, the reconstitution of CCR5-4m in DDM micelles appeared better suited for further NMR characterization.

CCR5-4m in LMNG micelles

CCR5-4m was also reconstituted in LMNG, which has been reported to increase the stability of GPCRs while retaining a small micelle size (219). The molecular weight of the monomeric fraction from size-exclusion chromatography and protein yield were similar to the preparation in DDM (Figure 4.6a). The $^1\text{H}^{\text{N}}$ T_2 was determined as ~ 2 ms (without glycerol in the buffer). The fold of CCR5-4m was assessed by 2D a $^1\text{H}\text{-}^1\text{H}$ NOESY experiment with $^1\text{H}^{\text{N}}\text{-}^1\text{H}^{\text{N}}$ cross peaks indicative for α -helices (Figure 4.6b).

CCR5-4m in LMNG micelles was also analyzed by the CPM thermostability assay (Figure 4.6c). The melting temperatures were increased in LMNG to 72°C and 56°C in the maraviroc-bound and apo states, respectively, as compared to DDM micelles (69°C and 49°C , respectively). The derivative of the melting curve revealed no clear transition for the thermal unfolding of CCR5-4m in LMNG (Figure 4.6d). This may be caused by aggregation.

Size-exclusion chromatography and initial NMR analysis of maraviroc-bound CCR5-4m did not show a difference between DDM and LMNG micelles. However, due to the unusual melting behavior in LMNG we continued the further studies with CCR5-4m in DDM micelles.

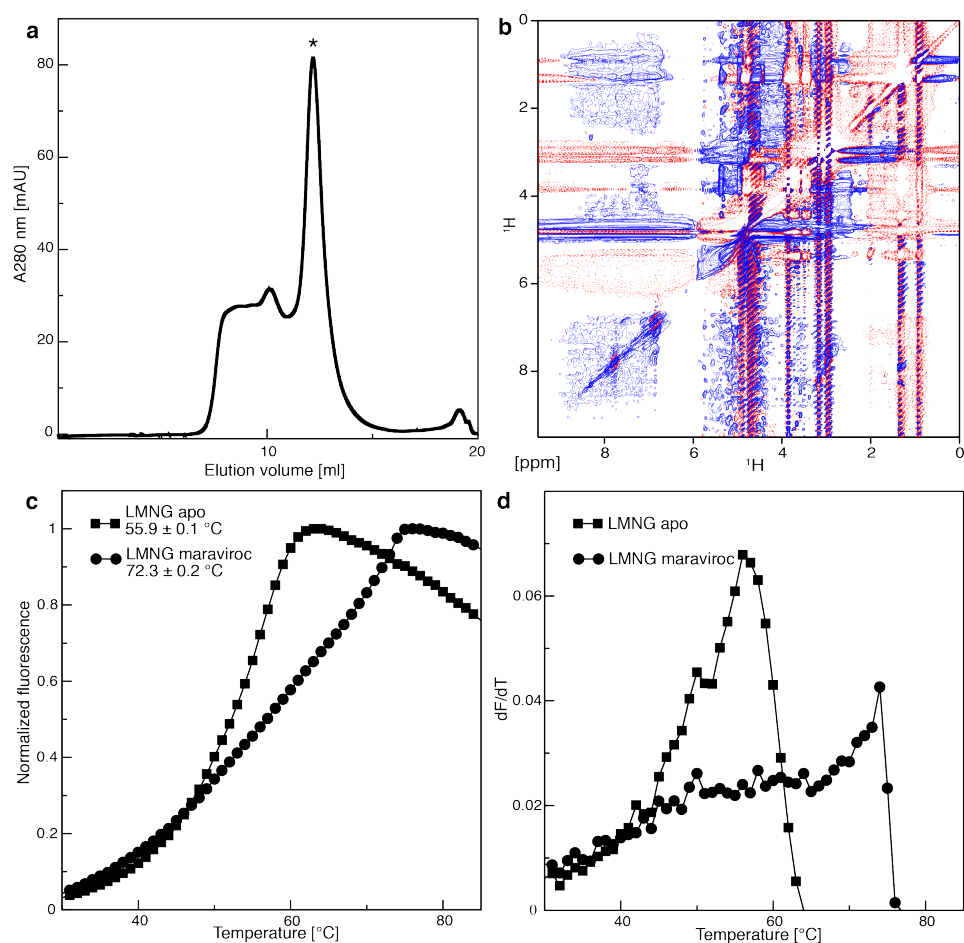


Figure 4.6 Characterization of CCR5-4m in LMNG micelles. **(a)** Size-exclusion analysis of CCR5-4m in LMNG, which contains oligomeric species and a monomeric fraction indicated by an asterisk. **(b)** 2D-NOESY spectrum with 1-1 detection of $75\ \mu\text{M}$ CCR5-4m at $298\ \text{K}$ on a $900\ \text{MHz}$ spectrometer. **(c)** Temperature-induced unfolding

of CCR5-4m in LMNG. Melting curves are shown for apo form (filled square) or maraviroc-bound (filled circle) receptor. The melting temperature was determined as the maximum of the computed derivative of the melting curve. **(d)** Derivative of the melting curve for CCR5-4m in LMNG for apo form (filled square) or maraviroc bound (filled circle).

Initial specific ^{15}N -valine-labeling of CCR5-4m

As a next step, we wanted to compare CCR5-4m to $\beta_1\text{AR}$, our model GPCR for backbone NMR, which is well characterized in its ^{15}N -valine-labeled form. CCR5-4m also contains 27 valines (~8 % of the sequence), which are spread throughout the structure (Figure 4.7). Labeling can be achieved by supplementing isotope-labeled valine to a valine-depleted, yeast extract-free medium (220), since valine is an essential amino acid and no scrambling is observed.

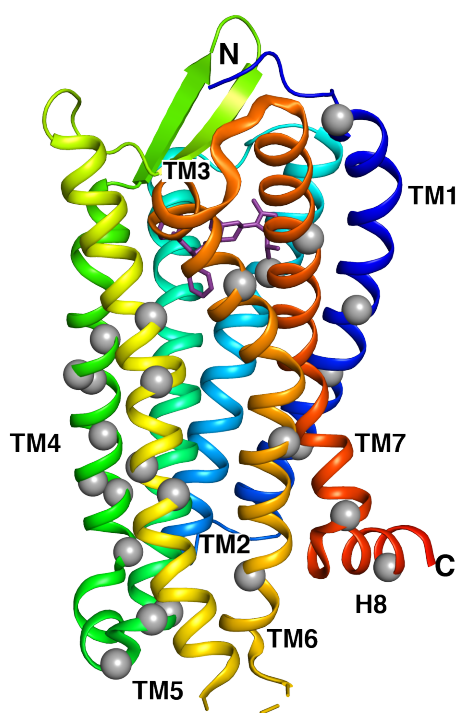


Figure 4.7 Location of valine residues in the structure of CCR5. Crystal structure of CCR5 in complex with maraviroc (4MBS, chain A). The protein backbone and maraviroc are shown in cartoon and stick respectively. The individual valines are depicted as grey spheres. Valine 5 and Valine 323 are not resolved in the crystal structure.

For expression of ^{15}N -valine-labeled CCR5-4m, insect cells were cultured in full medium and transferred to valine-depleted, yeast extract-free medium (ΔVal SF-4) supplemented with ^{15}N -valine prior to virus infection. The expression level of CCR5-4m was significantly reduced in the valine-labeled cultures (~0.15 mg/L) as compared to that in full medium (~0.3 mg/L) containing all amino acids and yeast extract (Figure 4.8a). The two preparations also showed differences in the amide region of 1D ^1H NMR spectra with less fine structure observed for the valine-labeled sample (Figure 4.8b, c). A ^1H - ^{15}N TROSY experiment on 80 μM ^{15}N -valine-labeled, maraviroc-bound CCR5-4m in DDM micelles was recorded for 36 hours (Figure 4.8d), which should be sufficient for a good signal-to-noise ratio (see Chapter 3.1). However, only 5

out of 27 expected resonances were observed, and the low spectral dispersion in the proton dimension indicated improperly folded CCR5-4m.

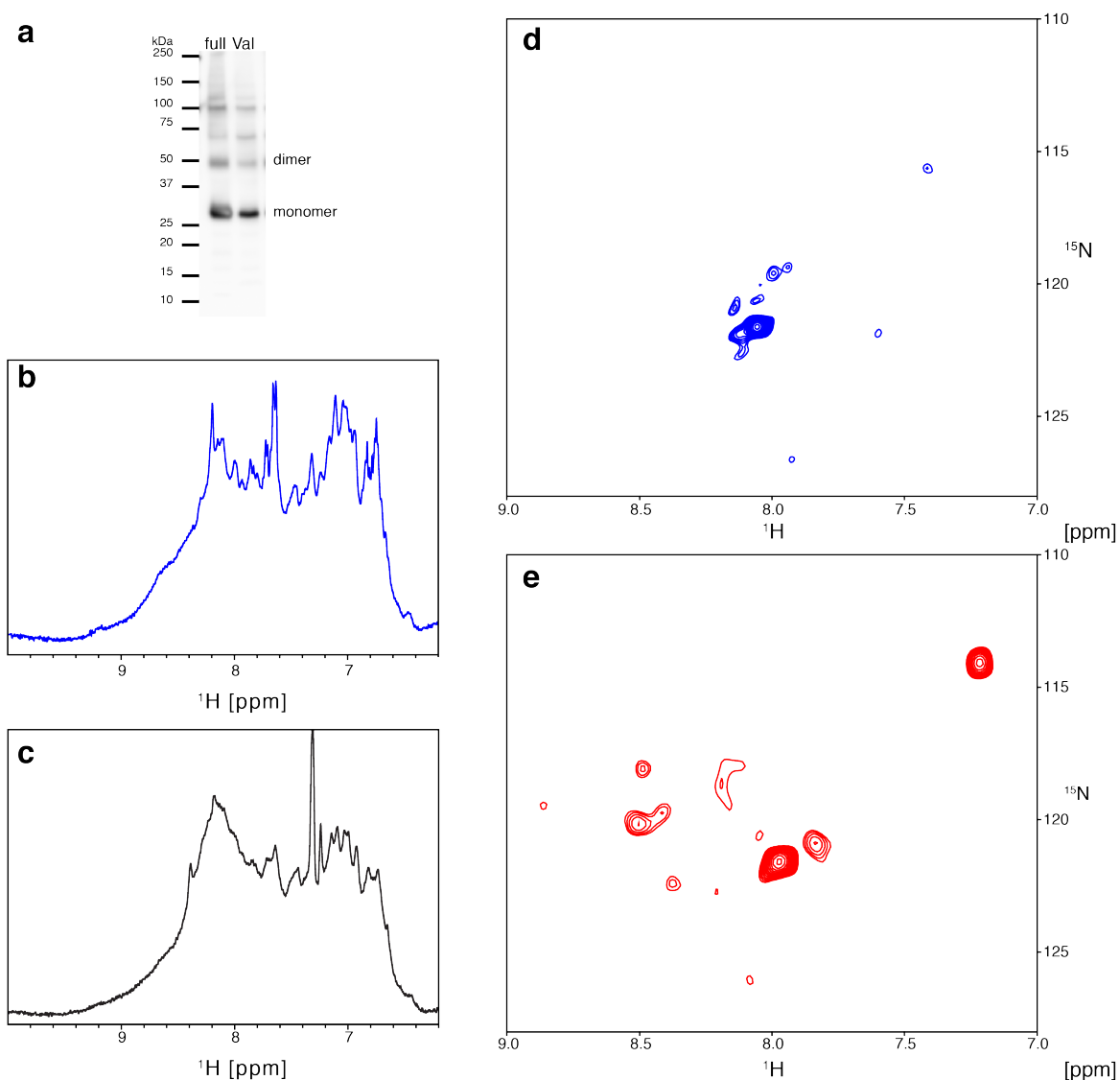


Figure 4.8 Initial expression and characterization of valine-labeled CCR5-4m in yeast extract-free insect-cell medium. **(a)** Insect-cell expression of CCR5-4m in full medium (full) and valine-depleted, yeast extract-free medium (Δ Val SF-4) supplemented with valine (Val) analyzed at 55 hpi by Western blot using a poly-His antibody. **(b)** H^N region from jump-return spin-echo spectrum of 80 μ M $^{13}C,^{15}N$ -valine-labeled, maraviroc-bound CCR5-4m in DDM at 298 K on a 900 MHz spectrometer. The sample was expressed using Δ Val SF-4 medium supplemented with ^{15}N -valine. **(c)** H^N region from jump-return spin-echo spectrum of 75 μ M unlabeled, maraviroc-bound CCR5-4m in DDM at 298 K on a 900 MHz spectrometer. The sample was expressed using full medium containing all amino acids and yeast extract. **(d-e)** 1H - ^{15}N TROSY spectra of ^{15}N -valine-labeled, maraviroc-bound CCR5-4m in DDM micelles. **(d)** CCR5-4m was expressed using Δ Val SF-4 medium supplemented with ^{15}N -valine. The spectrum of a 80 μ M sample was recorded at 298 K on a 900 MHz spectrometer for 36 hours. **(e)** CCR5-4m was expressed using Δ Val SF-4 medium supplemented with ^{15}N -valine and 0.6 g/L yeast extract. The spectrum of a 25 μ M sample was recorded at 308 K on a 600 MHz spectrometer for 100 hours.

The presence of yeast extract seems to have an influence on the expression of CCR5-4m in insect cells. Therefore, another approach for valine labeling was tested. It has been reported

that addition of 10 % of the commonly used amount of unlabeled yeast extract to the Δ Val SF-4 medium restores the protein yield without reducing the incorporation level of the isotope-labeled amino acid below 90 % (221). Addition of 0.6 g/L unlabeled yeast extract (~10 % of the normally used 6-8 g/L) to Δ Val SF-4 medium for expression of ^{15}N -valine-labeled CCR5-4m recovered the yield to 0.25 mg/L. ^1H - ^{15}N TROSY spectra were recorded at 308 K, an increase in temperature to reduce the rotational correlation time and achieve more favorable transverse relaxation (Figure 4.8e). More resonances were observed than in the spectrum without yeast extract supplementation (Figure 4.8d), and the peaks appear at a wider chemical shift range, indicative of a well-folded protein. Their location shows similarities to the pattern of the valine spectrum of $\beta_1\text{AR}$ (Chapter 3.1). However, only 10 out of the expected 27 valine resonances of CCR5-4m could be observed with a low signal-to-noise ratio. Therefore, the method was still not satisfying, and further efforts were undertaken to improve the protocol for amino acid-specific labeling of CCR5-4m.

The influence of yeast extract components on the expression of CCR5 in insect cells

To improve the amino acid-specific labeling of CCR5-4m further labeling conditions were tested. Preparation of a NMR sample for every condition is time-consuming and expensive. Therefore, flow cytometry assays with phycoerythrin (PE) conjugated antibodies were developed which enable small-scale culturing and rapid quantification during the expression. First, the influence of different components of yeast extract was investigated. Therefore, CCR5-4m was expressed in: (i) full medium (SF-4, containing yeast extract and all amino acids), (ii) amino acid-depleted, yeast extract-free medium (Δ SF-4) supplemented with 30 % of the amino acid composition of IPL-41 medium (222), which will be called 30 % IPL mix from now on, and (iii) Δ SF-4 medium supplemented with 30 % IPL mix and 8 g/L dialyzed yeast extract. Due to the dialysis, the latter does not contain free amino acids and small metabolites. This would be a suitable supplement for amino acid-specific labeling, because it does not dilute the isotope incorporation.

The viral infection was comparable for all three conditions, as tested by the gp64 assay (data not shown), where an AcV1 antibody recognizes the baculovirus envelope protein gp64 on the insect-cell surface 6 hpi. Cell viability and cell diameter were similar within the first 48 hpi. However, 72 hpi the viability and cell count decreased in both Δ SF-4 media (Figure 4.9a, b). Flow cytometry with CCR5-specific antibodies was used to determine the CCR5 expression on the cell surface (Figure 4.9c, d). The fraction of cells binding the conformation-specific 2D7 antibody increased in full medium from 86 % at 48 hpi to 98 % at 72 hpi (Figure 4.9c). In the Δ SF-4 medium supplemented with 30 % IPL mix, the fraction of cells recognized by the 2D7 antibody reached only 65 % at 72 hpi, but the level could be restored to that of full medium by supplementation of dialyzed yeast extract. The cells were also tested with T21/8 antibody recognizing an N-terminal sequence of CCR5. In full medium, the fraction of cells recognized by the T21/8 antibody corresponds well to the data observed for 2D7 (Figure 4.9d). In contrast, in the Δ SF-4 medium supplemented with 30 % IPL mix, the fraction of cells recognized by the T21/8 antibody was lower than the fraction recognized by 2D7 antibody, only 32 % at 72 hpi. Supplementation of dialyzed yeast extract recovered the fraction only to 79 % at 72 hpi. Western blot analysis of the whole cell fractions using a poly-His antibody indicated a reduction in CCR5-4m expression for the media not containing the full yeast extract (Figure 4.9e, IPL and Dia).

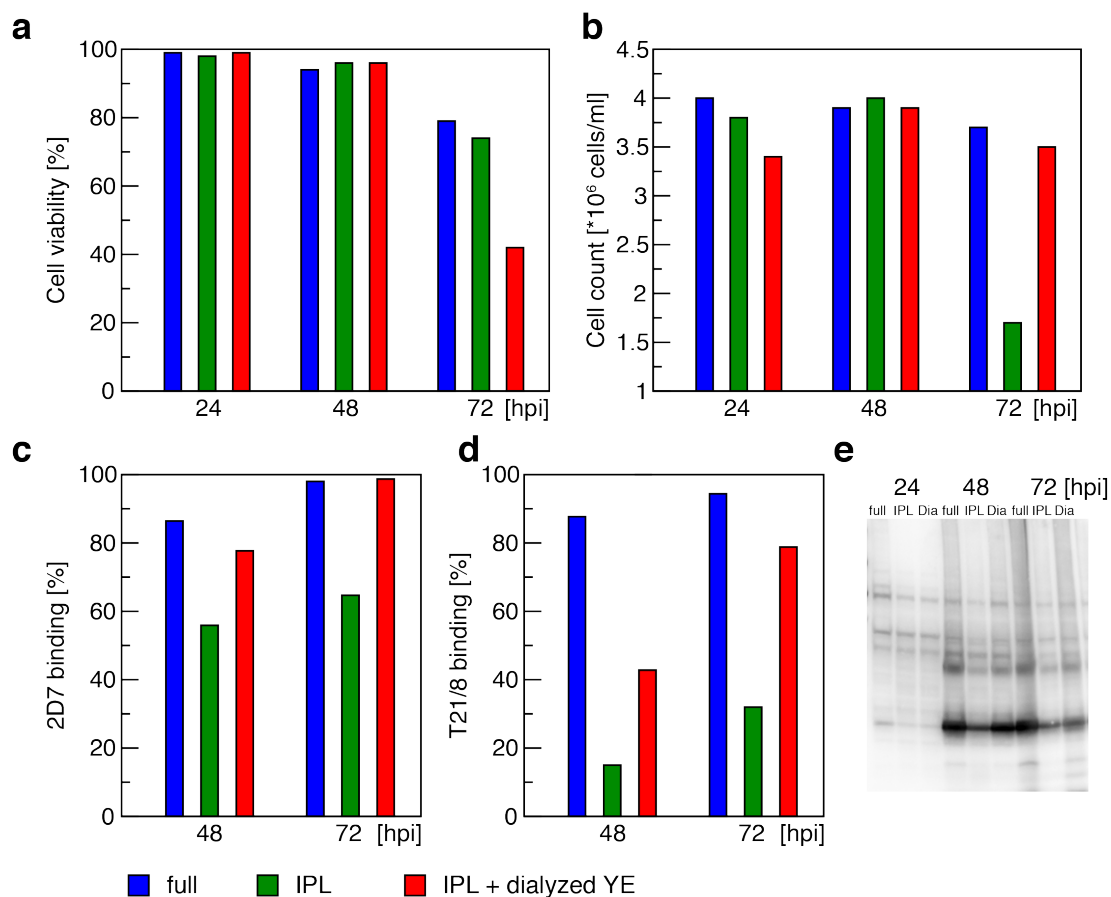


Figure 4.9 Analysis of CCR5-4m expressed in different medium compositions. Expression was tested in full medium (full), Δ SF-4 medium supplemented with 30 % IPL mix (IPL) and Δ SF-4 medium supplemented with 30 % IPL mix and 8 g/L of dialyzed yeast extract (IPL + dialyzed YE or Dia). Cells were changed from full medium to expression medium prior to virus infection and expression. Samples were taken at 24, 48, and 72 hpi. **(a)** Cell viability, **(b)** cell count, **(c)** flow cytometry with sequence-specific T21/8 PE-conjugated antibody, **(d)** flow cytometry with conformation-dependent 2D7 PE-conjugated antibody, **(e)** Western blot analysis of the cell samples using a poly-His antibody.

The insect-cell experiments showed that the viability of insect cells is decreased in medium without yeast extract. Furthermore, the amount of CCR5-4m expressed and inserted in the cell membrane is reduced as shown by Western blot analysis and flow cytometry experiments. However, the supplementation of dialyzed yeast extract only partially restored the yield and cell viability obtained in the full medium, making the method therefore not suitable for amino acid-specific isotope labeling.

Time point of medium change is essential for expression of CCR5

Therefore, another procedure was tested to overcome the limitations of isotope-labeled CCR5-4m expression. In this method, initial virus infection is performed in full medium, and cells are transferred to labeling medium only 16 hpi (209). This still provides efficient isotope labeling since the pool of unlabeled amino acids is small enough (207) and strong protein expression starts only around 24 hpi (223). The insect cells were infected with virus in SF-4 full medium and transferred 16 hpi to the media described above: full, Δ SF-4 supplemented with 30 % IPL mix or Δ SF-4 supplemented with 30 % IPL and 8 g/L dialyzed yeast extract.

Cell viability and cell count at 65 hpi were comparable in full medium and Δ SF-4 media supplemented with 30 % IPL mix (Figure 4.10a, b). 2D7 and T21/8 antibodies recognized ~95 % cells expressed in full medium (Figure 4.10c, d). A slightly lower fraction of cells (~80 %) was recognized in the Δ SF-4 medium supplemented with 30 % IPL mix. The additional supplementation of dialyzed yeast extract did not further increase the amount of CCR5 presented on the cell surface. Western blot analysis using a poly-His antibody of the whole cell fractions indicated similar expression levels among the three media compositions (Figure 4.10e).

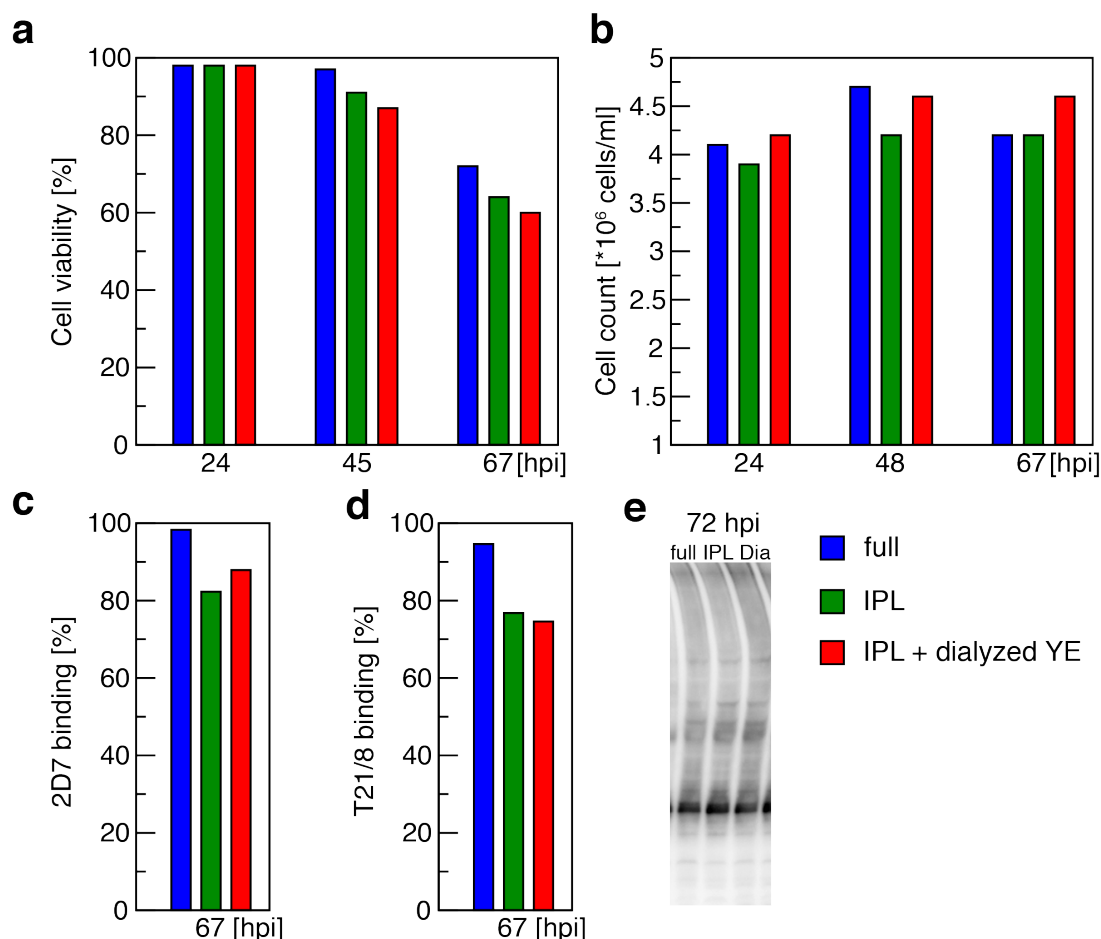


Figure 4.10 Analysis of CCR5-4m expression with a change from full medium to a different medium at 16 hpi. At 16 hpi, the change was performed to full medium (full), Δ SF-4 medium supplemented with 30 % IPL mix (IPL) and Δ SF-4 medium supplemented with 30 % IPL mix and 8 g/L dialyzed yeast extract (IPL + dialyzed YE or Dia). Samples were taken at 24, 48, and 67 hpi. **(a)** Cell viability, **(b)** cell count, **(c)** flow cytometry with sequence-specific T21/8 PE-conjugated antibody, **(d)** flow cytometry with conformation-dependent 2D7 PE-conjugated antibody. **(e)** Western blot analysis of the cell samples using a poly-His antibody.

In conclusion, the difficulties in the amino acid-specific labeled CCR5 expression could be resolved by culturing the insect cells in full medium containing yeast extract for the first 16 hours after virus infection and only changing at 16 hpi to the labeled medium. This later change causes only a small decrease in the expression yield of CCR5-4m. Additional supplementation of dialyzed yeast extract, depleted of free amino acids and small metabolites, did not further improve the expression.

Improved ^{15}N -valine-labeled CCR5-4m spectrum

The improved amino acid-specific labeling protocol in insect cells was used to express ^{15}N -valine-labeled CCR5-4m. For this, insect cells were infected with virus in SF-4 medium and the medium exchanged after 16 hours to ΔVal SF-4 medium supplemented with ^{15}N -valine. Flow-cytometry analysis of the cells at 48 hpi revealed that $\sim 98\%$ of the cells on the surface were recognized by the 2D7 antibody and $\sim 91\%$ by the T21/8 antibody. Solubilization and purification in DDM micelles yielded monomeric CCR5-4m comparable to full-medium expression. The amide proton T_2 time was determined to be ~ 3.2 ms, which is higher than the initially determined $^1\text{H}^{\text{N}}$ T_2 times, due to the increase in temperature from 298 to 308 K, reduction of the glycerol content from 10 to 5 % (v/v) and change from a 900 to a 600 MHz spectrometer. A ^1H - ^{15}N TROSY experiments on $200\ \mu\text{M}$ ^{15}N -valine-labeled, maraviroc-bound CCR5-4m in DDM micelles was recorded (Figure 4.11) revealing a much higher spectral dispersion and sensitivity than observed previously (Figure 4.8). The spectral dispersion is also comparable to ^{15}N -valine-labeled $\beta_1\text{AR}$ (Chapter 3.1), albeit sensitivity is still somewhat reduced. Despite broad lines and partial overlap, 20 out of the 27 expected resonances for valine in CCR5-4m were observed. Two strong peaks [8.0 (^1H) and 121.6 (^{15}N) ppm, respectively 7.2 (^1H) and 114.2 (^{15}N) ppm] were may be tentatively assigned to valine 5 and valine 323 in the flexible N- and C-termini, respectively. In the future, residue-specific assignments need to be established for further analysis.

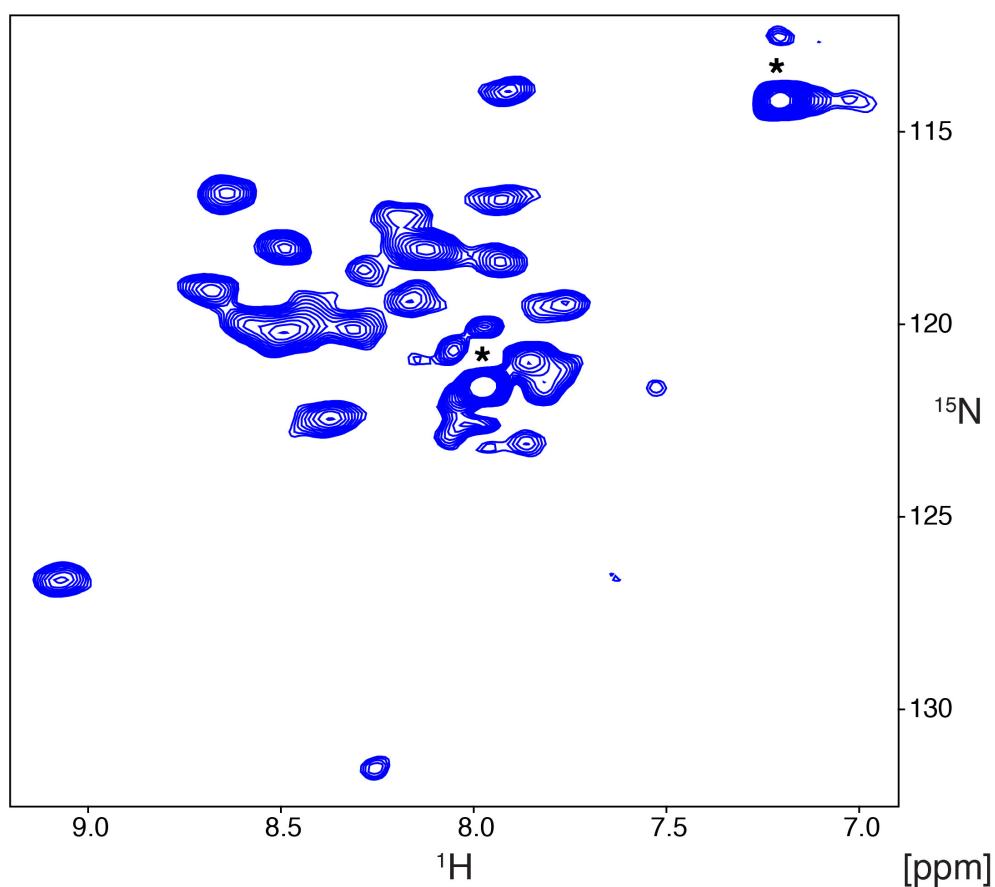


Figure 4.11 ^1H - ^{15}N TROSY spectrum of $200\ \mu\text{M}$ ^{15}N -valine-labeled, maraviroc-bound CCR5-4m in DDM micelles at 308 K recorded for 3 days on a 600 MHz spectrometer. Asterisks indicate the tentatively assigned resonances for valine 5 and valine 323.

Uniformly labeled CCR5-4m

In contrast to the amino acid-specific labeling, uniform isotope-labeling was much easier. For this, CCR5-4m was expressed in insect cells grown in Δ SF-4 medium supplemented with uniformly ^{15}N -labeled yeastolate and $^{14}\text{N}_2$ -glutamine as reported previously (112), and CCR5-4m expressed. Solubilization and purification of CCR5-4m in DDM micelles yielded 0.35 mg/L, which is comparable to the expression in full medium. The C-terminal affinity tags were cleaved after purification to remove strong signals from this flexible region. The amide proton T_2 time was determined to be 3.9 ms at 600 MHz (Figure 4.12a). The ^1H - ^{15}N TROSY spectrum of 105 μM ^{15}N -labeled CCR5-4m shows well dispersed resonances typical of a mostly α -helical protein (Figure 4.12b). Valine-labeled and uniformly labeled spectra are similar (Figure 4.11). Three out of the expected 5 tryptophan indole resonances were observed. Tryptophans are located in TM2, ECL1, TM4, TM5 and TM6 showing that observable resonances do not only belong to flexible non-membrane regions (Figure 4.12c). The spectral quality still suffers from signal overlap in the center of the spectrum, due to broad lines and low chemical shift dispersion for resonances in α -helical structures.

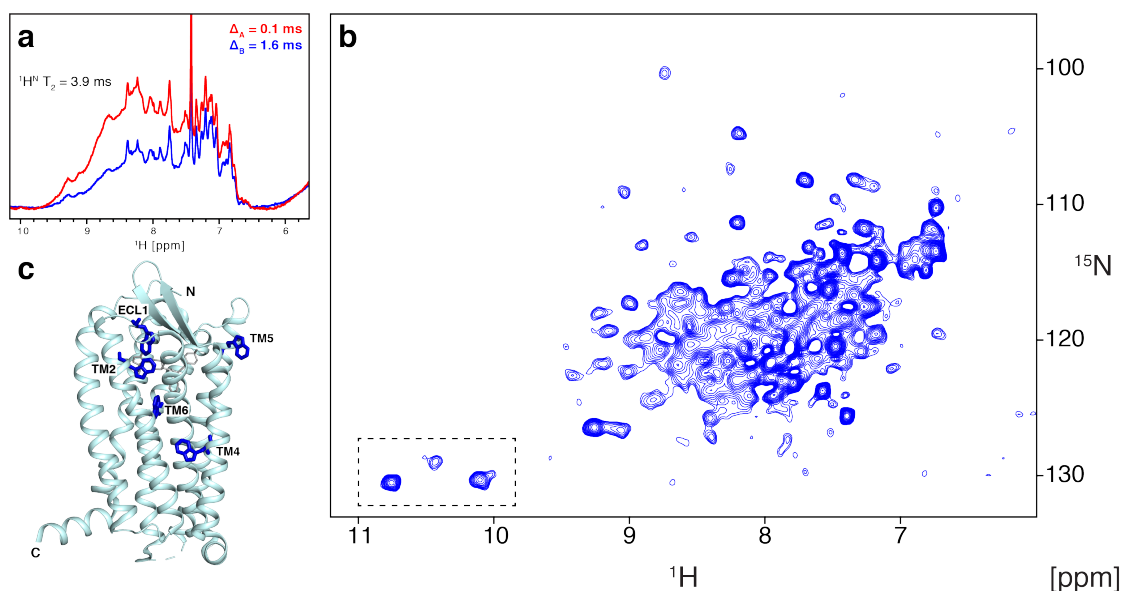


Figure 4.12 Spectra of 105 μM maraviroc-bound, ^{15}N -labeled CCR5-4m in DDM micelles recorded at 308 K on a 600 MHz spectrometer. (a) Jump-return spin-echo ^1H spectra recorded using effective relaxation delays 2Δ of 0.2 and 3.2 ms to estimate the $^1\text{H}^N T_2$ time. (b) ^1H - ^{15}N TROSY spectrum recorded for 68 hours. The dashed box highlights the tryptophan indole region. (c) Location of tryptophan residues in the crystal structure of CCR5 in complex with maraviroc (4MBS, chain A). The protein backbone and maraviroc are shown in cartoon and grey sticks, respectively. Tryptophans residues are depicted as blue sticks.

This problem can be partially overcome by deuteration of proteins to reduce transverse relaxation, resulting in decreased linewidth. Therefore, CCR5-4m was expressed as described above with supplementation of ^2H , ^{15}N yeastolate and protonated $^{14}\text{N}_2$ -glutamine.

The isotope incorporation level in CCR5-4m was determined to be 39 % for ^2H and 66 % for ^{15}N using mass spectrometry (19), which is lower than the previously reported uniform 90 % (^{15}N) and >60 % (^2H) labeling by yeastolate in insect cells (112). This may have been caused by the unlabeled glutamine and a low isotope incorporation of the used yeastolate batch.

However, the partial deuteration already increased the $H^N T_2$ time to 5.4 ms and allowed the INEPT transfer time to be extended to 3.6 ms for optimal magnetization transfer.

Within 17 hours, 1H - ^{15}N TROSY spectra were recorded at 600 and 900 MHz (Figure 4.13). The spectra were well dispersed, and even individual resonances were resolved in the center. However, some signals, for example in the tryptophan indole and glycine backbone region, are missing compared to the uniformly ^{15}N -labeled receptor. This may be due to the lower isotope incorporation (Figure 4.12b). Between 160 and 190 out of the expected 316 backbone resonances for CCR5-4m were detected. The receptor was isotopically labeled and expressed using protonated $^{14}N_2$ -glutamine. Therefore, glutamine and the amino acids alanine, asparagine, aspartate, glutamate and glycine, which metabolically interconvert with it, may not be labeled. This reduces the number of expected resonances to 238.

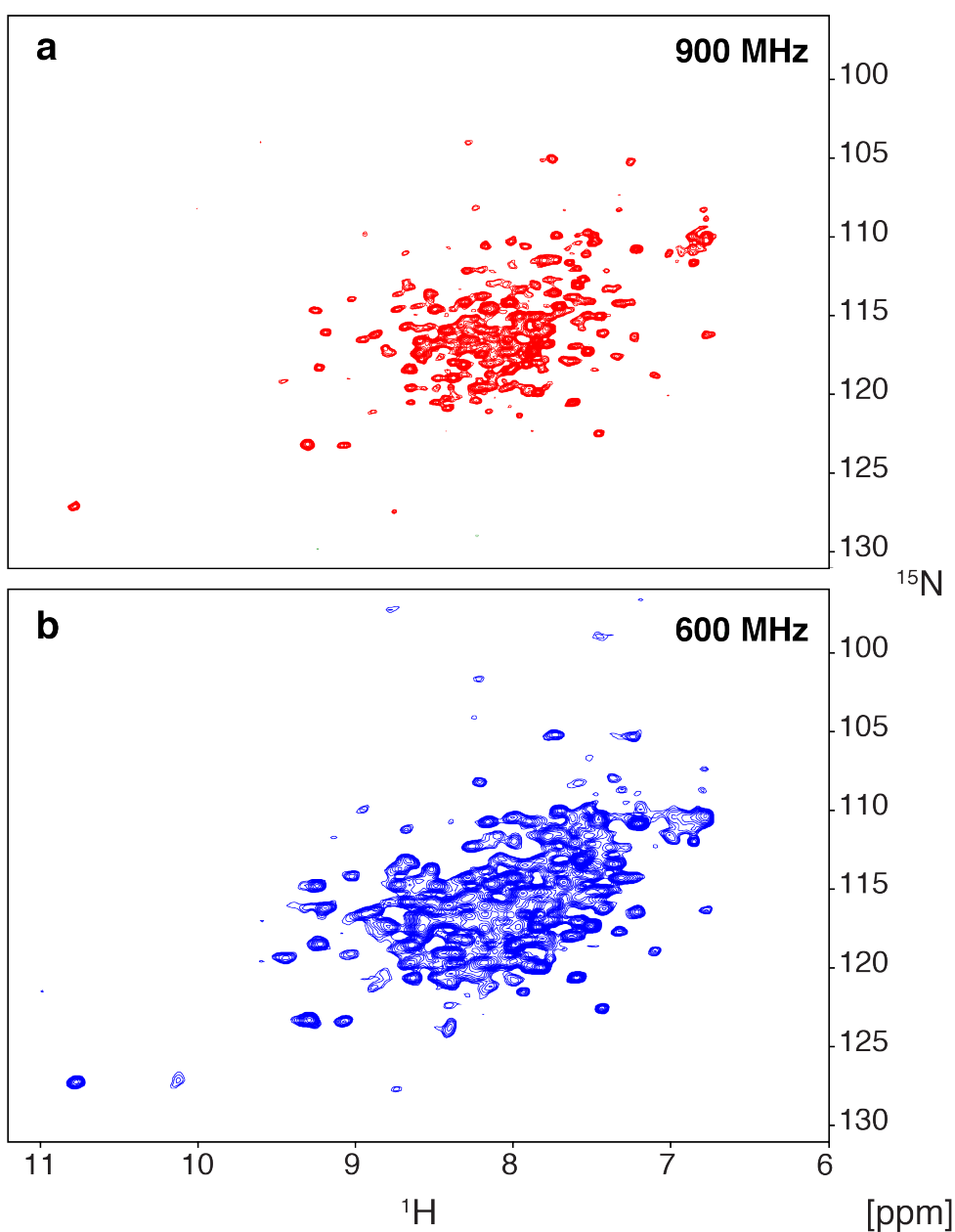


Figure 4.13 1H - ^{15}N TROSY spectrum of 80 μM 2H (39 %)/ ^{15}N (66 %)-labeled, maraviroc-bound CCR5-4m in DDM micelles recorded at 308 K for 17 hours on a (a) 900 MHz or (b) 600 MHz spectrometer.

Spectra of CCR5-4m did not provide the sensitivity and linewidth as observed for β_1 AR in DM micelles (Chapter 3.3). This may be due to the smaller size of the β_1 AR micelle complex and higher isotope incorporation levels [^2H (55 %)/ ^{15}N (78 %)] for the latter.

A remarkable observation was made that the spectral quality was better at 600 than 900 MHz besides the more pronounced signal overlap due to lower frequency separation. Less resonances are observable, and the signal intensity was lower (average 0.77) at 900 MHz than at 600 MHz (Figure 4.14) in contrast to what is expected for a ^1H - ^{15}N TROSY experiment. The reduction in peak intensity and fewer resonances observed at 900 MHz compared to 600 MHz are indicative of exchange in the micro- to millisecond regime. This suggests that the spectral quality is affected by line broadening from exchange contributions.

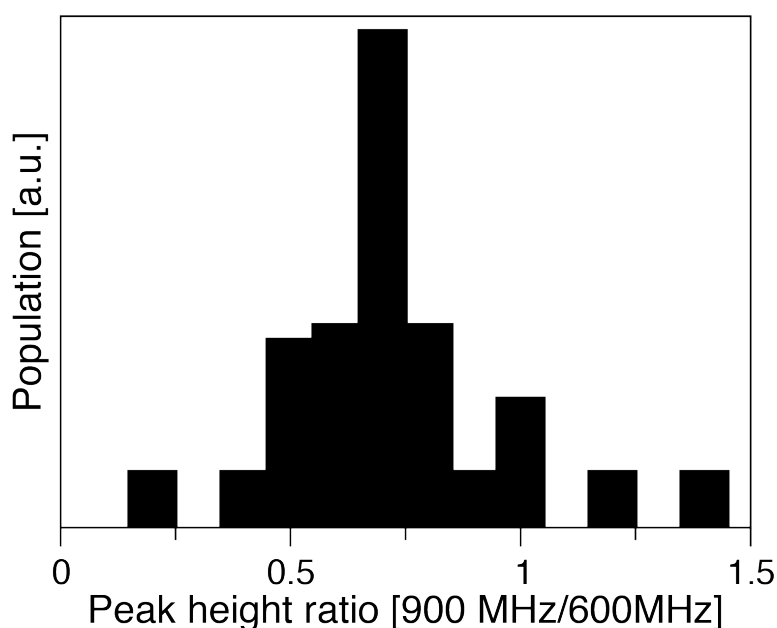


Figure 4.14 Comparison of signal amplitudes in ^1H - ^{15}N TROSY spectra of ^2H (39 %)/ ^{15}N (66 %), maraviroc-bound CCR5-4m in DDM micelles recorded at 600 and 900 MHz. Histogram of relative peak heights from ^1H - ^{15}N TROSY spectra at 900 and 600 MHz field strength. Only well resolved peaks were used for analysis. The average peak height ratio is 0.77

Global characterization of CCR5-4m by NMR

The global behavior of ^2H (39 %)/ ^{15}N (66 %)-labeled, maraviroc-bound CCR5-4m in DDM micelles was further characterized by ^{15}N relaxation experiments as described for β_1 AR (Chapter 3.1). ^{15}N relaxation rates at 14.1 T (600 MHz proton frequency) and 21.2 T (900 MHz) were extracted from 1D proton traces (Figure 4.15, Table 4.1).

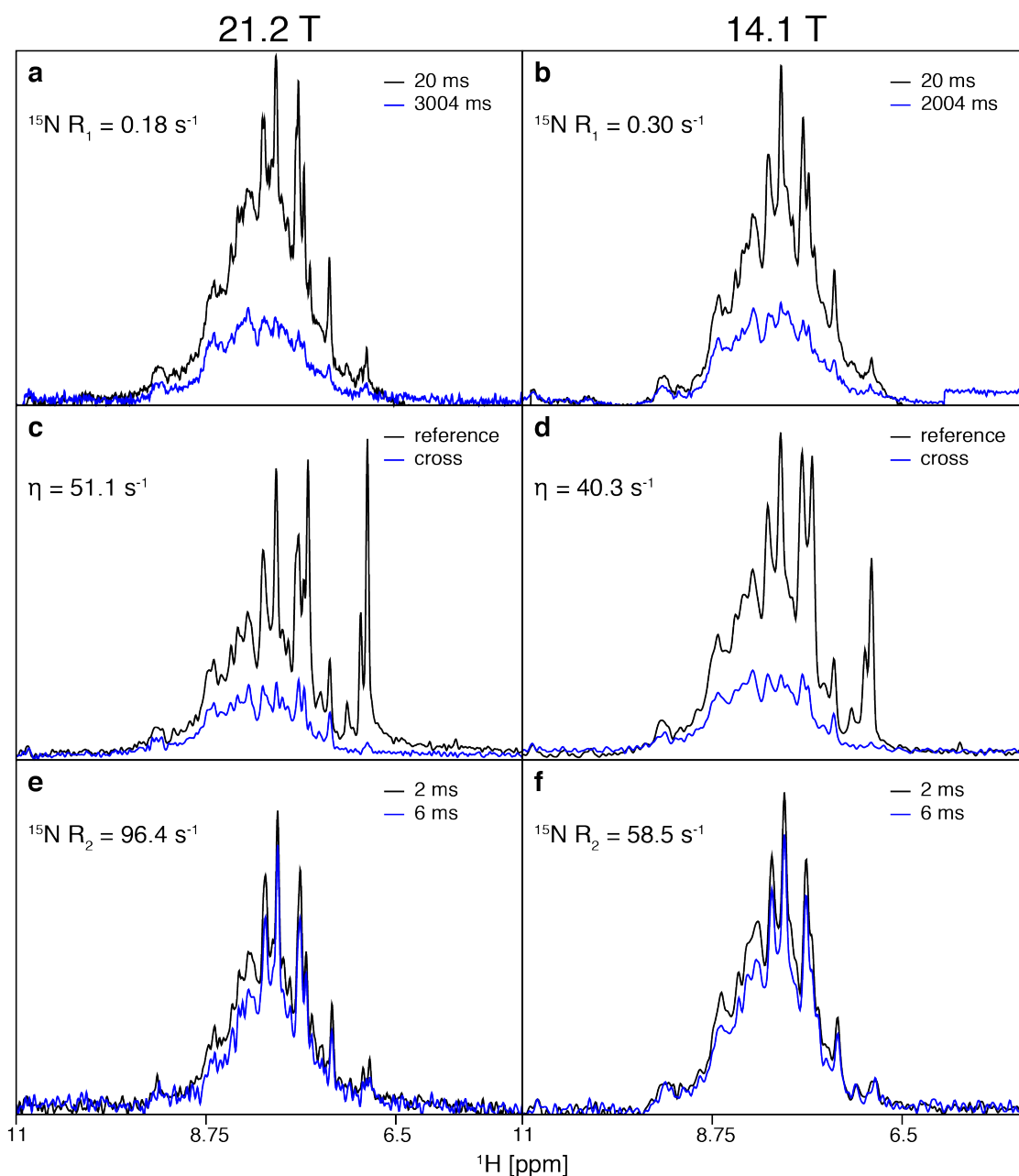


Figure 4.15 Global backbone dynamics of CCR5-4m determined from 1D ^1H -detected ^{15}N relaxation experiments. Experiments were carried out on ^2H (39 %)/ ^{15}N (66 %)-labeled, maraviroc-bound CCR5-4m in DDM micelles at 308 K on 21.2 T (**a**, **c**, **e**) and 14.1 T (**b**, **d**, **f**) spectrometer. Relaxation rates were determined from intensity ratios of attenuated (blue) vs. reference spectra (black). Determined relaxation rates and relaxation delays for R_1 and R_2 experiments are indicated. (**a**, **b**) ^{15}N longitudinal (R_1) relaxation experiments. (**c**, **d**) ^{15}N - ^1H dipolar coupling/ ^{15}N CSA cross-correlation experiments using a transfer time of 12 ms. (**e**, **f**) ^{15}N transverse (R_2) relaxation experiments.

The determined longitudinal ^{15}N R_1 rates decreased from 0.30 s^{-1} at 14.1 T to 0.18 s^{-1} at 21.2 T as expected from the field dependence in the slow-tumbling limit. These relaxation rates correspond to an isotopically tumbling particle with a rotational correlation time τ_c of 41.5 ns (41.2 ns) at 14.1 T (21.2 T). The ^{15}N - ^1H dipolar coupling/ ^{15}N CSA cross-correlation rate η increased from 40.3 s^{-1} at 14.1 T to 51.1 s^{-1} at 21.2 T, corresponding to τ_c values of 45.9 (38.8) ns at 14.1 (21.2) T. The average rotational correlation time τ_c from all four ^{15}N relaxation

rates is 41.9 ± 3.5 ns. This agrees within the error range with a τ_c of 45.1 ns, calculated independently using the Stokes-Einstein relation for a 130-kDa molecular weight complex as determined by multi-angle light scattering (MALS) of CCR5-4m in DDM micelles (Figure 4.16). The similar rotational correlation times determined by NMR on CCR5-4m and derived from light-scattering data of the receptor-micelle complex indicate that CCR5 rotates at the same speed as the micelle, and additional nanosecond motions of the receptor relative to the micelle can be excluded.

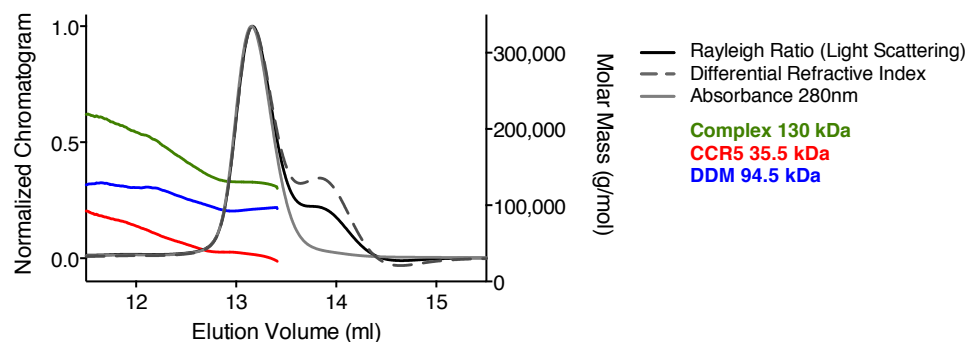


Figure 4.16 MALS chromatograms showing complex, protein, and detergent masses of CCR5-4m in DDM micelles.

Average transverse R_2 relaxation rates were determined as 58.5 (96.4) s^{-1} at 14.1 (21.2) T, which is significantly increased compared to the values of 51.4 (67.4) s^{-1} at 14.1 (21.2) T, expected for a spherical molecule tumbling at a τ_c of 41.9 ns. This indicates an exchange contribution (R_{ex}) of 7 (29) s^{-1} at 14.1 (21.2) T stemming from motions in the micro- to millisecond time range. The increase of R_{ex} at higher field indicates that these motions occur in the intermediate-to-fast exchange range.

Table 4.1 Average relaxation data and molecular weight of 2H (39 %)/ ^{15}N (66 %)-labeled, maraviroc-bound CCR5-4m in DDM micelles.

Field [T]	R_1 [s^{-1}]	R_2 [s^{-1}]	η [s^{-1}]	τ_c [ns] from R_1	τ_c [ns] from η	$\langle\tau_c\rangle$ [ns]	τ_c [ns] from MALS
21.2	0.18 ± 0.03	96.4 ± 14.5	51.1 ± 10.2	41.2 ± 6.2	38.8 ± 7.8	41.9 ± 3.5	45.1
14.1	0.30 ± 0.05	58.5 ± 8.8	40.3 ± 8.1	41.5 ± 6.2	45.9 ± 9.2		

Cryo-EM

With the recent progress in electron detection and image processing, cryo-EM reaches near-atomic resolution and provides insights into large protein structures (224). Cryo-EM has a lower size limit due to the limited image contrast of small particles. The structure of 64 kDa human hemoglobin at 3.8 Å resolution has been reported (225). It is expected that high-resolution structures of proteins in the ~ 50 kDa range can be obtained in the near future (226). CCR5 might be within these limits of cryo-EM analysis. For this reason, we have started a collaboration with the group of Prof. Henning Stahlberg, University of Basel. Within this collaboration currently CCR5 is being used as a test protein to develop imaging and processing strategies for proteins smaller than 100 kDa. In the future, this may serve as a basis to study biologically relevant complexes of CCR5.

For these studies, CCR5-rub, the construct with rubredoxin fusion in ICL3, was prepared as described for CCR5-4m. Initially, sample quality, homogeneity and particle distribution of CCR5-rub was assessed by negative-stain micrographs. CCR5-rub was reconstituted in mixed DDM/CHS micelles, because their large size and oblate shape was expected to facilitate particle identification. However, the sample appeared very heterogeneous and was therefore not further analyzed (Figure 4.17a). As a next step, CCR5-rub was reconstituted in LMNG, which has an about 10-fold lower critical micelle concentration (0.01 mM) than DDM (219). This allows to reduce the content of empty micelles in the sample. Homogenous samples were obtained even at high sample concentrations (Figure 4.17b). These samples then also provided high-quality cryo-EM micrographs, which are very promising for a full structural analysis (Figure 4.17c).

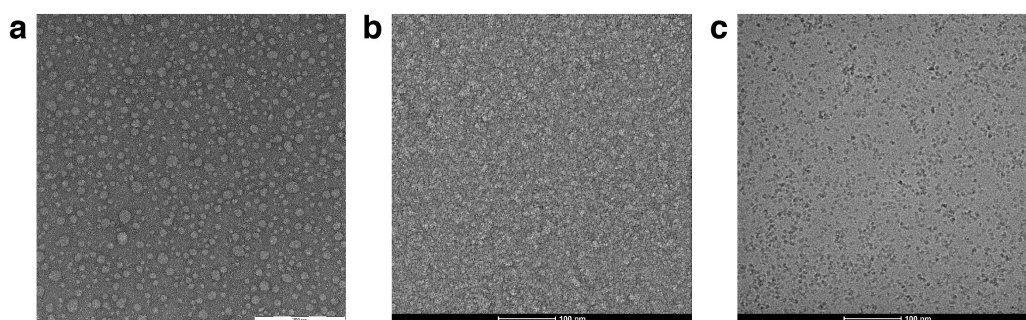


Figure 4.17 Electron microscopy images of CCR5-rub. Negative-stain images of CCR5-rub in (a) DDM/CHS and (b) LMNG micelles. (c) Cryo-electron micrograph of CCR5-rub in LMNG. All images were taken by Kenneth Goldie, University of Basel.

Conclusions and perspectives

In this chapter, an engineered construct of the human CCR5, CCR5-4m, was expressed in insect cells and reconstituted into different detergent micelles. The material obtained in DDM had high stability, homogeneity and a small complex size suitable for solution NMR studies. 0.3 mg/L pure, monomeric CCR5-4m in complex with the inverse agonist maraviroc was obtained. Initially, the recorded ^1H - ^{15}N TROSY spectrum of ^{15}N -valine-labeled CCR5-4m showed low spectral quality. The comparison of different media compositions indicated that the presence of yeast extract during the first 16 hpi is essential for expression of properly folded CCR5-4m in insect cells. Gossert *et al.* (221) have proposed that yeast extract leads to higher expression yields due to an influence on virus infection and cell viability. Interestingly, no difference in expression was observed for $\beta_1\text{AR}$ in full medium or medium depleted of yeast extract for ^{15}N -valine labeling. The main differences in these GPCR constructs are that CCR5 contains sites for posttranslational modifications like tyrosine sulfation and O-glycosylation whereas the N-glycosylation site was removed in TS- $\beta_1\text{AR}$. Additionally, CCR5-4m contains a signaling sequence for targeting membrane insertion.

Based on these observations, possible reasons for the need of yeast extract supplementation are that it (i) influences viral infection, (ii) is required for correct posttranslational modification, or (iii) contains metabolites required for expression and membrane trafficking.

Supplementation of ^{15}N or $^2\text{H},^{15}\text{N}$ yeastolate enabled expression of uniformly labeled CCR5-4m in insect cells. Well-dispersed ^1H - ^{15}N TROSY spectra of the 38 kDa receptor with an apparent molecular weight of 130 kDa were obtained. However, only 160 - 190 out of 316

backbone resonances were resolved. This may be a result of the low isotope incorporation of the NMR sample (39 % ^2H / 66 % ^{15}N). Furthermore, differences in the spectra obtained at 600 and 900 MHz indicate line broadening due to micro- to millisecond exchange, which may broaden resonances below the detection limit. Average ^{15}N R_1 and η relaxation rates revealed an overall global rotation correlation time of 42 ns, agreeing within experimental error with the 45 ns derived from static light scattering data. This suggests that significant motion of the protein relative to the detergent micelle is not occurring. However, conformational exchange within the protein on the micro- to millisecond time range is clearly evident from the increased ^{15}N R_2 relaxation rates.

Exchange broadening was also observed for the thermostabilized mutant of $\beta_1\text{AR}$ (Chapter 3.1 indicating a high intrinsic flexibility. Apparently, the exchange contributions for CCR5 are larger than for $\beta_1\text{AR}$. Therefore, the amplitudes and time scales of motion must be different. This may be caused by the different structure of the ligand recognition site, the different degree of inactive-state stabilization (TS- $\beta_1\text{AR}$ has been highly thermostabilized, whereas CCR5 has many fewer modifications), as well as the different detergent micelles.

So far, the dynamics of CCR5 have been globally characterized since no residue-specific assignments are available. Future studies should aim at insights into specific backbone sites. Successful expression of ^{15}N -valine-labeled CCR5-4m has been shown here. The next step will be resonance assignments. Besides the identification by point mutations, improvement in isotope incorporation would allow other strategies. In the PhD thesis of Christian Opitz, it was shown that sequential information could be obtained using ^{15}N -edited 3D NOESY experiments on ^2H , ^{15}N -labeled TS- $\beta_1\text{AR}$ due to the characteristic peak patterns of α -helical structures (227). The favorable effects of deuteration on relaxation might also enable heteronuclear triple-resonance assignment experiments (Chapter 3.3)

Once the receptor sites are assigned, backbone dynamics can be analyzed in the apo form, with small molecule ligands such as maraviroc, stabilizing CCR5 in an inactive state, and protein ligands such as RANTES analogs. Amino acid-specific labeled CCR5-4m would enable time-domain fitting to extract ^{15}N R_2 rates from 2D ^1H - ^{15}N TROSY spectra. This approach has been established for $\beta_1\text{AR}$ (Chapter 3.1). Due to spectral overlap such an approach will be difficult for uniformly labeled CCR5-4m.

Initial cryo-EM studies on CCR5 appear promising and may enable high-resolution structural studies in the future. This could open a new perspective to study CCR5 protein complexes with chemokines and effector proteins (Chapter 6).

Materials and Methods

Generation of expression construct

The CCR5 constructs were derived from the engineered human CCR5 mutant used in crystallographic studies (153).

The final CCR5-4m sequence is:

```
GAPDYQVSSPIYDINYYTSEPCQKINVKQIAARLLPPLYSLVFIFGFVGNMLVILILINYKR  
LKSMTDIYLLNLAIISDLFLLTVPFWAHYAAAQWDFGNTMCQLLTGLYFIFGFFSGIFFIILL  
TIDRYLAVVHAVFALKARTVTFGVVTSVITWVAVFASLPNIIFTRSQKEGLHYTCSSHPY  
SQYQFWKNFQTLKIVILGLVLP LLVMVICYSGILKTLLRCRNEKKRHRDVRLIFTIMIVYFL  
FWAPYNIVLLLNTFQEFFGLNNCSSNRLDQAMQVTETLGMTHCCINPIIYAFVGEEFRNYL  
LVFFQKHIAKRLEVLVLFQGPDYKDDDDKHHHHHHHHHH
```

and the final CCR5-rub sequence is:

```
GAPDYQVSSPIYDINYYTSEPCQKINVKQIAARLLPPLYSLVFIFGFVGNMLVILILINYKR  
LKSMTDIYLLNLAIISDLFLLTVPFWAHYAAAQWDFGNTMCQLLTGLYFIFGFFSGIFFIILL  
TIDRYLAVVHAVFALKARTVTFGVVTSVITWVAVFASLPNIIFTRSQKEGLHYTCSSHPY  
SQYQFWKNFQTLKIVILGLVLP LLVMVICYSGILKTLLRMKKYCTVCGYIYNPEDGDPDNG  
VNPGTDFKDI PDDWVCPLCGVGKDQFEEVEEKKRHRDVRLIFTIMIVYFLFWAPYNIVLLL  
NTFQEFFGLNNCSSNRLDQAMQVTETLGMTHCCINPIIYAFVGEEFRNYLLVFFQKHIAKR  
FCKCCSIFQOEAPERASSVYTRSTGEQEISVGLGRPLEVLVLFQGPDYKDDDDKHHHHHHHHHH
```

with the green residues corresponding to the CCR5 sequence.

Preparation of recombinant baculovirus

Maintenance Sf9 cultures were subcultured in mid-log phase and grown in full SF-4 medium (Bioconcept) or Insect Xpress medium (Lonza) at 27 °C and shaken at 160 rpm. Baculovirus for insect-cell expression was generated using the Bac-to-Bac system (Invitrogen) in *E. coli* DH10Bac cells using a pAB1G-Cter plasmid (Invitrogen). Baculovirus was generated in adherent cultures as described previously by O'Reilly *et al.* (222). In short, 2 mL 5×10^5 cells/mL Sf9 cells were infected with 5 μ l of the bacmid construct using FuGene HD (Promega) as transfection agent. P0 viral stock was isolated 3 days post infection. Subsequently, high-titer virus stocks for expression were produced by two additional amplification rounds in suspension cultures. 50 ml with 1.5×10^6 Sf9 cells/mL were infected with 1 mL of P0 virus and cultured until the viability decreased to <90 %. The supernatant (P1) was harvested by centrifugation at 1,500 g for 15 min. For the P2 virus stock, 100 ml of cells with 1.5×10^6 were infected with 200 μ l P1 and processed as before.

Functional titration of the P2 virus stock was performed in small-scale cultures to find the optimal virus titer for expression. Expression tests were performed in 20 ml Sf9 at 2.5×10^6 cells/ml and infected at concentrations of 2, 10 and 20 mL/L of P2 virus. Viability, total cell count and cell diameter were measured and cell samples were taken for Western blot analysis at 24, 48 and 72 hpi.

Large-scale expression

For large-scale expression, Sf9 cells were grown to a density of 2.5×10^6 cells/ml in SF-4 or Insect Xpress medium and infected with 10 ml/L P2 virus stock. 0.25x of a 100x Antibiotic-Antimycotic solution (Sigma-Aldrich) was added during expression. CCR5-4m was expressed until the viability decreased to 75-65 %, usually at 48-72 hpi. Cells were harvested by centrifugation at 1,500 g for 15 min, and the cell pellet resuspended in 30 ml 10 mM HEPES (pH 7.5), 10 mM MgCl₂ and 20 mM KCl (lysis buffer) and EDTA-free Complete protease inhibitor mix (Roche) and frozen at -80 °C until further usage.

Gel electrophoresis and Western blotting

Protein samples for SDS-PAGE were mixed with 4x non-reducing SDS sample buffer and directly loaded onto 4-20 % gradient gels (Bio-Rad). Staining was carried out using Coomassie brilliant blue.

For Western blots, the protein was blotted to nitrocellulose membranes using a Trans-Blot Turbo system (Bio-Rad). The transfer time was 3 min at 1.3 A and 25 V for a Mini-PROTEAN TGX gel (Bio-Rad). The membrane was blocked for 1 h using 3 % (w/v) BSA in Tris-buffered saline with 0.1 % Tween-20 (TBST). Subsequently, the membrane was incubated (1 hour) with a 1:5000 dilution of horseradish peroxidase (HRP)-conjugated His1 antibody (Sigma-Aldrich). Washing was performed for 3 x 5 min using TBST. Protein bands were visualized using a chemiluminescent HRP substrate (Roche) according to the manufacturer's instructions.

Purification of maraviroc

Maraviroc was isolated from Celsentri® tablets (Pfizer). In brief, tablets were pestled and dissolved in DMSO. Following removal of the solvent, maraviroc was recrystallized from toluene/hexane.

Membrane preparation and purification

The membrane preparation and purification of CCR5-4m was adapted from Tan *et al.* (153). In detail, the cell pellet corresponding to a 1-L expression culture was filled up to 80 ml with lysis buffer (10 mM HEPES (pH 7.5), 10 mM MgCl₂ and 20 mM KCl) and the cells disrupted for 10 s with an electric disperser. Membranes were spun down at 142,000 g at 4 °C for 1 h. The process was repeated twice with high osmotic buffer (lysis buffer supplemented with 1 M NaCl) and once again with lysis buffer to remove the salt. The membrane fraction was then resuspended in 15 ml 10 mM HEPES (pH 7.5), 30 % (v/v) glycerol, 10 mM MgCl₂, 20 mM KCl and EDTA-free Complete protease inhibitor mix (Roche) and flash-frozen at -80 °C.

For solubilization, 15-ml aliquots of membrane fractions were thawed and incubated with 10 ml lysis buffer containing EDTA-free Complete protease inhibitor mix (Roche), 200 µM maraviroc and 2 mg/ml iodoacetamide for 1 h at 4 °C. Then 25 ml solubilization buffer [100 mM HEPES (pH 7.5), 300 mM NaCl, 1 % (w/v) n-dodecyl-D-maltopyranoside (DDM, Anatrace), and 100 µM maraviroc] were added and incubation continued for 3 hours at 4 °C. After ultracentrifugation for 1 h at 140,000 g, the supernatant was added to a 2-ml Talon Superflow metal affinity resin (GE Healthcare, per 1 L of culture) and incubated overnight at 4 °C.

The talon resin was then washed with 10 column volumes (CV) 25 mM HEPES (pH 7.5), 150 mM NaCl, 10 % (v/v) glycerol, 0.05 % (w/v) DDM, 30 mM imidazole and 100 μ M maraviroc, followed by 10 CV 25 mM HEPES (pH 7.5), 150 mM NaCl, 10 % (v/v) glycerol, 0.05 % (w/v) DDM, 5 mM ATP, 10 mM MgCl₂, 100 μ M maraviroc, and then 5 CV 25 mM HEPES (pH 7.5), 150 mM NaCl, 10 % (v/v) glycerol, 0.05 % (w/v) DDM, 100 μ M maraviroc. CCR5 was eluted with 6 CV 25 mM HEPES (pH 7.5), 150 mM NaCl, 10 % (v/v) glycerol, 0.05 % (w/v) DDM, 300 mM imidazole and 300 μ M maraviroc and concentrated to 500 μ l using an Amicon Ultra 50 kDa MWCO (Millipore) at 4 °C and 2,500 g.

Monomeric CCR5 was obtained by size-exclusion chromatography (Superdex 200 Increase 10/300 GL, GE Healthcare) in 25 mM HEPES (pH 7.5), 150 mM NaCl, 5 % (v/v) glycerol, and 0.05 % (w/v) DDM. CCR5 was supplemented with an equimolar amount of His-tagged PreScission protease (homemade) and incubated overnight at 4 °C to remove the FLAG and His tags. The sample was then incubated with a Ni-NTA superflow resin (Qiagen) for 3 hours at 4 °C. The unbound material was concentrated using an Amicon Ultra-3 filtration device 50 kDa MWCO (Millipore), and buffer exchanged with the final buffer 25 mM HEPES (pH 7.5), 150 mM NaCl, 5 % (v/v) glycerol, and 0.05 % (w/v) DDM. The NaCl concentration was reduced from 150 mM to 75 mM for the deuterated NMR sample.

For reconstitution of CCR5-4m in DDM/CHS or LMNG micelles, the protocol was modified as follows. DDM/CHS: solubilization of CCR5-4m was carried out in 1 % (w/v) DDM and 0.2 % (w/v) CHS (cholesteryl hemisuccinate TRIS salt, Anatrace) and all following buffers were supplemented with 0.05 % (w/v) DDM/0.01 % (w/v) CHS. The purified receptor was concentrated in an Amicon centrifugal device with a 100 kDa MWCO (Millipore). LMNG: CCR5-4m was solubilized in 1 % (w/v) LMNG (lauryl maltose neopentyl glycol, Anatrace) and IMAC buffers supplemented with 0.1 % (w/v) LMNG. The LMNG concentration was subsequently reduced to 0.01 % (w/v).

Immunoprecipitation

Structural integrity of CCR5-4m following solubilization and purification was analyzed by immunoprecipitation using the conformation-specific 2D7 (BD Pharmingen) and sequence-specific T21/8 (eBioscience) CCR5 antibodies as well as the His_{6x} antibody (Sigma-Aldrich).

Antibodies were incubated with CCR5-4m for 1 hour at 4 °C. The solution was mixed with Protein G Mag Sepharose (GE Healthcare). Following incubation for 2 hours at 4 °C, the supernatant was removed. Protein G Sepharose was washed three times with 25 mM HEPES (pH 7.5), 150 mM NaCl, 5 % glycerol, 100 μ M maraviroc, 0.05 % DDM/0.01 % CHS or 0.05 % DDM (all w/v). Supernatant and bead fractions were analyzed by Western blot as described above.

CPM thermal-shift assay

Detergent-solubilized, purified apo or maraviroc-bound CCR5-4m was adjusted to 1 mg/ml concentration. 2 μ l of protein were diluted with 58 μ l 25 mM HEPES (pH 7.5), 150 mM NaCl, detergent (see below) and 50 μ M maraviroc for the maraviroc-bound CCR5-4m and incubated for 1 hour on ice. 5 μ l CPM dye (75 μ g/ μ l) were added and samples were heated from 25 to 95 °C at a rate of 2 °C/min in a Rotor-Gene Q (Qiagen) real-time PCR thermal cycler. Melting temperatures were determined as the maximum of the computed first derivative.

The following detergent concentrations were used: 0.05 % (w/v) DDM, 0.01 % (w/v) LMNG or 0.05 % (w/v) DDM with 0.01 % (w/v) CHS. The melting temperature in DM micelles was determined in the presence of 2 % (w/v) DM to achieve an efficient exchange of the micelle composition of CCR5-4m prepared in 0.05 % (w/v) DDM.

Flow cytometry

Virus infection and expression of CCR5 in Sf9 cells were monitored by flow cytometry with PE-coupled antibodies. 75 µl samples were taken from the insect-cell culture, washed three times with 100 µl PBS (Sigma-Aldrich), incubated 15 minutes in the dark with the appropriate antibody and washed another three times with 100 µl PBS. Cells were resuspended in 75 µl PBS and flow cytometry (Moxi Flow™, ORFLO Technologies) measurements were performed at 532 nm excitation with PE-conjugated antibodies. Virus infection was checked at 6 hpi using the baculovirus envelope gp64 monoclonal antibody [(AcV1), PE (eBioscience™)]. Cells expressing CCR5-4m were analyzed with the CCR5 sequence-specific antibody T21/8 (PE, eBioscience™) or the conformation-specific antibody 2D7 (PE, BD Pharmingen).

Test of different labeling strategies

Different media compositions were tested for the expression of CCR5-4m using the protocol from Gossert *et al.* (221). Amino acid-depleted, yeast extract-free SF-4 medium (Δ SF-4, Bioconcept) was supplemented with either 30 % IPL amino acid mix only or 30 % IPL amino acid mix and 8 g/L dialyzed yeast extract (SnakeSkin Dialysis tubing, 3.500 MWCO cutoff, Thermo Fisher™). pH and osmolarity were adjusted to the values determined for the full medium. 30 mL of Sf9 cells were cultured in SF-4 medium to a cell density of 2.5×10^6 cells/ml. Cells were transferred from full medium to the expression medium by centrifugation prior to virus infection or 16 hpi. Samples for the analysis of cell parameters, expression and flow-cytometry measurements were taken at several time points during expression.

Valine labeling

For selective valine labeling, Sf9 cells were cultured in SF-4 or Insect Xpress medium to a cell density of 3×10^6 cells/ml.

For the initial trial, cells were centrifuged at 500 g for 10 min and resuspended in valine-depleted, yeast extract-free SF-4 (Δ Val SF-4, Bioconcept) supplemented with 100 mg/L ^{15}N -valine (Sigma-Aldrich) and infected at the same time with virus. The second test with yeast extract supplementation was carried out in the same manner, but Δ Val SF-4 was supplemented with 120 mg/L ^{15}N -valine and 0.6 g/L yeast extract (BD Bacto™).

The final optimized protocol for amino acid-specific labeling uses virus infection for 16 h in full medium. Cells are then centrifuged at 300 g for 4 min, washed in Δ SF-4 medium with pH and osmolarity adjusted to the values determined for the full medium and spun down again before transfer to Δ Val SF-4 medium supplemented with 100 mg/L ^{15}N -valine.

Uniform labeling with yeastolate

Uniform labeling of CCR5-4m in Sf9 cells was achieved by supplementing isotope-enriched yeastolate (112). Sf9 cells were cultured in Insect Xpress medium to a cell density of

3×10^6 cells/ml, centrifuged at 500 g for 10 min and starved in Δ SF-4 medium for 2 hours. Afterwards cells were centrifuged at 500 g for 10 min and resuspended in Δ SF-4 medium supplemented with 1 g/L $^{14}\text{N}_2$ -glutamine and 8 g/L of ^{15}N yeastolate or 6 g/L of $^2\text{H},^{15}\text{N}$ yeastolate. pH and osmolarity were adjusted to the values determined for the full medium.

NMR experiments and data analysis

NMR samples of typically 25-200 μM CCR5-4m were prepared in 25 mM HEPES (pH 7.5), 150 mM NaCl, 5 % (v/v) glycerol, 0.05 % (w/v) DDM, 5 % D_2O and 0.02 % NaN_3 with two molar equivalents of maraviroc and concentrated to 250 μl in a Shigemi tube. For initial 1D and 2D experiments, CCR5-4m was prepared in 0.01 % LMNG, 0.05 % DDM or 0.05 % DDM/0.01 % CHS. For the deuterated sample, the NaCl concentration was reduced to 75 mM to shorten the proton pulse length.

All NMR experiments were performed on Bruker AVANCE 14.1 T (600 MHz ^1H frequency) or 21.2 T (900 MHz) spectrometers equipped with a TCI cryoprobe at an initial temperature of 298 K, which was later increased to 308 K to reduce the rotational correlation time. Amide proton T_2 times were determined from a jump-return spin-echo experiment (201). ^1H - ^{15}N TROSY experiments were recorded as 140 ($^2\text{H},^{15}\text{N}$) or 80 (all other samples) (^{15}N) \times 1024 (^1H) complex points and acquisition times of 28 ms or 16 ms (^{15}N) and 42 ms (^1H). For optimal sensitivity, the ^1H - ^{15}N transfer time was reduced to 3.6 ($^2\text{H},^{15}\text{N}$) or 3.0 ms and the interscan delay set to 1.5 ($^2\text{H},^{15}\text{N}$) or 1 s. ^{15}N R_1 and R_2 relaxation rates were determined using standard HSQC-based ^{15}N relaxation experiments (228, 229) on $^2\text{H},^{15}\text{N}$ CCR5-4m with relaxation delays of 20, 2004 ms (20, 3004 ms) at 14.1 (21.2) T for R_1 and 2, 6 ms for R_2 . ^{15}N - ^1H dipolar-coupling/ ^{15}N CSA cross-correlation rates η were determined from a quantitative comparison of in-phase and anti-phase ^{15}N magnetization (230) using a cross-relaxation delay of 12 ms.

All NMR spectra were processed with NMRPipe (204) and analyzed with SPARKY (205) or PIPP (231).

Multi-angle light-scattering and viscosity measurements

SEC-MALS and buffer viscosity measurements were carried out as described in Chapter 3.1 with the following adjustments. SEC-MALS measurements on maraviroc-bound CCR5-4m in DDM micelles were carried out at 299 K using a GE Healthcare Superdex 200 Increase 10/300 size-exclusion column on an Agilent 1260 HPLC with a column buffer of 25 mM HEPES (pH 7.5), 75 mM NaCl, 5 % (v/v) glycerol, 0.05 % (w/v) DDM. Weight-averaged molar masses (M_w) for the protein-detergent complex (130 kDa), and for the protein (35.5 kDa) and detergent components (94.5 kDa) of the complex were calculated using the protein conjugate method in the ASTRA 6 software (Wyatt Technology).

The viscosity of the receptor-micelle suspension was estimated from a viscosity measurement of 25 mM HEPES (pH 7.5), 75 mM NaCl, 5 % (v/v) glycerol, and 0.05 % (w/v) DDM suspension using an Anton Paar AMVn rolling-ball viscometer yielding a value of 0.8590 cP at 308 K corresponding to the temperature of NMR experiments.

Theoretical relaxation rates and determination of rotational correlation times

Theoretical ^{15}N relaxation rates and rotational correlation times τ_c were obtained as described in Chapter 3.1. Theoretical ^{15}N $R_2(\text{N}_x)$ (229) rates were calculated for $\tau_c = 41.9$ ns at 14.1 and 21.2 T. An independent estimate of the rotational correlation time τ_c was obtained from the 130 kDa molecular weight of the CCR5-4m DDM micelle complex determined by SEC-MALS. Using literature values (232) for the partial specific volumes of protein (average value 0.735 ml/g, 0.27 mass fraction) and DDM (0.815 ml/g, 0.73 mass fraction), the specific volume for the complex can be calculated as 0.792 ml/g. The non-hydrated radius r_{NH} of an assumed spherical detergent micelle is then 34.4 Å. Assuming a hydration layer thickness r_{W} of 3.2 Å, the isotropic rotational correlation time τ_c of the hydrated receptor-detergent complex is 45.1 ns using the Stokes-Einstein equation $\tau_c = \frac{4\pi\eta_s r_{\text{H}}^3}{3kT}$ with $r_{\text{H}} = r_{\text{NH}} + r_{\text{W}}$ and η_s being the viscosity of the receptor-micelle suspension.

Cryo-EM

CCR5-rub was prepared in 25 mM HEPES (pH 7.5), 150 mM NaCl with 0.01 % LMNG or 0.05 % DDM/0.01 % CHS. Samples (≤ 2 mg/ml) were prepared for cryo-EM by adsorbing 4 μl of the sample suspension onto lacey carbon film mounted on 300-mesh copper grids (Ted Pella, Inc). Prior to adsorption, the grid was rendered hydrophilic by glow discharge. The specimen was applied and after 1 min of incubation on the surface, the grid was blotted and snap-frozen in liquid ethane using a Leica EM GP automated plunging device (Leica Microsystems). The frozen grids were transferred under liquid nitrogen and loaded into a Gatan 626 cryo-holder (Gatan). The cryo-holder was then inserted into the stage of a FEI Talos transmission electron microscope (FEI Company) operated at 200 kV.

Imaging was performed at cryogenic temperatures (approx. -170 °C) in low-dose, bright-field mode. Electron micrographs were recorded digitally on a CETA 16M 4k x 4k CMOS Camera (FEI Company) at given defocus values of approximately -2.5 μm . The electron dose for imaging was maintained at 20 $\text{e}\text{\AA}^{-2}$

4.2 Production of isotope-labeled proteins in insect cells for NMR

Original Publication

Franke, B., Opitz, C., Isogai, S., Grahl, A., Delgado, L., Gossert, A. D., & Grzesiek, S.

Production of isotope-labeled proteins in insect cells for NMR

Journal of Biomolecular NMR, 22(3), 1–12.

Production of isotope-labeled proteins in insect cells for NMR

Bastian Franke^{1,3}, Christian Opitz^{1,3}, Shin Isogai¹, Anne Grahl¹, Leonildo Delgado¹, Alvar D. Gossert^{2*}, Stephan Grzesiek^{1*}

¹Focal Area Structural Biology and Biophysics, Biozentrum, University of Basel, 4056 Basel, Switzerland

²Department of Biology, ETH Zürich, 8093 Zürich, Switzerland

³These authors contributed equally to this work.

*Address correspondence to:

Stephan Grzesiek, Focal Area Structural Biology and Biophysics, Biozentrum, University of Basel, 4056 Basel, Switzerland. E-mail: stephan.grzesiek@unibas.ch; Phone: +41 61 207 21 00

Alvar D. Gossert, Department of Biology, ETH Zürich, 8093 Zürich, Switzerland, E-mail: alvar.gossert@mol.biol.ethz.ch; Phone: +41 44 633 3455

Keywords

Baculovirus, BEVS, yeast extract, algal extract, deuteration, GPCR, β -adrenergic receptor, CCR5, Abelson kinase, GFP

Summary

Baculovirus-infected insect cells have become a powerful tool to express recombinant proteins for structural and functional studies by NMR spectroscopy. This article provides an introduction into the insect cell/baculovirus expression system and its use for the production of recombinant isotope-labeled proteins. We discuss recent advances in inexpensive isotope-labeling methods using labeled algal or yeast extracts as the amino acid source and give examples of advanced NMR applications for proteins, which have become accessible by this eukaryotic expression host.

Introduction

Proteins expressed in *E. coli* dominate structural and biophysical studies due to the ease of genetic manipulation, rapid growth, and high expression yields. This is reflected in the large fraction of entries in the Protein Data Bank (PDB) derived from this system, which presently (12/2017) amounts to 74% (Table 1). The simple, efficient, and inexpensive ^{15}N , ^{13}C , and ^3H isotope labeling in this expression host from only ammonium chloride, glucose and water make *E. coli*-expressed proteins particularly accessible to analysis by heteronuclear NMR.

However, for more complex proteins originating from higher organisms, heterologous *E. coli* expression often fails to provide properly folded and functional material suitable for structural analysis. These proteins frequently require the complex machineries for protein folding, post-translational modification, or membrane insertion of higher eukaryotes, which are less developed or absent in *E. coli*. For this reason, the use of eukaryotic expression hosts like yeast, mammalian, or insect cells has increased steadily over the last 25 years (Figure 1) and accounts now for about 8% of all PDB entries. Half of these (4.3%) derive from insect cell expression, whereas much smaller fractions account for yeast and mammalian cells. For proteins with molecular weights higher than 100 kDa or of human origin, the fraction from insect cell expression increases to 7.3% and 10.4%, respectively, whereas for the ‘notoriously difficult to make’ G protein-coupled receptors (GPCRs), it even dominates with 70.5% (Table 1).

Despite this clear success for structure determination, the insect cell expression system has not seen wide use in NMR. Thus, the PDB currently comprises only two entries (1T50, 1QLO) derived from NMR data using insect cell-expressed, but unlabeled proteins. This is certainly due to the required more elaborate expression protocols as well as the higher costs for the incorporation of isotopes, which need to be provided as isotope-labeled amino acids. Nevertheless, insect cell expression with isotope-labeling has now been used successfully in a number of NMR studies on complex eukaryotic proteins, not accessible from *E. coli*, to provide valuable mechanistic insights into protein kinases¹⁻³ and GPCRs⁴⁻⁷. This is concomitant with the development of robust expression and isotope labeling protocols^{1,2,8-17}, which are easy to apply in a typical NMR protein production lab.

In this article, we give an introduction into the basic concepts of protein production for NMR using the insect cell system, highlight recent developments of inexpensive ^{15}N , ^{13}C , and ^3H -labeling methods and give several examples of advanced NMR applications.

The baculovirus expression vector system: baculovirus and insect cell lines

The baculovirus expressing vector system (BEVS) emerged in the 1980s as a novel technology for heterologous protein production¹⁸. It is based on insect cell lines in suspension cultures, which are infected by recombinant baculoviruses (BVs) to express the protein of interest.

The baculovirus

The best studied BV is the *Autographa californica* multiple nuclear polyhedrosis virus, which has been isolated from the alfalfa looper *Autographa californica*^{18,19}. Once inside a cell, the BV infection cycle spans three major phases – termed the early, late and very late phase. During the early phase, the budded baculovirus enters the cell by absorptive endocytosis. The late phase occurs 6 hours post infection (hpi) and is accompanied by viral DNA replication and gene expression as well as budded BV production. In the very late phase at 24–96 hpi, the cell starts to express the highly abundant polyhedrin, an envelope protein forming the so-called BV occlusion bodies that protect virus particles from the environment once they have been released from the host cell. In most BEVS, the viral polyhedrin gene is replaced by the gene of interest. The expression of the latter is then driven by the strong polyhedrin promoter in the very late phase of baculovirus gene expression in virus-infected cells. Alternatively, there is a second viral promoter with very similar characteristics, the p10 promoter. It is typically used when expressing multiple proteins on a single bacmid (e.g. MultiBac™, Geneva Biotech), as repeated use of the polyhedrin promoter may increase the risk of gene instability due to recombination²⁰. Historically, the polyhedrin promoter was favored, because replacing the polyhedrin gene leads to a visible phenotype lacking occlusion bodies, which allows identifying recombinant virus plaques. Replacing the p10 gene, however, has the advantage that the Baculovirus does not lyse the cells towards the end stage of infection, potentially leading to higher expression yields and expression times beyond 72 hours.

Generation of recombinant baculovirus

Today two main BEVS platforms are available: (i) the original baculovirus shuttle vector system²¹, commercially available under the name Bac-to-Bac™ (Invitrogen). This system is based on a modified *E. coli* strain (DH10Bac™), which produces recombinant, viral DNA (the bacmid) from a donor plasmid containing the gene of interest. The purified bacmid is then used to transfect insect cells that generate the virus particles. For production of multi-component protein complexes, a modified version of the Bac-to-Bac system (MultiBac™, Geneva Biotech) can be used, which provides expression of multiple proteins on a single bacmid²⁰. (ii) The *flashBAC*™ system (Oxford Expression Technologies) allows direct transfection of insect cells simultaneously with a bacmid and a vector containing the target DNA. Recombination then occurs directly in the insect cells²².

In both approaches, recombinant virus particles are collected from the supernatant of cultures and amplified by repeated rounds of infection. Usually three rounds (V_0 , V_1 and V_2) are sufficient to obtain ~200 mL of a high-titer virus stock. The titer is determined by adding diluted virus stock to insect cells grown in an adherent monolayer and counting the plaques of lysed cells caused by the infection. The titer value is the number of plaque forming units (pfu) per volume of virus, which for a high-titer V_2 amounts to typically $\sim 2 \times 10^8$ pfu/mL.

The virus stocks can be stored at 4°C for several weeks without reduction in titer. However, to achieve stability for several months and even years, the recombinant BV can be stored in form of cryo-preserved baculovirus-infected insect cells (BIICs)²³. The following protocol works well in our hands. Insect cells are infected at a density of 2.0×10^6 cells/mL with V_1 and harvested when the cell diameter increases by 20-30%, i.e. usually after 24-48 h. Cells are then centrifuged at 200 g for 10 min at room temperature and dissolved at a density of 10^7 cells/mL in a mixture of 45% of the used medium, 45% fresh medium, and 10 % DMSO for cryo storage. Expression yields of insect cells infected with either freshly made virus or BIICs are typically comparable within 20%.

Cell lines and their characteristics

At present, three main types of insect cells are used in research and biotechnological applications with BV infection – Sf21, Sf9 and Tn5. (*Drosophila melanogaster* S2 cell lines can also be used for stable transfection with target genes for protein production, but we limit this article to transient transfection.) Sf21 cells were originally isolated from primary explants of the American fall army worm's (*Spodoptera frugiperda*) ovarian pupal tissue and their clonal derived isolates were named Sf9²⁴. Tn5 (also called high five™) cells originate from the ovarian tissue of the cabbage looper (*Trichoplusia ni*)²⁵. These three strains have different characteristics in terms of growth rate, virus production capacity and protein expression. Tn5 cells have faster doubling times than Sf9 and Sf21 cells (18–24 h vs. 24–30 h, respectively), but produce less BV. Sf9 cell lines are regarded as the cell line with highest virus production. They form excellent monolayers due to their small size, making virus plaque determination easier in the initial steps of virus production. With respect to protein expression yield, the larger Sf21 cells may express more cytosolic protein compared to Sf9, whereas Tn5 cells have been reported to express 5–10-fold higher levels of secreted proteins than the Sf cell lines. Despite these general trends, both Sf and Tn cells should be tested in order to determine the highest expression yields for an individual protein construct.

Expression

Suspension cultures of insect cells can be grown in media containing a complex formulation of inorganic salts, carbohydrates, lipids, vitamins, and amino acids²⁶. Commercial media with optimized performance are further supplemented with algal or yeast extracts and possibly other components of plant or animal origin such as fetal calf serum. Typically, the cultures are grown at a temperature of 27°C in conical flasks or centrifugal tubes shaken at ~90 rpm and ~50 mm shaking diameter. Maintenance requires weekly serial passaging with about ten-fold dilution, and cells are kept in exponential growth phase ($\leq 4 \times 10^6$ cells/ml). Prior to infection, cells are grown to a density of $1.5\text{--}2.0 \times 10^6$ cells/ml. To optimize large-scale expression, functional titers of the virus stock should be determined using freshly made V_2 stocks or BIICs in small-scale cultures in order to determine the optimal virus-to-cell ratio – the multiplicity of infection – which yields the highest amounts of expressed protein. Cell diameter and viability should be checked every 24 hpi with an inverted microscope or a suitable automated cell counter. A functional virus infection leads to an increase in cell diameter from ~16 μm to above 20 μm , whereas a too strong virus infection is detected by a fast decline in viability (e.g. as assayed by trypan blue) to below 90% within less than 48 hpi.

Heterologous protein expression usually starts 24–48 hpi and peaks around 72 hpi. For optimal protein yield, insect cells should be harvested when cell viability drops to 80–90%.

The green fluorescent protein (GFP) is convenient to establish optimal expression conditions in small cell cultures without any purification by quantifying protein levels from the intrinsic fluorescence. In our hands, the truncated, cycle3 variant²⁷ of GFP provided high expression and at the same time high-quality NMR spectra, which are not affected by the exchange broadening present in other GFP variants.

The implementation of the baculovirus/insect cell system within a standard structural laboratory environment requires only a sterile hood, but no further modifications or expensive additional equipment, e.g. the same type of shaker incubators as for *E. coli* can be used. This is an important advantage over mammalian cell cultures, which are cultivated at 5% CO₂ and 75% humidity, requiring special incubators. Although BV is pathogenic to insect cells, it does not pose any threats to vertebrates allowing handling at standard biosafety level 1.

Isotope labeling

Since insect cells have a very limited capacity to synthesize amino acids from simpler precursors, the production of isotope-labeled proteins from insect cells is usually based on the supplementation of entire labeled amino acids to growth media depleted in amino acids and other proteinaceous material. Complete formulations of media for uniform ¹⁵N and ¹³C labeling are commercially available (BioExpress, CIL), but very costly. For in-house preparation of labeling media, custom-made media without amino acids, carbohydrates, yeast extracts or other sera from biological sources can be purchased from a variety of suppliers (e.g. Bioconcept, Lonza, Expression Systems, Gibco). In the simplest case, commercially available isotope-labeled amino acids are added to these media^{1-8,11,12,14,17}. This is very efficient for selective labeling of a few amino acids with specific labeling patterns, but becomes prohibitively expensive for uniform labeling. In particular, deuterated amino acids are very expensive and at the moment some are not even commercially available in ³H,¹³C,¹⁵N-labeled form. As a more economical alternative, the supplementation of labeled algal or yeast extracts as an amino acid source (Figure 2) has been developed in recent years^{9,10,13-16}. In this way, deuteration can also be achieved at moderate extra costs.

Selective labeling

Selective labeling of a few amino acid types with specific isotope patterns has the advantage of reducing spectral complexity and simplifies resonance assignments. However, due to the loss of backbone connectivity, application of conventional triple resonance NMR assignment strategies may not be possible. Not all amino acid types lend themselves equally well for selective isotope labeling. High labeling efficiency (>90%) can be achieved for a limited set of essential or semi-essential amino acids of the insect cell metabolism (i.e. isoleucine, leucine, lysine, methionine, phenylalanine, tyrosine, threonine, cysteine, tryptophan, and valine). Some further non-essential amino acids can be labeled with acceptable levels of scrambling, e.g. in a pioneering study on Abelson kinase ¹⁵N-glycine was incorporated to 78% and produced 7 additional signals on top of 16 expected ones¹. Scrambling values for serine, proline, arginine and histidine have not been reported so far. In contrast, amino acids directly related to glycolysis and the citric acid cycle (i.e. alanine, asparagine, aspartate, glutamine, and glutamate) are significantly affected by scrambling, which also causes ¹³C dilution if carbohydrates such as glucose are not provided in their

labeled form. For these amino acids, selective labeling can be achieved by suppressing unwanted metabolism (see section on amino acid metabolism below).

The selective labeling approach in combination with solution NMR has provided interesting functional information for a number of systems. In one of the first applications, the Abelson kinase domain, a drug target for chronic myelogenous leukemia (CML), was labeled uniformly and selectively in various isotope patterns by the addition of pure isotope-labeled amino acids^{12,28}. Due to the lack of deuteration, the sensitivity of NMR experiments involving ^{13}C or other side chain nuclei was very low for this 277-amino acid protein, but almost complete backbone assignment was achieved. The hitherto unknown conformation of the kinase activation loop in solution could then be derived from ^1H - ^{15}N RDC data for various inhibitor complexes (Figure 3a)³. In a further study using backbone NMR, 26 ^1H - ^{15}N resonances could be observed for the G protein-coupled turkey β_1 -adrenergic receptor ($\beta_1\text{AR}$), which was selectively labeled by ^{15}N -valine⁷. Due to the 100-kDa molecular weight of the receptor-detergent micelle and the absence of deuteration, the sensitivity of triple resonance assignment experiments was too low, but 21 ^1H - ^{15}N resonances could be assigned from point mutations. The response to six different agonist and antagonist ligands as well as the binding of a G protein mimetic nanobody could be followed on these valine resonances, revealing in particular the activating motion induced by the agonists (Figure 3b).

The favorable relaxation properties of methyl groups²⁹ provide higher sensitivity of NMR detection than backbone resonances albeit at the cost of a less clear correlation between chemical shift and the underlying structural determinants. Selective labeling by (*methyl*- ^{13}C)-methionine has been applied to the β_2 -adrenergic receptor ($\beta_2\text{AR}$) revealing changes in the equilibrium populations of methionine-82, which correlate to modulations of the signal transduction level in several ligand-receptor complexes⁴. More recently, (*methyl*- ^{13}C)-methionine labeling has also been applied to the $\beta_1\text{AR}$ ³⁰, and multiple equilibria of ligand-bound and G protein mimetic nanobody-bound forms as well as respective changes in receptor dynamics could be detected. Extending this approach, labeling by ($\alpha\beta\gamma$ - ^2H , *methyl*- ^1H - ^{13}C)-methionine has been combined with the use of commercial, highly deuterated algal amino acid mixtures to obtain selectively (*methyl*- ^1H - ^{13}C)-methionine labeled $\beta_1\text{AR}$ on a deuterated background. The protocol requires the careful supplementation of several, additional deuterated amino acids at well-defined time points during expression and achieved incorporation levels of ^1H into side chain and non-exchangeable backbone hydrogen positions as high as 90% for 14 amino acids. The approach enabled studies of the $\beta_1\text{AR}$ dynamics in nanodiscs⁶ and has also been applied to the μ -opioid GPCR³¹.

Uniform labeling using algal and yeast extracts

To overcome the high costs for uniform labeling that arise from adding pure isotope-labeled amino acids to the insect cell medium, several protocols have been described, which use isotope-labeled algal¹⁵ or yeast^{9,10,13,16} extracts as the principal amino acid source (Figure 2).

Algal extract

^{13}C -labeling of algae is cost-effective since $^{13}\text{CO}_2$ can be used as the sole carbon source. However, algae cultivation requires special bioreactors equipped with a light-source²⁷ and for ^{13}C -labeling a closed supply of $^{13}\text{CO}_2$. Algal extracts are commercially available in all combinations of uniform ^{15}N , ^{13}C , and ^2H labeling (e.g. ISOGRO[®] Sigma-Aldrich, Celtone[®] Cambridge Isotope Laboratories). Due to the acid hydrolysis during the commercial production, the amino acids cysteine and tryptophan are lost, whereas asparagine and

glutamine are hydrolyzed to the corresponding aspartic and glutamic acids. Supplementing the missing four amino acids in labeled form would be very costly. However, insect cells can produce cysteine from methionine and serine, which both are present in the medium. Furthermore, glutamine and asparagine can be produced upon addition of ammonium (see below) from glutamate and aspartate, respectively, which are abundant in the extract. In contrast, tryptophan is an essential amino acid and needs to be supplemented. A recent approach exploits this idea¹⁵ using commercially available algal extract (10 g/L), tryptophan (20 mg/L), glucose (5 g/L), and ammonium chloride (250 mg/L) with the desired isotope-labeling patterns as supplements to a serum-free medium depleted in amino acids and glucose (Figure 2). Incorporation levels of 80% were achieved for uniform ¹⁵N-labeling, 77% for ¹⁵N,¹³C-labeling, and ~73% for ³H,¹⁵N and ²H,¹³C,¹⁵N-labeling. Yields ranged between 2–5 mg/L for the tested membrane protein and 12–22 mg/L for various soluble human proteins. Using labeled ammonium as a substrate for producing labeled glutamine and asparagine in insect cells is cost-effective, but has the disadvantage that ammonium hinders virus entry into the cell. Therefore, when using this protocol, cells need to be infected in full medium and are only transferred to the labeling medium at 16 hpi, before the protein is expressed.

Yeast extract

Isotope-labeled yeast extracts as the amino acid source for insect cells can be produced with moderate effort using standard protein expression equipment^{9,10,16} or obtained commercially¹³ (Cortecnet). A step-by-step procedure to produce such yeast extracts from wild type *Pichia pastoris* has been described recently¹⁶. The yeast is grown in a fermenter under control of glucose feed, oxygen, pH, and temperature using a minimal medium based on glucose, ammonium, and water as the sole carbon, nitrogen and hydrogen sources. All desired isotope-labeling patterns can be achieved using these basic ingredients in suitable isotope-labeled forms (Figure 2). In particular, yeast growth is possible on 100% ³H₂O. After fermentation, yeast cells are autolysed during a high-temperature (50°C, 5 days) incubation step with papain before being micro-filtered with a 10 kDa cut-off and lyophilized to yield yeastolate. This procedure avoids the harsh acid hydrolysis used for commercial algal lysates and largely preserves all amino acids including asparagine and tryptophan (cysteine was not quantified) as determined by quantitative amino acid analysis¹⁶. In addition to free amino acids, yeastolate also contains incompletely cleaved polypeptides, sugars, and other cellular compounds, which may be metabolized by the insect cells. About 6.6 g yeastolate is obtained per liter of yeast culture from 27.5 g glucose and 4.3 g ammonium chloride. Although glutamine is present in low concentration in the yeast extract, its supplementation considerably boosted expression levels (see below). Thus a supplement of 8 g/L of ¹³C, ¹⁵N-yeastolate and 1 g/L of ¹⁵N₂-glutamine to the drop-out medium provided high yields (40–80 mg/L for soluble proteins such as the human Abl kinase domain or GFP, 1–2 mg/L for GPCRs) and high (~90%) uniform-¹⁵N/¹³C incorporation¹⁶. Deuterium incorporation levels of ~60% were achieved when supplementing ³H-labeled yeastolate obtained from yeast grown on 100% ³H₂O, but protonated glucose. Figures 3c,d show as examples the ¹H-¹⁵N TROSY and one-dimensional ¹⁵N T₁ and T₂ relaxation data obtained on the ¹⁵N/²H-labeled HIV coreceptor CCR5.

Algal vs yeast extracts

Both algal and yeast extracts have respective advantages and disadvantages when used as isotope-labeled amino acid sources. Commercial extracts provide a good starting point for

initial uniform labeling experiments. At the moment, only ^{15}N -labeled yeast extracts are commercially available (Cortecnet). In contrast, commercial algal extracts can be obtained in all uniform labeling patterns including ^2H , ^{13}C and ^{15}N at high isotope incorporation levels (98%). As they are a byproduct of commercial ^{13}C glucose production from $^{13}\text{CO}_2$, ^{13}C -labeled algal extracts are relatively inexpensive. However, we observed batch-to-batch variations within the commercial extracts, which occasionally resulted in significant reductions of expression levels. The acid hydrolysis step during the production destroys several amino acids, which need to be supplemented. In principle, the harsh hydrolysis could be avoided by producing the lysate from suitable algal starting material in the home laboratory or by an adaptation of the commercial production process. However, home growth of isotope-labeled algae itself seems very demanding.

In contrast, the production of yeast and yeastolate is less complicated and requires only standard equipment. Once established, it provides full control over all ingredients for the labeling. In particular, the mentioned acid hydrolysis can be avoided and most amino acids preserved. Furthermore, increased capabilities for customization of the labeling scheme become available. For example, yeast extracts with protonated methyl groups on a deuterated background may be produced from yeast cultures grown on $^2\text{H}_2\text{O}$ and protonated pyruvate as described for *E. coli*³³.

Due to the commercial production process, algal extracts from *Spirulina* contain a higher total fraction of amino acids (~65% dry weight) than yeast extracts (~33% dry weight). In the published protocols, algal extracts were added at 10 g/L concentration with the aim of highest isotope incorporation. This is close to the maximally tolerated concentration of about 12 g/L, at which the too high osmolarity of the medium severely affects the cell viability. In contrast, the yeast extracts were added at 8–10 g/L, which corresponds to about half of the concentration of amino acids in the final insect cell medium derived from algal extracts. Nevertheless, high ^{15}N and ^{13}C incorporation rates of ~90% are achieved under these conditions from the yeast extracts.

In our experience, expression of soluble proteins such as Abelson kinase and GFP and also of membrane proteins such as GPCRs worked well with either algal or yeast extracts, but we have not carried out a systematic analysis. It appears worth testing both extracts as well as their combination to obtain optimal expression of a certain protein.

Amino acid metabolism

While the glucose metabolism can be ignored for ^{15}N labeling, it must be considered for ^{13}C labeling and ^2H labeling. Glucose acts as precursor for alanine, glutamate/glutamine, and aspartate/asparagine through the citric acid cycle and further for serine and glycine through glycolysis. Therefore, ^{13}C labeling is considerably reduced for these amino acids, when glucose is supplemented in ^{13}C -labeled form to the medium, with isotope dilution being most severe for alanine, and decreasingly important for glutamate/glutamine, aspartate/asparagine, serine, and glycine.

For ^2H -labeling, the situation is further complicated, since deuterated glucose considerably reduces viability of insect cells. We have not systematically tried to adapt insect cells to ^2H -glucose, but initial results were discouraging. Thus, the ^2H incorporation level cannot easily be increased further by the use of deuterated glucose in the medium. This also represents a challenge for increasing deuteration levels using yeast extracts, since protein expression

levels in insect cells decreased considerably using extracts from yeast grown on deuterated glucose and $^3\text{H}_2\text{O}$ as compared to protonated glucose and $^3\text{H}_2\text{O}$.

Of the amino acids that are directly linked to carbohydrate metabolism, alanine is particularly strongly affected by isotope dilution. Incorporation levels of ^{13}C are typically below 30% if unlabeled glucose is used. However, ^{13}C -incorporation levels of alanine can be restored to ~80% for growth on ^{13}C -labeled algal extracts in the presence of unlabeled glucose when cycloserine is added to inhibit the pyruvate-alanine transaminase¹⁵.

Like glucose, glutamine acts as a metabolic precursor for glutamate, aspartate/asparagine as well as alanine and should be added in isotope-labeled form to obtain high labeling efficiencies for these amino acids.

Analysis of isotope incorporation by mass spectrometry

Detailed, quantitative knowledge on the isotope incorporation level of all amino acids is crucial as quality control and as input for strategies to improve labeling efficiencies. Total isotope incorporation of an entire biomolecule is best studied by ESI mass spectrometry, which provides the indiscriminate mass increase due to all ^{15}N , ^{13}C , and ^2H isotopes^{12,6,16}. In principle, atom-specific isotope incorporation levels may be obtained on intact proteins from a careful analysis of J-coupling transfer or splitting effects in NMR spectra^{2,6,16}. In practice, the NMR approach is limited by the spectral resolution and becomes rapidly insensitive for higher molecular weight biomolecules. Acid hydrolysis to single amino acids improves the spectral resolution in NMR³⁴, but still both sensitivity and resolution remain serious problems for the detection of the various isotopologues and isotopomers.

We found that separation of single amino acids by liquid chromatography coupled to mass spectrometry (LC/MS) is the most efficient and sensitive way to determine their isotope composition¹⁶. For this, the free amine groups of amino acid acids are derivatized by phenylisothiocyanate (PITC, Edman's reagent) to phenylthiocarbamyl-amino acids and separated via an HPLC column (Figure 4a) before being injected into an ESI mass spectrometer. The HPLC step separates single amino acids according to their type and also from higher peptides and other compounds. Thus the method can be used to detect single amino acids in crude cellular extracts. Besides cysteine, all amino acids are detectable by this method. The high resolution of modern Fourier transform mass spectrometers (Orbitrap Elite™, Thermofisher) separates the amino acids into individual isotopologues by the distinct mass differences of hydrogen, carbon, and nitrogen isotopes ($\Delta m(^2\text{H}-^1\text{H}) = 1.00628$, $\Delta m(^{13}\text{C}-^{12}\text{C}) = 1.00335$, $\Delta m(^{15}\text{N}-^{14}\text{N}) = 0.99704$). It is thus possible to simultaneously analyze ^2H , ^{13}C and ^{15}N incorporation in a single experiment. Figure 4b shows as an example the separation of phenylthiocarbamyl-histidine into $^2\text{H}_{n_1}^1\text{H}_{n_2}^{15}\text{N}_{n_3}^{14}\text{N}_{n_4}$ isotopologues. The entire analysis of the ^2H , ^{15}N incorporation of the free amino acids present in yeastolate grown on 98% ^{15}N ammonium chloride, 98% $^2\text{H}_2\text{O}$, and protonated glucose is depicted in Figure 4c. For almost all amino acids, the ^{15}N incorporation is around 95%. However, due to the protonated glucose the average ^2H incorporation is only about 70% and varies strongly for the different amino acid types.

The identical analysis can be carried out on acid-hydrolyzed proteins. During the acid hydrolysis asparagine and glutamine are converted to aspartate and glutamate, respectively, whereas tryptophan is destroyed. Typical results are shown in Figure 4d for hydrolyzed GFP expressed in Sf9 insect cells grown on ^2H , ^{15}N -yeastolate and ^{15}N -glutamine. Uniformly high (>85%) ^{15}N incorporation is achieved for all detected amino acids. Conversely, ^2H

incorporation is lower (~60% average) and strongly amino acid-dependent. Consistent with their metabolic reactions within the citric acid cycle, nearly complete protonation is observed for alanine, asparagine/aspartate and glutamine/glutamate. Glycine and methionine are also strongly protonated to about 60–70%. The remaining amino acids show only moderate (~50%, serine, threonine, phenylalanine, tyrosine, proline) to low (<40%, isoleucine, leucine, valine, arginine, lysine, histidine) protonation levels.

Such an analysis has not yet been carried out for expression based on algal extracts, where the starting deuteration level is 98% and higher overall incorporation of ~74% is achieved. The relatively low ^3H incorporation of about half of the amino acids in the yeast extract and the subsequently lower incorporation into the target protein is the result of the protonated glucose used for yeast growth. As indicated before, yeast can be grown on 100% $^3\text{H}_2\text{O}$ and deuterated glucose, but this caused a severe reduction in insect cell growth. It remains to be tested whether a suitable further fractionation of the fully deuterated yeast extract can yield higher deuteration levels. Furthermore, the citric acid cycle clearly causes additional loss of deuteration in insect cells growing in media containing protonated glucose. Suitable inhibitors may reduce this loss to some extent. Current efforts in our groups are directed to clarify these questions.

Costs

Uniform labeling can be achieved using commercial or homemade media for insect cells. Commercial media (BioExpress, Cambridge Isotope Laboratories) remain prohibitively expensive and so far, no deuterated media are available. The commercial labeling media have a very similar composition as standard full media. This allows passaging of insect cells for several times, thereby potentially increasing the isotope incorporation. However, such an approach is presently not affordable. In contrast, the discussed homemade media are cost-optimized by using bulk extracts as the amino acid source instead of purified amino acids. These roughly 10-fold less expensive media are designed for protein expression but not for continuous culture. Therefore they only sustain one or two passages.

Homemade labeling media are based on commercial unlabeled dropout media depleted in individual amino acids or devoid of all amino acid sources and carbohydrates. Such custom media can be presently obtained for about 50–100 € per L, depending on the vendor. For amino acid-type specific backbone or side chain labeling, the total costs comprise this base medium and the labeled target amino acid. In many cases, the costs for the labeled amino acid can be moderate, e.g. ~200 € per L for ^{15}N -valine, ^{15}N leucine, ^{15}N , phenylalanine or [*methyl*- ^{13}C]-methionine, of which ~60–200 mg/L are supplemented. The total costs of homemade media for uniform labeling are dominated by the algal or yeast extracts (Table 2). While the prices for individual components are subject to change, a few general observations can be made.

Obviously, ^{15}N labeling is the cheapest since inexpensive $^{15}\text{NH}_3/^{15}\text{NH}_4\text{Cl}$ can be used as the nitrogen source for algae/yeast. Glutamine is required for strong expression in insect cells and presents a source of isotope scrambling through its metabolism. Commercial prices for $^{15}\text{N}_2$ -labeled glutamine are currently about ~700 €/g, which presents a considerable cost factor if high ^{15}N labeling of all amino acids connected to the glutamine metabolism is desired. The cost for ^{15}N -labeled glutamine may be reduced to negligible levels (≤ 30 €/g) by enzymatic synthesis via ^{15}N -glutamate, which can be produced by glutamate dehydrogenase from ^{15}N -labeled ammonium and 2-oxoglutaric acid³⁵ and subsequently be converted to ^{15}N -glutamine

by glutamine synthetase under the addition of ^{15}N -labeled ammonium³⁶. With this procedure, ^{15}N labeling with homemade yeast extract and ^{15}N -glutamine supplementation is considerably cheaper (~100 €/L) than with commercial algal extract (~500 €/L, Table 2).

As mentioned, insect cells can synthesize glutamine from glutamate and added ammonium. This pathway was exploited by Meola *et al.*¹³ who supplemented the amino acid depleted medium with 10 g/L of commercial labeled yeast extract and 5 mM $^{15}\text{NH}_4\text{Cl}$ or 2 mM glutamine, respectively. No difference was reported for protein expression in stably transfected S2 cells. Sitarska *et al.*¹⁵ confirmed that supplementation of 5 mM $^{15}\text{NH}_4\text{Cl}$ instead of glutamine together with 10 g/L of algal extract did not affect cell growth and viability in Sf cell lines. However, NH_4Cl had an inhibitory effect on virus infection. For optimal expression, insect cells were therefore infected in full medium and transferred only 16 h after infection into labeling medium containing NH_4Cl . In both cases, expression yields were below 25 mg/L for all tested proteins. Using 1 g/L of $^{15}\text{N}_2$ -glutamine as a supplement to yeast extract, Opitz *et al.*¹⁶ reported expression yields ≥ 40 mg/L for several soluble proteins, but the yield dropped below 10% when substituting up to 10 mM NH_4Cl for glutamine. In the latter case, NH_4Cl had been added together with virus and likely inhibited virus entry. Recent ongoing experiments, however, confirm that even when supplying NH_4Cl only 16 h after infection, expression yields are more than two-fold lower compared to the glutamine supplementation.

Compared to ^{15}N -labeling, the additional costs for producing partially deuterated ^{15}N -labeled proteins are relatively small (~500 €/L) for both algal and yeast extracts. Since the additional costs for the yeast extract arise solely from D_2O , they may be reduced substantially by recycling D_2O via distillation. These cost estimates for deuterated yeast extracts are based on the use of protonated glucose, resulting in the mentioned lower overall deuteration of the yeast amino acids and leading to final deuteration levels in insect cell-expressed proteins of ~60% (Figure 4c,d). In contrast, commercial algal extracts have 98% enrichment for all isotopes, including ^3H . However, a significant part of this high deuteration is lost due to the insect cell metabolism, leading to final deuteration levels in insect cell-expressed proteins of $\leq 75\%$, making its impact more limited, unless the unwanted dilution can be suppressed by further improvements of labeling protocols.

Commercial ^{13}C -labeled algal extracts are by-products of ^{13}C -glucose production from algae grown on $^{13}\text{CO}_2$ as the sole carbon source. Thus, they are intrinsically cheaper as a source of ^{13}C -labeled amino acids than yeast grown on ^{13}C -glucose. This is reflected in the costs for ^{13}C , ^{15}N -labeled growth media derived from the two extracts (Table 2), which amount to ~1800 €/L and ~3200 €/L for algal and yeast extracts, respectively. The additional costs for producing partially deuterated ^{13}C , ^{15}N -labeled proteins are again only small for the homemade yeast extract (~450 €/L), but considerably larger for the commercial algal extract (~1400 €/L).

Further improvements may reduce the discussed costs. E.g. roughly double the concentration of amino acids was used for the algal extract media as compared to the yeast extract media. Thus it may be possible to reduce the added amount of either the algal extracts alone or in combination with yeast extract. Furthermore, ^{13}C -glucose dominates the cost of ^{13}C -labeled yeast extracts, which may be reduced to some extent via alternative carbon sources. Finally, bacterial production of glutamine^{37,38} may make this important supplement available in all desired isotope-labeled forms at very low cost.

Conclusion

Eukaryotic expression systems in combination with simple, inexpensive labeling protocols have a great potential to make biologically interesting, but difficult-to-express proteins accessible for NMR analysis. They are relatively easy to apply, since insect cell expression platforms are often already present in neighboring X-ray crystallography or electron microscopy laboratories, which may readily incorporate the described protocols for integrated structural biology projects with NMR. The current labeling procedures may be further improved and enhanced. In particular, it seems possible to (i) further increase deuteration levels via a proper understanding of the isotope dilution and scrambling, (ii) expand the described protocols to mammalian cell cultures, given the similarity between the expression systems. It is also hoped that inexpensive, commercial media for uniform labeling based on algal and yeast extracts will become available in the near future, which may further reduce the effort of isotope labeling in eukaryotic expression hosts.

Acknowledgments

This work was supported by the Swiss National Science Foundation (grants 31-149927 and 31-173089 to S.G.) and the Swiss Cancer League (grant KFS-3603-02-2015 to S.G.). We gratefully acknowledge the Biozentrum's proteomics and biophysics core facilities for expert mass spectrometric analysis as well as Drs. Alexander Schmidt, André Strauss and Binesh Shrestha for stimulating discussions.

Figure Legends

Figure 1: Timeline of the number PDB entries expressed in eukaryotic hosts. The number of these entries structures shows a strong increase over the last 25 years. Half of the structures derive from insect cell expression, with *Spodoptera frugiperda* (Sf9, Sf21) being the most used organism.

Figure 2: Overview of isotope-labeled protein expression in insect cells based on isotope-labeled commercial algal (top) or homemade yeast (bottom) extracts. The principal nitrogen, carbon, and hydrogen sources for the amino acids and their pathways are indicated.

Figure 3: NMR analysis of proteins expressed in isotope-labeled form in insect cells. (a) Comparison of $^1\text{H}^{\text{N}}\text{-}^{15}\text{N}$ residual dipolar couplings (RDCs) obtained experimentally (red) or derived from crystallographic structures (black) of Abelson kinase domain expressed in Sf9 cells and selectively labeled by ^{15}N -FGMY amino acids. Top: complex with imatinib inhibitor, bottom complex with dasatinib inhibitor. The good agreement between experimental solution NMR RDCs and their prediction from the crystal structures indicates that the activation loop adopts a similar conformation in solution as in the crystal for both imatinib (inactive conformation) and dasatinib (active conformation). Data replotted from Vajpai et al.³ (b) ^1H - ^{15}N -TROSY spectra of detergent-solubilized β_1 -adrenergic receptor expressed in Sf9 cells and selectively labeled by ^{15}N -valine. Differences in the spectra of the complexes with the agonist isoprenaline (red) and the antagonist atenolol (blue) indicate allosteric signal transmission from the ligand binding site (V172) to the G protein binding site (V226). Data replotted from Isogai et al.⁷ (c) ^1H , ^{15}N -TROSY spectrum (600 MHz, 308 K) of ^2H , ^{15}N -labeled CCR5 solubilized in n-dodecyl- β -D-maltopyranoside. ^2H , ^{15}N -labeled CCR5 was expressed in Sf9 cells grown on ^2H , ^{15}N -yeastolate and $^{14}\text{N}_2$ -glutamine. (d) Determination of average ^{15}N T_1 and T_2 relaxation times of ^2H , ^{15}N -labeled CCR5 (900 MHz, other conditions as panel (c)). The relaxation times are determined from the intensity ratios of one-dimensional, ^1H projections of standard ^1H - ^{15}N -edited ^{15}N relaxation experiments carried out at two different relaxation delays Δ .

Figure 4: LC/MS analysis of isotope content of individual amino acids in yeast extracts and proteins. (a) HPLC separation of amino acids obtained by PITC derivatization of a ^2H , ^{15}N -labeled yeast extract. Peaks are annotated by the corresponding amino acid. The derivatized amino acids were separated by HPLC (Agilent) using a Phenomenex Kinetex XB-C18 column (75 mm x 4.6 mm, 2.6 μm , 100 \AA) with a buffer gradient from 0.05% formic acid (FA)/water to 0.05% FA/100% acetonitrile at 50°C and detected by UV absorbance at 254 nm. (b) LC/MS spectrum of histidine obtained by acid hydrolysis of ^2H , ^{15}N -GFP. The different $^2\text{H}_n\text{H}_m\text{N}_3\text{N}_4$ isotopologues are indicated. The protein hydrolysate was derivatized by PITC and then separated on an EASY-nLC™ nano-HPLC system

(ThermoFisher) coupled to an Orbitrap Elite™ (ThermoFisher) mass spectrometer. HPLC separation was performed at room temperature using a silica (ReproSil-Pur 120 C18-AQ) self-packed column (150 mm x 75 µm, 1.9 µm, 120 Å) with a buffer gradient from 0.05% FA/water to 0.05% FA/80% acetonitrile. **(c)** $^2\text{H},^{15}\text{N}$ incorporation of individual amino acids of autolysed $^2\text{H},^{15}\text{N}$ -labeled yeast obtained by the LC/MS protocol described in **(b)**. The yeast had been grown on ^{15}N ammonium, D_2O , and protonated glucose. Due to the mild autolysis conditions, all amino remain intact, but cysteine is lost during PITC derivatization. **(d)** $^2\text{H},^{15}\text{N}$ incorporation of individual amino acids obtained from acid-hydrolyzed GFP expressed in Sf9 cells using $^2\text{H},^{15}\text{N}$ -labeled yeast extract supplemented by $^{15}\text{N}_2$ -glutamine. The same LC/MS protocol as in **(b)** was used. During the acid hydrolysis of the protein, asparagine and glutamine are converted to aspartate and glutamate, respectively, and tryptophan is degraded to undetected compounds.

Tables

Table 1: Protein structures obtained from samples produced in different expression hosts queried from the Protein Data Bank (PDB) (12/2017). Structures have been filtered for size (>100 kDa), human origin as well as G protein-coupled receptors (GPCRs).

	All structures	>100 kDa	Human	GPCRs
Total	135359 (100.0 ^a)	29791 (100.0)	37859 (100.0)	220 (100.0)
Bacterial^b	99765 (73.7)	21639 (72.6)	27169 (71.8)	18 (8.2)
Yeast^c	2353 (1.7)	582 (2.0)	1052 (2.8)	3 (1.4)
Insect^d	5811 (4.3)	2174 (7.3)	3945 (10.4)	155 (70.5)
Mammalian^e	3093 (2.3)	1190 (4.0)	2062 (5.4)	19 (8.6)

^a in percent

^b *E. coli*

^c *P. pastoris*, *S. pombe* and *S. cerevisiae*

^d *S. frugiperda*, *T. ni* and *D. melanogaster*

^e *H. sapiens*, *M. musculus* and *C. griseus*

Table 2: Costs (in €) for uniform isotope labeling in insect cells per liter of growth medium.

	Amount/L	¹⁵ N	² H, ¹⁵ N	¹³ C, ¹⁵ N	² H, ¹³ C, ¹⁵ N	
Algal extract	Commercial AE ^a	10 g	465	925	1150	2575
	¹⁵ NH ₄ Cl ^b	250 mg	4	4	4	4
	Tryptophan ^c	20 mg	42	100	250	250
	¹³ C ₆ -Glucose ^{d,e}	5 g			400	400
	Total AE		511	1029	1804	3229
Yeast extract	¹³ C ₆ -Glucose for YE ^{e,f}	33.3 g			2667	2667
	¹⁵ NH ₄ Cl for YE ^b	5.2 g	73	73	73	73
	D ₂ O for YE ^g	1 L		448		448
	¹⁵ N ₂ -Glutamine ^h	1 g	30	30	30	30
	¹³ C ₆ -Glucose ^{d,e}	5 g			400	400
	Total YE		103	551	3170	3618

^a Prices for ISOGRO algal extract (AE, Sigma-Aldrich) with the respective isotope labeling pattern at 98% incorporation. A 50% quantity discount on list prices is used, which was obtained when ordering material for 5 L of insect cell medium in 2017.

^b Assuming a price of 14 €/g

^c Current catalogue prices

^d Labeled glucose is added for obtaining higher incorporation of ¹³C for amino acids linked to carbohydrate metabolism (see text).

^e Assuming a price of 80 €/g

^f Cost of isotope labeled substrates for producing the amount of yeast extract (YE, 8 g) required for 1 L of insect cell medium. No costs for work or equipment are included. For reasons described in the text non-deuterated glucose is used for ²H labeling. Using deuterated glucose would result in considerably higher costs for ²H, ¹⁵N and ²H, ¹³C, ¹⁵N labeling.

^g Assuming a price of 370 €/L. Costs can be reduced by recycling D₂O.

^h Costs of homemade glutamine are assumed as 30 €/g, using the enzymatic reactions described in the main text. For all labeling patterns, only ¹⁵N₂-labeled glutamine was used. Commercial prices are considerably higher, e.g. ~700 €/g for ¹⁵N₂-labeled glutamine.

References

1. Strauss, A., Bitsch, F., Cutting, B., Fendrich, G., Graff, P., Liebetanz, J., Zurini, M. & Jahnke, W. Amino-acid-type selective isotope labeling of proteins expressed in Baculovirus-infected insect cells useful for NMR studies. *Journal of Biomolecular NMR* **26**, 367-372 (2003).
2. Strauss, A., Bitsch, F., Fendrich, G., Graff, P., Knecht, R., Meyhack, B. & Jahnke, W. Efficient uniform isotope labeling of Abl kinase expressed in Baculovirus-infected insect cells. *Journal of Biomolecular NMR* **31**, 343-349 (2005).
3. Vajpai, N., Strauss, A., Fendrich, G., Cowan-Jacob, S.W., Manley, P.W., Grzesiek, S. & Jahnke, W. Solution conformations and dynamics of ABL kinase-inhibitor complexes determined by NMR substantiate the different binding modes of imatinib/nilotinib and dasatinib. *Journal of Biological Chemistry* **283**, 18292-18302 (2008).
4. Kofuku, Y., Ueda, T., Okude, J., Shiraishi, Y., Kondo, K., Maeda, M., Tsujishita, H. & Shimada, I. Efficacy of the β 2-adrenergic receptor is determined by conformational equilibrium in the transmembrane region. *Nature Communications* **3**, 1045 (2012).
5. Nygaard, R., Zou, Y., Dror, R.O., Mildorf, T.J., Arlow, D.H., Manglik, A., Pan, A.C., Liu, C.W., Fung, J.J., Bokoch, M.P., Thian, F.S., Kobilka, T.S., Shaw, D.E., Mueller, L., Prosser, R.S. & Kobilka, B.K. The dynamic process of β 2-adrenergic receptor activation. *Cell* **152**, 532-542 (2013).
6. Kofuku, Y., Ueda, T., Okude, J., Shiraishi, Y., Kondo, K., Mizumura, T., Suzuki, S. & Shimada, I. Functional dynamics of deuterated β 2-adrenergic receptor in lipid bilayers revealed by NMR spectroscopy. *Angewandte Chemie International Edition in English* **53**, 13376-13379 (2014).
7. Isogai, S., Deupi, X., Opitz, C., Heydenreich, F.M., Tsai, C.-J., Brueckner, F., Schertler, G.F.X., Veprintsev, D.B. & Grzesiek, S. Backbone NMR reveals allosteric signal transduction networks in the β 1-adrenergic receptor. *Nature* **530**, 237-241 (2016).
8. Brüggert, M., Rehm, T., Shanker, S., Georgescu, J. & Holak, T.A. A novel medium for expression of proteins selectively labeled with ^{15}N -amino acids in *Spodoptera frugiperda* (Sf9) insect cells. *Journal of Biomolecular NMR* **25**, 335-348 (2003).
9. Egorova-Zachernyuk, T.A., Bosman, G.J.C.G.M., Pistorius, A.M.A. & DeGrip, W.J. Production of yeastolates for uniform stable isotope labelling in eukaryotic cell culture. *Applied Microbiology and Biotechnology* **84**, 575-581 (2009).
10. Egorova-Zachernyuk, T.A., Bosman, G.J.C.G.M., DeGrip, W.J. & Shvets, V.I. Stable isotope labelling of human histamine receptor H1R: prospects for structure-based drug design. *Doklady Biochemistry and Biophysics* **433**, 164-167 (2010).
11. Gossert, A.D., Hinniger, A., Gutmann, S., Jahnke, W., Strauss, A. & Fernández, C. A simple protocol for amino acid type selective isotope labeling in insect cells with improved yields and high reproducibility. *Journal of Biomolecular NMR* **51**, 449-456 (2011).
12. Saxena, K., Dutta, A., Klein-Seetharaman, J. & Schwalbe, H. Isotope labeling in insect cells. *Methods in Molecular Biology* **831**, 37-54 (2012).
13. Meola, A., Deville, C., Jeffers, S.A., Guardado-Calvo, P., Vasiliauskaite, I., Sizun, C., Girard-Blanc, C., Malosse, C., van Heijenoort, C., Chamot-Rooke, J., Krey, T., Guittet, E., Pêtres, S., Rey, F.A. & Bontems, F. Robust and low cost uniform ^{15}N -labeling of proteins expressed in *Drosophila* S2 cells and *Spodoptera frugiperda* Sf9 cells for NMR applications. *Journal of Structural Biology* **188**, 71-78 (2014).
14. Skora, L., Shrestha, B. & Gossert, A.D. Chapter Eleven - Isotope Labeling of Proteins

- in Insect Cells. in *Methods in Enzymology*, Vol. 565 (ed. Kelman, Z.) 245-288 (Academic Press, 2015).
15. Sitarska, A., Skora, L., Klopp, J., Roest, S., Fernández, C., Shrestha, B. & Gossert, A.D. Affordable uniform isotope labeling with ²H, ¹³C and ¹⁵N in insect cells. *Journal of Biomolecular NMR* **62**, 191-197 (2015).
 16. Opitz, C., Isogai, S. & Grzesiek, S. An economic approach to efficient isotope labeling in insect cells using homemade ¹⁵N-, ¹³C- and ²H-labeled yeast extracts. *Journal of Biomolecular NMR* **62**, 373-385 (2015).
 17. Zhang, Y., Wei, H., Xie, D., Calambur, D., Douglas, A., Gao, M., Marsilio, F., Metzler, W.J., Szapiel, N., Zhang, P., Witmer, M.R., Mueller, L. & Hedin, D. An improved protocol for amino acid type-selective isotope labeling in insect cells. *Journal of Biomolecular NMR* **68**, 237-247 (2017).
 18. Smith, G.E., Summers, M.D. & Fraser, M.J. Production of human beta interferon in insect cells infected with a baculovirus expression vector. *Molecular and Cellular Biology* **3**, 2156-2165 (1983).
 19. Kelly, D.C. Baculovirus Replication. *Journal of General Virology* **63**, 1-13 (1982).
 20. Berger, I., Fitzgerald, D.J. & Richmond, T.J. Baculovirus expression system for heterologous multiprotein complexes. *Nature Biotechnology* **22**, 1583-1587 (2004).
 21. Luckow, V.A., Lee, S.C., Barry, G.F. & Olins, P.O. Efficient generation of infectious recombinant baculoviruses by site-specific transposon-mediated insertion of foreign genes into a baculovirus genome propagated in *Escherichia coli*. *Journal of Virology* **67**, 4566-4579 (1993).
 22. Possee, R.D., Hitchman, R.B., Richards, K.S., Mann, S.G., Siaterli, E., Nixon, C.P., Irving, H., Assenberg, R., Alderton, D., Owens, R.J. & King, L.A. Generation of baculovirus vectors for the high-throughput production of proteins in insect cells. *Biotechnology and Bioengineering* **101**, 1115-1122 (2008).
 23. Wasilko, D.J., Edward Lee, S., Stutzman-Engwall, K.J., Reitz, B.A., Emmons, T.L., Mathis, K.J., Bienkowski, M.J., Tomasselli, A.G. & Fischer, D.H. The titerless infected-cells preservation and scale-up (TIPS) method for large-scale production of NO-sensitive human soluble guanylate cyclase (sGC) from insect cells infected with recombinant baculovirus. *Protein Expression and Purification* **65**, 122-132 (2009).
 24. Vaughn, J.L., Goodwin, R.H., Tompkins, G.J. & McCawley, P. The establishment of two cell lines from the insect *Spodoptera frugiperda* (Lepidoptera; Noctuidae). *In Vitro* **13**, 213-217 (1977).
 25. Hink, W.F. Established insect cell line from the cabbage looper, *Trichoplusia ni*. *Nature* **226**, 466-467 (1970).
 26. O'Reilly, D.R., Miller, L.K. & Luckow, V.A. *Baculovirus expression vectors: a laboratory manual*, (Oxford University Press, 1994).
 27. Huang, J.-R., Craggs, T.D., Christodoulou, J. & Jackson, S.E. Stable intermediate states and high energy barriers in the unfolding of GFP. *Journal of Molecular Biology* **370**, 356-371 (2007).
 28. Vajpai, N., Strauss, A., Fendrich, G., Cowan-Jacob, S.W., Manley, P.W., Jahnke, W. & Grzesiek, S. Backbone NMR resonance assignment of the Abelson kinase domain in complex with imatinib. *Biomolecular NMR Assignments* **2**, 41-42 (2008).
 29. Sprangers, R., Velyvis, A. & Kay, L. Solution NMR of supramolecular complexes: providing new insights into function. *Nature Methods* **4**, 697-703 (2007).
 30. Solt, A.S., Bostock, M.J., Shrestha, B., Kumar, P., Warne, T., Tate, C.G. & Nietlispach, D. Insight into partial agonism by observing multiple equilibria for ligand-bound and Gs-mimetic nanobody-bound β 1-adrenergic receptor. *Nature Communications* **8**, 1795 (2017).

31. Okude, J., Ueda, T., Kofuku, Y., Sato, M., Nobuyama, N., Kondo, K., Shiraishi, Y., Mizumura, T., Onishi, K., Natsume, M., Maeda, M., Tsujishita, H., Kuranaga, T., Inoue, M. & Shimada, I. Identification of a Conformational Equilibrium That Determines the Efficacy and Functional Selectivity of the μ -Opioid Receptor. *Angewandte Chemie International Edition in English* **54**, 15771-15776 (2015).
32. Ugwu, C.U., Aoyagi, H. & Uchiyama, H. Photobioreactors for mass cultivation of algae. *Bioresource Technology* **99**, 4021-4028 (2008).
33. Rosen, M.K., Gardner, K.H., Willis, R.C., Parris, W.E., Pawson, T. & Kay, L.E. Selective methyl group protonation of perdeuterated proteins. *Journal of Molecular Biology* **263**, 627-636 (1996).
34. Hochuli, M., Szyperski, T. & Wuthrich, K. Deuterium isotope effects on the central carbon metabolism of *Escherichia coli* cells grown on a D₂O-containing minimal medium. *Journal of Biomolecular NMR* **17**, 33-42 (2000).
35. Kragl, U., Gödde, A., Wandrey, C., Kinzy, W., Cappon, J. & Lugtenburg, J. Repetitive batch as an efficient method for preparative-scale enzymatic-synthesis of 5-azido-neuraminic acid and N¹⁵-L-glutamic acid. *Tetrahedron: Asymmetry* **4**, 1193-1202 (1993).
36. Hansen, A.P., Petros, A.M., Mazar, A.P., Pederson, T.M., Rueter, A. & Fesik, S.W. A practical method for uniform isotopic labeling of recombinant proteins in mammalian cells. *Biochemistry* **31**, 12713-12718 (1992).
37. Kusumoto, I. Industrial production of L-glutamine. *Journal of Nutrition* **131**, 2552S-5S (2001).
38. Li, J., Ma, C., Ma, Y., Li, Y., Zhou, W. & Xu, P. Medium optimization by combination of response surface methodology and desirability function: an application in glutamine production. *Applied Microbiology and Biotechnology* **74**, 563-571 (2007).

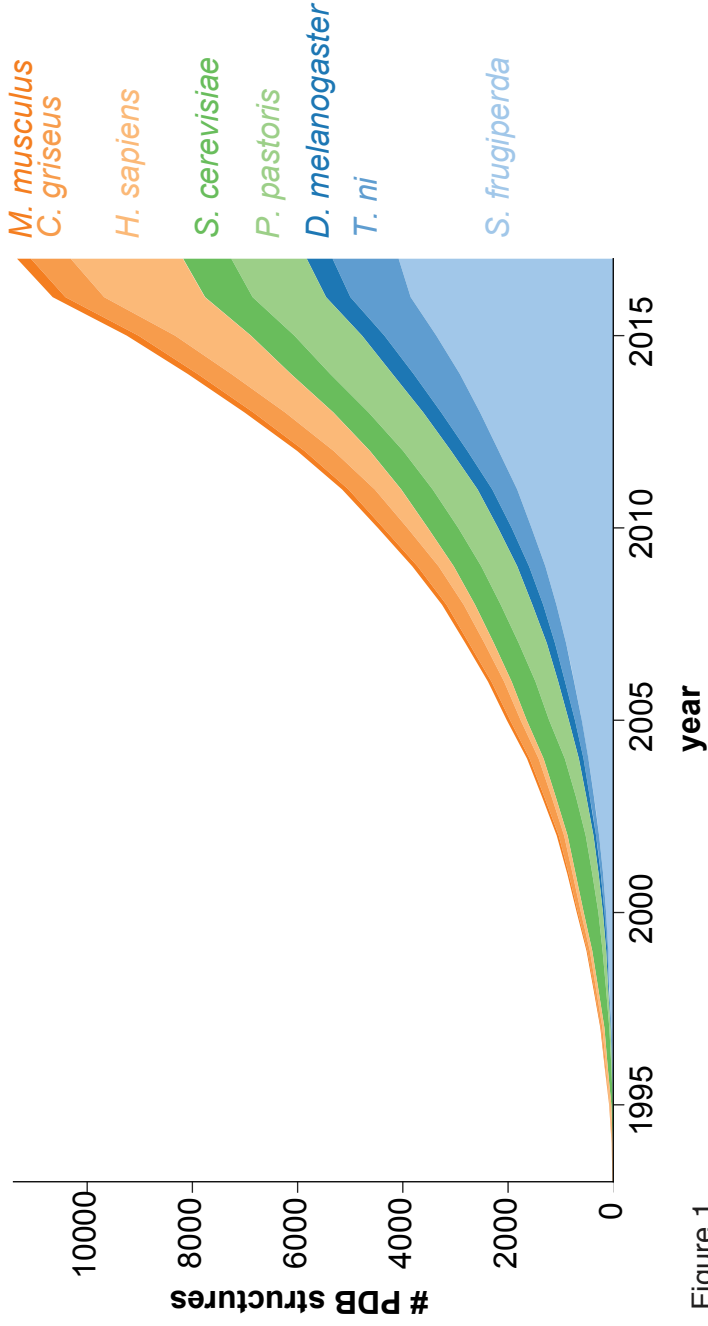


Figure 1

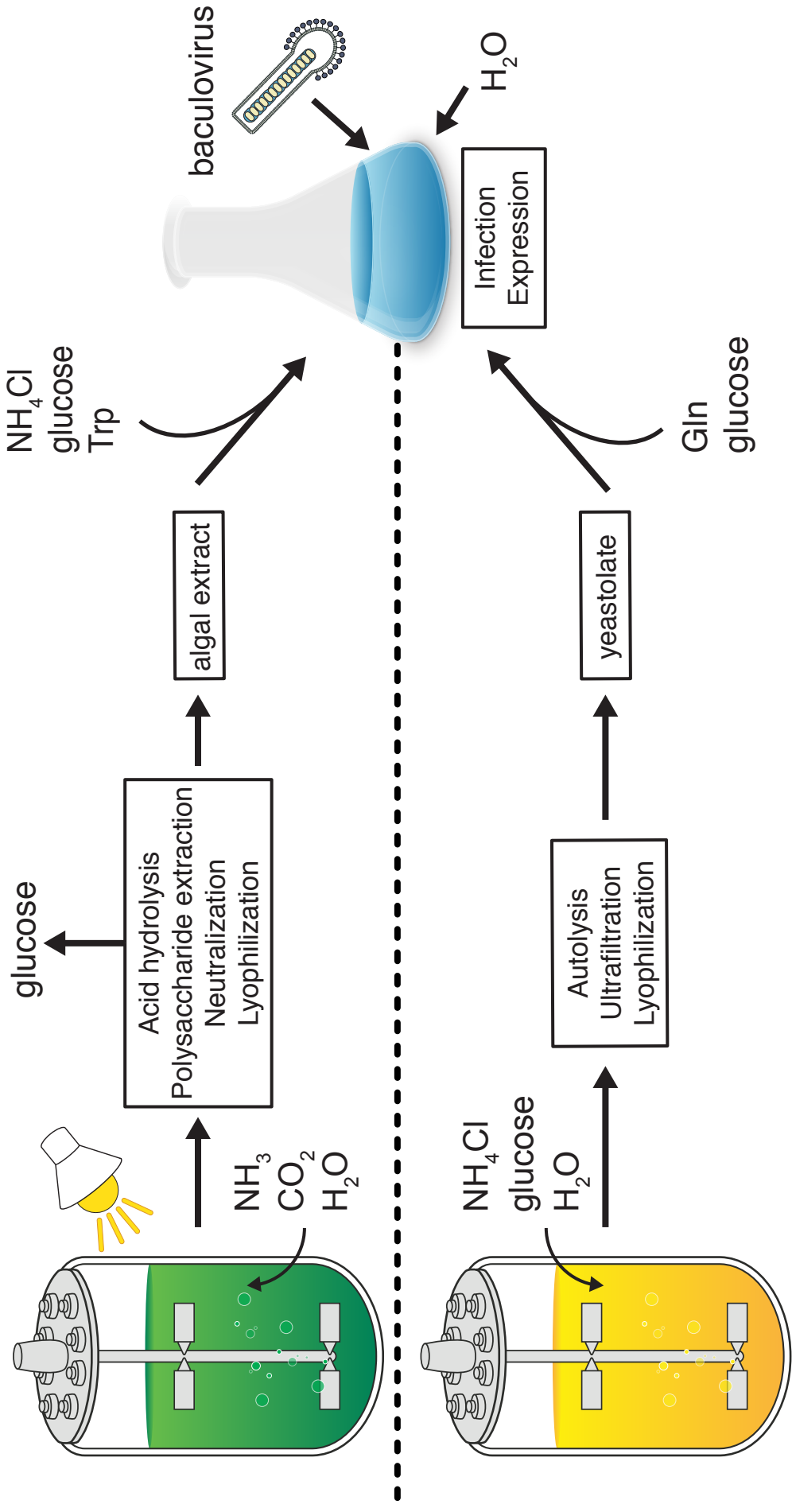


Figure 2

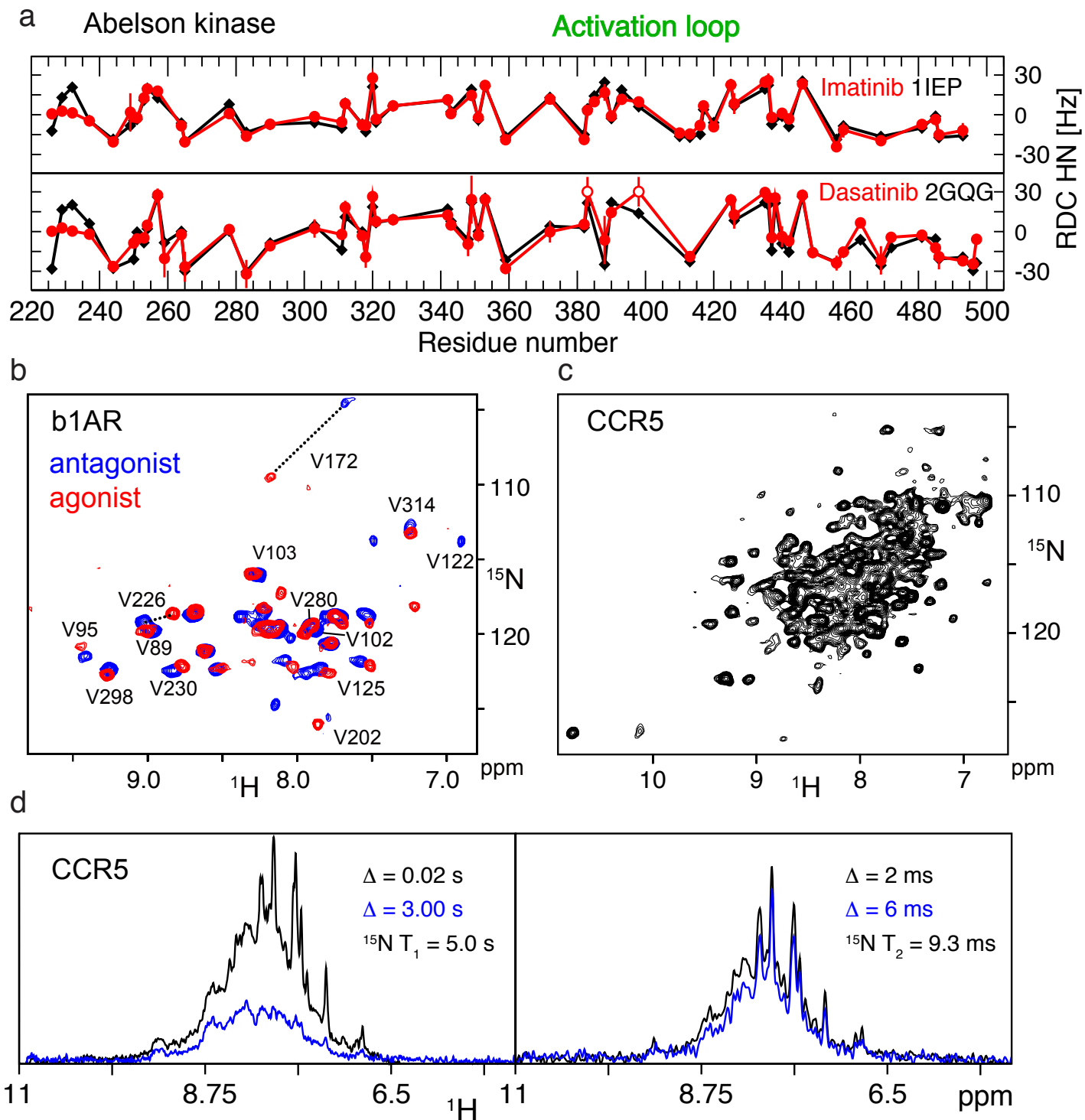


Figure 3

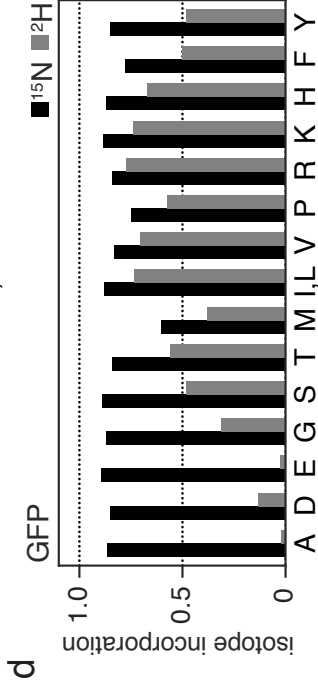
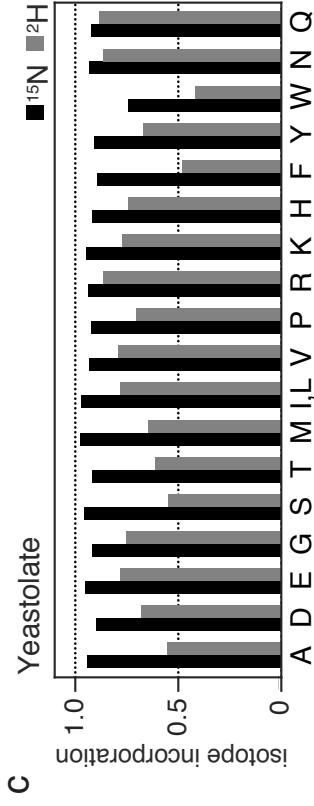
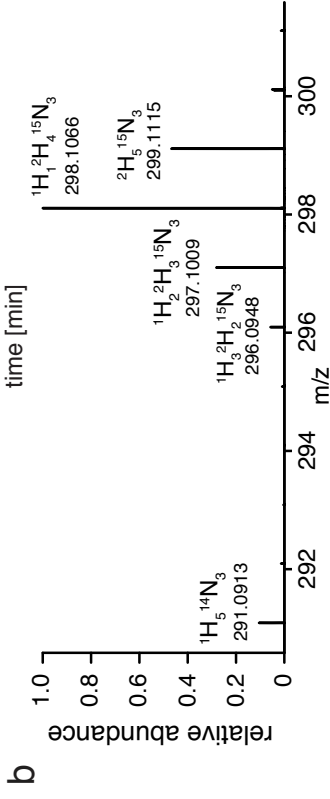
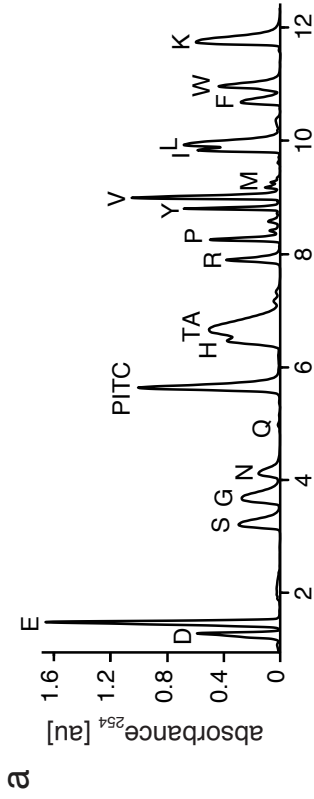


Figure 4

5 Detergent and heparin disaccharide interactions of 5P12-RANTES-E66S

Introduction

Previous structural characterizations of wild-type RANTES were mostly carried out at low pH, because it heavily aggregates at $\text{pH} \geq 4.0$ (233). These aggregates consist of long, oligomeric structures, which are stabilized by the interaction with glycosaminoglycan (234). The linear oligomers are formed from monomeric RANTES by two distinct interactions. While an intermolecular β -sheet is formed between the N-termini of two monomers providing the dimerization interface, higher oligomerization occurs by the interactions of the second β -sheet of one monomer with the C-terminal α -helix of a monomer from another dimer. Introduction of the C-terminal E66S mutation (235) suppresses this higher oligomerization (236). RANTES-E66S still exists in a pH-, temperature and concentration-dependent monomer-dimer equilibrium (237). RANTES-E66S retains CCR5 binding and G_i -dependent signaling, but loses the ability for leukocyte activation and migration through protein tyrosine kinase activation (171). The RANTES analog 5P12-RANTES shows very promising features as microbicide for HIV-1 prevention (167, 219). The non-aggregating mutant 5P12-RANTES-E66S was previously characterized by NMR (238). The core structure is preserved, but 5P12-RANTES-E66S comprises a more flexible N-terminus. The N-terminal intermolecular β -sheet is disturbed due to mutations, and the protein is monomeric.

Albeit the interaction of CCR5 with RANTES is less pH-sensitive than for other GPCR-ligand complexes, the complex still dissociates at a pH lower than 4 (239). The physiological interaction occurs in the extracellular space at pH 7.4. For this reason, the following chapter describes the characterization of 5P12-RANTES-E66S at this physiological pH.

Results

NMR characterization of 5P12-RANTES-E66S at pH 7.5

The ^1H - ^{15}N HSQC spectrum of ^2H , ^{15}N -labeled 5P12-RANTES-E66S at 310 K and pH 3.8 is well dispersed, characteristic for β -sheet secondary structures, and all 63 observable backbone resonances (sequence contains 5 prolines) were detected (Figure 5.1a). At the increased pH of 7.5, only 42 peaks were observed (Figure 5.1b) due to fast amide exchange with water. Lowering the temperature to 298 K led to the appearance of 6 additional resonances (Figure 5.1c). Resonance assignment was obtained using standard 3D experiments (HNCO, HNCA, HNCACB). Resonances affected by fast amide exchange with water are located in less stable secondary elements like the flexible N-terminus, but also in the N-loop, 30s-loop, 40s-loop and at the start of the C-terminal α -helix (Figure 5.1d, e). Significant chemical shift changes between pH 3.8 and 7.5 occur only for a few resonances in the first β -sheet, which might be caused by their ionizable side chains. The overall fold of 5P12-RANTES-E66S is not affected by the increase in pH.

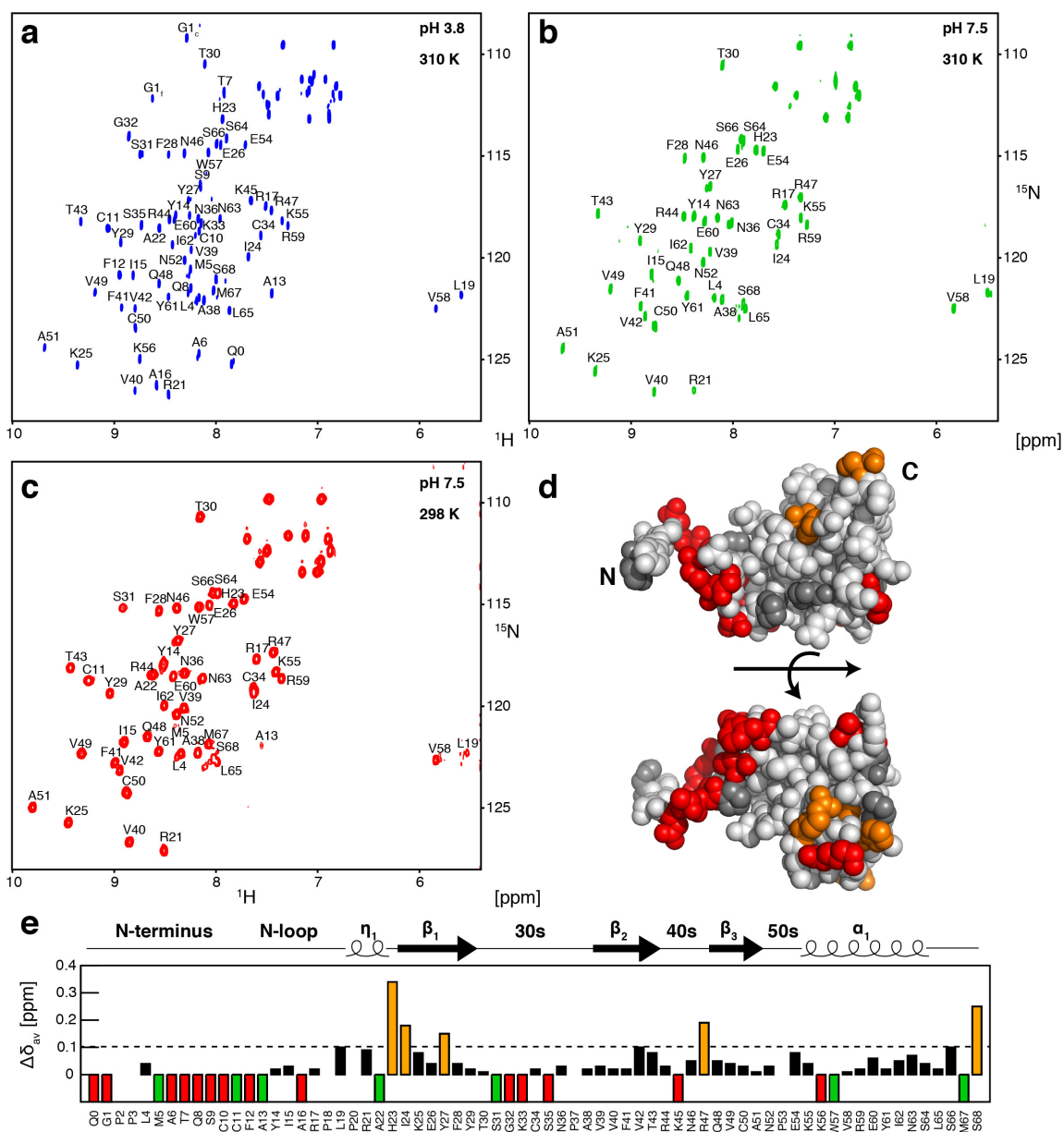


Figure 5.1 Effect of pH and temperature on ^1H - ^{15}N HSQC spectrum of 5P12-RANTES-E66S on a 900 MHz spectrometer. Backbone amide resonances are labeled with the assignments. The N-terminal glutamine Q0 is cyclized to pyroglutamate (238). The resonances G1_f and G1_c correspond to the free and cyclized N-terminus. Spectra of 50 μM ^2H , ^{15}N -labeled 5P12-RANTES-E66S were recorded at 310 K with (a) pH 3.8 and (b) pH 7.5 or (c) at 298 K with pH 7.5. (d) Weighted chemical shift differences $\Delta\delta_{av} = [\Delta\delta_H^2 + (\Delta\delta_N/5)^2]^{1/2}$ for 5P12-RANTES-E66S at pH 7.5 relative to pH 3.8. Significantly perturbed residues ($\Delta\delta_{av} > 0.1$ ppm) are marked in orange. Resonances not observable at pH 7.5 are highlighted in red and resonances detected only at 298 K are shown in green. Prolines without observable ^1H - ^{15}N resonance are left blank. (e) Surface representation of a RANTES monomer (1B3A, chain A). Residues, for which no resonances can be observed at pH 7.5, are depicted in red. Resonances significantly perturbed upon change from pH 3.8 to pH 7.5 are highlighted in orange according to panel c. Prolines are depicted in dark grey.

Interaction of 5P12-RANTES-E66S with the detergent micelle

To make CCR5 accessible for interaction studies with 5P12-RANTES-E66S by solution NMR, the receptor must be solubilized in detergent. However, it was shown previously that

RANTES-E66S and 5P12-RANTES-E66S also interact with detergent micelles, leading to inconclusive results in the interaction studies with CCR5 (240, 241). The detergent fos-choline-12 (FC-12) disturbed the secondary structure of 5P12-RANTES-E66S, whereas maltoside detergents such as DDM showed a much weaker effect. The increase of the pH from 3.8 to 6.0 alleviated the detergent effect.

To investigate the effect of DDM or mixed DDM/CHS micelles as used for the reconstitution of CCR5 (Chapter 4.1), HSQC spectra of 5P12-RANTES-E66S in the absence and presence of detergent were recorded at pH 7.5 (Figure 5.2a, b). No significant chemical shift changes were observed, which indicates that the structure of 5P12-RANTES-E66S is not perturbed by the presence of these detergents. As minor effects, the resonance of glycine 1 became observable, and also the signal intensity of further resonances increased (Figure 5.2c). Mapping the intensity changes onto the structure of RANTES (Figure 5.2d) revealed that mainly residues in the N-terminus and N-loop are affected. In these regions, fast amide exchange with water at pH 7.5 was observed in the detergent-free case. Apparently, the presence of detergent decreases this exchange. The effect was stronger for mixed DDM/CHS micelles, but it was not further investigated whether it arises from the higher concentration of micelles used in the experiment or by a specific contribution from CHS.

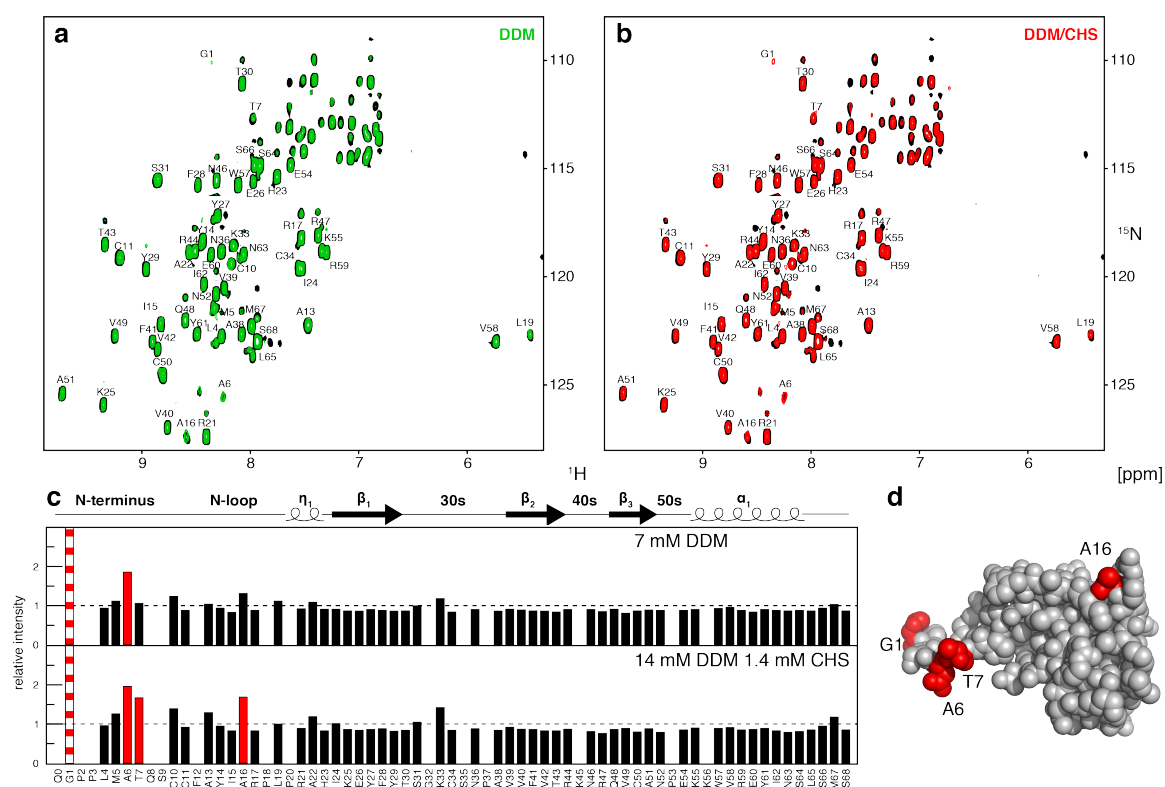


Figure 5.2 Interaction of 5P12-RANTES-E66S with DDM or mixed DDM/CHS micelles. The ^1H - ^{15}N TROSY spectrum of $50\ \mu\text{M}$ ^2H , ^{15}N -labeled 5P12-RANTES-E66S recorded at 298 K on a 900 MHz spectrometer is shown in black. **(a)** Spectra after the addition of 7 mM DDM are shown in green or **(b)** of 14 mM DDM/1.4 mM CHS in red. **(c)** Intensities of 5P12-RANTES-E66S backbone resonances in the presence of detergent relative to the ones without. Residues with significantly increased intensities upon addition of detergent micelles are marked in red. The resonance G1 was only observed in the presence of detergent and is marked with red stripes. Residues without observable ^1H - ^{15}N resonance are not shown. **(d)** Intensity changes due to detergent mapped onto the RANTES surface (1B3A, chain A). Strongly affected residues are highlighted in red according to panel c.

Interaction of 5P12-RANTES-E66S with heparin disaccharide

Besides the binding to chemokine receptors, the interaction with glycosaminoglycan is fundamental for the biological function of RANTES (167). Glycosaminoglycans are long, linear, sulfated saccharides and RANTES shows a high affinity for heparin, a highly charged glycosaminoglycan (242). Short-chain heparin saccharides allow the analysis in solution whereas RANTES aggregates upon addition of longer saccharides (243). The complex structure of dimeric RANTES with heparin disaccharide I-S was solved by crystallography (244). We wanted to test whether the physiologically relevant glycosaminoglycan interaction can also be observed with monomeric 5P12-RANTES-E66S.

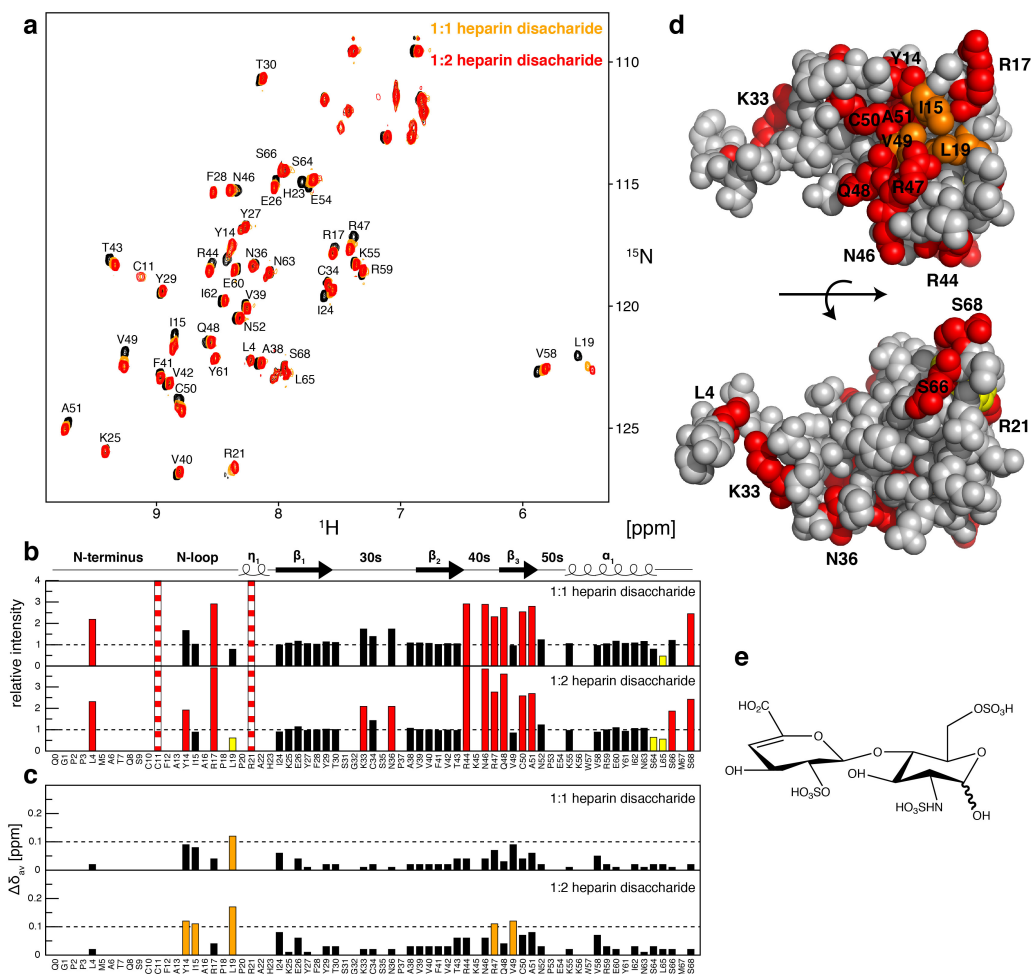


Figure 5.3 Heparin disaccharide I-S induced changes on 5P12-RANTES-E66S. **(a)** ^1H - ^{15}N HSQC spectrum of $50\ \mu\text{M}$ ^2H , ^{15}N -labeled 5P12-RANTES-E66S recorded at 310 K on a 600 MHz spectrometer is shown in black. Addition of 1:1 or 2:1 molar amount heparin disaccharide I-S is shown in orange or red, respectively. The resonances for H23 and E54 were not analyzed because the assignment upon titration of heparin disaccharide I-S is ambiguous. **(b)** Intensities of 5P12-RANTES-E66S backbone resonances in the presence of heparin disaccharide I-S relative to the ones without. Residues with significantly increased intensities upon addition of heparin are marked in red and decreased ones in yellow. The resonances of C11 and R21 appeared only in the presence of heparin disaccharide and are marked with red stripes. Residues without observable ^1H - ^{15}N resonance are not shown. **(c)** Weighted chemical shift differences between 5P12-RANTES-E66S in the presence and absence of heparin disaccharide I-S. Significantly perturbed residues ($\Delta\delta_{av} > 0.1$ ppm) are marked in orange. **(d)** 5P12-RANTES-E66S residues perturbed by heparin disaccharide are mapped on the RANTES surface (1B3A, chain A), colored according to panels **b** and **c**. **(e)** Chemical structure of heparin disaccharide I-S.

The HSQC spectrum of 5P12-RANTES-E66S (Figure 5.3a) showed changes upon addition of 1:1 or 2:1 molar amounts of heparin disaccharide I-S (Figure 5.3e). Several residues experienced a change in signal intensity (Figure 5.3b) or chemical shift (Figure 5.3c). An extended interaction surface can be mapped on the chemokine structure mostly comprising the N-loop, 40s-loop and the third β -strand (Figure 5.3d). Significant changes were observed for R44, N46 and R47 (K45 is not observable in the spectrum). The residues of the BXBB motif (R44-R47) in the 40s-loop are essential for high-affinity RANTES glycosaminoglycan interaction (244, 245). The 40s-loop is also important for the high-affinity interaction with CCR5 (237, 246). Residues C11, Y14, I15 R17, and R21 were also affected by the presence of heparin disaccharide. These N-loop residues, in particular R17, have also been shown to be a second binding epitope for glycosaminoglycan (243). As a caveat it needs to be mentioned that the experiments were conducted in the absence of salt. Thus, the interaction may be weakened at physiological salt concentrations

Conclusions and perspectives

In this chapter, NMR studies on 5P12-RANTES-E66S at physiological pH 7.5 were described. Resonances of the N-terminus and loops are not observable due to the fast exchange of the amide protons with water. In contrast to previous studies with FC-12 (238), DDM micelles had no effect on the 5P12-RANTES-E66S structure. However, the amide exchange for the 5P12-RANTES-E66S N-terminus is reduced in the presence of detergents.

The interaction of the monomeric RANTES analog with heparin disaccharide can be measured at physiological pH and may serve as model for the general RANTES glycosaminoglycan interaction. The sulfated disaccharide interacts mostly with two basic patches on the 5P12-RANTES-E66S surface. The regions overlap with the binding surface for the chemokine receptor CCR5 (191, 237).

Further detailed studies of the RANTES glycosaminoglycan interaction should be interesting for several reasons. The interaction is essential for immobilizing RANTES at inflammatory sites and to present the chemokine for recognition by CCR5. The transition from the oligomeric state, stabilized by the glycosaminoglycan, to the CCR5-bound chemokine monomer is not well understood. Furthermore, a glycosaminoglycan-bound form of 5P12-RANTES is being proposed for long-term drug delivery of this microbicide (247).

Materials and Methods

Expression and purification

^{15}N -, ^2H , ^{15}N - or ^2H , ^{13}C , ^{15}N ,-labeled 5P12-RANTES-E66S was expressed and purified as described previously (237, 238). The N-terminal glutamate residue was cyclized to pyroglutamate at 37 °C for ~24 h in 100 mM NaH_2PO_4 (pH 6.0).

NMR experiments and data analysis

For assignment, NMR samples of 50 μM 5P12-RANTES-E66S were prepared in 25 mM HEPES (pH 7.5) or 25 mM NaH_2PO_4 (pH 3.8) with 5 % D_2O and 0.02 % NaN_3 . All NMR experiments were performed on Bruker AVANCE 600 MHz or 900 MHz spectrometers equipped with a TCI cryoprobe at a temperature of 298 K or 310 K (the temperature used for each experiment is indicated in the respective figure caption). Resonances of ^{13}C , ^{15}N -labeled

5P12-RANTES-E66S were assigned using HNCACB, HNCO and HNCA spectra at 298 K. All NMR spectra were processed with NMRPipe (204) and analyzed with SPARKY (205) or PIPP (231).

For characterizing the interaction with the detergent, ^1H - ^{15}N TROSY experiments were recorded on 70 μM ^2H , ^{15}N -labeled 5P12-RANTES-E66S in 25 mM HEPES (pH 7.5), 150 mM NaCl with 5 % D_2O and 0.02 % NaN_3 at 298 K on a 900 MHz spectrometer. Detergent micelles were added from stock solutions (10 % DDM or 10 % DDM, 2 % CHS) to final concentrations of 0.35 % (7 mM) DDM or 0.7 % (14 mM) DDM/0.07 % (1.4 mM) CHS.

For characterizing the interaction with heparin disaccharide I-S, ^1H - ^{15}N HSQC experiments were recorded on 70 μM ^{15}N -labeled 5P12-RANTES-E66S in 25 mM HEPES (pH 7.5) with 5 % D_2O and 0.02 % NaN_3 at 310 K on 600 MHz spectrometer. Heparin disaccharide I-S (Dextra Laboratories Ltd) was added as 1:1 or 2:1 equimolar amounts relative to 5P12-RANTES-E66S.

6 Interaction of 5P12-RANTES-E66S with CCR5

Introduction

The identification of CCR5 as the major HIV-1 coreceptor has made CCR5 a very interesting drug target for HIV prevention and therapy. Initial observations indicated that the wild-type chemokine RANTES has weak anti-HIV potency accompanied by activation of the immune response (174). Further studies with RANTES peptides have proven that the antiviral activity can be uncoupled from the proinflammatory effect of the endogenous ligand (179). RANTES-derived peptides show potential as HIV-1 entry inhibitors (246), but the highest anti-HIV potency is achieved by N-terminal modifications of full-length RANTES (180, 182, 248). RANTES analogs, identified as efficient HIV-1 entry inhibitors, are ranging from antagonists (e.g. 5P12-RANTES) to agonists (e.g. 6P4-RANTES) effecting CCR5 signaling and internalization (182). The CCR5 binding mode and interaction surface with the chemokine protein ligands is considerably more complex than for most other class A GPCRs, which bind only small molecules. For these reasons, a detailed understanding of the CCR5•RANTES interaction and its functional consequences is of high interest.

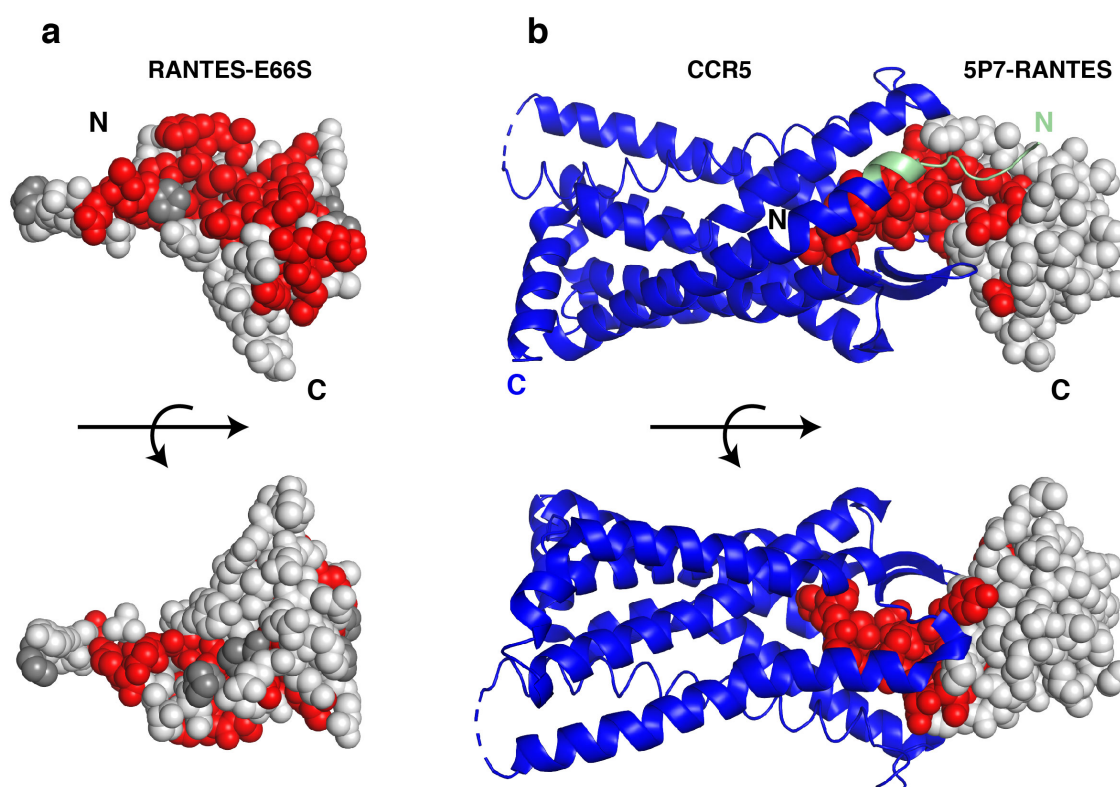


Figure 6.1 Insight into the RANTES interaction surface with CCR5. **(a)** RANTES-E66S residues significantly perturbed upon binding of the sulfated CCR5 N-terminal peptide (residues 1-25) (237) are highlighted in red on the monomer surface (1B3A, chain A). Prolines are indicated in dark gray. **(b)** Crystal structure of the 5P7-RANTES•CCR5 complex (5UIW) (191). CCR5 is shown in blue and the N-terminal residues 16 to 25 are highlighted in green. Residues 1-15 are not visible in the crystal structure. 5P7-RANTES residues observed to interact with CCR5 are highlighted as red spheres in the structure.

A two-site binding model for chemokine-receptor interaction has been proposed based on biophysical data and mutational analysis (249-251). Chemokine recognition site (CRS) 1 is

formed by the receptor N-terminus, which interacts with the core of the chemokine and positions it above the transmembrane region. CRS1 is considered a high-affinity binding determinant (161, 162, 237, 252). CRS2 is formed by the transmembrane helix bundle accommodating the chemokine N-terminus and is assumed to trigger different receptor responses depending on the chemokine N-terminal sequence (190). The model has been refined further to include CRS1.5 acting as a hinge between the CRS1 and CRS2 and forming one extended binding surface on the chemokine (168).

Previous NMR analyses of RANTES-E66S with CCR5-derived peptides representing CRS1, comprised of the soluble N-terminus (residues 1-25) and the extracellular loops, have shown that monomeric RANTES is the relevant state for interaction with CCR5 and confirmed the significance of N-terminal sulfation of CCR5 for high-affinity binding (237, 253). The studies have revealed an extensive, basic surface on RANTES interacting with CRS1 (Figure 6.1a). The interaction of the chemokine N-terminus, which determines the pharmacological specificity, was not detected due to the absence of the transmembrane helix bundle (CRS2). Recently, the crystal structure of CCR5 with the chemokine analog 5P7-RANTES has been solved, and high-resolution insight has been obtained for this chemokine•receptor complex (191). The binding interface on 5P7-RANTES partially overlaps with the interaction sites obtained on RANTES-E66S by NMR and shows additionally the interaction of the chemokine N-terminus with the transmembrane helix bundle (CRS2) (Figure 6.1b). CRS1.5 packs against the conserved disulfide bonds of the chemokine. However, information on the interaction with the basic patch on the RANTES core mediating high-affinity binding is missing, because the N-terminal residues of CCR5 (1-15) (part of CRS1) are not resolved in the structure, either due to sample heterogeneity, flexibility or crystal packing (191, 254). Based on the crystal structure and mutation analysis, the complex of CCR5 with wt-RANTES was obtained by molecular modeling (191). The contacts of the N-terminus of either 5P7- or wt-RANTES with the CCR5 transmembrane binding pocket are mostly mediated by water and hydrogen bonds, which may allow to accommodate very diverse N-terminal chemokine sequences. These previous studies have provided partial structural insights into the interactions of CCR5 with various RANTES forms. However, detailed insights how the various RANTES forms elicit distinct CCR5 responses are still missing.

The objective of this work is to develop solution and solid-state NMR methods to study RANTES analogs in complex with CCR5 based on the results from Chapter 4.1 (CCR5) and Chapter 5 (5P12-RANTES-E66S).

Results

CCR5 interaction with RANTES analogs as tested by co-immunoprecipitation

The interactions of detergent-reconstituted wild-type CCR5 with the chemically modified PSC-RANTES, oligomerization-deficient RANTES-E66S and the antagonist 5P12-RANTES-E66S had been studied earlier by surface plasmon resonance (data not shown, Sébastien Morin, unpublished results). Here, the interaction of the CCR5 constructs CCR5-4m, intact ICL3, and CCR5-rub, rubredoxin fusion in ICL3, (further description in Chapter 4.1) with these RANTES analogs was tested by co-immunoprecipitation. Detergent-solubilized CCR5 was incubated with RANTES analogs and subsequently immunoprecipitated with

FLAG-specific antibody beads targeting its C-terminus. Supernatant and immunoprecipitated fractions were analyzed by Western blot using a RANTES-specific antibody (Figure 6.2).

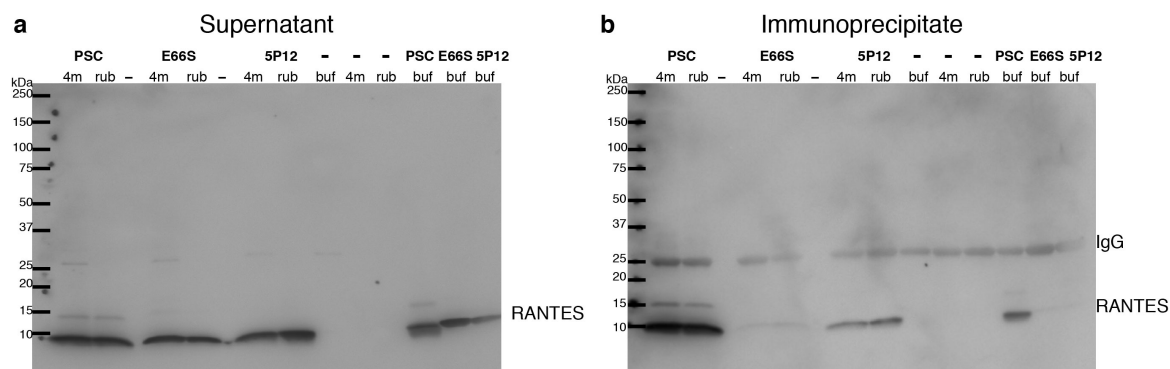


Figure 6.2 Interaction of CCR5 with RANTES analogs analyzed by co-immunoprecipitation. Western blot analysis of (a) supernatant and (b) immunoprecipitated fractions with a RANTES-specific antibody (AF-278-NA). CCR5-4m (4m) and CCR5-rub (rub) constructs were immunoprecipitated with Anti-FLAG M2 affinity gel and the interactions with PSC-RANTES (PSC), RANTES-E66S (E66S) and 5P12-RANTES-E66S (5P12) were tested. Samples without RANTES analogs (-) were tested as well. Samples containing RANTES analogs in buffer (buf) only without CCR5 were used as controls.

In all supernatant fractions, a prominent band for RANTES below 10 kDa was observed (Figure 6.2a). 5P12-RANTES-E66S (5P12) was also detected in the immunoprecipitated fraction of CCR5-4m and CCR5-rub. This suggests the formation of a stable, specific 5P12-RANTES-E66S•CCR5 complex. PSC-RANTES (PSC) was detected in the immunoprecipitated fraction (Figure 6.2b), but a strong band in the buffer control indicated precipitation or unspecific interactions with the detergent. A low-intensity band was observed in the immunoprecipitated fraction of RANTES-E66S (E66S), indicating a very weak interaction with CCR5. Presumably, the experimental conditions, pH 7.5 and 4 °C, favored the formation of dimeric RANTES-E66S, which is the binding-incompetent form of CCR5 (237). Additionally, the CCR5 constructs contained the A233D(6.33) mutation, which reduces affinity for the endogenous ligands and stabilizes the inactive state of CCR5 (153). The formation of RANTES-E66S•CCR5 complex should be repeated in the future with an activatable CCR5 construct at lower concentration and elevated temperature to favor the interaction with monomeric RANTES-E66S.

Purification and characterization of the 5P12-RANTES-E66S•CCR5-4m complex

As a next step, a homogenous sample of 5P12-RANTES-E66S in complex with CCR5-4m was prepared for NMR studies. Isotope-labeled 5P12-RANTES-E66S was chosen for NMR detection, because its preparation in *E. coli* is established, and the resonance assignments are available (Chapter 5) (238). CCR5-4m was expressed in insect cells, solubilized in DDM and purified by IMAC as described in Chapter 4.1 without addition of maraviroc. Subsequently, 5P12-RANTES-E66S was added to the CCR5-4m sample, incubated and further purified by size-exclusion chromatography (Figure 6.3a, b). CCR5-4m and 5P12-RANTES-E66S eluted together in one peak corresponding to a molecular weight of ~110 kDa. The procedure yielded ~0.25 mg of the 5P12-RANTES-E66S•CCR5-4m complex in DDM micelles per liter of insect cell culture.

The stability of the chemokine•receptor complex was tested by the CPM thermal shift assay (Figure 6.3c). Thermal unfolding of CCR5-4m in complex with 5P12-RANTES-E66S indicated a melting temperature of 60 °C, which is higher than for the apo form (48.5 °C) and lower than the maraviroc-bound state (69 °C) (Chapter 4.1). The stability of the complex should be suitable for extended NMR measurements.

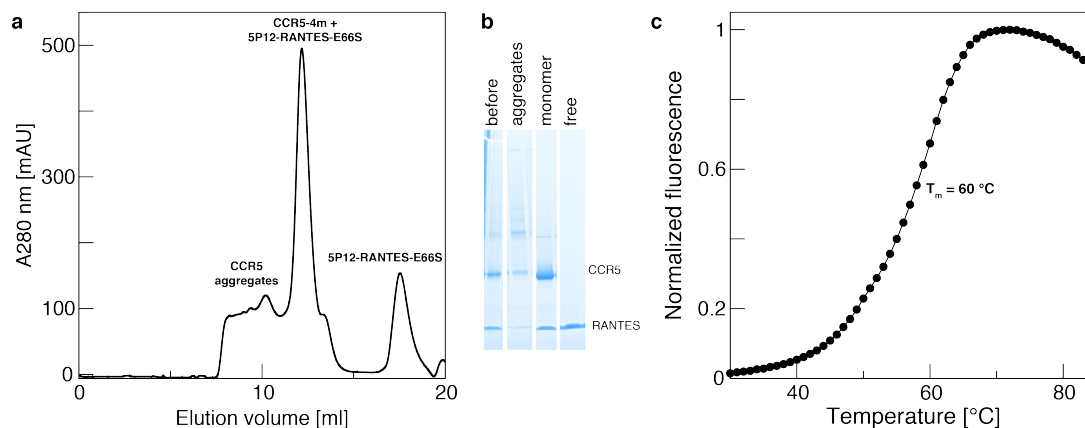


Figure 6.3 (a) Size-exclusion analysis of the 5P12-RANTES-E66S•CCR5-4m complex in DDM micelles revealing oligomeric species, monomeric complex and free 5P12-RANTES-E66S. (b) Coomassie-stained SDS-PAGE of the size-exclusion fractions: before column (before), CCR5 aggregates (aggregates), CCR5-4m + 5P12-RANTES-E66S (monomer) and 5P12-RANTES-E66S (free). (c) Temperature-induced unfolding of 5P12-RANTES-E66S•CCR5-4m in DDM micelles. The melting temperature (T_m) was determined as the maximum of the computed derivative of the melting curve.

Solution NMR characterization of ^2H , ^{15}N -labeled 5P12-RANTES-E66S in complex with CCR5

Compared to free 5P12-RANTES-E66S in the presence of detergent micelle, the ^1H - ^{15}N TROSY spectrum of ^2H , ^{15}N -labeled 5P12-RANTES-E66S in complex with CCR5-4m showed large changes (Figure 6.4a, b). For the complex, fewer backbone resonances were observed and the signal intensity of the peaks varied more than in the free form. This indicates different dynamics within 5P12-RANTES-E66S bound to CCR5. The complex formation changes the apparent molecular weight of 5P12-RANTES-E66S from 8 kDa to over 100 kDa, which was shown by the reduction of ^{15}N TROSY T_2 times from 120 ms (free) to 30 ms (in complex). This is in agreement with the tumbling of such a molecular weight since the ^{15}N TROSY T_2 time for partially deuterated TS- $\beta_1\text{AR}$ was ~ 30 ms (Chapter 3.3).

19 amide backbone resonances were broadened beyond detection. The extreme linewidth cannot be attributed to the slow tumbling of the complex as similar experiments can observe resonances of protonated CCR5-4m bound to maraviroc (see Chapter 4.1). The reason must be additional dynamics at the 5P12-RANTES-E66S•CCR5-4m interface in the micro- to millisecond time range.

The specificity of the complex was analyzed using the small-molecule ligand maraviroc, which has been shown to promote the dissociation of chemokines from CCR5 (157). Maraviroc also competes with 5P12-RANTES for CCR5 binding (Sébastien Morin, unpublished results). This is apparently due to overlapping binding sites for CCR5 (191). Following the addition of two molar equivalents of maraviroc to the chemokine•receptor complex, a TROSY spectrum corresponding to the free 5P12-RANTES-E66S was observed, indicating its release from CCR5 (Figure 6.4c).

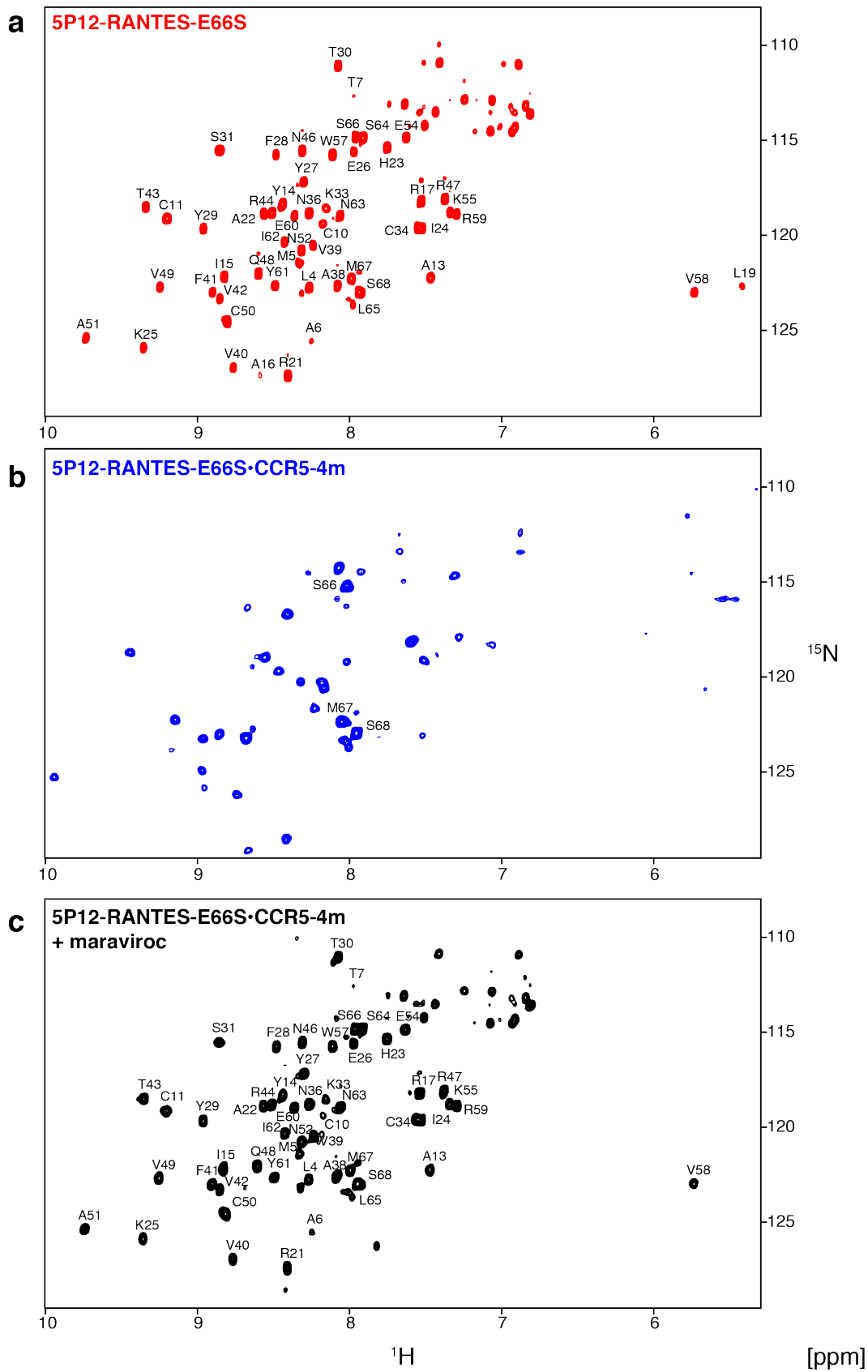


Figure 6.4 ^1H - ^{15}N TROSY-HSQC spectra of $90\ \mu\text{M}$ ^2H , ^{15}N -labeled 5P12-RANTES-E66S (a) free, (b) in complex with CCR5-4m in DDM micelles and (c) after addition of two molar equivalents of maraviroc recorded on a 900 MHz spectrometer at 298 K.

Triple-resonance experiment for assignment

With the exception of the C-terminal resonances S66, M67 and S68, resonance assignments of the free 5P12-RANTES-E66S were not transferable to the complex-bound state. Thus triple-resonance experiments were attempted to obtain assignments. However, a TROSY-HNCO experiment carried out on 230 μM ^2H , ^{13}C , ^{15}N -labeled 5P12-RANTES-E66S•CCR5-4m gave only one peak after 24 h of measurement time, which correlated the NH group of S68 to the carbonyl of M67 (Figure 6.5). Due to the limited sample stability (see below), the experiment could not be continued further. Apparently, the C-terminal resonance could be detected due to its increased mobility, but the sensitivity of the experiment was not high enough to permit further resonance assignments. This must be attributed to the high molecular weight and the additional dynamics in the complex

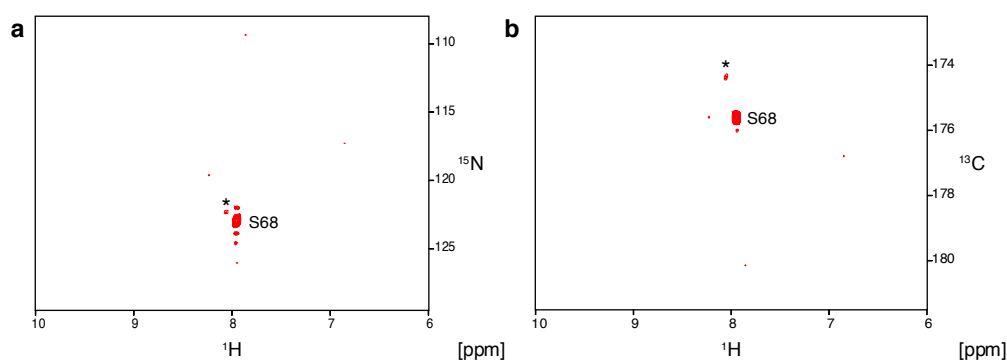


Figure 6.5 TROSY-HNCO experiment recorded on 230 μM ^2H , ^{13}C , ^{15}N -labeled 5P12-RANTES-E66S•CCR5-4m for 20 hours on a 900 MHz spectrometer at 298 K. 2D projections onto (a) the ^1H and ^{15}N plane and (b) the ^1H and ^{13}C plane. The asterisk marks an unidentified impurity.

Chemical shift mapping of the CCR5 binding interface

In the absence of assignments, the minimal chemical shift change criterion was used to gain insights into the 5P12-RANTES-E66S interface with CCR5 by chemical shift mapping (Figure 6a) (255, 256). In brief, a peak in the complex spectrum is linked to the resonance of free 5P12-RANTES-E66S, which has the smallest combined ^1H and ^{15}N chemical shift distance. The assignment of this resonance in the free form is taken as the tentative assignment for the resonance in the complex. The obtained chemical shift difference then presents a lower limit of its true value. The procedure leaves a number of residues detected in the free form unassigned. These residues were assumed to be broadened beyond detection in the complex.

The combination of resonances that disappeared due to line broadening and resonances undergoing significant chemical shift changes ($>0.1\text{ppm}$) revealed an extended CCR5 binding surface on the RANTES structure (Figure 6.6b, c), which agrees with interaction sites determined previously (Figure 6.1) (191, 237).

Resonances of N-terminal residues L4 to C11 were strongly affected by CCR5 binding, which corresponds to the interaction site observed in the peptide NMR studies and the crystal structure. The interaction with the core of 5P12-RANTES-E66S is larger than previously described and extends even to the C-terminal helix. Residues in the first and third β -sheet experience strong chemical shifts changes. Disappearance and chemical shift changes of resonances in the N-, 30s- and 40s-loop illustrate their role in the binding of CCR5 and indicate

Stability of the 5P12-RANTES-E66S•CCR5-4m complex in solution

A more detailed analysis of 5P12-RANTES-E66S•CCR5-4m by solution NMR was not possible due to the low stability of the complex. After 20 h, more than 10 % of the signal decayed as judged from 1D experiments (Figure 6.7a), and precipitate was observed in the NMR tube. A ^1H - ^{15}N TROSY spectrum recorded after ~ 3 days even led to the detection of weak signals arising from free 5P12-RANTES-E66S (Figure 6.7b). Analysis of the precipitate by Coomassie-stained SDS-PAGE revealed the presence of both 5P12-RANTES-E66S and CCR5-4m, and the latter showed signs of aggregation (Figure 6.7c).

In summary, the 5P12-RANTES-E66S•CCR5-4m complex is very difficult to study by solution NMR due to limited sample stability and strong line broadening at the interaction surface. However, the precipitated 5P12-RANTES-E66S•CCR5-4m complex shows very good prospects for analysis by solid-state NMR (see below).

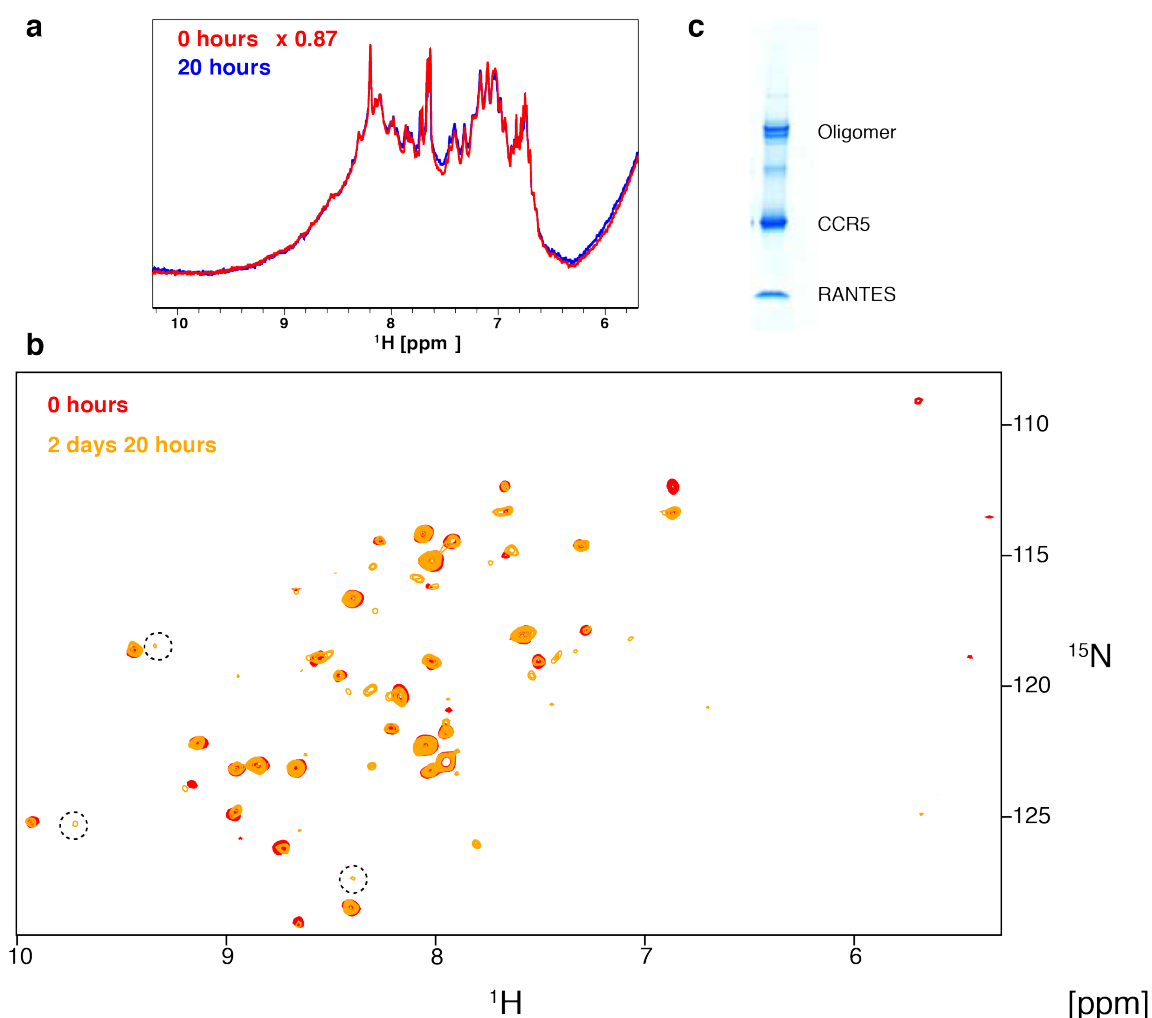


Figure 6.7 Stability of the 230 μM ^2H , ^{13}C , ^{15}N -labeled 5P12-RANTES-E66S•CCR5-4m complex during solution NMR measurements. **(a)** Decrease of signal intensity after 20 hours observed in the amide region of the 1D ^1H spectrum. **(b)** ^1H - ^{15}N TROSY-HSQC spectra after 0 hours (red) and 2 days 20 hours (orange). Resonances belonging to free 5P12-RANTES-E66S are shown in a dashed circle. **(c)** Precipitate after NMR measurement analyzed by Coomassie-stained SDS-PAGE.

Analysis of precipitated 5P12-RANTES-E66S•CCR5-4m by solid-state NMR

Solid-state NMR provides a tool for the analysis of immobilized, large molecules. Unlike solution NMR, the method is not affected by rapid transverse relaxation for such challenging objects. MAS spinning frequencies above 60 kHz, which remove strong homonuclear ^1H dipolar couplings, allow to record proton-detected experiments of a quality similar to solution NMR (257).

In the following, solid-state NMR experiments are described on the ^2H , ^{13}C , ^{15}N -labeled 5P12-RANTES-E66S•CCR5-4m complex. These experiments were recorded in the group of Prof. Józef Lewandowski, University of Warwick.

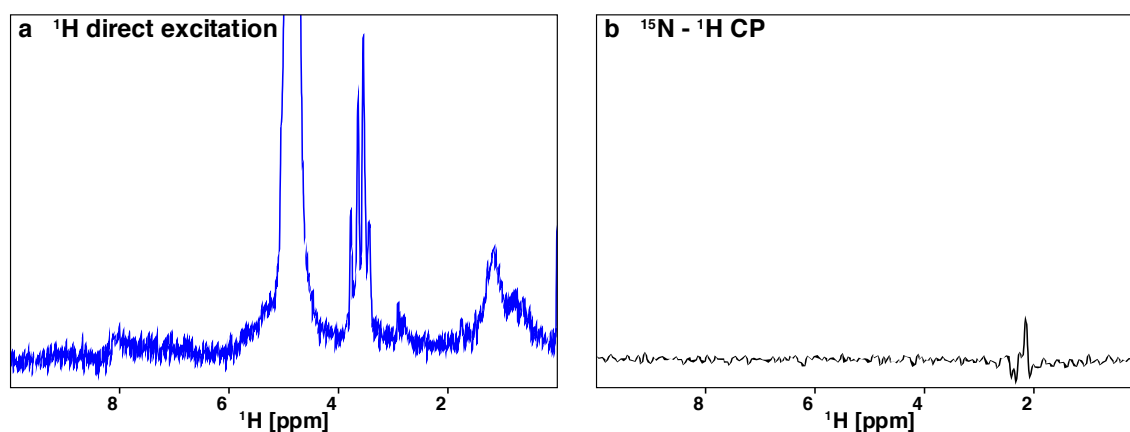


Figure 6.8 1D ^1H solid-state NMR spectra of precipitated ^2H , ^{13}C , ^{15}N -labeled 5P12-RANTES-E66S•CCR5-4m recorded on a 600 MHz spectrometer at ~ 298 K and 60 kHz MAS frequency. **(a)** Direct ^1H excitation spectrum. **(b)** ^{15}N - ^1H cross-polarization spectrum.

1D proton-detected spectra of the precipitated, ^2H , ^{13}C , ^{15}N -labeled 5P12-RANTES-E66S•CCR5-4m complex from solution were recorded at 60 kHz MAS frequency. In the amide proton region of a direct excitation spectrum, protein signals were detected. (Figure 6.8a). In contrast, ^{15}N - ^1H (Figure 6.8b) or ^{13}C - ^1H (not shown) cross-polarization (CP) experiments did not yield any signal. CP transfer is based on heteronuclear dipolar couplings, which transfer magnetization from one spin-locked nucleus to another. Polarization transfer occurs if the Hartmann-Hahn conditions between both nuclei are matched during the contact time (258). CP is only efficient for immobile molecules since rotational motion averages dipolar couplings to zero. No detectable protein signal in ^{15}N - ^1H or ^{13}C - ^1H CP-based experiments indicates that isotope-labeled 5P12-RANTES-E66S is not fully immobilized in the precipitate

2D solid-state NMR spectra of sedimented 5P12-RANTES-E66S•CCR5-4m

Lipid bilayers are commonly used to study membrane proteins in a close-to-natural environment by solid-state NMR. The embedded membrane proteins are strongly immobilized. Such preparations would have required time-consuming sample optimization for 5P12-RANTES-E66S•CCR5-4m. Sedimentation by ultracentrifugation was shown to be an alternative method to immobilize large soluble proteins for solid-state NMR (259). We tested whether this method would immobilize the chemokine•receptor complex in detergent micelles sufficiently for solid-state NMR.

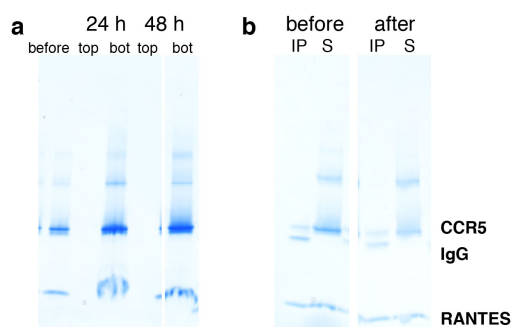


Figure 6.9 Stability of the 5P12-RANTES-E66S•CCR5-4m complex during ultracentrifugation. **(a)** Coomassie-stained SDS-PAGE of samples taken during ultracentrifugation: before, after 24 h and 48 h from the top and the bottom (bot) of the tube. **(b)** Integrity of the 5P12-RANTES-E66S•CCR5-4m complex after sedimentation, tested by co-immunoprecipitation with Anti-FLAG M2 affinity gel. Coomassie-stained SDS-PAGE of immunoprecipitate (IP) and supernatant (S) fractions of the sample before ultracentrifugation and the sediment after ultracentrifugation.

Initial tests showed that CCR5 and 5P12-RANTES-E66S could be detected in a gel-like pellet at the bottom of the ultracentrifugation tube after ultracentrifugation at 300,000g for 24 or 48 h (Figure 6.9a). The integrity of the 5P12-RANTES-E66S•CCR5-4m complex after ultracentrifugation in this pellet was confirmed by co-immunoprecipitation (Figure 6.9b). Samples for solid-state NMR were then prepared by ultracentrifugation of ^2H , ^{13}C , ^{15}N -labeled 5P12-RANTES-E66S•CCR5-4m for 20 hours at 700,000 g. The obtained sediment was transferred to the MAS rotor. CP-based experiments on the sediment gave detectable NMR signals, thereby proving that 5P12-RANTES-E66S was immobilized in the sediment.

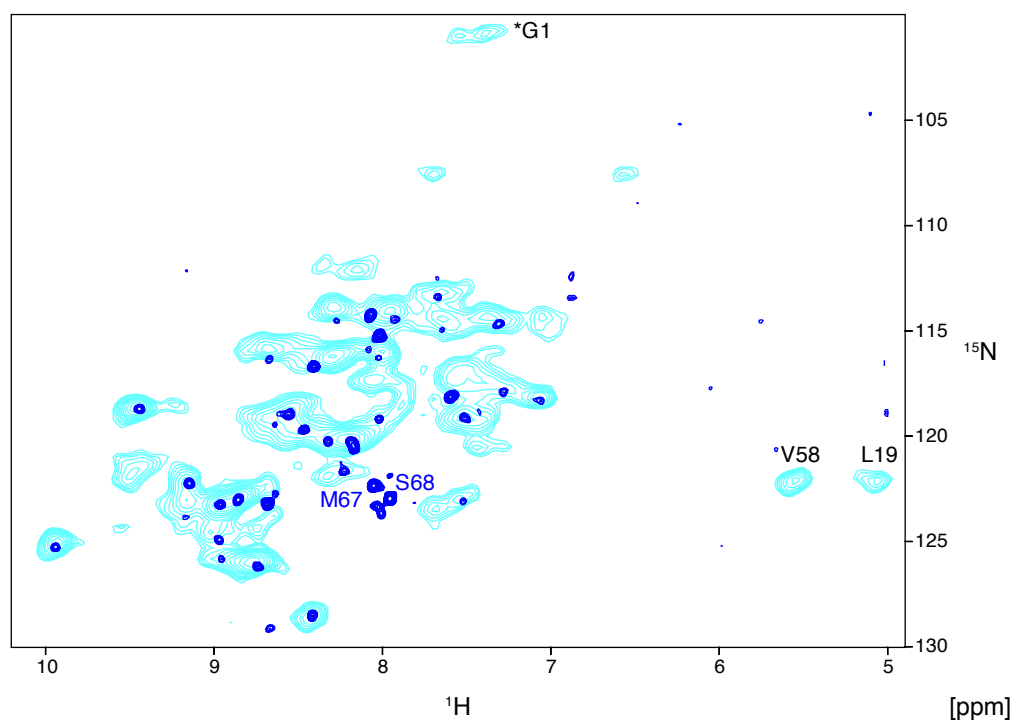


Figure 6.10 Comparison of solid-state ^1H - ^{15}N CP-based (cyan) and solution ^1H - ^{15}N TROSY-HSQC (blue) spectra of 5P12-RANTES-E66S•CCR5-4m. The solid-state experiment was recorded on 1.8 mg sedimented ^2H , ^{13}C , ^{15}N -labeled 5P12-RANTES-E66S•CCR5-4m on a 700 MHz spectrometer at ~ 298 K and 60 kHz MAS frequency. The solution experiment was recorded on 90 μM ^2H , ^{15}N -labeled 5P12-RANTES-E66S •CCR5-4m on a 900 MHz spectrometer at 298 K. The tentative assignment of G1 is indicated by an asterisk.

2D proton-detected ^1H - ^{15}N CP experiments revealed very good spectral quality for solid-state NMR at 60 kHz spinning speed (Figure 6.10). Still, the ^1H linewidths of ~ 100 Hz led to spectral overlap and complicated the identification of single resonances. Approximately 40 cross peaks were detected in the solid-state spectrum. Many resonances were similar to the peaks in the solution TROSY spectrum, and small shifts between solid-state and solution spectra might be caused from slightly different sample temperatures.

In the solid-state spectra, ~ 10 resonances were detected which are not observable in solution due to line broadening or exchange with water. Two peaks at 5.6 and 5.0 ppm in the ^1H dimension were observed, which could be assigned to V58 and L19 from the free 5P12-RANTES-E66S spectrum in solution. Furthermore, a resonance strongly upfield shifted in the ^{15}N dimension at 100 ppm was observed and predicted to be glycine 1. Hence the chemokine N-terminus, invisible in solution, seems to be observable by solid-state NMR, which may give insight into this crucial CCR5 interaction site. The C-terminal resonances M67 and S68 were both missing in the CP solid-state spectrum compared to the one from solution NMR. They might be too flexible for CP-based coherence transfer.

INEPT-based correlation solid-state experiments were also recorded, which can report on mobile regions in a solid sample. In the INEPT experiment, the magnetization transfer is based on scalar coupling. The efficiency of INEPT-based experiment depends on the transverse magnetization, and completely immobilized nuclei relax too fast for an efficient magnetization transfer.

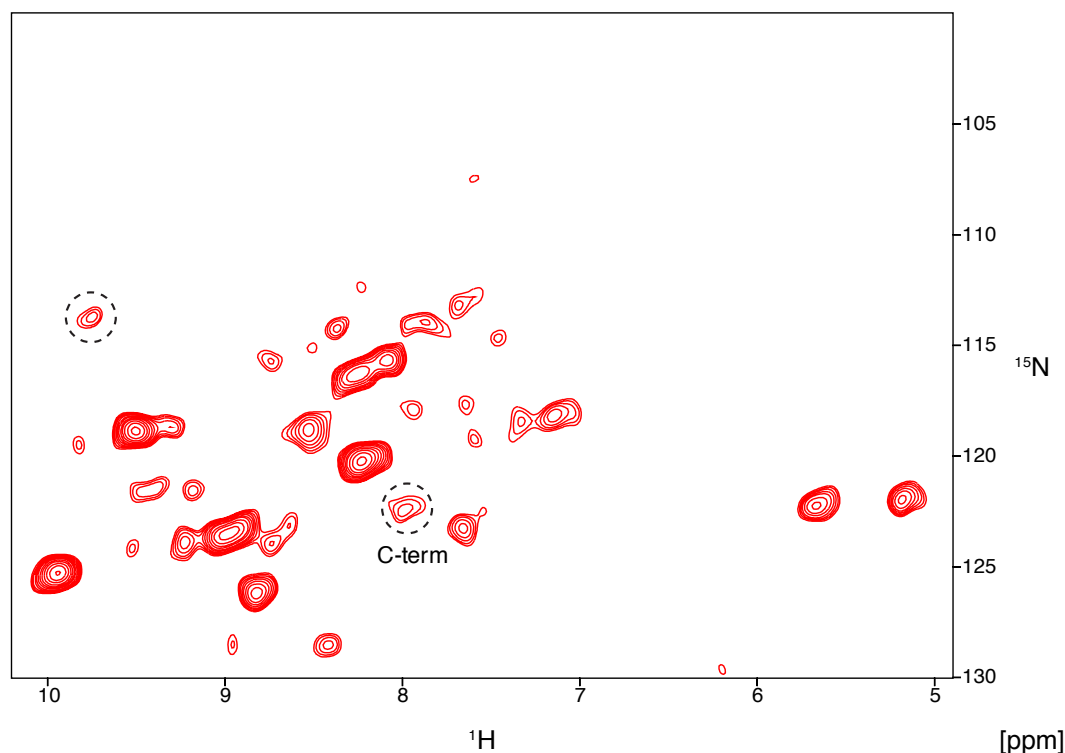


Figure 6.11 Solid-state ^1H - ^{15}N INEPT-based spectrum of 1.8 mg sedimented ^2H , ^{13}C , ^{15}N -labeled 5P12-RANTES-E66S•CCR5-4m on a 850 MHz spectrometer at ~ 298 K and 60 kHz MAS frequency. Cross-peaks observable only in the INEPT-based experiment are marked with a dashed circle.

In the INEPT-based ^1H - ^{15}N spectrum of 5P12-RANTES-E66S•CCR5-4m (Figure 6.11), only two new weak cross peaks were detected compared to the CP-based experiment (Figure

6.10). The resonance at 8.0 (^1H) and 122.5 (^{15}N) ppm very likely belongs to the C-terminal S68, which was not detected in the CP-spectrum. Overall, CP- and INEPT-based experiments, with the former having a higher sensitivity, show almost identical resonances. The 5P12-RANTES-E66S•CCR5-4m complex seems to be immobilized by sedimentation, but retains some dynamics.

3D heteronuclear solid-state experiments

No changes in the spectra of 5P12-RANTES-E66S•CCR5-4m were observed over weeks, which indicated that the complex was more stable in the sediment compared to the sample in solution. In conjunction with the good quality of the 2D spectra, this made it possible to record ^1H -detected triple-resonance experiments for assignment (260).

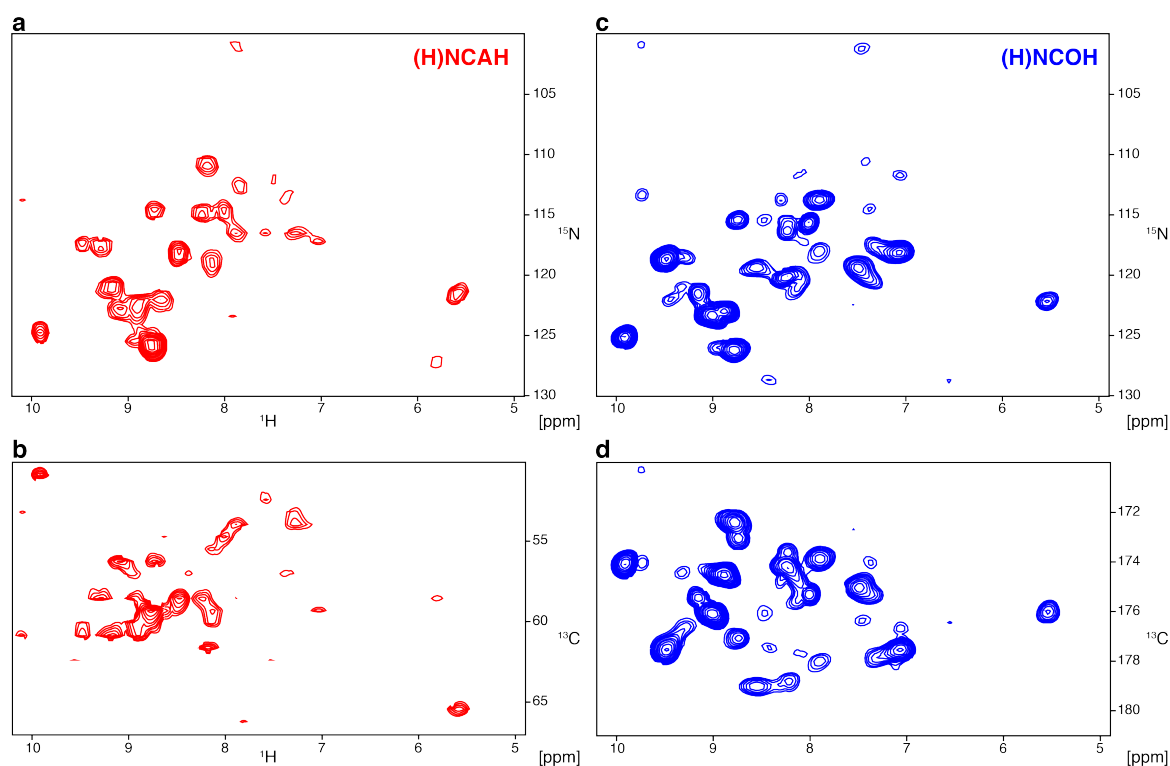


Figure 6.12 3D CP-based experiments of 4.1 mg sedimented ^2H , ^{13}C , ^{15}N -labeled 5P12-RANTES-E66S•CCR5-4m recorded on a 850 MHz spectrometer at ~ 298 K and 60 kHz MAS frequency. 2D projections onto (a) the ^1H and ^{15}N plane and (b) the ^1H and ^{13}C plane of an (H)CANH experiment. 2D projections onto (c) the ^1H and ^{15}N plane and (d) the ^1H and ^{13}C plane of an (H)CONH experiment.

Three-dimensional CP-based (H)NCAH (Figure 6.12a, b) and (H)NCOH (Figure 6.12c, d) experiments were recorded for 2.5 and 3 days, respectively. In both experiments, ~ 15 cross peaks were observed as estimated from the 2D projections onto the ^1H - ^{15}N plane (Figure 6.12a, c) with the signal intensity being higher in the (H)NCOH experiment than in the (H)NCAH. The dispersion in the carbon dimensions of (H)NCAH and (H)NCOH was good and will allow to identify single resonances due to the increased separation by the third dimension.

These data suggest that resonance assignment of 5P12-RANTES-E66S in complex with CCR5 will be feasible by solid-state NMR. Longer measurement times will still be required to

detect all the cross peaks in the 3D experiments which were observed in the 2D spectrum. (H)NCAH and (H)NCOH experiments would allow the identification of resonances based on the carbon chemical shift of free 5P12-RANTES-E66S in solution. In order to gain backbone connectivity for sequential-resonance identification, less sensitive experiments such as (H)(CO)CA(CO)NH or (H)(CA)CB(CACO)NH will be required. MAS spinning rates at 100 kHz may improve the sensitivity of the experiments due to the increased coherence lifetimes and reduced proton linewidths. However, the sample amount and thus the sensitivity will be decreased due to the requirement of a 0.8 mm rotor instead of the 1.3 mm rotor used for the 60 kHz experiments.

Conclusions and perspectives

A stable complex of CCR5-4m with 5P12-RANTES-E66S, an antagonistic RANTES analog, was prepared. Initially, the chemokine•receptor interaction was studied on ^2H , ^{15}N -labeled 5P12-RANTES-E66S in complex with unlabeled CCR5-4m by solution NMR. Large spectral changes were observed between free and complex-bound 5P12-RANTES-E66S. Several resonances disappeared in the spectrum, which indicates severe line broadening due to dynamics in the micro- to millisecond time range. Resonance assignment of 5P12-RANTES-E66S in complex with CCR5-4m was not feasible, due to low sensitivity of the triple-resonance experiments and the limited stability of the complex in solution. Still, an interaction surface with CCR5 could be derived using the minimal-chemical shift change procedure. This surface comprises almost the entire chemokine and is larger than what was observed previously in NMR studies of RANTES with CCR5 peptides (237, 253, 254) as well as within the crystal structure of the 5P7-RANTES•CCR5 complex (191). Obviously the interaction of the full CCR5 with the chemokine covers a larger surface (in particular β -sheet 1 and the C-terminal α -helix) than observed in previous CCR5 peptide NMR studies (237, 253, 254). Although the soluble peptides were covalently linked in one study (253), they apparently do not fully mimic the three-dimensional arrangement of the receptor. Furthermore, the current NMR experiments were carried out at the physiological pH 7.5, which further increases the strength of the interaction (237). The binding surface observed in the present work is also larger than in the crystal structure (191). This is due to the missing electron density for the CCR5 N-terminus in the latter. Unfortunately, we could not fully observe the highly interesting chemokine N-terminus by solution NMR due to fast amide exchange and line broadening.

Solid-state NMR was applied to get further insights into the chemokine•receptor interaction. Precipitated 5P12-RANTES-E66S•CCR5-4m from solution was not sufficiently immobilized for CP-based solid-state experiments. However, sedimentation of 5P12-RANTES-E66S•CCR5-4m in DDM micelles by ultracentrifugation provided sufficient immobilization for solid-state NMR experiments. The quality of the proton-detected CP spectra of the sedimented complex is very good for a solid-state NMR spectrum at 60 kHz MAS frequency. More resonances were observed than in the solution NMR spectrum. The tentative assignment for glycine 1 indicates that structural information on the N-terminus of 5P12-RANTES-E66S in complex with CCR5-4m can be obtained. The broad ^1H linewidths complicated the identification of single resonances in the spectrum. This could be partially resolved by recording triple-resonance experiments to increase the frequency separation through a third dimension. Preliminary 3D experiments indicate that a complete resonance assignment will be feasible. The spectral quality might be further increased by spinning at 100 kHz MAS

frequency. The next step of this project will be to assign 5P12-RANTES-E66S in complex with CCR5-4m by solid-state NMR.

The sedimented 5P12-RANTES-E66S•CCR5-4m complex still retained some dynamics, because most chemokine resonances observed in CP-based experiments were also detected by INEPT-based experiments. In contrast, chemokine resonances in a recent MAS solid-state NMR study of the interleukin-8•CXCR1 complex were detected either by CP- or INEPT-based experiments, but not in both cases (261). The different dynamics of 5P12-RANTES-E66S and interleukin-8 in their receptor complexes may be due to genuine differences of these receptor systems, but could also result from the different membrane mimetics used, i.e. detergent micelles in the case of CCR5 and phospholipid bilayers for CXCR1. It will be interesting to study the influence of lipids on the dynamics of the 5P12-RANTES-E66S•CCR5-4m complex in lipid bilayers or nanodiscs.

The work presented here establishes a framework to investigate structural and dynamic features of isotope-labeled 5P12-RANTES-E66S in complex with CCR5 by NMR. As a next step an in-depth analysis of this complex should be carried out using detection on the easy-to-label 5P12-RANTES-E66S. However, it will also be very interesting to observe the CCR5 part of the interaction. The strategies to achieve isotope labeling of CCR5 expressed in insect cells have been established in Chapter 4.1. Amino acid-specific labeling with tyrosine might provide the most interesting backbone reporter sites giving insights into several important interactions: (i) N-terminal sulfated tyrosines are essential for high-affinity interaction with the RANTES core (162, 237), (ii) tyrosines in the ligand binding pocket interact with RANTES N-terminal residues (190, 191, 262, 263), and (iii) tyrosines are conserved switches for receptor activation (264-266).

After an in-depth analysis of the 5P12-RANTES-E66S•CCR5-4m complex, future work could address complexes with other RANTES analogs, which are different by 3-6 mutations in the proximal N-terminus compared to 5P12-RANTES. They have similar biochemical properties, because the dimerization interface is also broken compared to wt-RANTES, but act as agonist (6P4-) or biased agonist (5P14-) compared to the antagonist 5P12-RANTES. The comparison of the interactions with the different RANTES analogs may reveal the underlying structural mechanism how N-terminal modifications trigger different functional CCR5 behavior.

The initial cryo-EM analysis of CCR5 (Chapter 4.1) indicated the feasibility of such structural studies for CCR5. In the future, it will be of high interest to investigate CCR5 complexes with RANTES analogs and intracellular effector proteins like G protein or arrestin by this method. Especially a ternary complex with RANTES and arrestin is of high interest due to its role in biased signaling and internalization of various RANTES analogs.

In summary, initial work on 5P12-RANTES-E66S•CCR5-4m is presented here, which will allow future extensive structural and dynamic characterization of RANTES analogs in complex with CCR5 to understand their pharmacological effects on CCR5 signaling and internalization.

Materials and Methods

Expression and purification of RANTES

Unlabeled RANTES-E66S and unlabeled, $^2\text{H},^{15}\text{N}$ - or $^2\text{H},^{13}\text{C},^{15}\text{N}$ -labeled 5P12-RANTES-E66S were expressed and purified as described previously (237, 238). PSC-RANTES was a generous gift from Prof. Oliver Hartley, University of Geneva.

Co-immunoprecipitation

CCR5-4m or CCR5-rub were solubilized as described in Chapter 4.1. The receptors in 25 mM HEPES (pH 7.5), 150 mM NaCl, 10 % (v/v) glycerol, 0.05 % (w/v) DDM, 0.01 % (w/v) CHS were incubated with PSC-RANTES, RANTES-E66S or 5P12-RANTES-E66S for 10 minutes at room temperature. The mixture was then added to Anti-FLAG M2 affinity gel (Sigma). After 2 hours of incubation the supernatant was removed and the gel washed three times with 25 mM HEPES (pH 7.5), 150 mM NaCl, 10 % (v/v) glycerol, 0.05 % (w/v) DDM, 0.01 % (w/v) CHS. Supernatant and immunoprecipitated fractions were analyzed by Western blot with a RANTES-specific antibody AF-278-NA (R&D systems) and secondary HRP-coupled anti-goat antibody (Abcam).

Purification of 5P12-RANTES-E66S•CCR5-4m complex

CCR5-4m was expressed in insect cells, solubilized in DDM and purified by IMAC as described in Chapter 4.1 except that maraviroc was not added during the procedure.

5P12-RANTES-E66S was added in equimolar amount to the CCR5-4m IMAC elution fraction (yield ~1.3 mg per 1 L expression culture) and incubated for 20 min at 4 °C. The solution was concentrated to 500 μl using an Amicon Ultra 50 kDa MWCO (Millipore) at 4 °C and 2,500 g. The monomeric complex was separated by size-exclusion chromatography (Superdex 200 Increase 10/300 GL, GE Healthcare) in 25 mM HEPES (pH 7.5), 150 mM NaCl, 5 % (v/v) glycerol, 0.05 % (w/v) DDM. The complex was then concentrated with an Amicon Ultra-3 filtration device 50 kDa MWCO (Millipore) to the desired concentration in 25 mM HEPES (pH 7.5), 150 mM NaCl, 5 % (v/v) glycerol, 0.05 % (w/v) DDM.

CPM thermal-shift assay

Protein thermal stability was measured by the microscale fluorescent stability assay as described in Chapter 4.1. For this 0.6 mg/mL 5P12-RANTES-E66S•CCR5-4m complex was prepared in 25 mM HEPES (pH 7.5), 150 mM NaCl, 5 % (v/v) glycerol, 0.05 % (w/v) DDM.

Solution NMR and binding interface

NMR samples (250 μl volume) of 90 μM $^2\text{H},^{15}\text{N}$ - or 230 μM $^2\text{H},^{13}\text{C},^{15}\text{N}$ -labeled 5P12-RANTES-E66S•CCR5-4m, 25 mM HEPES (pH 7.5), 150 mM NaCl, 0.05 % (w/v) DDM, 5 % (v/v) glycerol, 5 % D_2O and 0.02 % NaN_3 were prepared in Shigemi tubes. All NMR experiments were performed on a Bruker AVANCE 900 MHz spectrometer equipped with a TCI cryoprobe at 298 K.

^1H - ^{15}N TROSY experiments were recorded as 120 (^{15}N) x 1024 (^1H) complex points and acquisition times of 24 ms (^{15}N) and 42 ms (^1H). For optimal sensitivity, the ^1H - ^{15}N transfer time was reduced to 3.6 ms and the interscan delay set to 1.3 s. Maraviroc was added in 2:1

stoichiometry to the complex. ^{15}N TROSY spin-echo T_2 times were determined from 1D ^1H -detected experiments with relaxation delays of 0.2 ms, 120.2 ms (free) or 0.2 ms, 40.2 ms (complex) with 3.6 ms ^1H - ^{15}N transfer time. The TROSY version of a 3D HNC0 (267) was recorded with 76 (^{15}N), 72 (^{13}C), and 1024 (^1H) complex points and acquisition times of 15.2 ms (^{15}N), 16.5 ms (^{13}C), and 42.5 ms (^1H) for a total experimental time of 20 hours. All NMR spectra were processed with NMRPipe (204) and analyzed with SPARKY (205).

Average chemical shift differences for backbone ^1H and ^{15}N were calculated for every cross peak in the spectrum of free and CCR5-4m-bound 5P12-RANTES-E66S as

$$\Delta\delta_{av} = \sqrt{\Delta\delta_H^2 + \left(\frac{\Delta\delta_N}{5}\right)^2}$$

Minimal chemical shift change differences were used for the tentative assignment of 5P12-RANTES-E66S in the complex (see main text).

Initial sedimentation tests

For initial sedimentation tests, 150 μl of 15 μM complex were centrifuged at 4 $^\circ\text{C}$ and 300,000 g. 10 μl samples were taken from the top and bottom of the tube after 24 and 48 hours, respectively, for analysis by Coomassie-stained SDS-PAGE. The integrity of the 5P12-RANTES-E66S•CCR5-4m complex was tested subsequently by co-immunoprecipitation

Solid-state NMR

For solid-state NMR analysis of the solution precipitate, 0.3 mg of the precipitate of ^2H , ^{13}C , ^{15}N -labeled 5P12-RANTES-E66S•CCR5-4m was taken up in 15 μl 25 mM HEPES (pH 7.5), 150 mM NaCl, 0.05 % (w/v) DDM, 5 % (v/v) glycerol, 2 % DSS (dimethyl silapentane sulfonate), 5 mM Gd(DTPA-BMA) and filled into a 1.3 mm MAS rotor.

For solid-state NMR analysis of sedimented receptor 500 μl of 1.9 mg/ml ^2H , ^{13}C , ^{15}N -labeled 5P12-RANTES-E66S•CCR5-4m in 25 mM HEPES (pH 7.5), 150 mM NaCl, 0.05 % DDM, 5 % glycerol, 1.5 % DSS were spun for 20 hours at 700,000 g at 5 $^\circ\text{C}$. The pellet was the transferred into a 1.3 mm MAS rotor.

All solid-state NMR experiments were recorded by Prof. Józef Lewandowski, University of Warwick, United Kingdom. The experiments were performed on Bruker AVANCE 700 or 850 MHz spectrometers equipped with Bruker 1.3 mm triple resonance probes at MAS frequencies of 60 kHz. The internal sample temperature was adjusted to ~ 298 K from the position of water relative to the internal standard DSS.

2D proton-detected ^1H - ^{15}N heteronuclear correlation spectra with INEPT- or CP- based transfer were recorded, as well as the 3D CP-based experiments (H)CONH and (H)CANH. CP contact times were optimized for every sample and were typically: ^1H - ^{15}N 0.8-1.5 ms, ^1H - ^{13}C ~ 2 ms, and ^{13}C - ^{15}N ~ 5 ms.

7 Initial characterization of ^{15}N -valine-labeled human β_2 -adrenergic receptor by NMR

Introduction

The human β_2 -adrenergic receptor is one of the best characterized GPCRs, both by molecular biology and structural biology. The crystal structure of $\beta_2\text{AR}$ in complex with heterotrimeric G protein was a breakthrough in the understanding of GPCR signaling (90). Biophysical methods such as single-molecule fluorescence spectroscopy, double electron-electron resonance (DEER) spectroscopy and progress in MD simulations have been used to characterize dynamic features of human $\beta_2\text{AR}$. The results also serve as a model for other class A GPCRs (103, 106-108). Side-chain NMR studies of $\beta_2\text{AR}$ have given insights into local dynamics and conformational diversity (113, 115, 268, 269). So far, no backbone NMR studies reporting on long-range motions have been published for this receptor. Compared to turkey $\beta_1\text{AR}$, human $\beta_2\text{AR}$ displays a higher stability in detergent micelles and requires less protein engineering. In the following, some initial experiments are described to make $\beta_2\text{AR}$ accessible for backbone NMR experiments and to establish a comparison to $\beta_1\text{AR}$.

Results

Construct design and expression

For the following characterization, the same $\beta_2\text{AR}$ construct was used as described by Liu *et al.* for ^{19}F NMR experiments (116). The full sequence is given in the Methods section. Compared to the wild-type receptor, residues 245 to 259 in the third intracellular loop were deleted, the C-terminus was truncated after residue 348 and an N-terminal FLAG tag as well as a C-terminal His_{10x} tag were added. The mutation E122W was introduced to obtain a higher expression yield and stability (270).

^{15}N -valine labeled $\beta_2\text{AR}$ was expressed in insect cells using valine-depleted, yeast extract-free medium supplemented with ^{15}N -valine as described previously for the thermostabilized turkey $\beta_1\text{AR}$ (114).

Purification

$\beta_2\text{AR}$ was solubilized in mixed DDM/CHS micelles and further purified in pure DDM micelles. Coomassie-stained gel after IMAC purification showed a prominent band below 37 kDa, which is smaller than the expected molecular weight of 40 kDa due to ‘gel shifting’ (Figure 7.1a) (213). An additional band occurs at a slightly lower molecular weight and might be the result of partial proteolysis (271) or heterogenous N-glycosylation (272).

N-glycosylation of $\beta_2\text{AR}$ occurs by the covalently attachment of oligosaccharides to N6 and N15 in the N-terminus as well as N187 in the ECL2 (273, 274). Glycosylation of $\beta_2\text{AR}$ was analyzed using PNGaseF, which hydrolyzes the N-linked oligosaccharide between the proximal N-acetylglucosamine and asparagine. Western blot analysis with an antibody against the C-terminal His tag revealed the heterogeneity of the $\beta_2\text{AR}$ sample. Treatment with PNGaseF resulted in a reduction of the molecular weight by ~5 kDa (Figure 7.1b), indicating that the $\beta_2\text{AR}$ expressed in insect cells was glycosylated. However, the sample still remained heterogenous with two bands on the Western blot.

An additional affinity purification step using the N-terminal FLAG tag was introduced to further polish the β_2 AR protein sample. The fractions were analyzed by Western blot using an antibody against the C-terminal His tag (Figure 7.1c). The low-molecular-weight species was detected in the wash fractions whereas the higher-molecular-weight species was bound to the affinity material and eluted by competition with FLAG peptide. Detection of both species by the poly-His antibody, but binding of only the higher-molecular-weight species to the M1 FLAG affinity material, indicated that proteolytic degradation of β_2 AR occurred at the N-terminus.

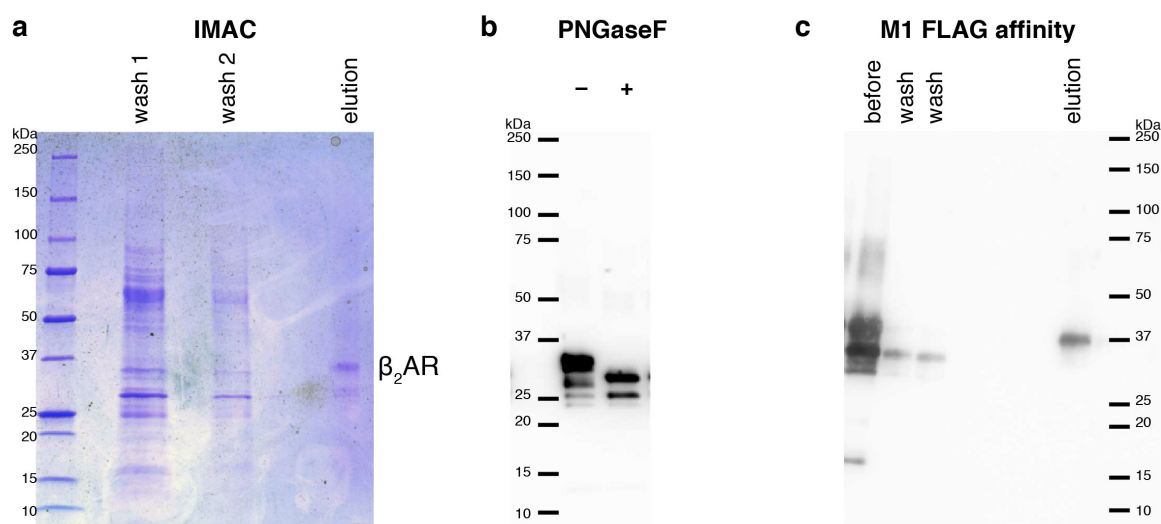


Figure 7.1 (a) Coomassie-stained SDS-PAGE showing fractions of the IMAC purification of β_2 AR. (b) Western blot analysis of β_2 AR samples before and after treatment with PNGaseF using a poly-His antibody. (c) Fractions of the M1 FLAG affinity chromatography exploring the N-terminal FLAG tag were analyzed by Western blot with a poly-His antibody specific for the C-terminal tag.

NMR characterization

A homogeneous sample of 20 μ M 15 N-valine-labeled β_2 AR in DDM micelles was obtained by FLAG affinity purification and characterized using 1D and 2D NMR experiments. The amide region in the 1D 1 H NMR spectra showed broad lines mixed with sharp signals, probably arising from flexible regions of the receptor (Figure 7.2a). The amide proton T_2 time for folded parts of the protein was determined as 2.7 ms from resonances above 8 ppm. This relaxation time is in the expected range for an apparent molecular weight above 100 kDa experiencing fast transverse relaxation. The receptor signals only span a range between 6 to 9 ppm. In contrast, the 1 H spectrum of the well-folded β_1 AR also contains signals above 9 ppm. The low spectral dispersion of β_2 AR is similar to the initial CCR5 samples expressed in the absence of yeast extract (Chapter 4.1), which was then considerably improved by the addition of yeast extract. This comparison seems to indicate that the β_2 AR preparation is not properly folded.

This suspicion was confirmed by the appearance of the 2D 1 H- 15 N TROSY spectrum (Figure 7.2b), in which only a single, strong resonance was observed instead of the 32 resonances expected for all valines in β_2 AR. This single resonance has a similar chemical shift as the single resonance observed in the initial 15 N-valine labeling attempts of CCR5 without yeast-extract supplementation during the insect-cell expression (Chapter 4.1).

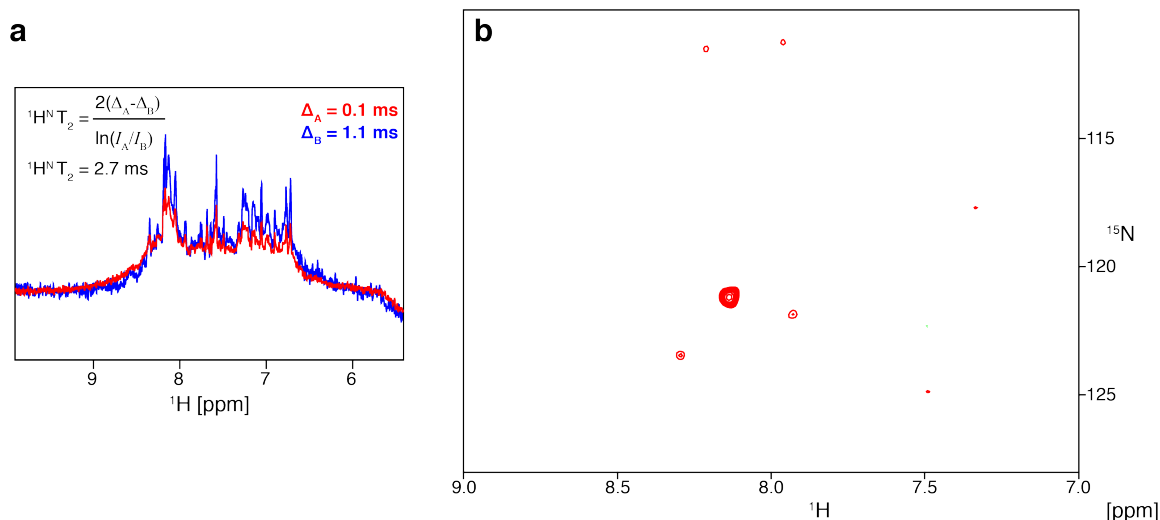


Figure 7.2 Spectra of 20 μM ^{15}N -valine-labeled $\beta_2\text{AR}$ in DDM micelles recorded at 298 K on a 900 MHz spectrometer. **(a)** Jump-return spin-echo ^1H spectra recorded using effective relaxation delays 2Δ of 0.2 or 2.2 ms to estimate ^1H T_2 time. **(b)** ^1H - ^{15}N TROSY spectrum recorded for 21 hours.

Conclusions and perspective

The initial attempt to establish human $\beta_2\text{AR}$ as a comparison for the thermostabilized turkey $\beta_1\text{AR}$ was not successful. The ^1H - ^{15}N TROSY spectrum of ^{15}N -valine-labeled $\beta_2\text{AR}$ was of low spectral quality and indicated an improperly folded receptor. ^{15}N -valine-labeled $\beta_2\text{AR}$ was expressed in insect cells using a yeast extract-depleted medium, whereas yeast extract was shown to be an essential component for functional expression of CCR5 (Chapter 4.1). Most probably $\beta_2\text{AR}$ is also not functionally expressed under these conditions. This indication is supported by biochemical data, since ^{15}N -valine-labeled $\beta_2\text{AR}$ did not bind to the alprenolol ligand-affinity chromatography column (personal communication Shin Isogai) (275) and was not capable to activate G protein (personal communication Dmitry Veprintsev). Due to time restrictions, insect cell expression of $\beta_2\text{AR}$ in full medium to study the influence of yeast extract and to validate the purification protocols has not been performed so far.

For future studies, human $\beta_2\text{AR}$ should be expressed under conditions optimized for amino acid-specific labeling of CCR5 (Chapter 4.1). Backbone NMR characterization could be integrated with biophysical data and side-chain NMR studies to understand the full extent of dynamics and conformational diversity. Especially, a comparison with the thermostabilized $\beta_1\text{AR}$ would be interesting. The $\beta_2\text{AR}$ construct is close to a wild-type GPCR and it should be investigated whether it gives similar spectral quality.

Materials and Methods

Generation of the expression construct

The β_2 AR construct was derived from the human β_2 AR mutant used in NMR studies (116). The final β_2 AR sequence for NMR studies is:

DYKDDDDAGQPGNGSAFLLAPNGSHAPDHDVTQQRDEVWVVGMGIVMSLIVLAIVFGNVLVI
TAIAKFERLQTVTNYFITSLACADLVMGLAVVPPFGAAHILMKMWTFGNFWCFWTSIDVLCV
TASIWTLCVIAVDRYFAITSPFKYQSLLTKNKARVILMVWIVSGLTSFLPIQMHWRATHQ
EAINCYAETCCDFFTNQAYAIASSIVSFYVPLVIMVFVYSRVFQEAQRQLQKIDKSEGRFH
VQNRSSKFCLKEHKALKTLGIIMGTFTLCWLPFFIVNIVHVIQDNLIRKEVYILLNWIGYVN
SGFNPLIYCRSPDFRIAFQELLCLRRSSLKHHHHHHHHHH

with the green residues corresponding to the β_2 AR sequence.

Expression in insect cells

Preparation of recombinant baculovirus and expression of ^{15}N -valine-labeled β_2 AR were carried out as described in Chapter 4.1 and according to Isogai *et al.* (114).

Membrane preparation and purification

The membrane preparation and purification of β_2 AR was adapted from Liu *et al.* (116). In detail, the cell pellet corresponding to 1 L expression culture was filled up to 80 ml with lysis buffer (10 mM HEPES pH (7.5), 10 mM MgCl_2 , 20 mM KCl) and cells were disrupted for 10 s with an electric disperser. Membranes were spun down at 142,000 g for 1 h at 4 °C. This membrane wash was repeated a second time with lysis buffer, a further three times with high osmotic buffer (lysis buffer supplemented with 1 M NaCl), and once again with lysis buffer to remove salt. The membrane pellet fraction was resuspended in 15 ml 10 mM HEPES (pH 7.5), 40 % (v/v) glycerol, 10 mM MgCl_2 , 20 mM KCl and EDTA-free Complete protease inhibitor mix (Roche) and flash frozen at -80 °C.

For solubilization, a 15-ml membrane fractions was thawed and incubated with 15 ml lysis buffer containing EDTA-free Complete protease inhibitor mix (Roche), 1 mM atenolol and 2 mg/ml iodoacetamide for 1 h at 4 °C. Then 25 ml solubilization buffer [100 mM HEPES (pH 7.5), 300 mM NaCl, 1 % (w/v) DDM, 0.2 % CHS (w/v)] was added and incubation continued for 3 hours at 4 °C. After ultracentrifugation for 1 h at 140,000 g, the supernatant was added to 2 ml (per 1 L of culture) Talon Superflow metal affinity resin (GE Healthcare) and incubated overnight at 4 °C.

The Talon resin was then washed with 10 CV 25 mM HEPES (pH 7.5), 800 mM NaCl, 10 % (v/v) glycerol, 0.05 % (w/v) DDM, 10 mM MgCl_2 , 8 mM ATP, 5 mM imidazole, and subsequently with 5 CV 25 mM HEPES (pH 7.5), 150 mM NaCl, 10 % (v/v) glycerol, 0.05 % (w/v) DDM, 5 mM imidazole. β_2 AR was then eluted with 10 CV 25 mM HEPES (pH 7.5), 150 mM NaCl, 10 % (v/v) glycerol, 0.05 % (w/v) DDM, 200 mM imidazole.

β_2 AR was further purified by M1 FLAG affinity chromatography. For this, the sample was supplemented with 5 mM CaCl_2 , added to an Anti-FLAG M1 agarose affinity gel (Sigma-Aldrich) and incubated overnight at 4 °C. After a wash step with 25 mM HEPES (pH 7.5), 150 mM NaCl, 0.05 % (w/v) DDM, 5 mM CaCl_2 , β_2 AR was eluted with 25 mM HEPES (pH 7.5), 150 mM NaCl, 0.05 % (w/v) DDM, 5 mM EDTA and 0.1 mg/ml FLAG peptide. The protein was concentrated using an Amicon centrifugal device with a 50 kDa MWCO

(Millipore) at 4 °C and 2,000 g. β_2 AR was deglycosylated by incubation with 2 μ l PNGase F (75,000 units, NEB) for 1 h at 4 °C.

Gel electrophoresis and Western blotting

Gel electrophoresis and Western blot analysis with poly-His antibody were performed as described in Chapter 4.1.

NMR experiments and data analysis

An NMR sample containing 20 μ M receptor was prepared in 25 mM HEPES (pH 7.5), 150 mM NaCl, 0.05 % (w/v) DDM and concentrated to 250 μ l in a Shigemi tube and supplemented with 5 % D₂O and 0.02 % NaN₃. All NMR experiments were performed at a temperature of 298 K on a Bruker AVANCE 900 MHz spectrometer equipped with a TCI cryoprobe. Amide proton T₂ times were determined from a jump-return spin-echo experiment (201). ¹H-¹⁵N TROSY experiments were recorded with 80 (¹⁵N) x 1024 (¹H) complex points and acquisition times of 16 ms (¹⁵N) and 42 ms (¹H). For optimal sensitivity, the ¹H-¹⁵N transfer time was reduced to 3.0 ms and the interscan delay set to 1 s. All NMR spectra were processed with NMRPipe (204) and analyzed with SPARKY (205).

References

1. I. T. Arkin, A. T. Brunger, D. M. Engelman, Are there dominant membrane protein families with a given number of helices? *Proteins*. **28**, 465–466 (1997).
2. E. Wallin, G. V. Heijne, Genome-wide analysis of integral membrane proteins from eubacterial, archaean, and eukaryotic organisms. *Protein Science*. **7**, 1029–1038 (2008).
3. J. Drews, Drug Discovery: A Historical Perspective. *Science*. **287**, 1960–1964 (2000).
4. R. B. Russell, D. S. Eggleston, New roles for structure in biology and drug discovery. *Nat. Struct. Mol. Biol.* **7**, 928–930 (2000).
5. F. C. Bernstein, T. F. Koetzle, G. J. B. Williams, E. F. Meyer Jr., M. D. Brice, J. R. Rodgers, O. Kennard, T. Shimanouchi, M. Tasumi, The protein data bank: A computer-based archival file for macromolecular structures. *Journal of Molecular Biology*. **112**, 535–542 (1977).
6. H.-H. Shen, T. Lithgow, L. L. Martin, Reconstitution of Membrane Proteins into Model Membranes: Seeking Better Ways to Retain Protein Activities. *IJMS*. **14**, 1589–1607 (2013).
7. R. Böhm, G. Wagner, S. Hiller, Solution Nuclear Magnetic Resonance Spectroscopy of Integral Membrane Proteins. *Reference Module in Life Sciences* (2017).
8. R. Henderson, P. N. T. Unwin, Three-dimensional model of purple membrane obtained by electron microscopy. *Nature*. **257**, 28–32 (1975).
9. J. Deisenhofer, O. Epp, K. Miki, R. Huber, H. Michel, X-ray structure analysis of a membrane protein complex: Electron density map at 3 Å resolution and a model of the chromophores of the photosynthetic reaction center from *Rhodospseudomonas viridis*. *Journal of Molecular Biology*. **180**, 385–398 (1984).
10. E. M. Landau, J. P. Rosenbusch, Lipidic cubic phases: a novel concept for the crystallization of membrane proteins. *Proc. Natl. Acad. Sci. U.S.A.* **93**, 14532–14535 (1996).
11. H. J. Kang, C. Lee, D. Drew, Breaking the barriers in membrane protein crystallography. *The International Journal of Biochemistry & Cell Biology*. **45**, 636–644 (2013).
12. M. Caffrey, Crystallizing Membrane Proteins for Structure Determination: Use of Lipidic Mesophases. *Annu. Rev. Biophys.* **38**, 29–51 (2009).
13. N. Thonghin, V. Kargas, J. Clews, R. C. Ford, Cryo-electron microscopy of membrane proteins. *Methods*. **147**, 176–186 (2018).

14. R. De Zorzi, W. Mi, M. Liao, T. Walz, Single-particle electron microscopy in the study of membrane protein structure. *Microscopy (Oxf)*. **65**, 81–96 (2016).
15. S. J. Opella, F. M. Marassi, Applications of NMR to membrane proteins. *Archives of Biochemistry and Biophysics*. **628**, 92–101 (2017).
16. K. H. Gardner, L. E. Kay, THE USE OF ²H, ¹³C, ¹⁵N MULTIDIMENSIONAL NMR TO STUDY THE STRUCTURE AND DYNAMICS OF PROTEINS. *Annu Rev Biophys Biomol Struct*. **27**, 357–406 (1998).
17. Y. Fan, S. Emami, R. Munro, V. Ladizhansky, L. S. Brown, Isotope Labeling of Eukaryotic Membrane Proteins in Yeast for Solid-State NMR. *Meth. Enzymol*. **565**, 193–212 (2015).
18. M. Sastry, C. A. Bewley, P. D. Kwong, Effective Isotope Labeling of Proteins in a Mammalian Expression System. *Meth. Enzymol*. **565**, 289–307 (2015).
19. B. Franke, C. Opitz, S. Isogai, A. Grahl, L. Delgado, A. D. Gossert, S. Grzesiek, Production of isotope-labeled proteins in insect cells for NMR. *J Biomol NMR*. **22**, 1–12 (2018).
20. B. Liang, L. K. Tamm, NMR as a tool to investigate the structure, dynamics and function of membrane proteins. *Nat. Struct. Mol. Biol*. **23**, 468–474 (2016).
21. K. Pervushin, R. Riek, G. Wider, K. Wüthrich, Attenuated T₂ relaxation by mutual cancellation of dipole–dipole coupling and chemical shift anisotropy indicates an avenue to NMR structures of very large biological macromolecules in solution. *Proc. Natl. Acad. Sci. U.S.A.* **94**, 12366–12371 (1997).
22. R. Riek, G. Wider, K. Pervushin, K. Wüthrich, Polarization transfer by cross-correlated relaxation in solution NMR with very large molecules. *Proc. Natl. Acad. Sci. U.S.A.* **96**, 4918–4923 (1999).
23. A. C. Wang, S. Grzesiek, R. Tschudin, P. J. Lodi, A. Bax, Sequential backbone assignment of isotopically enriched proteins in D₂O by deuterium-decoupled HA(CA)N and HA(CACO)N. *J Biomol NMR*. **5**, 376–382 (1995).
24. M. Sattler, S. W. Fesik, Use of deuterium labeling in NMR: overcoming a sizeable problem. *Structure*. **4**, 1245–1249 (1996).
25. H. Yagi, T. Tsujimoto, T. Yamazaki, M. Yoshida, H. Akutsu, Conformational Change of H⁺-ATPase β Monomer Revealed on Segmental Isotope Labeling NMR Spectroscopy. *J. Am. Chem. Soc.* **126**, 16632–16638 (2004).
26. D.-W. Sim, Z. Lu, H.-S. Won, S.-N. Lee, M.-D. Seo, B.-J. Lee, J.-H. Kim, Application of Solution NMR to Structural Studies on α -Helical Integral Membrane Proteins. *Molecules*. **22**, 1347 (2017).

27. J. Fiaux, E. B. Bertelsen, A. L. Horwich, K. Wüthrich, Uniform and Residue-specific ¹⁵N-labeling of Proteins on a Highly Deuterated Background. *J Biomol NMR*. **29**, 289–297 (2004).
28. S. Hiller, R. G. Garces, T. J. Malia, V. Y. Orekhov, M. Colombini, G. Wagner, Solution Structure of the Integral Human Membrane Protein VDAC-1 in Detergent Micelles. *Science*. **321**, 1206–1210 (2008).
29. K. Oxenoid, Y. Dong, C. Cao, T. Cui, Y. Sancak, A. L. Markhard, Z. Grabarek, L. Kong, Z. Liu, B. Ouyang, Y. Cong, V. K. Mootha, J. J. Chou, Architecture of the mitochondrial calcium uniporter. *Nature*. **533**, 269–273 (2016).
30. S. Bibow, S. Hiller, A guide to quantifying membrane protein dynamics in lipids and other native-like environments by solution-state NMR spectroscopy. *The FEBS Journal*. **38**, 4905 (2018).
31. J. H. Chill, J. M. Louis, J. L. Baber, A. Bax, Measurement of ¹⁵N relaxation in the detergent-solubilized tetrameric KcsA potassium channel. *J Biomol NMR*. **36**, 123–136 (2006).
32. R. M. Pielak, K. Oxenoid, J. J. Chou, Structural Investigation of Rimantadine Inhibition of the AM2-BM2 Chimera Channel of Influenza Viruses. *Structure*. **19**, 1655–1663 (2011).
33. M. Zhang, R. Huang, R. Ackermann, S.-C. Im, L. Waskell, A. Schwendeman, A. Ramamoorthy, Reconstitution of the Cytb5–CytP450 Complex in Nanodiscs for Structural Studies using NMR Spectroscopy. *Angew. Chem. Int. Ed. Engl.* **55**, 4497–4499 (2016).
34. L. Frey, S. Hiller, R. Riek, S. Bibow, Lipid- and Cholesterol-Mediated Time-Scale-Specific Modulation of the Outer Membrane Protein X Dynamics in Lipid Bilayers. *J. Am. Chem. Soc.*, jacs.8b09188 (2018).
35. G. E. Pake, Nuclear Resonance Absorption in Hydrated Crystals: Fine Structure of the Proton Line. *J. Chem. Phys.* **16**, 327–336 (1948).
36. R. K. Hester, J. L. Ackerman, B. L. Neff, J. S. Waugh, Separated Local Field Spectra in NMR: Determination of Structure of Solids. *Phys. Rev. Lett.* **36**, 1081–1083 (1976).
37. E. R. ANDREW, A. BRADBURY, R. G. EADES, Nuclear Magnetic Resonance Spectra from a Crystal rotated at High Speed. *Nature*. **182**, 1659 EP —1659 (1958).
38. S. H. Park, B. B. Das, F. Casagrande, Y. Tian, H. J. Nothnagel, M. Chu, H. Kiefer, K. Maier, A. A. De Angelis, F. M. Marassi, S. J. Opella, Structure of the chemokine receptor CXCR1 in phospholipid bilayers. *Nature*. **491**, 779–783 (2012).
39. T. Gopinath, K. R. Mote, G. Veglia, Sensitivity and resolution enhancement of oriented solid-state NMR: Application to membrane proteins. *Progress in Nuclear Magnetic Resonance Spectroscopy*. **75**, 50–68 (2013).

40. S. K. Hansen, K. Bertelsen, B. Paaske, N. C. Nielsen, T. Vosegaard, Solid-state NMR methods for oriented membrane proteins. *Progress in Nuclear Magnetic Resonance Spectroscopy*. **88-89**, 48–85 (2015).
41. Y. Li, D. A. Berthold, H. L. Frericks, R. B. Gennis, C. M. Rienstra, Partial ¹³C and ¹⁵N Chemical-Shift Assignments of the Disulfide-Bond-Forming Enzyme DsbB by 3D Magic-Angle Spinning NMR Spectroscopy. *Chembiochem*. **8**, 434–442 (2007).
42. M. T. Eddy, T.-C. Ong, L. Clark, O. Tejjido, P. C. A. van der Wel, R. Garces, G. Wagner, T. K. Rostovtseva, R. G. Griffin, Lipid Dynamics and Protein–Lipid Interactions in 2D Crystals Formed with the β -Barrel Integral Membrane Protein VDAC1. *J. Am. Chem. Soc.* **134**, 6375–6387 (2012).
43. S. A. Shahid, S. Markovic, D. Linke, B.-J. van Rossum, Assignment and secondary structure of the YadA membrane protein by solid-state MAS NMR. *Sci. Rep.* **2**, 803 (2012).
44. Y. Ishii, R. Tycko, Sensitivity Enhancement in Solid State ¹⁵N NMR by Indirect Detection with High-Speed Magic Angle Spinning. *Journal of Magnetic Resonance*. **142**, 199–204 (2000).
45. Y. Ishii, J. P. Yesinowski, R. Tycko, Sensitivity Enhancement in Solid-State ¹³C NMR of Synthetic Polymers and Biopolymers by ¹H NMR Detection with High-Speed Magic Angle Spinning. *J. Am. Chem. Soc.* **123**, 2921–2922 (2001).
46. B. Reif, R. G. Griffin, ¹H detected ¹H,¹⁵N correlation spectroscopy in rotating solids. *Journal of Magnetic Resonance*. **160**, 78–83 (2003).
47. V. Chevelkov, K. Rehbein, A. Diehl, B. Reif, Ultrahigh Resolution in Proton Solid-State NMR Spectroscopy at High Levels of Deuteration. *Angew. Chem. Int. Ed. Engl.* **45**, 3878–3881 (2006).
48. R. Linser, M. Dasari, M. Hiller, V. Higman, U. Fink, J. M. L. del Amo, S. Markovic, L. Handel, B. Kessler, P. Schmieder, D. Oesterhelt, H. Oschkinat, B. Reif, Proton-Detected Solid-State NMR Spectroscopy of Fibrillar and Membrane Proteins. *Angew. Chem. Int. Ed. Engl.* **50**, 4508–4512 (2011).
49. V. Agarwal, S. Penzel, K. Szekely, R. Cadalbert, E. Testori, A. Oss, J. Past, A. Samoson, M. Ernst, A. Böckmann, B. H. Meier, De Novo 3D Structure Determination from Sub-milligram Protein Samples by Solid-State 100 kHz MAS NMR Spectroscopy. *Angew. Chem. Int. Ed. Engl.* **53**, 12253–12256 (2014).
50. T. Kimura, K. Vukoti, D. L. Lynch, D. P. Hurst, A. Grossfield, M. C. Pitman, P. H. Reggio, A. A. Yeliseev, K. Gawrisch, Global fold of human cannabinoid type 2 receptor probed by solid-state ¹³C-, ¹⁵N-MAS NMR and molecular dynamics simulations. *Proteins*. **82**, 452–465 (2014).
51. S. Tapaneyakorn, A. D. Goddard, J. Oates, C. L. Willis, A. Watts, Solution- and solid-state NMR studies of GPCRs and their ligands. *BBA - Biomembranes*. **1808**, 1462–1475 (2011).

52. M. F. Brown, M. P. Heyn, C. Job, S. Kim, S. Moltke, K. Nakanishi, A. A. Nevzorov, A. V. Struts, G. F. J. Salgado, I. Wallat, Solid-State ²H NMR spectroscopy of retinal proteins in aligned membranes. *BBA - Biomembranes*. **1768**, 2979–3000 (2007).
53. M. Hong, Y. Su, Structure and dynamics of cationic membrane peptides and proteins: Insights from solid-state NMR. *Protein Science*. **20**, 641–655 (2011).
54. R. Fu, Y. Miao, H. Qin, T. A. Cross, Probing Hydronium Ion Histidine NH Exchange Rate Constants in the M2 Channel via Indirect Observation of Dipolar-Dephased ¹⁵N Signals in Magic-Angle-Spinning NMR. *J. Am. Chem. Soc.* **138**, 15801–15804 (2016).
55. M. P. Bhate, B. J. Wylie, L. Tian, A. E. McDermott, Conformational Dynamics in the Selectivity Filter of KcsA in Response to Potassium Ion Concentration. *Journal of Molecular Biology*. **401**, 155–166 (2010).
56. Y. Miao, H. Qin, R. Fu, M. Sharma, T. V. Can, I. Hung, S. Luca, P. L. Gor'kov, W. W. Brey, T. A. Cross, M2 Proton Channel Structural Validation from Full-Length Protein Samples in Synthetic Bilayers and E. coli Membranes. *Angew. Chem. Int. Ed. Engl.* **51**, 8383–8386 (2012).
57. M. Renault, R. T.-V. Boxtel, M. P. Bos, J. A. Post, J. Tommassen, M. Baldus, Cellular solid-state nuclear magnetic resonance spectroscopy. *Proc. Natl. Acad. Sci. U.S.A.* **109**, 4863–4868 (2012).
58. M. Kaplan, S. Narasimhan, C. de Heus, D. Mance, S. van Doorn, K. Houben, D. Popov-Čeleketić, R. Damman, E. A. Katrukha, P. Jain, W. J. C. Geerts, A. J. R. Heck, G. E. Folkers, L. C. Kapitein, S. Lemeer, P. M. P. van Bergen en Henegouwen, M. Baldus, EGFR Dynamics Change during Activation in Native Membranes as Revealed by NMR. *CELL*. **167**, 1241–1251.e11 (2016).
59. S. Takeda, S. Kadowaki, T. Haga, H. Takaesu, S. Mitaku, Identification of G protein-coupled receptor genes from the human genome sequence. *FEBS Lett.* **520**, 97–101 (2002).
60. R. Fredriksson, M. C. Lagerström, L.-G. Lundin, H. B. Schiöth, The G-Protein-Coupled Receptors in the Human Genome Form Five Main Families. Phylogenetic Analysis, Paralagon Groups, and Fingerprints. *Molecular Pharmacology*. **63**, 1256–1272 (2003).
61. M. C. Lagerström, H. B. Schiöth, Structural diversity of G protein-coupled receptors and significance for drug discovery. *7*, 339–357 (2008).
62. S. P. Alexander, A. Christopoulos, A. P. Davenport, E. Kelly, N. V. Marrion, J. A. Peters, E. Faccenda, S. D. Harding, A. J. Pawson, J. L. Sharman, C. Southan, J. A. Davies, THE CONCISE GUIDE TO PHARMACOLOGY 2017/18: G protein-coupled receptors. *Br J Pharmacol*. **174**, S17–S129 (2017).
63. J. P. Overington, B. Al-Lazikani, A. L. Hopkins, How many drug targets are there? *Nature Reviews Drug Discovery* 2017 16:12. **5**, 993 EP —996 (2006).

64. A. J. Venkatakrisnan, X. Deupi, G. Lebon, C. G. Tate, G. F. Schertler, M. M. Babu, Molecular signatures of G-protein-coupled receptors. *Nature*. **494**, 185–194 (2013).
65. L. Mengjie, W. Beili, Structural studies of G protein-coupled receptors. *IUBMB Life*. **68**, 894–903 (2016).
66. J. Bockaert, J.-P. Pin, Molecular tinkering of G protein-coupled receptors: an evolutionary success. *EMBO J*. **18**, 1723–1729 (1999).
67. D. Filmore, It's a GPCR world. *Modern Drug Discovery*. **7**, 24–28 (2004).
68. A. S. Hauser, M. M. Attwood, M. Rask-Andersen, H. B. Schiöth, D. E. Gloriam, Trends in GPCR drug discovery: new agents, targets and indications. *Nature Reviews Drug Discovery 2017 16:12*. **16**, 829–842 (2017).
69. K. L. Pierce, R. T. Premont, R. J. Lefkowitz, Signalling: Seven-transmembrane receptors. *Nature Publishing Group*. **3**, 639–650 (2002).
70. W. M. Oldham, H. E. Hamm, Heterotrimeric G protein activation by G-protein-coupled receptors. *Nat. Rev. Mol. Cell Biol*. **9**, 60 EP —71 (2008).
71. D. J. Dupré, M. Robitaille, R. V. Rebois, T. E. Hébert, The Role of G $\beta\gamma$ Subunits in the Organization, Assembly, and Function of GPCR Signaling Complexes. *Annu. Rev. Pharmacol. Toxicol*. **49**, 31–56 (2009).
72. M. I. Simon, M. P. Strathmann, N. Gautam, Diversity of G proteins in signal transduction. *Science*. **252**, 802–808 (1991).
73. J. A. Pitcher, N. J. Freedman, R. J. Lefkowitz, G Protein–Coupled Receptor Kinases. *Annu. Rev. Biochem*. **67**, 653–692 (1998).
74. V. V. Gurevich, E. V. Gurevich, Analyzing the roles of multi-functional proteins in cells: The case of arrestins and GRKs. *Critical Reviews in Biochemistry and Molecular Biology*. **50**, 440–452 (2015).
75. O. B. Goodman, J. G. Krupnick, F. Santini, V. V. Gurevich, R. B. Penn, A. W. Gagnon, J. H. Keen, J. L. Benovic, Beta-arrestin acts as a clathrin adaptor in endocytosis of the beta2-adrenergic receptor. *Nature*. **383**, 447–450 (1996).
76. A. Marchese, M. M. Paing, B. R. S. Temple, J. Trejo, G Protein–Coupled Receptor Sorting to Endosomes and Lysosomes. *Annu. Rev. Pharmacol. Toxicol*. **48**, 601–629 (2008).
77. A. C. Hanyaloglu, M. V. Zastrow, Regulation of GPCRs by Endocytic Membrane Trafficking and Its Potential Implications. *Annu. Rev. Pharmacol. Toxicol*. **48**, 537–568 (2008).
78. E. Galliera, V. R. Jala, J. O. Trent, R. Bonecchi, P. Signorelli, R. J. Lefkowitz, A. Mantovani, M. Locati, B. Haribabu, beta-Arrestin-dependent constitutive internalization of the human chemokine decoy receptor D6. *J. Biol. Chem*. **279**, 25590–25597 (2004).

79. P. H. McDonald, C.-W. Chow, W. E. Miller, S. A. Laporte, M. E. Field, F.-T. Lin, R. J. Davis, R. J. Lefkowitz, β -Arrestin 2: A Receptor-Regulated MAPK Scaffold for the Activation of JNK3. *Science*. **290**, 1574–1577 (2000).
80. A. R. B. Thomsen, B. Plouffe, T. J. Cahill III, A. K. Shukla, J. T. Tarrasch, A. M. Dosey, A. W. Kahsai, R. T. Strachan, B. Pani, J. P. Mahoney, L. Huang, B. Breton, F. M. Heydenreich, R. K. Sunahara, G. Skiniotis, M. Bouvier, R. J. Lefkowitz, GPCR-G Protein- β -Arrestin Super-Complex Mediates Sustained G Protein Signaling. *CELL*. **166**, 907–919 (2016).
81. K. Palczewski, T. Kumasaka, T. Hori, C. A. Behnke, H. Motoshima, B. A. Fox, I. Le Trong, D. C. Teller, T. Okada, R. E. Stenkamp, M. Yamamoto, M. Miyano, Crystal Structure of Rhodopsin: A G Protein-Coupled Receptor. *Science*. **289**, 739–745 (2000).
82. S. Maeda, G. F. Schertler, Production of GPCR and GPCR complexes for structure determination. *Current Opinion in Structural Biology*. **23**, 381–392 (2013).
83. D. M. Rosenbaum, V. Cherezov, M. A. Hanson, S. G. F. Rasmussen, F. S. Thian, T. S. Kobilka, H.-J. Choi, X. J. Yao, W. I. Weis, R. C. Stevens, B. K. Kobilka, GPCR engineering yields high-resolution structural insights into beta2-adrenergic receptor function. *Science*. **318**, 1266–1273 (2007).
84. D. Milić, D. B. Veprintsev, Large-scale production and protein engineering of G protein-coupled receptors for structural studies. *Front Pharmacol*. **6**, 66 (2015).
85. V. Cherezov, D. M. Rosenbaum, M. A. Hanson, S. G. F. Rasmussen, F. S. Thian, T. S. Kobilka, H. J. Choi, P. Kuhn, W. I. Weis, B. K. Kobilka, R. C. Stevens, High-Resolution Crystal Structure of an Engineered Human β_2 -Adrenergic G Protein-Coupled Receptor. *Science*. **318**, 1258–1265 (2007).
86. S. G. F. Rasmussen, H.-J. Choi, D. M. Rosenbaum, T. S. Kobilka, F. S. Thian, P. C. Edwards, M. Burghammer, V. R. P. Ratnala, R. Sanishvili, R. F. Fischetti, G. F. X. Schertler, W. I. Weis, B. K. Kobilka, Crystal structure of the human beta2 adrenergic G-protein-coupled receptor. *Nature*. **450**, 383–387 (2007).
87. G. Pándy-Szekeres, C. Munk, T. M. Tsonkov, S. Mordalski, K. Harpsøe, A. S. Hauser, A. J. Bojarski, D. E. Gloriam, GPCRdb in 2018: adding GPCR structure models and ligands. *Nucleic Acids Res*. **46**, D440–D446 (2018).
88. G. Lebon, T. Warne, P. C. Edwards, K. Bennett, C. J. Langmead, A. G. W. Leslie, C. G. Tate, Agonist-bound adenosine A2A receptor structures reveal common features of GPCR activation. *Nature*. **474**, 521–525 (2011).
89. D. M. Thal, A. Glukhova, P. M. Sexton, A. Christopoulos, Structural insights into G-protein-coupled receptor allostery. *Nature*. **559**, 45–53 (2018).
90. S. G. F. Rasmussen *et al.*, Crystal structure of the β_2 adrenergic receptor–Gs protein complex. *Nature*. **477**, 549 EP —555 (2011).

91. S. G. F. Rasmussen, H.-J. Choi, J. J. Fung, E. Pardon, P. Casarosa, P. S. Chae, B. T. DeVree, D. M. Rosenbaum, F. S. Thian, T. S. Kobilka, A. Schnapp, I. Konetzki, R. K. Sunahara, S. H. Gellman, A. Pautsch, J. Steyaert, W. I. Weis, B. K. Kobilka, Structure of a nanobody-stabilized active state of the $\beta(2)$ adrenoceptor. *Nature*. **469**, 175–180 (2011).
92. A. M. Ring, A. Manglik, A. C. Kruse, M. D. Enos, W. I. Weis, K. C. Garcia, B. K. Kobilka, Adrenaline-activated structure of $\beta(2)$ -adrenoceptor stabilized by an engineered nanobody. *Nature*. **502**, 575–579 (2013).
93. Y. Kang *et al.*, Crystal structure of rhodopsin bound to arrestin by femtosecond X-ray laser. *Nature*. **523**, 561–567 (2015).
94. X. E. Zhou *et al.*, Identification of Phosphorylation Codes for Arrestin Recruitment by G Protein-Coupled Receptors. *CELL*. **170**, 457–469.e13 (2017).
95. A. Gautier, H. R. Mott, M. J. Bostock, J. P. Kirkpatrick, D. Nietlispach, Structure determination of the seven-helix transmembrane receptor sensory rhodopsin II by solution NMR spectroscopy. *Nat. Struct. Mol. Biol.* **17**, 768–774 (2010).
96. S. Reckel, D. Gottstein, J. Stehle, F. Löhr, M.-K. Verhoefen, M. Takeda, R. Silvers, M. Kainosho, C. Glaubitz, J. Wachtveitl, F. Bernhard, H. Schwalbe, P. Güntert, V. Dötsch, Solution NMR Structure of Proteorhodopsin. *Angew. Chem. Int. Ed. Engl.* **50**, 11942–11946 (2011).
97. Y. Zhang, B. Sun, D. Feng, H. Hu, M. Chu, Q. Qu, J. T. Tarrasch, S. Li, T. Sun Kobilka, B. K. Kobilka, G. Skiniotis, Cryo-EM structure of the activated GLP-1 receptor in complex with a G protein. *Nature*. **546**, 248 EP —253 (2017).
98. C. J. Draper-Joyce, M. Khoshouei, D. M. Thal, Y.-L. Liang, A. T. N. Nguyen, S. G. B. Furness, H. Venugopal, J.-A. Baltos, J. M. Plitzko, R. Danev, W. Baumeister, L. T. May, D. Wootten, P. M. Sexton, A. Glukhova, A. Christopoulos, Structure of the adenosine-bound human adenosine A₁ receptor–G_i complex. *Nature*. **63**, 1–563 (2018).
99. J. García-Nafria, R. Nehmé, P. C. Edwards, C. G. Tate, Cryo-EM structure of the serotonin 5-HT_{1B} receptor coupled to heterotrimeric G_o. *Nature*. **7**, 118 (2018).
100. H. A. Safdari, S. Pandey, A. K. Shukla, S. Dutta, Illuminating GPCR Signaling by Cryo-EM. *Trends in Cell Biology*. **28**, 591–594 (2018).
101. B. K. Kobilka, X. Deupi, Conformational complexity of G-protein-coupled receptors. *Trends in Pharmacological Sciences*. **28**, 397–406 (2007).
102. N. R. Latorraca, A. J. Venkatakrishnan, R. O. Dror, GPCR Dynamics: Structures in Motion. *Chem. Rev.* **117**, 139–155 (2016).
103. S. Bockenhauer, A. Fürstenberg, X. J. Yao, B. K. Kobilka, W. E. Moerner, Conformational Dynamics of Single G Protein-Coupled Receptors in Solution. *J Phys Chem B*. **115**, 13328–13338 (2011).

104. L. Olofsson, S. Felekyan, E. Doumazane, P. Scholler, L. Fabre, J. M. Zwier, P. Rondard, C. A. M. Seidel, J.-P. Pin, E. Margeat, Fine tuning of sub-millisecond conformational dynamics controls metabotropic glutamate receptors agonist efficacy. *Nature Communications*. **5**, 5206 (2014).
105. R. Vafabakhsh, J. Levitz, E. Y. Isacoff, Conformational dynamics of a class C G-protein-coupled receptor. *Nature*. **524**, 497–501 (2015).
106. R. Lamichhane, J. J. Liu, G. Pljevaljcic, K. L. White, E. van der Schans, V. Katritch, R. C. Stevens, K. Wüthrich, D. P. Millar, Single-molecule view of basal activity and activation mechanisms of the G protein-coupled receptor β 2AR. *Proc. Natl. Acad. Sci. U.S.A.* **112**, 14254–14259 (2015).
107. A. Manglik, T. H. Kim, M. Masureel, C. Altenbach, Z. Yang, D. Hilger, M. T. Lerch, T. S. Kobilka, F. S. Thian, W. L. Hubbell, R. S. Prosser, B. K. Kobilka, Structural Insights into the Dynamic Process of β 2-Adrenergic Receptor Signaling. *CELL*. **161**, 1101–1111 (2015).
108. R. O. Dror, D. H. Arlow, P. Maragakis, T. J. Mildorf, A. C. Pan, H. Xu, D. W. Borhani, D. E. Shaw, Activation mechanism of the β 2-adrenergic receptor. *Proceedings of the National Academy of Sciences*. **108**, 18684–18689 (2011).
109. R. O. Dror, A. C. Pan, D. H. Arlow, D. W. Borhani, P. Maragakis, Y. Shan, H. Xu, D. E. Shaw, Pathway and mechanism of drug binding to G-protein-coupled receptors. *Proceedings of the National Academy of Sciences*. **108**, 13118–13123 (2011).
110. A. Gonzalez, T. Perez-Acle, L. Pardo, X. Deupi, Molecular Basis of Ligand Dissociation in β -Adrenergic Receptors. *PLoS ONE*. **6**, e23815 (2011).
111. H. C. S. Chan, S. Filipek, S. Yuan, The Principles of Ligand Specificity on beta-2-adrenergic receptor. *Sci. Rep.* **6**, 34736 (2016).
112. C. Opitz, S. Isogai, S. Grzesiek, An economic approach to efficient isotope labeling in insect cells using homemade ^{15}N -, ^{13}C - and ^2H -labeled yeast extracts. *J Biomol NMR*. **62**, 373–385 (2015).
113. Y. Kofuku, T. Ueda, J. Okude, Y. Shiraishi, K. Kondo, M. Maeda, H. Tsujishita, I. Shimada, Efficacy of the β 2-adrenergic receptor is determined by conformational equilibrium in the transmembrane region. *Nature Communications*. **3**, 1045 (2012).
114. S. Isogai, X. Deupi, C. Opitz, F. M. Heydenreich, C.-J. Tsai, F. Brueckner, G. F. X. Schertler, D. B. Veprintsev, S. Grzesiek, Backbone NMR reveals allosteric signal transduction networks in the β 1-adrenergic receptor. *Nature*. **530**, 237 EP —241 (2016).
115. M. P. Bokoch, Y. Zou, S. G. F. Rasmussen, C. W. Liu, R. Nygaard, D. M. Rosenbaum, J. J. Fung, H.-J. Choi, F. S. Thian, T. S. Kobilka, J. D. Puglisi, W. I. Weis, L. Pardo, R. S. Prosser, L. Mueller, B. K. Kobilka, Ligand-specific regulation

- of the extracellular surface of a G-protein-coupled receptor. *Nature*. **463**, 108–112 (2010).
116. J. J. Liu, R. Horst, V. Katritch, R. C. Stevens, K. Wüthrich, Biased signaling pathways in β 2-adrenergic receptor characterized by 19F-NMR. *Science*. **335**, 1106–1110 (2012).
117. Y. Kofuku, T. Ueda, J. Okude, Y. Shiraishi, K. Kondo, T. Mizumura, S. Suzuki, I. Shimada, Functional dynamics of deuterated β 2 -adrenergic receptor in lipid bilayers revealed by NMR spectroscopy. *Angew. Chem. Int. Ed. Engl.* **53**, 13376–13379 (2014).
118. R. Nygaard, R. O. Dror, T. J. Mildorf, D. H. Arlow, A. Manglik, A. C. Pan, C. W. Liu, J. J. Fung, M. P. Bokoch, F. S. Thian, T. S. Kobilka, D. E. Shaw, L. Mueller, R. S. Prosser, B. K. Kobilka, The dynamic process of β (2)-adrenergic receptor activation. *CELL*. **152**, 532–542 (2013).
119. A. S. Solt, M. J. Bostock, B. Shrestha, P. Kumar, T. Warne, C. G. Tate, D. Nietlispach, Insight into partial agonism by observing multiple equilibria for ligand-bound and Gs-mimetic nanobody-bound β 1-adrenergic receptor. *Nature Communications*. **8**, 1795 (2017).
120. Y. Kofuku, T. Yokomizo, S. Imai, Y. Shiraishi, M. Natsume, H. Itoh, M. Inoue, K. Nakata, S. Igarashi, H. Yamaguchi, T. Mizukoshi, E.-I. Suzuki, T. Ueda, I. Shimada, Deuteration and selective labeling of alanine methyl groups of β 2-adrenergic receptor expressed in a baculovirus-insect cell expression system. *J Biomol NMR*. **71**, 185–192 (2018).
121. J. Klein-Seetharaman, N. V. K. Yanamala, F. Javeed, P. J. Reeves, E. V. Getmanova, M. C. Loewen, H. Schwalbe, H. G. Khorana, Differential dynamics in the G protein-coupled receptor rhodopsin revealed by solution NMR. *Proc. Natl. Acad. Sci. U.S.A.* **101**, 3409–3413 (2004).
122. H. J. Kim, S. C. Howell, W. D. Van Horn, Y. H. Jeon, C. R. Sanders, Recent Advances in the Application of Solution NMR Spectroscopy to Multi-Span Integral Membrane Proteins. *Progress in Nuclear Magnetic Resonance Spectroscopy*. **55**, 335–360 (2009).
123. M. L. Nasr, D. Baptista, M. Strauss, Z.-Y. J. Sun, S. Grigoriu, S. Huser, A. Plückthun, F. Hagn, T. Walz, J. M. Hogle, G. Wagner, Covalently circularized nanodiscs for studying membrane proteins and viral entry. *Nat Meth*. **14**, 49–52 (2017).
124. M. T. Eddy, M.-Y. Lee, Z.-G. Gao, K. L. White, T. Didenko, R. Horst, M. Audet, P. Stanczak, K. M. McClary, G. W. Han, K. A. Jacobson, R. C. Stevens, K. Wüthrich, Allosteric Coupling of Drug Binding and Intracellular Signaling in the A2A Adenosine Receptor. *CELL*. **172**, 68–80.e12 (2018).
125. M. R. G. Taylor, Pharmacogenetics of the human beta-adrenergic receptors. *Pharmacogenomics J*. **7**, 29–37 (2007).

126. M. J. Serrano-Vega, C. G. Tate, Transferability of thermostabilizing mutations between β -adrenergic receptors. *Mol. Membr. Biol.* **26**, 385–396 (2009).
127. T. Warne, M. J. Serrano-Vega, C. G. Tate, G. F. X. Schertler, Protein Expression and Purification. *Protein Expression and Purification.* **65**, 204–213 (2009).
128. J. G. Baker, R. G. W. Proudman, C. G. Tate, The pharmacological effects of the thermostabilising (m23) mutations and intra and extracellular (β 36) deletions essential for crystallisation of the turkey β -adrenoceptor. *Naunyn Schmiedebergs Arch. Pharmacol.* **384**, 71–91 (2011).
129. F. Brueckner, C. L. Piscitelli, C.-J. Tsai, J. Standfuss, X. Deupi, G. F. X. Schertler, Structure of β -adrenergic receptors. *Meth. Enzymol.* **520**, 117–151 (2013).
130. C. R. BALISTRERI, C. CARUSO, M. P. GRIMALDI, F. LISTÌ, S. VASTO, V. ORLANDO, A. M. CAMPAGNA, D. LIO, G. CANDORE, CCR5 Receptor. *Annals of the New York Academy of Sciences.* **1100**, 162–172 (2007).
131. A. BreLOT, L. A. Chakrabarti, CCR5 Revisited: How Mechanisms of HIV Entry Govern AIDS Pathogenesis. *Journal of Molecular Biology.* **430**, 2557–2589 (2018).
132. C. J. Raport, J. Gosling, V. L. Schweickart, P. W. Gray, I. F. Charo, Molecular cloning and functional characterization of a novel human CC chemokine receptor (CCR5) for RANTES, MIP-1 β , and MIP-1 α . *J. Biol. Chem.* **271**, 17161–17166 (1996).
133. M. Baggiolini, Chemokines and leukocyte traffic. *Nature.* **392**, 565–568 (1998).
134. L. Vangelista, S. Vento, The Expanding Therapeutic Perspective of CCR5 Blockade. *Front Immunol.* **8**, 657 (2018).
135. I. Scurci, E. Martins, O. Hartley, CCR5: Established paradigms and new frontiers for a “celebrity” chemokine receptor. *Cytokine.* **109**, 81–93 (2018).
136. G. Alkhatib, C. Combadiere, C. C. Broder, Y. Feng, P. E. Kennedy, P. M. Murphy, E. A. Berger, CC CKR5: A RANTES, MIP-1 α , MIP-1 β Receptor as a Fusion Cofactor for Macrophage-Tropic HIV-1. *Science.* **272**, 1955–1958 (1996).
137. T. Dragic, V. Litwin, G. P. Allaway, S. R. Martin, Y. Huang, K. A. Nagashima, C. Cayanan, P. J. Maddon, R. A. Koup, J. P. Moore, W. A. Paxton, HIV-1 entry into CD4⁺ cells is mediated by the chemokine receptor CC-CKR-5. *Nature.* **381**, 667 EP—673 (1996).
138. B. J. Doranz, J. Rucker, Y. Yi, R. J. Smyth, M. Samson, S. C. Peiper, M. Parmentier, R. G. Collman, R. W. Doms, A Dual-Tropic Primary HIV-1 Isolate That Uses Fusin and the β -Chemokine Receptors CKR-5, CKR-3, and CKR-2b as Fusion Cofactors. *CELL.* **85**, 1149–1158 (1996).
139. H. Deng, R. Liu, W. Ellmeier, S. Choe, D. Unutmaz, M. Burkhart, P. Di Marzio, S. Marmon, R. E. Sutton, C. M. Hill, C. B. Davis, S. C. Peiper, T. J. Schall, D. R.

- Littman, N. R. Landau, Identification of a major co-receptor for primary isolates of HIV-1. *Nature*. **381**, 661–666 (1996).
140. H. Choe, K. A. Martin, M. Farzan, J. Sodroski, N. P. Gerard, C. Gerard, Structural interactions between chemokine receptors, gp120 Env and CD4. *Semin. Immunol.* **10**, 249–257 (1998).
141. R. W. Doms, S. C. Peiper, Unwelcomed guests with master keys: how HIV uses chemokine receptors for cellular entry. *Virology*. **235**, 179–190 (1997).
142. M. M. Lederman, A. Penn-Nicholson, M. Cho, D. Mosier, Biology of CCR5 and Its Role in HIV Infection and Treatment. *JAMA*. **296**, 815–826 (2006).
143. E. Oberlin, A. Amara, F. O. Bachelier, C. Bessia, J.-L. Virelizier, F. Arenzana-Seisdedos, O. Schwartz, J.-M. Heard, I. Clark-Lewis, D. F. Legler, M. Loetscher, M. Baggiolini, B. Moser, The CXC chemokine SDF-1 is the ligand for LESTR/fusin and prevents infection by T-cell-line-adapted HIV-1. *Nature*. **382**, 833–835 (1996).
144. Y. Feng, C. C. Broder, P. E. Kennedy, E. A. Berger, HIV-1 entry cofactor: functional cDNA cloning of a seven-transmembrane, G protein-coupled receptor. *Science*. **272**, 872–877 (1996).
145. E. A. Berger, P. M. Murphy, J. M. Farber, Chemokine receptors as HIV-1 coreceptors: Roles in viral entry, tropism, and disease. *Annu. Rev. Immunol.* **17**, 657–700 (1999).
146. R. Liu, W. A. Paxton, S. Choe, D. Ceradini, S. R. Martin, R. Horuk, M. E. MacDonald, H. Stuhlmann, R. A. Koup, N. R. Landau, Homozygous defect in HIV-1 coreceptor accounts for resistance of some multiply-exposed individuals to HIV-1 infection. *CELL*. **86**, 367–377 (1996).
147. M. Samson *et al.*, Resistance to HIV-1 infection in Caucasian individuals bearing mutant alleles of the CCR-5 chemokine receptor gene. *Nature*. **382**, 722 EP —725 (1996).
148. P. Dorr, M. Westby, S. Dobbs, P. Griffin, B. Irvine, M. Macartney, J. Mori, G. Rickett, C. Smith-Burchnell, C. Napier, R. Webster, D. Armour, D. Price, B. Stammen, A. Wood, M. Perros, Maraviroc (UK-427,857), a potent, orally bioavailable, and selective small-molecule inhibitor of chemokine receptor CCR5 with broad-spectrum anti-human immunodeficiency virus type 1 activity. *Antimicrobial Agents and Chemotherapy*. **49**, 4721–4732 (2005).
149. R. S. Veazey, B. Ling, L. C. Green, E. P. Ribka, J. D. Lifson, M. Piatak Jr, M. M. Lederman, D. Mosier, R. Offord, O. Hartley, Topically Applied Recombinant Chemokine Analogues Fully Protect Macaques from Vaginal Simian-Human Immunodeficiency Virus Challenge. *J INFECT DIS*. **199**, 1525–1527 (2009).
150. B. L. Gilliam, D. J. Riedel, R. R. Redfield, Clinical use of CCR5 inhibitors in HIV and beyond. *Journal of Translational Medicine*. **9**, S9 (2011).

151. R. M. Gulick *et al.*, Safety and Tolerability of Maraviroc-Containing Regimens to Prevent HIV Infection in Women: A Phase 2 Randomized Trial. *Ann Intern Med.* **167**, 384–393 (2017).
152. R. K. Malcolm, C. J. Forbes, L. Geer, R. S. Veazey, L. Goldman, P. Johan Klasse, J. P. Moore, Pharmacokinetics and efficacy of a vaginally administered maraviroc gel in rhesus macaques. *J Antimicrob Chemother.* **68**, 678–683 (2013).
153. Q. Tan, Y. Zhu, J. Li, Z. Chen, G. W. Han, I. Kufareva, T. Li, L. Ma, G. Fenalti, W. Zhang, X. Xie, H. Yang, H. Jiang, V. Cherezov, H. Liu, R. C. Stevens, Q. Zhao, B. Wu, Structure of the CCR5 Chemokine Receptor-HIV Entry Inhibitor Maraviroc Complex. *Science.* **341**, 1387–1390 (2013).
154. M. Baggiolini, B. Dewald, B. Moser, Human Chemokines: An Update. *Annu. Rev. Immunol.* **15**, 675–705 (1997).
155. J. Garcia-Perez, P. Rueda, J. Alcami, D. Rognan, F. Arenzana-Seisdedos, B. Lagane, E. Kellenberger, Allosteric Model of Maraviroc Binding to CC Chemokine Receptor 5 (CCR5). *Journal of Biological Chemistry.* **286**, 33409–33421 (2011).
156. J. Jin, F. Momboisse, G. Boncompain, F. Koensgen, Z. Zhou, N. Cordeiro, F. Arenzana-Seisdedos, F. Perez, B. Lagane, E. Kellenberger, A. BreLOT, CCR5 adopts three homodimeric conformations that control cell surface delivery. *Sci. Signal.* **11**, eaal2869–650 (2018).
157. J. Garcia-Perez, P. Rueda, I. Staropoli, E. Kellenberger, J. Alcami, F. Arenzana-Seisdedos, B. Lagane, New insights into the mechanisms whereby low molecular weight CCR5 ligands inhibit HIV-1 infection. *Journal of Biological Chemistry.* **286**, 4978–4990 (2011).
158. M. A. Lobritz, A. N. Ratcliff, A. J. Marozsan, D. M. Dudley, J. C. Tilton, E. J. Arts, Multifaceted Mechanisms of HIV Inhibition and Resistance to CCR5 Inhibitors PSC-RANTES and Maraviroc. *Antimicrobial Agents and Chemotherapy.* **57**, 2640–2650 (2013).
159. M. Roche, K. Borm, J. K. Flynn, S. R. Lewin, M. J. Churchill, Molecular Gymnastics: Mechanisms of HIV-1 Resistance to CCR5 Antagonists and Impact on Virus Phenotypes. *Current Topics in Medicinal Chemistry.* **16**, 1091–1106 (2016).
160. C. Blanpain, B. Lee, J. Vakili, B. J. Doranz, C. Govaerts, I. Migeotte, M. Sharron, V. Dupriez, G. Vassart, R. W. Doms, M. Parmentier, Extracellular cysteines of CCR5 are required for chemokine binding, but dispensable for HIV-1 coreceptor activity. *J. Biol. Chem.* **274**, 18902–18908 (1999).
161. M. Farzan, T. Mirzabekov, P. Kolchinsky, R. Wyatt, M. Cayabyab, N. P. Gerard, C. Gerard, J. Sodroski, H. Choe, Tyrosine sulfation of the amino terminus of CCR5 facilitates HIV-1 entry. *CELL.* **96**, 667–676 (1999).
162. N. Bannert, S. Craig, M. Farzan, D. Sogah, N. V. Santo, H. Choe, J. Sodroski, Sialylated O-Glycans and Sulfated Tyrosines in the NH₂-Terminal Domain of CC

- Chemokine Receptor 5 Contribute to High Affinity Binding of Chemokines. *J. Exp. Med.* **194**, 1661–1674 (2001).
163. E. G. Cormier, M. Persuh, D. A. D. Thompson, S. W. Lin, T. P. Sakmar, W. C. Olson, T. Dragic, Specific interaction of CCR5 amino-terminal domain peptides containing sulfotyrosines with HIV-1 envelope glycoprotein gp120. *Proc. Natl. Acad. Sci. U.S.A.* **97**, 5762–5767 (2000).
164. C. Blanpain, V. Wittamer, J. M. Vanderwinden, A. Boom, B. Renneboog, B. Lee, E. Le Poul, L. El Asmar, C. Govaerts, G. Vassart, R. W. Doms, M. Parmentier, Palmitoylation of CCR5 is critical for receptor trafficking and efficient activation of intracellular signaling pathways. *J. Biol. Chem.* **276**, 23795–23804 (2001).
165. M. Oppermann, M. Mack, A. E. Proudfoot, H. Olbrich, Differential effects of CC chemokines on CC chemokine receptor 5 (CCR5) phosphorylation and identification of phosphorylation sites on the CCR5 carboxyl terminus. *J. Biol. Chem.* **274**, 8875–8885 (1999).
166. M. Arimont, S.-L. Sun, R. Leurs, M. Smit, I. J. P. de Esch, C. de Graaf, Structural Analysis of Chemokine Receptor-Ligand Interactions. *J. Med. Chem.* **60**, 4735–4779 (2017).
167. A. E. I. Proudfoot, Z. Johnson, P. Bonvin, T. M. Handel, Glycosaminoglycan Interactions with Chemokines Add Complexity to a Complex System. *Pharmaceuticals*. **10** (2017).
168. I. Kufareva, M. Gustavsson, Y. Zheng, B. S. Stephens, T. M. Handel, What Do Structures Tell Us About Chemokine Receptor Function and Antagonism? *Annu. Rev. Biophys.* **46**, 175–198 (2017).
169. D. P. Dyer, C. L. Salanga, B. F. Volkman, T. Kawamura, T. M. Handel, The dependence of chemokine-glycosaminoglycan interactions on chemokine oligomerization. *Glycobiology*. **26**, 312–326 (2015).
170. K. B. Bacon, B. A. Premack, P. Gardner, T. J. Schall, Activation of dual T cell signaling pathways by the chemokine RANTES. *Science*. **269**, 1727–1730 (1995).
171. V. Appay, A. Brown, S. Cribbes, E. Randle, L. G. Czaplewski, Aggregation of RANTES Is Responsible for Its Inflammatory Properties: CHARACTERIZATION OF NONAGGREGATING, NONINFLAMMATORY RANTES MUTANTS. *Journal of Biological Chemistry*. **274**, 27505–27512 (1999).
172. K. B. Bacon, M. C. Szabo, H. Yssel, J. B. Bolen, T. J. Schall, RANTES induces tyrosine kinase activity of stably complexed p125FAK and ZAP-70 in human T cells. *J. Exp. Med.* **184**, 873–882 (1996).
173. M. C. Szabo, E. C. Butcher, B. W. McIntyre, T. J. Schall, K. B. Bacon, RANTES stimulation of T lymphocyte adhesion and activation: role for LFA-1 and ICAM-3. *Eur. J. Immunol.* **27**, 1061–1068 (1997).

174. F. Cocchi, A. L. DeVico, A. Garzino-Demo, S. K. Arya, R. C. Gallo, P. Lusso, Identification of RANTES, MIP-1 alpha, and MIP-1 beta as the major HIV-suppressive factors produced by CD8+ T cells. *Science*. **270**, 1811–1815 (1995).
175. O. Hartley, K. Dorgham, D. Perez-Bercoff, F. Cerini, A. Heimann, H. Gaertner, R. E. Offord, G. Pancino, P. Debre, G. Gorochov, Human Immunodeficiency Virus Type 1 Entry Inhibitors Selected on Living Cells from a Library of Phage Chemokines. *Journal of Virology*. **77**, 6637–6644 (2003).
176. P. Proost, Amino-terminal Truncation of Chemokines by CD26/Dipeptidyl-peptidase IV. CONVERSION OF RANTES INTO A POTENT INHIBITOR OF MONOCYTE CHEMOTAXIS AND HIV-1-INFECTION. *Journal of Biological Chemistry*. **273**, 7222–7227 (1998).
177. D. Schols, P. Proost, S. Struyf, A. Wuyts, I. De Meester, S. Scharpé, J. Van Damme, E. De Clercq, CD26-processed RANTES(3-68), but not intact RANTES, has potent anti-HIV-1 activity. *Antiviral Res.* **39**, 175–187 (1998).
178. S. Polo, V. Nardese, C. De Santis, C. Arcelloni, R. Paroni, F. Sironi, A. Verani, M. Rizzi, M. Bolognesi, P. Lusso, Enhancement of the HIV-1 inhibitory activity of RANTES by modification of the N-terminal region: dissociation from CCR5 activation. *Eur. J. Immunol.* **30**, 3190–3198 (2000).
179. V. Nardese, R. Longhi, S. Polo, F. Sironi, C. Arcelloni, R. Paroni, C. DeSantis, P. Sarmientos, M. Rizzi, M. Bolognesi, V. Pavone, P. Lusso, Structural determinants of CCR5 recognition and HIV-1 blockade in RANTES. *Nature Structural Biology*. **8**, 611 EP —615 (2001).
180. M. M. Lederman, R. S. Veazey, R. Offord, D. E. Mosier, J. Dufour, M. Mefford, M. Piatak, J. D. Lifson, J. R. Salkowitz, B. Rodriguez, A. Blauvelt, O. Hartley, Prevention of vaginal SHIV transmission in rhesus macaques through inhibition of CCR5. *Science*. **306**, 485–487 (2004).
181. K. Dorgham, F. Cerini, H. Gaertner, A. Melotti, I. Rossitto-Borlat, G. Gorochov, O. Hartley, Generating Chemokine Analogs with Enhanced Pharmacological Properties Using Phage Display. *Meth. Enzymol.* **570**, 47–72 (2016).
182. H. Gaertner, F. Cerini, J.-M. Escola, G. Kuenzi, A. Melotti, R. Offord, I. Rossitto-Borlat, R. Nedellec, J. Salkowitz, G. Gorochov, D. Mosier, O. Hartley, Highly potent, fully recombinant anti-HIV chemokines: reengineering a low-cost microbicide. *Proceedings of the National Academy of Sciences*. **105**, 17706–17711 (2008).
183. C. Pastore, G. R. Picchio, F. Galimi, R. Fish, O. Hartley, R. E. Offord, D. E. Mosier, Two mechanisms for human immunodeficiency virus type 1 inhibition by N-terminal modifications of RANTES. *Antimicrobial Agents and Chemotherapy*. **47**, 509–517 (2003).
184. P. Colin, Y. Bénureau, I. Staropoli, Y. Wang, N. Gonzalez, J. Alcami, O. Hartley, A. Brelot, F. Arenzana-Seisdedos, B. Lagane, HIV-1 exploits CCR5 conformational

- heterogeneity to escape inhibition by chemokines. *Proceedings of the National Academy of Sciences*. **110**, 9475–9480 (2013).
185. R. Nedellec, M. Coetzer, M. M. Lederman, R. E. Offord, O. Hartley, D. E. Mosier, Resistance to the CCR5 Inhibitor 5P12-RANTES Requires a Difficult Evolution from CCR5 to CXCR4 Coreceptor Use. *PLoS ONE*. **6**, e22020 EP – (2011).
 186. F. Cerini, A. Landay, C. Gichinga, M. M. Lederman, R. Flyckt, D. Starks, R. E. Offord, F. Le Gal, O. Hartley, Chemokine Analogues Show Suitable Stability for Development as Microbicides. *J. Acquir. Immune Defic. Syndr*. **49**, 472–476 (2008).
 187. D. A. Zidar, Endogenous Ligand Bias by Chemokines: Implications at the Front Lines of Infection and Leukocyte Trafficking. *Endocrine, Metabolic & Immune Disorders - Drug Targets*. **11**, 120–131 (2011).
 188. Z. Truan, L. T. Díez, C. Bönsch, S. Malkusch, U. Endesfelder, M. Munteanu, O. Hartley, M. Heilemann, A. Fürstenberg, Journal of Structural Biology. *Journal of Structural Biology*. **184**, 329–334 (2013).
 189. C. Bönsch, M. Munteanu, I. Rossitto-Borlat, A. Fürstenberg, O. Hartley, Potent Anti-HIV Chemokine Analogs Direct Post-Endocytic Sorting of CCR5. *PLoS ONE*. **10**, e0125396 (2015).
 190. W. T. Choi, R. Nedellec, M. Coetzer, P. Colin, B. Lagane, R. E. Offord, O. Hartley, D. E. Mosier, CCR5 Mutations Distinguish N-Terminal Modifications of RANTES (CCL5) with Agonist versus Antagonist Activity. *Journal of Virology*. **86**, 10218–10220 (2012).
 191. Y. Zheng, G. W. Han, R. Abagyan, B. Wu, R. C. Stevens, V. Cherezov, I. Kufareva, T. M. Handel, Structure of CC Chemokine Receptor 5 with a Potent Chemokine Antagonist Reveals Mechanisms of Chemokine Recognition and Molecular Mimicry by HIV. *Immunity*. **46**, 1005–1017.e5 (2017).
 192. J. S. Burg, J. R. Ingram, A. J. Venkatakrishnan, K. M. Jude, A. Dukkipati, E. N. Feinberg, A. Angelini, D. Waghray, R. O. Dror, H. L. Ploegh, K. C. Garcia, Structural basis for chemokine recognition and activation of a viral G protein-coupled receptor. *Science*. **347**, 1113–1117 (2015).
 193. L. Qin, I. Kufareva, L. G. Holden, C. Wang, Y. Zheng, C. Zhao, G. Fenalti, H. Wu, G. W. Han, V. Cherezov, R. Abagyan, R. C. Stevens, T. M. Handel, Crystal structure of the chemokine receptor CXCR4 in complex with a viral chemokine. *Science*. **347**, 1117–1122 (2015).
 194. G. S. Rule, K. T. Hitchens, *Fundamentals of Protein NMR Spectroscopy* (Springer, Dordrecht, 2006; <https://doi.org/10.1007/1-4020-3500-4>).
 195. G. Wagner, The importance of being floppy. *Nat. Struct. Mol. Biol.* **2**, 255–257 (1995).

196. G. Lipari, A. Szabo, Model-free approach to the interpretation of nuclear magnetic resonance relaxation in macromolecules. 1. Theory and range of validity. *J. Am. Chem. Soc.* **104**, 4546–4559 (1982).
197. A. G. REDFIELD, On the Theory of Relaxation Processes. *IBM J. Res. & Dev.* **1**, 19–31 (1957).
198. H. M. McConnell, Reaction Rates by Nuclear Magnetic Resonance. *J. Chem. Phys.* **28**, 430–431 (1958).
199. J. Cavanagh, W. J. Fairbrother, A. G. Palmer, M. Rance, N. J. Skelton, Eds., *Protein NMR Spectroscopy (Second Edition)* (Academic Press, Burlington, 2007).
200. D. P. Staus, R. T. Strachan, A. Manglik, B. Pani, A. W. Kahsai, T. H. Kim, L. M. Wingler, S. Ahn, A. Chatterjee, A. Masoudi, A. C. Kruse, E. Pardon, J. Steyaert, W. I. Weis, R. S. Prosser, B. K. Kobilka, T. Costa, R. J. Lefkowitz, Allosteric nanobodies reveal the dynamic range and diverse mechanisms of G-protein-coupled receptor activation. *Nature*. **535**, 448–452 (2016).
201. V. Sklenář, A. Bax, Spin-echo water suppression for the generation of pure-phase two-dimensional NMR spectra. *Journal of Magnetic Resonance (1969)*. **74**, 469–479 (1987).
202. K. Y. Chung, T. H. Kim, A. Manglik, R. Alvares, B. K. Kobilka, R. S. Prosser, Role of Detergents in Conformational Exchange of a G Protein-coupled Receptor. *Journal of Biological Chemistry*. **287**, 36305–36311 (2012).
203. R. Dawaliby, C. Trubbia, C. Delporte, M. Masureel, P. Van Antwerpen, B. K. Kobilka, C. Govaerts, Allosteric regulation of G protein-coupled receptor activity by phospholipids. *Nature Chemical Biology* (2015).
204. F. Delaglio, S. Grzesiek, G. W. Vuister, G. Zhu, J. Pfeifer, A. Bax, NMRPipe: A multidimensional spectral processing system based on UNIX pipes. *J Biomol NMR*. **6**, 277–293 (1995).
205. T. D. Goddard, D. G. Kneller, *SPARKY, version 3* (University of California, 2008).
206. F. Hagn, M. Etzkorn, T. Raschle, G. Wagner, Optimized Phospholipid Bilayer Nanodiscs Facilitate High-Resolution Structure Determination of Membrane Proteins. *J. Am. Chem. Soc.* **135**, 1919–1925 (2013).
207. L. Skora, B. Shrestha, A. D. Gossert, Isotope Labeling of Proteins in Insect Cells. *Meth. Enzymol.* **565**, 245–288 (2015).
208. A. Strauss, F. Bitsch, B. Cutting, G. Fendrich, P. Graff, J. Liebetanz, M. Zurini, W. Jahnke, Amino-acid-type selective isotope labeling of proteins expressed in Baculovirus-infected insect cells useful for NMR studies. *J Biomol NMR*. **26**, 367–372 (2003).

209. A. Sitarska, L. Skora, J. Klopp, S. Roest, C. Fernández, B. Shrestha, A. D. Gossert, Affordable uniform isotope labeling with (2)H, (13)C and (15)N in insect cells. *J Biomol NMR*. **62**, 191–197 (2015).
210. L. Nisius, M. Rogowski, L. Vangelista, S. Grzesiek, Large-scale expression and purification of the major HIV-1 coreceptor CCR5 and characterization of its interaction with RANTES. *Protein Expression and Purification*. **61**, 155–162 (2008).
211. C. Yoshiura, Y. Kofuku, T. Ueda, Y. Mase, M. Yokogawa, M. Osawa, Y. Terashima, K. Matsushima, I. Shimada, NMR Analyses of the Interaction between CCR5 and Its Ligand Using Functional Reconstitution of CCR5 in Lipid Bilayers. *J. Am. Chem. Soc.* **132**, 6768–6777 (2010).
212. X. M. Guan, T. S. Kobilka, B. K. Kobilka, Enhancement of membrane insertion and function in a type IIIb membrane protein following introduction of a cleavable signal peptide. *J. Biol. Chem.* **267**, 21995–21998 (1992).
213. A. Rath, M. Glibowicka, V. G. Nadeau, G. Chen, C. M. Deber, Detergent binding explains anomalous SDS-PAGE migration of membrane proteins. *Proceedings of the National Academy of Sciences*. **106**, 1760–1765 (2009).
214. T. Mirzabekov, N. Bannert, M. Farzan, W. Hofmann, P. Kolchinsky, L. J. Wu, R. Wyatt, J. Sodroski, Enhanced expression, native purification, and characterization of CCR5, a principal HIV-1 coreceptor. *J. Biol. Chem.* **274**, 28745–28750 (1999).
215. L. Wu, G. LaRosa, N. Kassam, C. J. Gordon, H. Heath, N. Ruffing, H. Chen, J. Humblías, M. Samson, M. Parmentier, J. P. Moore, C. R. Mackay, Interaction of chemokine receptor CCR5 with its ligands: multiple domains for HIV-1 gp120 binding and a single domain for chemokine binding. *J. Exp. Med.* **186**, 1373–1381 (1997).
216. A. A. Thompson, J. J. Liu, E. Chun, D. Wacker, H. Wu, V. Cherezov, R. C. Stevens, GPCR stabilization using the bicelle-like architecture of mixed sterol-detergent micelles. *Methods*. **55**, 310–317 (2011).
217. A. I. Alexandrov, M. Mileni, E. Y. T. Chien, M. A. Hanson, R. C. Stevens, Microscale fluorescent thermal stability assay for membrane proteins. *Structure*. **16**, 351–359 (2008).
218. F. C. Ayers, G. L. Warner, K. L. Smith, D. A. Lawrence, Fluorometric quantitation of cellular and nonprotein thiols. *Analytical Biochemistry*. **154**, 186–193 (1986).
219. P. S. Chae, S. G. F. Rasmussen, R. R. Rana, K. Gotfryd, R. Chandra, M. A. Goren, A. C. Kruse, S. Nurva, C. J. Loland, Y. Pierre, D. Drew, J.-L. Popot, D. Picot, B. G. Fox, L. Guan, U. Gether, B. Byrne, B. Kobilka, S. H. Gellman, Maltose-neopentyl glycol (MNG) amphiphiles for solubilization, stabilization and crystallization of membrane proteins. *Nat Meth.* **7**, 1003–1008 (2010).

220. A. Strauss, F. Bitsch, G. Fendrich, P. Graff, R. Knecht, B. Meyhack, W. Jahnke, Efficient uniform isotope labeling of Abl kinase expressed in Baculovirus-infected insect cells. *J Biomol NMR*. **31**, 343–349 (2005).
221. A. D. Gossert, A. Hinniger, S. Gutmann, W. Jahnke, A. Strauss, C. Fernández, A simple protocol for amino acid type selective isotope labeling in insect cells with improved yields and high reproducibility. *J Biomol NMR*. **51**, 449–456 (2011).
222. D. R. O'Reilly, L. Miller, V. A. Luckow, *Baculovirus expression vectors : a laboratory manual* (Oxford University Press, New York, 1994).
223. A. Meola, C. Deville, S. A. Jeffers, P. Guardado-Calvo, I. Vasiliauskaite, C. Sizun, C. Girard-Blanc, C. Malosse, C. van Heijenoort, J. Chamot-Rooke, T. Krey, E. Guittet, S. Pêtres, F. A. Rey, F. Bontems, Robust and low cost uniform (15)N-labeling of proteins expressed in Drosophila S2 cells and Spodoptera frugiperda Sf9 cells for NMR applications. *Journal of Structural Biology*. **188**, 71–78 (2014).
224. Y. Cheng, Single-Particle Cryo-EM at Crystallographic Resolution. *CELL*. **161**, 450–457 (2015).
225. M. Khoshouei, M. Radjainia, W. Baumeister, R. Danev, Cryo-EM structure of haemoglobin at 3.2 Å determined with the Volta phase plate. *Nature Communications*. **8**, 16099 (2017).
226. K. Murata, M. Wolf, Cryo-electron microscopy for structural analysis of dynamic biological macromolecules. *Biochimica et Biophysica Acta (BBA) - General Subjects*. **1862**, 324–334 (2018).
227. C. Opitz, “PhD thesis: Development and application of an economic approach to isotope labeling in higher eukaryotes for NMR studies” (2016), pp. 1–201.
228. S. Grzesiek, A. Bax, J. S. Hu, N. Tjandra, J. Kaufman, I. Palmer, S. J. Stahl, P. T. Wingfield, Refined solution structure and backbone dynamics of HIV-1 Nef. **6**, 1248–1263 (1997).
229. L. E. Kay, D. A. Torchia, A. Bax, Backbone dynamics of proteins as studied by nitrogen-15 inverse detected heteronuclear NMR spectroscopy: application to staphylococcal nuclease. *Biochemistry*. **28**, 8972–8979 (1989).
230. N. Tjandra, A. Szabo, A. Bax, Protein Backbone Dynamics and 15N Chemical Shift Anisotropy from Quantitative Measurement of Relaxation Interference Effects. *J. Am. Chem. Soc.* **118**, 6986–6991 (1996).
231. D. S. Garrett, R. Powers, A. M. Gronenborn, G. M. Clore, A common sense approach to peak picking in two-, three-, and four-dimensional spectra using automatic computer analysis of contour diagrams. *Journal of Magnetic Resonance (1969)*. **95**, 214–220 (1991).
232. P. Schuck, H. Zhao, C. A. Brautigam, R. Ghirlando, *Basic Principles of Analytical Ultracentrifugation* (CRC Press, 2016).

233. N. J. Skelton, F. Aspiras, J. Ogez, T. J. Schall, Proton NMR Assignments and Solution Conformation of RANTES, a Chemokine of the C-C Type. *Biochemistry*. **34**, 5329–5342 (1995).
234. Arlene J Hoogewerf, Gabriele S V Kuschert, Amanda E I Proudfoot, Frederic Borlat, Ian Clark-Lewis, A. Christine A Power, T. N. C. Wells, *Glycosaminoglycans Mediate Cell Surface Oligomerization of Chemokines* (American Chemical Society, 1997), vol. 36.
235. L. G. Czaplewski *et al.*, Identification of amino acid residues critical for aggregation of human CC chemokines macrophage inflammatory protein (MIP)-1alpha, MIP-1beta, and RANTES. Characterization of active disaggregated chemokine variants. *J. Biol. Chem.* **274**, 16077–16084 (1999).
236. X. Wang, C. Watson, J. S. Sharp, T. M. Handel, J. H. Prestegard, Oligomeric Structure of the Chemokine CCL5/RANTES from NMR, MS, and SAXS Data. *Structure*. **19**, 1138–1148 (2011).
237. L. Duma, D. Häussinger, M. Rogowski, P. Lusso, S. Grzesiek, Recognition of RANTES by extracellular parts of the CCR5 receptor. *Journal of Molecular Biology*. **365**, 1063–1075 (2007).
238. M. Wiktor, O. Hartley, S. Grzesiek, Characterization of Structure, Dynamics, and Detergent Interactions of the Anti-HIV Chemokine Variant 5P12-RANTES. *Biophysj.* **105**, 2586–2597 (2013).
239. N. Signoret, T. Christophe, M. Oppermann, M. Marsh, pH-Independent Endocytic Cycling of the Chemokine Receptor CCR5. *Traffic*. **5**, 529–543 (2004).
240. L. Nisius, PhD thesis: Expression, Purification and Characterization of the HIV-1 coreceptor CCR5 and its ligand RANTES and High-pressure NMR investigations of hydrogen bonds in biomolecules, 1–130 (2010).
241. M. Wiktor, PhD thesis: Towards NMR analysis of the HIV-1 coreceptor CCR5 and its interaction with RANTES, 1–187 (2013).
242. G. S. V. Kuschert, F. Coulin, C. A. Power, A. E. I. Proudfoot, R. E. Hubbard, A. J. Hoogewerf, T. N. C. Wells, Glycosaminoglycans Interact Selectively with Chemokines and Modulate Receptor Binding and Cellular Responses. *Biochemistry*. **38**, 12959–12968 (1999).
243. C. Deshauer, A. M. Morgan, E. O. Ryan, T. M. Handel, J. H. Prestegard, X. Wang, Interactions of the Chemokine CCL5/RANTES with Medium-Sized Chondroitin Sulfate Ligands. *Structure*. **23**, 1066–1077 (2015).
244. J. P. Shaw, Z. Johnson, F. Borlat, C. Zwahlen, A. Kungl, K. Roulin, A. Harrenga, T. N. C. Wells, A. E. I. Proudfoot, The X-Ray Structure of RANTES Heparin-Derived Disaccharides Allows the Rational Design of Chemokine Inhibitors. *Structure*. **12**, 2081–2093 (2004).

245. A. E. Proudfoot, S. Fritchley, F. Borlat, J. P. Shaw, F. Vilbois, C. Zwahlen, A. Trkola, D. Marchant, P. R. Clapham, T. N. Wells, The BBXB motif of RANTES is the principal site for heparin binding and controls receptor selectivity. *J. Biol. Chem.* **276**, 10620–10626 (2001).
246. M. Secchi, R. Longhi, L. Vassena, F. Sironi, S. Grzesiek, P. Lusso, L. Vangelista, Enhancement of Anti-HIV-1 Activity by Hot Spot Evolution of RANTES-Derived Peptides. *Chemistry & Biology.* **19**, 1579–1588 (2012).
247. N. X. Wang, S. F. Sieg, M. M. Lederman, R. E. Offord, O. Hartley, H. A. von Recum, Using Glycosaminoglycan/Chemokine Interactions for the Long-Term Delivery of 5P12-RANTES in HIV Prevention. *Mol. Pharmaceutics.* **10**, 3564–3573 (2013).
248. G. Simmons, P. R. Clapham, L. Picard, R. E. Offord, M. M. Rosenkilde, T. W. Schwartz, R. Buser, T. N. C. Wells, A. E. I. Proudfoot, Potent Inhibition of HIV-1 Infectivity in Macrophages and Lymphocytes by a Novel CCR5 Antagonist. *Science.* **276**, 276–279 (1997).
249. Deepika R Pakianathan, Ellen G Kuta, Dean R Artis, A. Nicholas J Skelton, C. A. Hébert, Distinct but Overlapping Epitopes for the Interaction of a CC-Chemokine with CCR1, CCR3, and CCR5. *Biochemistry.* **36**, 9642–9648 (1997).
250. C. Blanpain, B. J. Doranz, A. Bondue, C. Govaerts, A. De Leener, G. Vassart, R. W. Doms, A. Proudfoot, M. Parmentier, The Core Domain of Chemokines Binds CCR5 Extracellular Domains while Their Amino Terminus Interacts with the Transmembrane Helix Bundle. *Journal of Biological Chemistry.* **278**, 5179–5187 (2003).
251. D. J. Scholten, M. Canals, D. Maussang, L. Roumen, M. J. Smit, M. Wijtmans, C. de Graaf, H. F. Vischer, R. Leurs, Pharmacological modulation of chemokine receptor function. *Br J Pharmacol.* **165**, 1617–1643 (2012).
252. J. P. Ludeman, M. J. Stone, The structural role of receptor tyrosine sulfation in chemokine recognition. *Br J Pharmacol.* **171**, 1167–1179 (2014).
253. E. Schnur, N. Kessler, Y. Zherdev, E. Noah, T. Scherf, F.-X. Ding, S. Rabinovich, B. Arshava, V. Kurbatska, A. Leonciks, A. Tsimanis, O. Rosen, F. Naider, J. Anglister, NMR mapping of RANTES surfaces interacting with CCR5 using linked extracellular domains. *FEBS J.* **280**, 2068–2084 (2013).
254. M. Abayev, J. P. G. L. M. Rodrigues, G. Srivastava, B. Arshava, Ł. Jaremko, M. Jaremko, F. Naider, M. Levitt, J. Anglister, The solution structure of monomeric CCL5 in complex with a doubly sulfated N-terminal segment of CCR5. *The FEBS Journal.* **285**, 1988–2003 (2018).
255. H. Lüttgen, R. Robelek, R. Mühlberger, T. Diercks, S. C. Schuster, P. Köhler, H. Kessler, A. Bacher, G. Richter, Transcriptional Regulation by Antitermination. Interaction of RNA with NusB Protein and NusB/NusE Protein Complex of *Escherichia coli*. *Journal of Molecular Biology.* **316**, 875–885 (2002).

256. M. P. Williamson, Using chemical shift perturbation to characterise ligand binding. *Progress in Nuclear Magnetic Resonance Spectroscopy*. **73**, 1–16 (2013).
257. J. R. Lewandowski, J.-N. Dumez, Ü. Akbey, S. Lange, L. Emsley, H. Oschkinat, Enhanced Resolution and Coherence Lifetimes in the Solid-State NMR Spectroscopy of Perdeuterated Proteins under Ultrafast Magic-Angle Spinning. *J Phys Chem Lett*. **2**, 2205–2211 (2011).
258. S. R. Hartmann, E. L. Hahn, Nuclear Double Resonance in the Rotating Frame. *Phys. Rev.* **128**, 2042–2053 (1962).
259. I. Bertini, C. Luchinat, G. Parigi, E. Ravera, B. Reif, P. Turano, Solid-state NMR of proteins sedimented by ultracentrifugation. *Proceedings of the National Academy of Sciences*. **108**, 10396–10399 (2011).
260. E. Barbet-Massin *et al.*, Rapid proton-detected NMR assignment for proteins with fast magic angle spinning. *J. Am. Chem. Soc.* **136**, 12489–12497 (2014).
261. S. H. Park, S. Berkamp, J. Radoicic, A. A. De Angelis, S. J. Opella, Interaction of Monomeric Interleukin-8 with CXCR1 Mapped by Proton-Detected Fast MAS Solid-State NMR. *Biophys. J.* **113**, 2695–2705 (2017).
262. C. Govaerts, A. Bondue, J.-Y. Springael, M. Olivella, X. Deupi, E. Le Poul, S. J. Wodak, M. Parmentier, L. Pardo, C. Blanpain, Activation of CCR5 by chemokines involves an aromatic cluster between transmembrane helices 2 and 3. *J. Biol. Chem.* **278**, 1892–1903 (2003).
263. K. Maeda, D. Das, H. Ogata-Aoki, H. Nakata, T. Miyakawa, Y. Tojo, R. Norman, Y. Takaoka, J. Ding, G. F. Arnold, E. Arnold, H. Mitsuya, Structural and molecular interactions of CCR5 inhibitors with CCR5. *J. Biol. Chem.* **281**, 12688–12698 (2006).
264. O. Fritze, S. Filipek, V. Kuksa, K. Palczewski, K. P. Hofmann, O. P. Ernst, Role of the conserved NPxxY(x)5,6F motif in the rhodopsin ground state and during activation. *Proc. Natl. Acad. Sci. U.S.A.* **100**, 2290–2295 (2003).
265. J. A. Goncalves, K. South, S. Ahuja, E. Zaitseva, C. A. Opefi, M. Eilers, R. Vogel, P. J. Reeves, S. O. Smith, Highly conserved tyrosine stabilizes the active state of rhodopsin. *Proc. Natl. Acad. Sci. U.S.A.* **107**, 19861–19866 (2010).
266. H. Nomiya, O. Yoshie, Functional roles of evolutionary conserved motifs and residues in vertebrate chemokine receptors. *Journal of Leukocyte Biology*. **97**, 39–47 (2015).
267. M. Salzmann, K. Pervushin, G. Wider, H. Senn, K. Wüthrich, TROSY in triple-resonance experiments: new perspectives for sequential NMR assignment of large proteins. *Proc. Natl. Acad. Sci. U.S.A.* **95**, 13585–13590 (1998).
268. R. Horst, J. J. Liu, R. C. Stevens, K. Wüthrich, β 2-Adrenergic Receptor Activation by Agonists Studied with ^{19}F NMR Spectroscopy. **52**, 10762–10765 (2013).

269. T. H. Kim, K. Y. Chung, A. Manglik, A. L. Hansen, R. O. Dror, T. J. Mildorf, D. E. Shaw, B. K. Kobilka, R. S. Prosser, The role of ligands on the equilibria between functional states of a G protein-coupled receptor. *J. Am. Chem. Soc.* **135**, 9465–9474 (2013).
270. C. B. Roth, M. A. Hanson, R. C. Stevens, Stabilization of the human beta2-adrenergic receptor TM4-TM3-TM5 helix interface by mutagenesis of Glu122(3.41), a critical residue in GPCR structure. *Journal of Molecular Biology.* **376**, 1305–1319 (2008).
271. A. Luxembourg, M. Hekman, E. M. Ross, Immunologic mapping of the amino- and carboxy-termini of the turkey erythrocyte β -adrenergic receptor; Selective proteolysis of both domains. *FEBS Lett.* **283**, 155–158 (1991).
272. F. Boege, M. Ward, R. Jürss, M. Hekman, E. J. Helmreich, Role of glycosylation for beta 2-adrenoceptor function in A431 cells. *J. Biol. Chem.* **263**, 9040–9049 (1988).
273. E. Rands, M. R. Candelore, A. H. Cheung, W. S. Hill, C. D. Strader, R. A. Dixon, Mutational analysis of beta-adrenergic receptor glycosylation. *J. Biol. Chem.* **265**, 10759–10764 (1990).
274. J. Mialet-Perez, S. A. Green, W. E. Miller, S. B. Liggett, A primate-dominant third glycosylation site of the beta2-adrenergic receptor routes receptors to degradation during agonist regulation. *J. Biol. Chem.* **279**, 38603–38607 (2004).
275. M. G. Caron, Y. Srinivasan, J. Pitha, K. Kociolek, R. J. Lefkowitz, Affinity chromatography of the beta-adrenergic receptor. *J. Biol. Chem.* **254**, 2923–2927 (1979).